

The University of Maine

DigitalCommons@UMaine

Electronic Theses and Dissertations

Fogler Library

Spring 5-3-2024

Understanding the Role of Fatty Acid Metabolism in Hematological Malignancies Through the Lens of the Acyl-CoA Synthetase Long Chain Isozyme Family

Connor Murphy

University of Maine, connor.s.murphy@maine.edu

Follow this and additional works at: <https://digitalcommons.library.umaine.edu/etd>



Part of the [Medicine and Health Sciences Commons](#)

Recommended Citation

Murphy, Connor, "Understanding the Role of Fatty Acid Metabolism in Hematological Malignancies Through the Lens of the Acyl-CoA Synthetase Long Chain Isozyme Family" (2024). *Electronic Theses and Dissertations*. 3988.

<https://digitalcommons.library.umaine.edu/etd/3988>

This Open-Access Dissertation is brought to you for free and open access by DigitalCommons@UMaine. It has been accepted for inclusion in Electronic Theses and Dissertations by an authorized administrator of DigitalCommons@UMaine. For more information, please contact um.library.technical.services@maine.edu.

**UNDERSTANDING THE ROLE OF FATTY ACID METABOLISM IN
HEMATOLOGICAL MALIGNANCIES THROUGH THE LENS
OF THE ACYL-COA SYNTHETASE LONG CHAIN
ISOZYME FAMILY**

By

Connor Spencer Murphy

B.S. Brandeis University, 2014

A DISSERTATION

Submitted in Partial Fulfillment of the
Requirements for the Degree of
Doctor of Philosophy
(in Biomedical Science)

The Graduate School
The University of Maine
May 2024

Advisory Committee:

Michaela R. Reagan, Advisor, Faculty Scientist II, MaineHealth Institute for Research

Chair: Calvin P. H. Vary, Faculty Scientist III, MaineHealth Institute for Research

Thomas Gridley, Faculty Scientist III, MaineHealth Institute for Research

Benjamin King, Associate Professor, University of Maine Orono

Robert Koza, Faculty Scientist II, MaineHealth Institute for Research

Lucy Liaw, Faculty Scientist III, MaineHealth Institute for Research

© 2024 Connor S. Murphy
All Rights Reserved

**UNDERSTANDING THE ROLE OF FATTY ACID METABOLISM IN
HEMATOLOGICAL MALIGNANCIES THROUGH THE LENS
OF THE ACYL-COA SYNTHETASE LONG CHAIN
ISOZYME FAMILY**

By Connor Spencer Murphy

Dissertation Advisor: Dr. Michaela Reagan

An Abstract of the Dissertation Presented
in Partial Fulfillment of the Requirements for the
Degree of Doctor of Philosophy
(in Biomedical Science)
May 2024

Multiple myeloma (MM) is an incurable cancer of plasma cells with a 5-year survival rate of 60%. Obesity correlates with increased incidence of MM and high body mass index correlates with a poor treatment response. Studies of obesity and myeloma are mainly at the epidemiological level and have not extensively explored the molecular mechanisms of this relationship. Therefore, there is a critical need to understand how obesity contributes to support cancers such as MM. The intersection of obesity and MM and the largely understudied role of fatty acid (FA) metabolism in MM cells motivated the immediate goals of this work: to identify the molecular components of FA metabolism that contribute to MM cell survival and proliferation and understand the mechanisms of how those components contribute MM cell fitness. To help combat MM cell drug resistance, the ultimate goal of this research is to identify novel therapeutic targets in MM cells and possibly other hematological malignancies.

To achieve our goals, we used bioinformatic approaches to first identify candidate FA metabolism genes and molecular phenotyping and unbiased

transcriptomic and proteomic approaches to understand the mechanisms of the phenotypes that were observed. An *in vitro* system of human cell lines of both MM and acute myeloid leukemia and of human bone marrow adipocytes differentiated from human mesenchymal stem cells was used.

This body of work provides evidence that the acyl-CoA synthetase long chain family members (ACSLs) support MM cell mitochondrial function, survival, and proliferation. The ACSL family convert free long-chain fatty acids into fatty acyl-CoA esters and play key roles in catabolic and anabolic fatty acid metabolism. Here, we show that inhibition of ACSLs in human myeloma cell lines using the pharmacological inhibitor Triascin C (TriC) causes apoptosis and decreases proliferation in a dose- and time-dependent manner, induces a transcriptome associated with the integrated stress response and cell death, a proteomic and functional profile associated with mitochondrial dysfunction. This work demonstrates that targeting the ACSL family in MM cells holds promise as a novel therapeutic target and warrants additional mechanistic studies to understand how the ACSL family MM cells respond to terminal stressors.

DEDICATION

To all those who are fighting cancer, their families, and healthcare providers. For all those lost and found.

ACKNOWLEDGEMENTS

I want to thank Dr. Michaela Reagan for allowing me to grow as a scientist and person under her mentorship. I am tremendously grateful for the continuous support and patience of my committee members: my chair, Dr. Calvin Vary, Dr. Thomas Gridley, Dr. Benjamin King, Dr. Robert Koza, Dr. Lucy Liaw and former member Dr. Vicki Losick.

Thank you to Dr. Johnson Liu, Dr. Andrew Rodgers for their invaluable clinical insight and mentorship.

Thank you to Dr. Clifford Rosen, Dr. Joseph Nadeau and Dr. Judith Storch for their scientific insight and career advice.

To the members of the Reagan lab, thank you for creating a supportive, team-oriented and fun environment, you made taking on multiple myeloma fun and exciting. Thank you especially to Heather Fairfield Campbell, Mariah Farrell, Michelle Karam, Samaa Fadel, Dr. Carolyn Falank and Dr. Ya-Wei Qiang for your kindness and help with this project. Thank you to the rest of the lab: Kehinde Abayomi, Kaitlyn Belknap, Haylee Duval, Kathrine Knox, Allyson Schimelman, Samantha Costa, Charlotte Crist, Anastasia D'Amico, Dr. Andie Dodge, Justin Ham, Patricia Kayoyo Masengo, Lauren McGuinness, Constance Marques-Moulet, Dr. Majdi Masarwi, Madeleine Nowak, Ashley Soucy and Sasha Weller.

Thank you to my co-authors: Victoria E. DeMambro, Samaa Fadel, Mariah Farrell, Heather Fairfield, Dr. Carlos A. Garter, Christian Potts, Dr. Princess Rodriguez, Dr. Ya-Wei Qiang, Dr. Calvin P. H. Vary, and Dr. Michaela R. Reagan.

I appreciate the help of Dr. Julie Dragon, Scott Tighe, Kristiaan Finstad, and all members of the Vermont Integrated Genomics Resource for their assistance with RNA-Seq sample preparation. Thank you to the following: Michele Karolak, Edward Jachimowicz and Dr. Yulica Santos-Ortega of the MHIR Molecular Phenotyping, Flow Cytometry and Proteomics and Lipidomics Cores, respectively, Toni St. Peter, Lisa Fellows, Lynn MacLean of the MHIR animal facility, Dr. Igor Prudovsky of the MHIR Confocal Microscopy Core, Dr. Anne Breggia and the entire MHIR Biobank, Victoria DeMambro of the Physiology Core for her superb expertise and being an excellent friend and role model, Liz Bergst, Christine Ellis, Gayle Desjardins, Leisa Collins, Cole Ferm, Ally Hinton, Liz Scharnetzki, Jacyln Janis, all the members of the MHIR Grants Office and Accounts with special thanks to Gwen Swan, Michele Locker, Carolyn Elliot-Farino, Elena Odlin, Kelly Crowe and all the members of the MHIR IACUC, Dr. Katherine Motyl, Dr. Aaron Brown, Dr. Anyonya Guntur, Dr. Sergey Ryzhov, Dr. Arturo Hernandez, Dr. Peter Brooks, Dr. Ziru Li, Dr. Robert Smith, Dr. Xuehui Yang, Dr. Becky Mountain, Dr. Robert Burgess Dr. Don St. Germain, Dr. Elizabeth Jacobs, Dr. Douglas Sawyer, Dr. Adriana Rosato, Dr. Dustin Updike, Dr. James Coffman, Dr. Viravuth Yin, Nanette Herbert, Claire Stull, Robert Hammond.

Karen Corts, you are a true friend and mentor and I am eternally grateful for your support and all the work you do to keep MHIR running.

Thank you to the GSBSE program administration: Dr. David Neivandt, Dr. Clarissa Henry, Dr. Lenard Kaye, Dr. Gregory Cox, Tammy Crosby, Zhen Zhang, Kristen Freeman, Jennifer Chiarell and Vitaliia Tomakhi.

Thank you to Dr. Ian Gans, Dr. Shivangi Pande, Dr. Matthew Siviski, Dr. Kyle Bond, Dr. Cara Sullivan, Dr. Beth Whitmore, Dr. Katie Ellis, Dr. Marrisona McGilvery, Dr. Chenhao Yang, John Butts, Sophie Craig, Madeleine Nowak, Carolina Cora, Christian Potts, Benjamin Tero, Michayla Moore, Audrie Langlais, Becca Peters and Logan Douglas.

I am forever grateful to Dr. Ralph Isberg for introducing me to scientific research and truly making me into scientist I am today. Thank you to Dr. Abraham Sonenshein, Dr. Joan Meccas, Dr. Alexander Ensminger, Dr. Eva Haenssler, Dr. Gregory Crimmins, Dr. Dervla Isaac, Dr. Kimberly Davis. Dr. Tamara O'Connor, Dr. Lindsay Busch, Dr. Dennise De Jesús-Díaz, Dr. Asaf Sol, Dr. Kerri Sheehan, Dr. Dagmar Ringe, Dr. Andrew Hempstead, Dr. Stacie Clark and Dr. Kristen Kotewicz.

Thank you to my mentors at Brandeis for providing me the tools to understand scientific research in a wholistic manner and to emphasize how to make learning and teaching both exciting and engaging: Dr. Nelson Lau, Dr. Michael Marr II, Dr. Mei Zhang, Dr. Joseph Clark, Dr. Melissa Kosinski-Collins, Dr. Jason Pontrello, Dr. Daniel Oprian, Dr. Rachel Woodruff, and Rev. Walter Cuenin.

Thank you to my teachers and staff at Hull High School that made a true impact in my journey: John Donohue, Jeffrey Fuller, Timothy MacKenzie, David Milner, and Fran Troy.

Thank you to Dr. Sharon Milgrim and her team at the Office of Intramural Training and Education for their *Becoming a Resilient Scientist* workshop. The tools that I learned there were critical for graduating and growing professionally and personally.

Thank you to the NCI (1F31CA257695-0), NIGMS (1T32GM132006-01) and the Kane Foundation for funding this work.

Thank you to Calvin, Dave, CLEMMM, Adam, Sarah, Allie, Gina, and Lou for making life fun.

This would not be possible without the unwavering love and support of my parents, my brother, and second parents and my sisters of the Levenson, Dubreuil, and Favakeh families.

TABLE OF CONTENTS

TABLE OF CONTENTS	vi
LIST OF FIGURES.....	x
LIST OF TABLES.....	xii
1. CHAPTER 1: INTRODUCTION.....	1
1.1. Multiple Myeloma (MM).....	1
1.2. Acute Myeloid Leukemia.....	9
1.3. Basics of Cell Metabolism.....	10
1.4. Obesity and Metabolic Disease are Risk Factors of Cancer	15
1.5. Intersection of Obesity, Type II Diabetes and Cancer.....	21
1.6. Acyl-CoA Synthetase Long Chain (ACSL) Isozyme Family in Cancer	25
1.7. Triacsin C and Cancer	30
2. CHAPTER 2: MATERIALS AND METHODS	32
2.1. Cancer Dependency Map Analysis	32
2.2. Cell Lines and Culture Conditions.....	32
2.3. Assessment of Single Nucleotide Variants (SNVs) via Sanger sequencing	34
2.4. Assessment of predicted deletion on chromosome 17 by gel electrophoresis	35
2.5. Primary Human Bone Marrow Mesenchymal Stem Cell Isolation	35
2.6. Human Bone Marrow Adipocyte Differentiation	37
2.7. Fluorescent Fatty Acid Transfer Assay Between hBMAds and HL-60 Cells in Transwells.....	37
2.8. Bone Marrow Adipocyte and HL-60 Transwell Co-culture	38
2.9. Magnetic Activated Cell Sorting of CD138 (Syndecan-1)-Positive Cells from Primary Multiple Myeloma Patients	39
2.10. Miltenyi Magnetic Activated Cell Sorting of CD138 (Syndecan-1)-Positive Cells from Primary Multiple Myeloma Patients	40
2.11. Triacsin C Treatment.....	41
2.12. Myeloma Cell Quantification, Viability and Apoptosis.....	42
2.13. Bioluminescent Assays Measuring Cell Viability	42
2.14. RealTime-Glo™ MT Cell Viability Assay to Measure Cellular Redox Potential	43

2.15.	Intracellular Characterization of BAX Protein	43
2.16.	Myeloma Cell Cycle and Ki-67 Staining	44
2.17.	Flow Cytometric Characterization of Mitochondrial Number/Mass, Mitochondrial Membrane Potential, and Mitochondrial Superoxide Levels.....	44
2.18.	Cellular Metabolic Analysis.....	45
2.19.	Acyl-CoA Synthetase Long-chain Activity Assay.....	45
2.20.	Total mRNA extraction and quantitative real-time polymerase chain reaction (qRT-PCR)	47
2.21.	RNA Sequencing Sample Preparation and Analysis	47
2.22.	Sample Preparation for Mass Spectrometry Proteomics of TriC treated MM.1S cells	48
2.23.	Mass Spectrometry Proteomics of TriC-treated MM.1S Cells	49
2.24.	Lipofectamine-based Transfection of Short-Interfering RNAs (siRNAs) Against <i>DGAT1</i>	51
2.25.	Dicer-Substrate Short Interfering RNA-Mediated Knockdown of <i>ACSL3</i>	53
2.26.	Addition of Exogenous Oleic Acid to HL-60 Cells.....	55
2.27.	Triacsin C and Oleic Acid Co-treatment	56
2.28.	Measuring Intracellular Neutral Lipids with Flow Cytometry	56
2.29.	Diacylglycerol Acyltransferase Inhibitor Treatment.....	56
2.30.	Data Availability Statement.....	57
2.31.	Statement Regarding the Use of Human Samples.....	57
2.32.	Statistical Analysis.....	57
3.	CHAPTER 3: RESULTS	59
3.1.	Identity of Presumed OPM-2 ^{mCherry/Luc} Line as HL-60mCherry/Luc Cells	59
3.2.	Mutations present in mislabeled cells in the CDKN2A gene are largely consistent with HL-60 cells	59
3.3.	Mutations present in mislabeled cells in the NRAS gene are consistent with HL-60 cells	60
3.4.	Mutations present in mislabeled cells in the TP53 gene are consistent with HL-60 cells.....	62
3.5.	Conclusions	64
3.6.	Inhibition of the Acyl-CoA Synthetase Family with Triacsin C in Multiple Myeloma and Acute Myeloid Leukemia Cell Lines	64

3.6.1.	Pharmacological Inhibition of the Long-Chain Acyl-CoA Synthetase (ACSL) Family Decreases Multiple Myeloma Cell Proliferation and Survival	65
3.6.2.	Triacsin C Induces Transcriptional Changes in MM.1S Cells Associated with Cell Death and the Integrated Stress Response	79
3.6.3.	Triacsin C Treatment Induces Proteomic Changes Associated with Mitochondrial Dysfunction and Reactive Oxygen Species Detoxification in MM.1S Cells	85
3.6.4.	Triacsin C Treatment Negatively Impacts Multiple Myeloma Cell Metabolism and Mitochondrial Function in MM.1S and HL-60 Cells	88
3.7.	Exploration of the Role of Lipid Droplets in Human Multiple Myeloma and Acute Myeloid Leukemia Cell Lines	92
3.7.1.	Defining and Modulating the Lipid Droplet Landscape in MM and AML Cell Lines	92
3.7.2.	Efforts to Knockdown ACSL3 and DGAT1 Expression Levels by RNA Interference.....	100
3.8.	Characterizing Bone Marrow Adipocyte-Dependent Modulation of Fatty Acid Metabolism in HL-60 and MM.1S Cells	103
3.8.1.	Development of Fatty Acid Transfer Assay Between Bone Marrow Adipocytes and HL-60 Cells.....	103
3.8.2.	Characterization of hBMAAd and hMSC-dependent Changes in Lipid Droplets in HL-60 Cells.....	106
3.8.3.	MM.1S Cells Pre-exposed to BMAdS in Transwells Are Sensitive to Triacsin C Treatment.....	110
4.	CHAPTER 4: DISCUSSION.....	111
4.1.	Major Findings of Triacsin C Phenotypes in MM and AML Cell Lines.....	112
4.2.	Possible Explanations of Why U226B1 Cell Viability is Unchanged after 48 h of TriC Treatment.....	113
4.3.	The Mutational Landscape of U266B1 Cells Does Not Provide a Clear Explanation of the Lack of a Viability Response to TriC	115
4.4.	Mitochondrial-Derived Signals that Activate the Integrated Stress Response	122
4.5.	The ACSL Family, Triacsin C and Ferroptosis	125
4.6.	Triacsin C, ROS Detoxification and Connections with TriC-Associated Transcriptome.....	128
4.7.	TriC and Mitogen-Activated Protein Kinase Signaling.....	130

4.8.	The Potential Implications of Triacsin C Use and Approved Therapies for Multiple Myeloma and Acute Myeloid Leukemia.....	131
4.9.	Experimental Limitations.....	132
4.9.1.	ACSL Homology to Luciferase.....	132
4.9.2.	<i>In vitro</i> Culture Conditions.....	132
4.9.3.	Triacsin C is a Pan-ACSL Small Molecule Inhibitor	133
4.9.4.	Limited Number of Donors.....	133
4.9.5.	RNA Interference Experimental Design	134
4.10.	Summary of Conclusions and Significance	134
5.	CHAPTER 5: UNANSWERED QUESTIONS AND FUTURE DIRECTIONS	136
5.1.	Genetic Targeting of the ACSL Family.....	136
5.2.	Confirmation of Activation of the Integrated Stress Response.....	137
5.3.	Cardiolipin Biosynthesis and Remodeling.....	140
5.4.	Regulation of Bioenergetics by Cardiolipins.....	140
5.5.	Oxidized Cardiolipins Are a Signal of Mitochondrial Stress and Activate Apoptosis and the ISR.....	141
5.6.	Triacsin C Drug Synergy Studies.....	142
5.7.	Treatment of MM Mouse Models with Triacsin C	143
5.8.	Treating Primary MM Cells with Triacsin C	145
5.9.	ACSLs, SREBP Signaling and MYC.....	150
5.10	The ACSL-Adenylate Kinase Connection	150
6.	BIBLIOGRAPHY	153
7.	APPENDIX.....	183
8.	BIOGRAPHY OF AUTHOR.....	242

LIST OF FIGURES

Figure 1. The Electron Transport Chain.....	11
Figure 2. Mitochondria Play a Central Role in Intrinsic Apoptosis.....	14
Figure 3. Contributions of Obesity to Multiple Myeloma.....	22
Figure 4 Fatty Acids have Diverse Cellular Functions.....	25
Figure 5 General Fatty Acid Metabolism.....	26
Figure 6 Human ACSL Isozyme Family Protein Homology.....	28
Figure 7. General Live Cell ACSL Activity Assay.....	46
Figure 8. Confirmation of OPM-2 and HL60 Cell Identity.....	61
Figure 9. OPM-2 and HL-60 Related Genotyping Regarding TP53.....	63
Figure 10. Optimization of Live Cell Activity Assay with HL-60 and ATCC MM.1S Cells.....	68
Figure 11. Targeting the ACSLs using Triacsin C Inhibits Myeloma Cell Proliferation and Survival.....	71
Figure 12. Gating Strategies for Ki-67 and Cell Cycle Distribution.....	73
Figure 13. Gating Strategies for Apoptosis and BAX Staining.....	74
Figure 14. Triacsin C has Batch-Dependent Effects on Ki-67 Levels.....	75
Figure 15. ACSL Gene and Protein Expression, Early and Late Apoptosis and Cell Cycle Distribution of OPM-2 and RPMI-8226 Cells Treated with TriC.....	76
Figure 16. Triacsin C Decreases HL-60 Redox Potential, Survival and Lipid Droplets.....	78
Figure 17. Triacsin C Treatment of MM.1S Cells Induces Transcriptional Changes Associated with Cell Death and the Integrated Stress Response.....	82
Figure 18. Significantly Upregulated Transcripts in MM.1S Cells Treated with TriC for 24 hours.....	83
Figure 19. Quality Control Parameters for RNA-Sequencing of TriC-Treated MM.1S Cells and Downregulated Pathways.....	85
Figure 20. Triacsin C Treatment of MM.1S Cells Induces Proteomic Changes Associated with Mitochondrial Dysfunction and Reactive Oxygen Species.....	88
Figure 21. Triacsin C Induces Mitochondrial Dysfunction in MM Cells.....	91
Figure 22. Total Intracellular Neutral Lipids are Dynamic in HL-60 Cells and Can be Decreased by Triacsin C Treatment.....	93
Figure 23. Exogenous Oleic Acid Increases Lipid Droplets and Decreases HL-60 Cell Viability.....	95
Figure 24. Exogenous Oleic Acid May Confer Minor Protection Against TriC-Induced Changes in HL-60 Cell Viability.....	97
Figure 25. Pharmacological Inhibition of DGAT1/2 for 48 Hours Does Not Change HL-60, MM.1S and RPMI-8226 Cell Viability.....	99
Figure 26. Delivery of siRNAs Targeting ACSL3 and DGAT1 in HL-60 Cells.....	102
Figure 27. Human Bone Marrow Adipocytes Take Up a 12-Carbon Fluorescent Fatty Acid.....	103

Figure 28. Fluorescent Fatty Acids Transfer from Human Bone Marrow Adipocytes to HL-60 Cells in a Contact-Independent Manner	106
Figure 29. The Percentage of HL-60 Cells with Lipid Droplets Decreases in Co-Culture with either hBMAds or hMSCs	108
Figure 30. hBMAd and hMSCs Do Not Alter HL-60 Cell Gene Expression of DGAT1 or DGAT2.....	109
Figure 31. MM.1S Cells Pre-exposed to hBMAds.	
Are Sensitive to TriC Treatment	110
Figure 32. Summary of Phenotypes of Triacsin C Treatment.....	112
Figure 33. The Integrated Stress Response Signaling	118
Figure 34. ATF4-Regulated Transcripts Support.....	
Both Cell Survival and Apoptosis	121
Figure 35. Triacsin C Upregulates Transcripts Associated with Ferroptosis	124
Figure 36. Lentiviral Vector Schematic.....	137
Figure 37. Cardiolipin Biosynthesis and Remodeling	139
Figure 38. Potential Combination Treatments to Test in Myeloma	143
Figure 39. Triacsin C in MM Mouse Models	144
Figure 40. Magnetic Activated Cell Sorting (MACS) of Primary MM Cells.....	146
Figure 41. Triacsin C Treatment of Primary MM Cells.....	147
Figure 42. MM.1S Cells May Utilize Fatty Acid Oxidation for their Respiration	183

LIST OF TABLES

Table 1. Diagnostic Criteria for Monoclonal Gammopathy of Undetermined Significance (MGUS), Smoldering Multiple Myeloma (SMM), and Multiple Myeloma (MM) from the International Myeloma Working Group 12	7
Table 2. Drugs Approved for Treatment of Multiple Myeloma and their Mechanisms as of 2022	8
Table 3. ACSL Isozyme Family Function and Regulation	29
Table 4. Human MM and AML Cell Lines Used	34
Table 5 Primary Human Donor Information	36
Table 6. Human DGAT1 Short-Interfering RNA Sequences.....	52
Table 7. Human ACSL3 Double-Stranded Dicer-Substrate RNA Sequences	54
Table 8. Short-Tandem Repeat Profiling Results of HL-60mCherry/luc Cell Line	59
Table 9. Double Times of Cell Lines Used in this Work.....	114
Table 10 CD138(+) Yield from Primary MM Patient Bone Marrow Aspirates	145
Table 11. qRT-PCR Forward Primers	184
Table 12. qRT-PCR Reverse Primer Information	185
Table 13 Primers For Determining OPM-2 and HL-60 Identity	186
Table 14. Average Chronos Scores of Modified Hallmark Fatty Acid Metabolism Genes in 21 Human Myeloma Cell Lines from the Cancer Dependency Map	187
Table 15 Significantly Differentially Expressed Upregulated Genes.....	198
Table 16 Significantly Differentially Expressed Downregulated Genes	202
Table 17 Top 10 Significantly Upregulated Reactome Pathways in MM.1S Cells Treated with Triacsin C for 24 hours	203
Table 18. Top 10 Significantly Upregulated KEGG Pathways in MM.1S Cells Treated with Triacsin C for 24 hours	204
Table 19 Significantly Upregulated Proteins of MM.1S ^{gfp/luc} Cells Treated with 1.0 μM Triacsin for 48 hours	205
Table 20 Significantly Downregulated Proteins of MM.1S ^{gfp/luc} Cells Treated with 1.0 μM Triacsin for 48 hours	206
Table 21 Significantly Upregulated Proteins of MM.1S ^{gfp/luc} Cells Treated	212
Table 22 Significantly Downregulated Proteins of MM.1S ^{gfp/luc}	221
Table 23 Proteomics Hits in MM.1S ^{gfp/luc} Cells Treated with 1 μM Triacsin for 48 Hours Compared to Vehicle Treated Cells	231
Table 24. Proteomics Hits in MM.1S ^{gfp/luc} Cells	234
Table 25. Top 10 Significantly Downregulated Reactome Pathways in MM.1S Cells Treated with Triacsin C for 24 hours	240
Table 26. Top 10 Significantly Downregulated KEGG Pathways in MM.1S Cells Treated with Triacsin C for 24 hours.....	241

1. CHAPTER 1: INTRODUCTION

1.1. Multiple Myeloma (MM)

Multiple myeloma (**MM**) is an incurable hematological malignancy that is characterized by the clonal expansion of plasma cells with a 60% 5-year survival rate¹. MM is the second most common hematological malignancy with an estimated number of 35,780 newly diagnosed cases in the U.S.¹. The cause of MM is unknown, however, risk factors include: dioxin (Agent Orange) exposure², career as a firefighter³, being of the male sex⁴, age⁴ and obesity⁵⁻⁷. In the U.S., Black individuals are more at risk of developing MM than other populations⁸.

MM cells secrete monoclonal free light chains of immunoglobulin (**FLC**, most commonly kappa (κ) or (γ) gamma sub-types) into the serum, deemed M protein⁹. The measurement of M protein (commonly the ratio of κ FLC / γ FLC or *vice versa*) is a key diagnostic and prognostic factor positively correlated with MM progression^{9,10}. One sub-type is produced monoclonally and this is deemed the “involved” FLC and can be determined by the FLC ratio. There is strong evidence that MM is always preceded by a non-symptomatic premalignant condition, monoclonal gammopathy of undetermined significance (**MGUS**)¹¹. Clinically, MGUS is characterized by the serum M protein < 3 g per dL, urinary monoclonal protein, < 500 mg per 24 hours, < 10% bone marrow (**BM**) plasma cells, and without “clinical manifestations or other laboratory abnormalities attributable to monoclonal gammopathy”¹² (See **Table 1** for comparisons of the clinical parameters of the stages of MM). MGUS is present in 3% of people over 50 years old and its frequency increases with age¹³. The risk of developing MM for MGUS patients

increases between 0.5-3% annually^{14,15}, therefore patients must be closely monitored for evidence for progression to the next stage of MM.

The next stage in MM progression, smoldering multiple myeloma (**SMM**), is defined by serum levels of M protein ≥ 3 g per dL, ≥ 500 mg per 24 hours, $\geq 10\%$ bone marrow plasma cells and without “clinical manifestations or other laboratory abnormalities attributable to monoclonal gammopathy”¹². Patients with SMM have a risk of progression to MM of 10% per year in the first 5 years of diagnosis, with the time to progression to MM ranging from 2-19 years (median time to progression = 4.7 years)^{14,16}. SMM patients with the highest risk of progression have three key clinical characteristics: > 20 serum FLC ratio, serum M protein levels > 2 g per dL and $> 20\%$ bone marrow PCs^{17,18}. Treatment of high-risk SMM patients has been shown to increase the time to progression to MM, the 3-year survival rate and partial response to treatment or better in 79% of patients¹⁹⁻²¹. Despite improvements in our understanding and clinical management of SMM, 50% patients with high-risk SMM develop MM within 2 years^{14,16}.

MM is diagnosed if patients have $\geq 10\%$ bone marrow plasma cells and at least one end-organ damage event attributable to plasma cell neoplasm (hypercalcemia, renal dysfunction, anemia or bone lesions, **CRAB**) or myeloma-defining event (clonal BM plasma cells $\geq 60\%$, ratio of involved to uninvolved FLC ≥ 100 and involved FLC of ≥ 0.001 g per dL, or >1 focal lesion on magnetic resonance imaging (**MRI**) ≥ 5 mm (**Table 1**)^{12,22}. Focal lesions are areas in which plasma cells accumulate and are detectable via MRI or ¹⁸fluoro-deoxyglucose positron emission tomography computed tomography

(**FDG PET-CT**)²³. Although MM remains incurable, modern therapies improved the 5-year survival rate by nearly two-fold between 2000 and 2016 from 35.6% to 60.6%⁸.

Treatment of MM primarily aims to prolong survival and mitigate disease and treatment-related complications to improve the quality of life of the patient. Reducing the number of malignant plasma cells in the BM has been shown to improve treatment outcomes of MM²⁴ and therefore is the primary goal of most MM treatments. To treat MM, clinicians utilize a combination of glucocorticoids^{25–28} (*i.e.* dexamethasone²⁵), proteasome inhibitors (*i.e.* bortezomib^{29,30}, ixazomib^{31,32}, and carfilzomib^{33–36}), immunomodulatory agents (**IMiDs**, *i.e.* thalidomide, lenalidomide, and pomalidomide), monoclonal antibodies against MM/PC-specific antigens (*i.e.* daratumumab^{37–41}, isatuximab and lotuzumab^{42,43}), selective inhibitors of nuclear export (**SINEs**, selinexor⁴⁴), alkylating agents (*i.e.* melphalan and cyclophosphamide⁴⁵), autologous stem cell transplant (**ASCT**), antibody-drug conjugates (*i.e.* belantamab mafodotin⁴⁶) and chimeric antigen receptor T cell (**CAR-T**, *i.e.* idecabtagene vicleucel^{47,48}) therapy. See **Table 2** for more information about the mechanism of action of each treatment. Despite the myriad of treatments available, all MM patients develop drug resistance.

Treatment resistant MM is commonly referred to as relapsed and/or refractory multiple myeloma (**RRMM**). Refractory myeloma occurs when patients are not responsive to therapy within the last 60 days of the last line of therapy⁴⁹. Relapsed myeloma is defined as a patient whose MM cells are non-responsive to the current therapy and require a new therapeutic regime⁴⁹. MM patients are closely monitored for drug responsiveness so treatments can be personalized. More granular details of defining responsiveness to treatment are reviewed here^{49–51}. Genetic heterogeneity of

MM cells and the BM microenvironment are some of the most significant contributors to drug resistance in MM.

Individuals with a family member with MM have a 2-4-fold increased risk of developing MM⁵². Indeed, genome-wide association studies (**GWAS**) of >4,600 MM patients and 10,990 healthy individuals identified seven loci that are associated with a moderate increase the risk of developing MM^{53,54}. Together these mutated loci accounted for close to 13% of the familial risk of MM and interestingly were associated with increased risk of developing MGUS⁵³⁻⁵⁵. The genetic burden in MM is progressive and dynamic; there are primary mutations and throughout disease progression there are treatment-dependent and independent mutations⁵⁶. The primary events that occur that most commonly translocations of oncogenic driver genes (cyclin D1; **CCND1**^{57,58}, fibroblast growth factor receptor 3/multiple myeloma suppressor of variegation, Enhancer of zeste, and Trithorax; **FGFR3 /MMSET**^{59,60}, cyclin D3; **CCND3**⁶¹, musculoaponeurotic fibrosarcoma bZIP transcription factor; **MAF**^{62,63} and **MAFB**⁵⁸) fusing to the enhancers of IgH, IgL, or IgK or copy-number variations that involve trisomy of chromosomes 3, 5, 7, 9, 11, 15, 19 or 21^{64,65}. Secondary mutational events include chromosome gains of oncogenes, chromosome losses of tumor suppressors, translocations affecting MYC proto-oncogene, bHLH transcription factor (**MYC**) and somatic mutations⁶⁶. Many of the mutations in MM affect genes in a diverse array of pathways such as: the rat sarcoma proto-oncogene family- mitogen-activated protein kinase (**RAS-MAPK**) pathway, nuclear factor kappa-light-chain-enhancer of activated B cells (**NFKB**) pathway, MYC pathway, cell cycle and DNA damage checkpoints, RNA processing machinery, epigenetic modifiers, B cell development^{56,66}. Adding to the

complex genetic composition of MM, most myeloma patients have multiple malignant clones simultaneously and/or over the course of their treatment^{66,67}. Strikingly, in one study whole exome sequencing of 203 MM patients showed among the top 14 most frequently mutated genes, ~86% have been them were subclonal⁶⁸. Genetic markers in MM have been shown to have prognostic value⁶⁹, therefore, it would improve patient outcomes if it was standard clinical practice to longitudinally monitor the mutational landscape of MM patients to make treatments more personalized.

Through dynamic juxtacrine, paracrine and autocrine signaling, the BM microenvironment plays a significant role to support MM cell growth, survival, migration, and drug resistance. Indeed, MM cells enhance NF κ B -dependent transcription and secrete IL-6 upon adhesion to stromal cells, endothelial cells, and extra cellular proteins (laminin and fibronectin), resulting in increased growth, survival and drug resistance⁷⁰⁻⁷². In turn, MM adhesion triggers the BM stroma to secrete tumor supportive cytokines and growth factors like interleukin-6 (**IL-6**), insulin growth factor 1 (**IGF1**), tumor necrosis factor alpha (**TNFA**), stromal cell-derived factor 1 (**SDF-1 α**), transforming growth factor beta (**TGFB**), pro-angiogenic factors like vascular endothelial growth factor (**VEGF**) and basic fibroblast growth factor (**bFGF**). A similar positive feedback loop, known as “the vicious cycle” exists between MM cells and the cells responsible for bone turnover.

A MM diagnosis is associated with a 40-50% risk of developing fractures or bone pain⁷³ and 90% of MM patients experience bone lesions through the course of disease progression⁷⁴. MM bone-related disease is because of the “vicious cycle”, a positive feedback loop between MM cells and the cells involved in bone homeostasis that can

cause bone lesions. Briefly, secreted factors from MM cells like macrophage inflammatory protein-1 alpha (**MIP-1A**; Chemokine ligand 3, CCL3) human growth factor (**HGF**) and interleukin-34 (**IL-34**) cause mesenchymal stem cells and osteoblasts in the bone marrow to produce receptor activator of nuclear factor- κ B ligand (**RANKL**) which binds to its receptor, RANK which promotes bone resorption by increasing osteoclastogenesis and osteoclast activity. There is a concurrent repression of the decoy receptor for RANKL, osteoprotegerin (**OPG**), further enhancing the effects of RANK/RANKL signaling⁷⁵. MM-associated osteoclasts secrete proteins supportive of MM cell growth and survival like a proliferation inducing ligand (**APRIL**) and B cell activating factor (**BAFF**)⁷⁶. Bone formation is suppressed in the MM BM microenvironment by the secretion of inhibitors of wingless (**WNT**) signaling, a key pathway that regulates bone formation by osteoblasts⁷⁷⁻⁸⁰. Both bone anabolic agents and treatments targeting MM cells directly improve MM-associated bone disease⁸¹. In Chapter 3, the relationship between bone marrow adipocytes (**BMA**s) and MM cells will be briefly touched upon⁸². The MM-bone marrow microenvironment presents a dynamic niche that supports MM cell survival, proliferation, and resistance to therapies. Drug response in MM and other hematological malignancies has been linked to MM cell metabolism⁸³, making it critical to understand the metabolic state of MM cells to inform clinical practice.

Table 1. Diagnostic Criteria for Monoclonal Gammopathy of Undetermined Significance (MGUS), Smoldering Multiple Myeloma (SMM), and Multiple Myeloma (MM) from the International Myeloma Working Group 12⁸⁴

Criteria	Monoclonal Gammopathy Of Undetermined Significance	Smoldering Multiple Myeloma	Multiple Myeloma
Serum Monoclonal Protein	< 3 g/dL	≥ 3 g /dL	Present (in 98% of cases)
Bone Marrow Plasma Cells (CD138 ⁺ cells)	<10%	≥10%	≥10%
Urinary Monoclonal Protein	<500 mg / 24 h	≥500 mg / 24 h	Present (in 98% of cases)
Myeloma-defining Events	Absent		<p>End-organ damage attributable to plasma cell neoplasm:</p> <ul style="list-style-type: none"> • Hypercalcemia (serum calcium >1 mg/dL higher than upper limit of normal or >11 mg/dL) • Kidney injury (serum creatinine >2 mg/dL or creatinine clearance <40 mL/min/1.73 m²) • Anemia (hemoglobin >2 g/dL below lower limit of normal or <10 g/dL) • Bone lesions (≥1 osteolytic lesions) <p>More than 1 of the following biomarkers of myeloma:</p> <ul style="list-style-type: none"> • Clonal bone marrow plasma cells ≥60% • Ratio of involved to uninvolved serum free light chains ≥100 and involved FLC concentration 10 mg/dL or higher • >1 focal lesion on MRI ≥5 mm

Table 2. Drugs Approved for Treatment of Multiple Myeloma and their Mechanisms as of 2022 ⁸⁴

Drug Class	Mechanism of Action	Name
Glucocorticoids	The mechanism in which glucocorticoids induce apoptosis is not known. Indirectly represses MM supportive proteins Nuclear factor kappa-light-chain-enhancer of activated B cells (NFKB) and activating protein 1 (AP-1) ²⁶ Induces reactive oxygen species and ER stress ^{27,28}	Dexamethasone ²⁵
Proteasome Inhibitors	Inhibits 20S subunit of the proteasome to induce ROS, terminal ER stress and represses NF-κB ⁸⁴⁻⁹⁰	Bortezomib ^{29,30}
		Ixazomib ^{31,32}
		Carfilzomib ³³⁻³⁶
Immunomodulatory Agents	Modulates substrate specificity of E3 ubiquitin ligase-cereblon complex causing proteasomal degradation of MM-related proteins ⁹¹⁻⁹³	Thalidomide ⁹⁴
		Lenalidomide ^{95,96}
		Pomalidomide ⁹⁷⁻⁹⁹
Monoclonal Antibodies	Monoclonal antibody that targets CD38 to induce complement-mediated and antibody-dependent cell-mediated cytotoxic effects, antibody-dependent cellular phagocytosis and apoptosis ^{41,100,101}	Daratumumab ³⁷⁻⁴¹ Isatuximab
	Monoclonal antibody that targets SLAMF7 to induce antibody-dependent cell-mediated cytotoxic effects and activates natural killer cells through interleukin-2 (IL-2) and tumor necrosis factor alpha (TNF-α) ^{102,103}	Elotuzumab ^{42,43}
Selective Inhibitors of Nuclear Export	Inhibits exportin 1, preventing the nuclear export of tumor suppressor proteins leading to apoptosis of MM cells ¹⁰⁴	Selinexor ⁴⁴
Alkylating Agents	Crosslinks guanine nucleotides to induce the DNA-damage response and apoptosis ¹⁰⁵	Melphalan + cyclophosphamide ⁴⁵

Table 2 Continued		
Antibody-Drug Conjugates	Monoclonal antibody targeting B cell maturation antigen (BCMA), highly expressed on PC cells with a drug conjugate, Monomethyl auristatin F, a tubulin polymerization inhibitor	Belantamab mafodotin ⁴⁶
Chimeric Antigen Receptor T Cells	Autologous T cells are collected from a patient, transduced using a viral vector with a chimeric antigen receptor targeting BCMA, injected back into the patient where the engineered T cells mediate killing of tumor cells.	Idecabtagene vicleuce ^{47,48}

1.2. Acute Myeloid Leukemia

The major focus of this dissertation is MM, however, an acute myeloid leukemia (**AML**) cell line was used for a portion of this work because a cell line that we received from a collaborator was misidentified. Understanding basic AML biology will assist in comparing the phenotypes observed between MM and AML. Similar to MM, AML is a hematological malignancy derived from hematopoietic stem cells (**HSCs**) but undergo myeloid differentiation where leukemia stem cells (**LSCs**) emerge from granulocyte macrophage progenitors (**GMP**) that gain self-renewable potential after a series of driver mutations^{106–108}. AML is age-associated with a median age diagnosis of 67 years old and has a 23.4% 5-year survival rate^{109–111}. The bone marrow microenvironment also supports AML proliferation, survival and drug resistance, though it is extremely rare that AML patients have the bone lesions associated with MM^{112,113}. The AML cell line used (HL-60) has a mutations that allow uncontrolled proliferation including a *TP53* deletion, with a cyclin dependent kinase inhibitor 2A (**CDKN2A**; (p16/INK4A) p.R80Ter mutation

causing a truncated and inactive protein and a neuroblastoma RAS Proto-Oncogene (**NRAS**) p.Gln61Leu mutation which are all relatively uncommon in AML¹¹¹.

1.3. Basics of Cell Metabolism

Mitochondrion is an organelle at the intersection of key metazoan cellular processes including metabolism, bioenergetics, redox homeostasis, apoptosis, cell signaling, macromolecule biosynthesis and calcium and iron homeostasis¹¹⁴. This section will cover mitochondrial structure, oxidative phosphorylation, reactive oxygen species as byproducts of mitochondrial processes, the tricarboxylic acid cycle, the role of glycolysis in cancer and mitochondrial regulation of cell survival.

The double-membrane of mitochondria form functionally distinct compartments. The mitochondrial outer membrane (**MOM**) is permeable to ions and small molecules, acting as a bridge from the cytoplasm to the mitochondria (**Figure 1**). In contrast, the inner mitochondrial membrane (**IMM**) is impermeable to most small molecules and ions, including hydrogen (H^+), and is the location of the electron transport chain and membrane-bound transporters for specific cargo. The compartment that the IMM encloses is called the mitochondrial matrix and is the site of the tricarboxylic acid cycle (**TCA**), fatty acid oxidation (**FAO**), the pyruvate dehydrogenases (**PDHs** pyruvate \rightarrow actyl-CoA), mitochondrial DNA (**mtDNA**) and mitochondrial ribosomes^{115,116}.

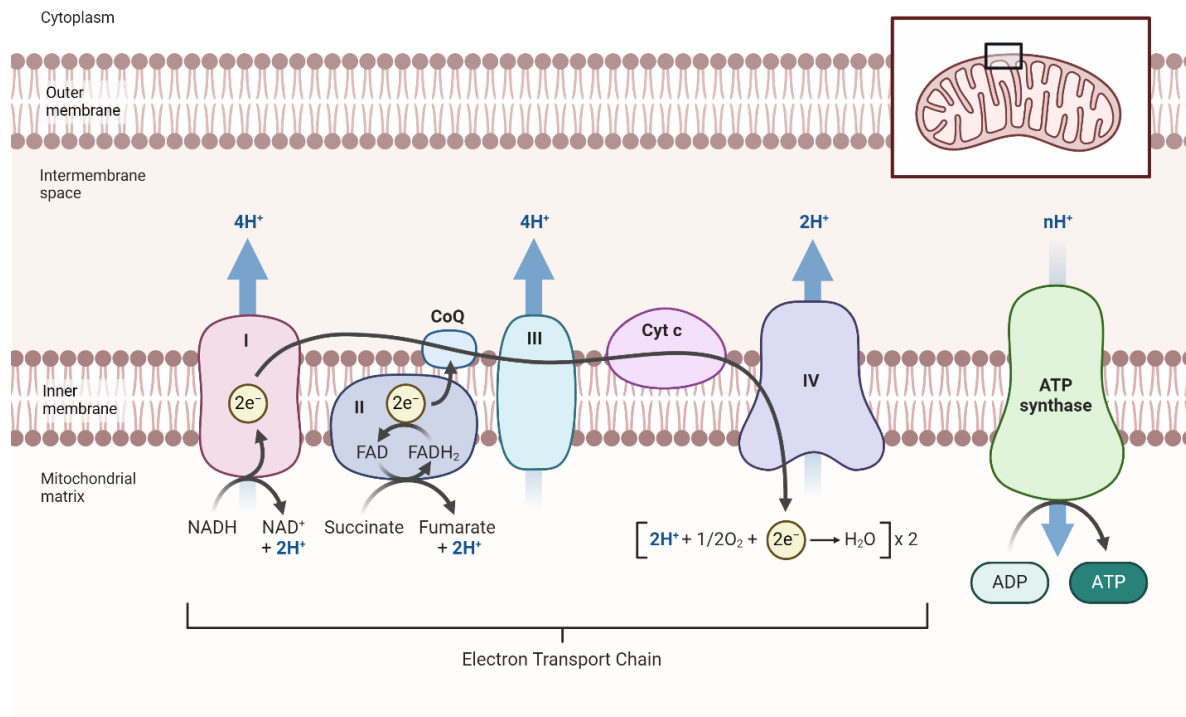


Figure 1. The Electron Transport Chain.
 Made with Biorender.com

Oxidative phosphorylation (**OXPHOS**) is a major source of cellular energy generation in the form of adenosine triphosphate (**ATP**) synthesis in aerobic metazoans. In order to produce ATP, electrons are transported through a chain of five enzyme complexes (the ETC) facilitated by the electron donors; nicotinamide adenine dinucleotide (**NADH**) for Complex I and flavin adenine dinucleotide (**FADH₂**) or succinate for Complex II¹¹⁶. The electrons from Complex I and II are transported to Complex III and IV by other electron carriers, ubiquinol (**QH₂**), coenzyme Q10 and cytochrome c (**Cyt c**). Cyt c and Complex IV facilitate the reduction of O₂ to H₂O. The electron flow is coupled to H⁺ transport from the mitochondrial matrix to the intermembrane space and creates an electrochemical gradient and the basis of mitochondrial membrane potential (**ΔΨ_m**)¹¹⁶. The high ΔΨ_m allows adenosine

triphosphate (**ATP**) synthase (Complex V) to transport H^+ from the intermembrane space to the mitochondrial matrix to phosphorylate adenosine diphosphate (**ADP**) to **ATP**¹¹⁶. **ATP** can then be used as a source of energy for key biochemical reactions; however, it is important to consider byproducts of OXPHOS and the metabolites that fuel it.

Reactive oxygen species (**ROS**) are a byproduct of a transfer of electrons from $\bullet Q$ (an intermediate from the electron transfer between Complex I to QH_2 or QH_2 to Complex III) to O_2 to form superoxide ($\bullet O_2^-$). Superoxide is highly reactive and can damage proteins, lipids and nucleic acids and induce programmed cell death or apoptosis^{117,118}. **ROS** is detoxified by both superoxide dismutases in the cytoplasm (**SOD1**) and mitochondria (**SOD2**) by forming hydrogen peroxide (**H₂O₂**). Additionally, the glutathione (**GSH**) and thioredoxin (**TXN**) systems act as major anti-oxidant systems. Cytoplasmic **H₂O₂** is further detoxified to **H₂O** by a coordination of **GSH**, glutathione s-transferases (**GST**) and glutathione peroxidases (**GPXs**)^{116,119}. **TXN** and thioredoxin reductases (**TXNRD**) and **NADH** both can reduce disulfide bonds and quench **ROS**¹²⁰. **ROS** are key signaling molecules and they activate key pathways involved in cell growth and proliferation like phosphatidylinositol 3 kinase (**PI3K**), mitogen activated-protein kinase (**MAPK**/extracellular-regulated kinase 1/2 (**ERK1/2**))^{117,118}. Chapter 4 will delve deeper into particular anti-oxidant signal mechanisms pertinent to the phenotypes observed in this study in MM cell lines.

Within the mitochondrial matrix, the TCA cycle is critical for the regeneration of **NADH** and **FADH₂**. In the TCA cycle, citrate synthase combines acetyl-CoA (produced from glycolysis, **FAO** or the deamination of amino acids) with oxaloacetate to form

citrate, a metabolite key to anabolic fatty acid metabolism¹²¹. The subsequent seven biochemical reactions in the TCA cycle generate metabolic intermediates critical cell growth and proliferation for the biosynthesis of purines, pyrimidines, amino acids, and fatty acids^{114,121}. In addition to acetyl-CoA, TCA cycle intermediates are replenished by glutamine being broken down to alpha-ketoglutarate (**α-KG**). Glutamine has been shown to be supportive of MM growth and proliferation and glutamine transporters are promising targets in similarly “glutamine addicted” cancers¹²². Glutamine’s role in MM mitochondrial function will be discussed further in Chapter 4.

Glycolysis is the process of glucose being broken down into pyruvate. Under aerobic conditions, most non-transformed cells primarily shuttle pyruvate to the mitochondria to be oxidized into acetyl-CoA to support energy production in the TCA cycle; while in anaerobic conditions, glycolysis is favored to fuel lactic acid fermentation by the action of lactate dehydrogenase A and B (**LDHA** and **LDHB**). Otto Warburg first observed the phenomenon, “aerobic glycolysis” (later named the Warburg Effect), in which cancer cells favor the fermentation of glucose into lactate for energy generation even in the presence of oxygen^{123–125}. Most cancer cells upregulate glucose transporters like glucose transporters 1 and 4 (**GLUT1**, **GLUT4**) (upregulated in MM¹²⁶) to partially compensate for the near 18-fold defect of ATP production that glycolysis has compared to OXPHOS^{125,127–129}. Common mutations in MM and other cancers in oncogenes like *KRAS*, *NRAS*, *MYC* and tumor suppressors like *TP53* are associated with rewired metabolism favoring glycolysis^{68,114,125,127,128,130–132}. The hypoxic environment that MM cells and other cancers often reside in upregulates glycolysis by the activation of hypoxia inducible factors (**HIF1α**, **HIF2α**). Although OXPHOS is

repressed in most cancers, it has been shown that upon knockdown of LDHA in mouse mammary tumors, OXPHOS activity is increased¹³³. These data highlight the metabolic flexibility that cancer cells exhibit and the merit of studying cancer metabolism to identify novel vulnerabilities.

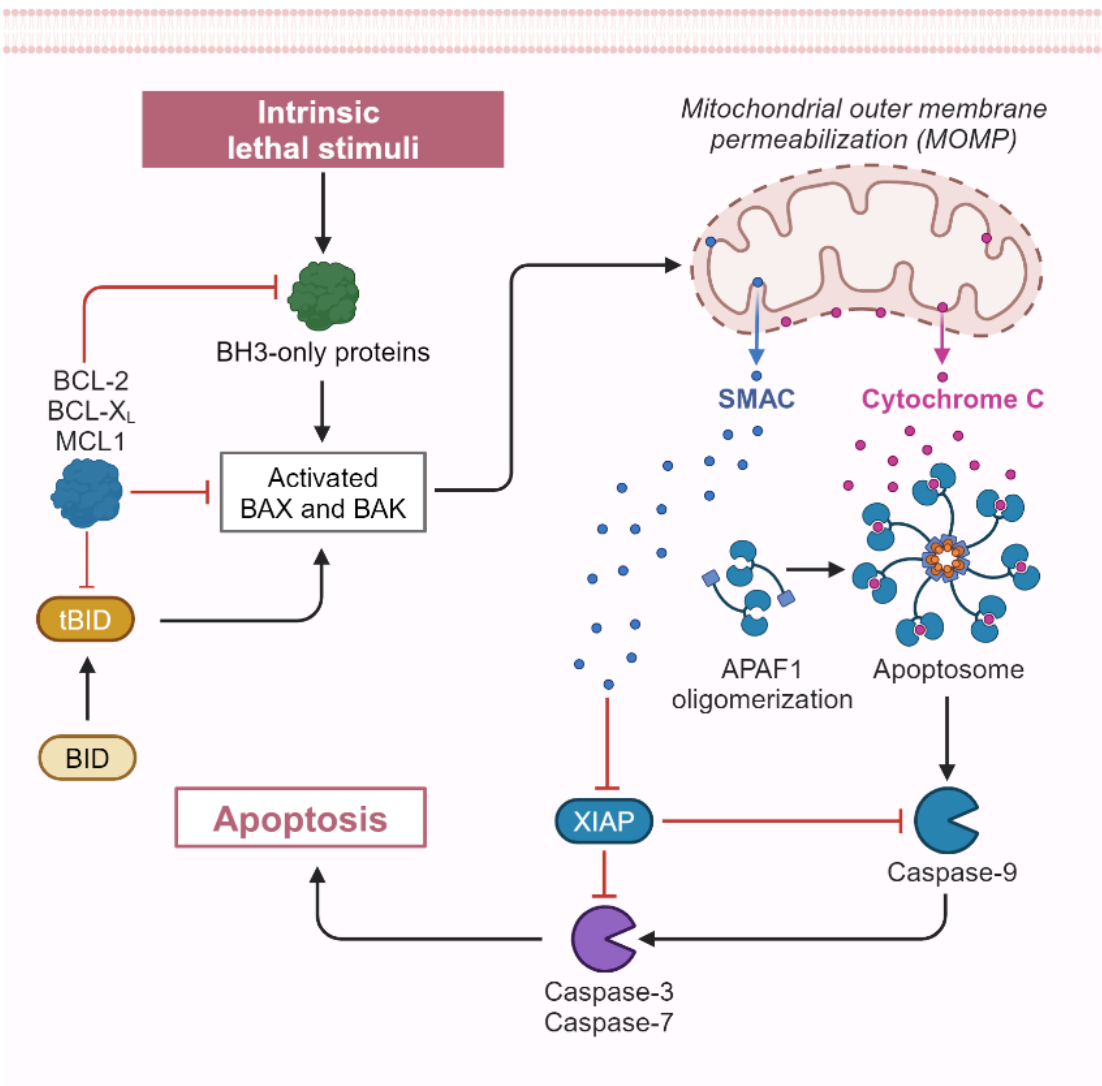


Figure 2. Mitochondria Play a Central Role in Intrinsic Apoptosis
Made with Biorender.com

In addition to regulating key metabolic processes, mitochondria are critical in the intrinsic apoptosis pathway (**Figure 2**). Intrinsic stressors like increases in cytosolic Ca^{2+} , growth factor deprivation, ROS, DNA damage and hypoxia induce the intrinsic

apoptotic response¹³⁴. The B-cell lymphoma 2 (**BCL-2**) family are critical mitochondrial pro- and anti-apoptotic proteins. Pro-apoptotic proteins in the BCL-2 family contain a single BH3 domain and include BCL-2 interacting mediator of cell death (**BIM**), Bcl-2-binding component 3 (**BBC3** / p53 upregulated modulator of apoptosis **PUMA**), and truncated BH3 interacting domain death agonist (tBID)^{114,135}. Upon exposure to a stress signal, BH3-only containing proteins release from the anti-apoptotic multi BH3-containing protein family members (BCL-2, **BCL-xL**, myeloid cell leukemia 1 (**MCL-1**), **BCL-w** and **A1**). BH3-only proteins then associate with the pro-apoptotic effectors BCL-2 associated X protein (**BAX**) and BCL-2 antagonist/killer (**BAK**) so that they can form pores in the MOM to trigger the release of Cyt c and second mitochondria-derived activator of caspase (**SMAC**). Cyt c binds to apoptotic protease activating factor-1 (**APAF1**) to activate the caspase-9 proteolytic signal cascade, while SMAC binds to inhibitor of X-linked inhibitor of apoptosis protein (**XIAP**), an inhibitor of caspase 9^{114,135}.

1.4. Obesity and Metabolic Disease are Risk Factors of Cancer

Much like the waistlines of the world's population, the literature regarding the distinct types of adipose tissue has been expanding over the years. The growth in literature is partially due to the discovery of 5 distinct adipose tissue types: white adipose tissue (**WAT**), brown adipose tissue (**BAT**), beige/brite adipose tissue, bone marrow adipose tissue (**BMAT**), and perivascular adipose tissue (**PVAT**). Given the rich literature on the subject and the limited scope of this review, we will only highlight a few major features of each depot here. A more detailed account of each depot can be found in these comprehensive reviews^{136–140}.

Adipocytes are the primary cellular component of adipose tissue, but adipose tissue is also composed of nervous and connective tissue and vasculature. Adipocytes found in WAT possess the morphology commonly associated with a fat cell, a cell with one large lipid droplet (**LD**), which occupies most of the cellular space, forcing the nucleus and cytoplasm to the periphery of the cell. The two main WAT depots, visceral (**VAT**) and subcutaneous (**SAT**), are functionally different. VAT is essential for the protection of inner organs and a major contributor to obesity^{141,142}. Conversely, SAT is primarily responsible for insulation and has been associated with improving insulin sensitivity¹⁴³. Although VAT and SAT appear to have opposing functions, they both regulate energy homeostasis. For energy homeostasis, exogenous energy sources such as glucose are stored as glycogen and subsequently converted into triacylglycerols (**TGs**), the major component of the energy storing organelle, the lipid droplet, in adipocytes¹⁴⁴. As the cellular need for energy increases, lipases release TGs causing lipid droplets to degrade, in a process known as lipolysis. TGs are subsequently broken down into glycerol and fatty acids, which eventually produce ATP through glycolysis or β -oxidation, respectively¹⁴⁵.

The connection between adipocytes and insulin make adipocytes one of the most significant cell types to regulate systemic insulin levels¹⁴⁶. Insulin bears much of the responsibility for promoting the cellular uptake of glucose through upregulating the GLUT4 glucose transporter¹⁴⁷. To promote energy storage, insulin also inhibits lipolysis through the inhibition of protein kinase A (**PKA**)¹⁴⁸, and it is thus integral for adipocyte maintenance and function¹⁴⁹. Adipose vascularization and innervation also reflect the crosstalk that occurs between adipose and distant tissues. For decades, adipocytes

were assumed to simply function as cells that store and release energy and provide mechanical and thermal insulation. However, the complexity of adipocytes was revealed when substances specifically secreted by adipocytes, known as adipokines, were identified in the 1980's and 90's¹⁵⁰⁻¹⁵².

The adipokine leptin was found to regulate feeding, fatty acid utilization, and energy balance by serving as a feedback mechanism between adipose and other tissues throughout the body¹⁵³⁻¹⁵⁵. Leptin activates 5' adenosine monophosphate-activated protein kinase (**AMPK**), leading to an increase in fatty acid oxidation and inhibition of the rate-limiting step to lipogenesis, acetyl-CoA carboxylase (**ACACA**) action¹⁵⁶. Leptin also serves to protect against lipotoxicity by shuttling fatty acids away from non-adipose tissue¹⁵⁷. Another key adipokine, adiponectin (**ADIPOQ**), is expressed exclusively by mature adipocytes but decreased in the context of obesity, supports insulin sensitivity, and has a protective effect against cardiac hypertrophy and atherosclerosis¹⁵⁸⁻¹⁶⁰. Indeed, adiponectin receptors 1 and 2 (**ADIPOR1** and **ADIPOR2**) have anti-diabetic effects¹⁶¹. The broad effects of ADIPOQ on metabolism and cardiac health can be attributed to its formation of trimers, hexamers and even higher molecular weight forms of the protein¹⁶². Interestingly, each ADIPOQ complex can act on different pathways; for example, while the trimeric form activates AMPK, the higher molecular weight form activates NFκB^{163,164}.

Brown adipose tissue, an adipose depot unique to mammals, is found at distinct locations: the major depots of BAT in adult mice and rats can be found in the scapulae and thoracic regions, where they serve as the major source of non-shivering thermogenesis¹⁶⁵. Similarly, adult human BAT is primarily located in the cervical-

supraclavicular depot and is identified by the uptake of ^{18}F -fluorodeoxyglucose via PET-CT due to the propensity of BAT to consume more glucose than other healthy tissues^{166,167}. Unlike WAT, BAT is multilocular and takes advantage of the mitochondrial membrane protein, uncoupling protein 1 (**UCP-1**), to produce heat instead of ATP during the process of fatty acid oxidation^{168,169}. UCP-1 functions by increasing membrane permeability of the mitochondrial membrane to disrupt the proton motive force at the heart of ATP synthesis. BAT is characterized by the high expression of PR domain containing 16 (**PRDM16**), Peroxisome proliferator-activated receptor gamma coactivator 1-alpha (**PPARGC1A**), type 2 deiodinase (**DIO2**) and UCP-1^{170,171}. Brown and white fat also differ in their progenitors, with the lineage of BAT being traced to a myogenic precursor which is Paired box protein 7 positive/ myogenic factor 5 positive (**Pax7+/Myf5+**), while the WAT progenitor is Pax7-/Myf5-^{170,172}.

Beige fat or inducible brown fat is a prime example of the dynamism that adipocytes exhibit. Upon prolonged cold exposure or adrenergic signaling, a subset of white adipocytes upregulate UCP-1 and adopt a more BAT-like phenotype, a process termed "browning"^{138,173}. Browning initiates a switch from a unilocular white adipocyte to a beige adipocyte that is multilocular and thermogenic and has an increased number of mitochondria. Both browning and BAT may be protective from obesity based on observations that browning in obese strains of mice is decreased compared to strains resistant to obesity, while the thermogenic capacity of BAT remains the same^{174,175}. Additional evidence for the protective effects of beige and brown fat suggests they play a major role in decreasing circulating TG and glucose levels¹⁷⁶. Deeper investigations into brown and beige fat biology will likely help combat metabolic syndromes like obesity

and type 2 diabetes mellitus (**T2DM**) that are reaching epidemic levels in many countries.

Peering into the bone marrow within the long bones of an adult human or mouse, one would observe that 50-70% of the bone marrow has distinct yellow hue¹⁷⁷. This hue is due to the presence of bone marrow adipose tissue (BMAT). BMAT is induced by common medical practices such as the administration thiazolidinediones (such as the anti-diabetic drug rosiglitazone), radiation and chemotherapy¹⁷⁸⁻¹⁸¹. Studies suggest that BMAT may have a complicated role in global metabolism since BMAT is increased both in obesity and paradoxically, in patients suffering from anorexia nervosa or starvation^{182,183}. BMAT appears to have a distinct lineage from other adipose depots; bone marrow MSCs that are CD45⁻/CD31⁻/PdgfRa⁺/Sca1⁺ differentiate into adipocytes¹⁸⁴. Additionally, BM adipocytes originate from osterix⁺ cells while other adipocytes do not¹⁸⁵. The role of BMAT with respect to global metabolism and the effects of BMAT on the local bone marrow microenvironment remain important questions to address in the field.

Perivascular adipose tissue, the fat depot adjacent to the adventitia of most arteries, is an integral signaling component of the vascular microenvironment. Expansion of PVAT is associated with obesity and cardiovascular disease in humans, with pathological changes described in patients with localized vasospasm, abdominal aortic aneurysm, and coronary artery disease¹⁸⁶⁻¹⁸⁹. In addition to its basal ability to store and release fatty acids, PVAT alters vascular tone, smooth muscle cell proliferation and migration, inflammatory programs, and oxidative stress pathways. PVAT exerts its influence on the surrounding tissues through the secretion of adipokines

and cytokines such as leptin, adiponectin, TNF- α and IL-6^{190–193}. Although healthy PVAT is considered vasoprotective, obesity and hyperlipidemia induce changes that can promote vascular disease progression. In a genetic mouse model of atherosclerosis, the PVAT from a apolipoprotein E-null (**ApoE**^{-/-}) mouse promoted atherosclerotic plaques in a region where it does not usually form in ApoE^{-/-} mice^{194,195}. The phenotype of mouse and human PVAT depends on its location. While PVAT near the carotid artery adopts a BAT-like morphology it more closely resembles WAT in the mesenteric arteries. Indeed, the thermogenic properties and BAT-like expression pattern of thoracic aorta-associated PVAT proved to attenuate atherosclerosis¹⁹⁶, suggesting PVAT as an important source of paracrine regulation in vascular disease. There is some question about how well mouse models of PVAT expansion and pathology can mimic these processes in humans, since aortic PVAT derived from adult humans is morphologically more similar to WAT than BAT. However, human aortic PVAT, even from patients with cardiovascular disease, express thermogenic markers including UCP-1, which is absent in human WAT. Within the thoracic aorta, PVAT adopts a more BAT-like phenotype^{196,197}. Studies of human PVAT have shown that PVAT-derived adipocyte progenitor cell differentiation is dependent on Rab27a, a GTPase important for secretory vesicle trafficking¹⁹⁸. One could imagine that the bi-directional communication between PVAT and the blood vessel relies on Rab27a-dependent trafficking and secretion of signaling molecules. These interesting results highlight that the full potential of targeting PVAT with respect to cardiovascular disease and obesity has yet to be realized and requires further study.

As researchers delved deeper into adipocyte biology, they have come to appreciate that adipocytes are highly sensitive to metabolites, cytokines and hormones,

and can also regulate processes like angiogenesis, inflammation, immunity, reproduction and cardiac homeostasis^{152,199–206}. Given that adipose tissue is intimately intertwined in a diverse number of biological processes, it is imperative to understand the intricacies of this tissue.

1.5. Intersection of Obesity, Type II Diabetes and Cancer

Obesity is a worldwide health concern that affects roughly a third of the population and costs an estimated \$209.7 billion dollars a year in the United States alone^{207,208}. Obesity is defined as having a BMI of $>30 \text{ kg/m}^2$, is characterized by excess accumulation of adipose, and is a major risk factor for various health issues including T2DM, cardiovascular disease and many cancers^{209–211}. Obesity correlates with increased incidence of MM^{6,7} and high BMI correlates with a poor treatment response^{212–216}. Obesity is a major risk factor for many cancers²¹⁷, however, given the complexity of obesity, there are an array of mechanisms by which obesity may support tumor cells. Hypoxic-driven expansion of fat mass in obesity triggers adipocytes to convert to a dysfunctional state, defined by increased proinflammatory cytokine secretion, apoptosis and free fatty acid release^{218,219}. Studies of obesity and myeloma are mainly at the epidemiological level and have not extensively explored the mechanism of this relationship^{6,7}. For a summary of specific factors linked to obesity that support MM see Figure 3 and these reviews^{220,221}. Obesity has been difficult to study because the regulation of adipocytes is influenced by environmental, genetic and epigenetic factors, but the development of tissue-engineered models could aid in providing insight into this complicated disease^{222–224}.



Figure 3. Contributions of Obesity to Multiple Myeloma

A) Bone marrow adiposity is increased in obesity and bone marrow adipocytes support MM survival, migration and drug resistance^{225–229}. **B)** Acetyl-CoA Synthetase 2 (ACSS2)²³⁰ is positively correlated with a higher body mass index (BMI) and it was shown to stabilize interferon regulatory factor 4 (IRF4) and support MM proliferation²³⁰. **C)** Leptin increases MM Interleukin-6 (IL-6) production, angiogenesis, protein kinase B/signal transducer and activator of transcription 3 (AKT/STAT3) signaling and increases resistance to apoptosis^{231–233}. **D)** Adiponectin, an anti-myeloma adipokine is decreased in obesity. Decreased levels of adiponectin are associated with increased pro-myeloma cytokines IL-6, tumor necrosis factor- α (TNF- α), nuclear transcription factor kappa B (NF- κ B) signaling, nerve growth factor (NGF) levels, and the maturation of osteoclasts by increasing mammalian target of rapamycin (mTOR), eukaryotic translation Initiation factor 4E-binding protein (4EBP1) signaling^{226,234–236}. **E)** Obesity creates a proinflammatory environment that increases local and systemic levels of proinflammatory cytokines like IL-6, TNF- α and c-reactive protein (CRP)^{237–239}. **F)** There is increased IGF1 in obese patients and IGF signaling has been shown to be supportive of MM proliferation and survival^{240–242}. **G)** MM patient-derived differentiated bone marrow adipocytes increase MM cell proliferation. MM cells induce lipolysis of bone marrow adipocytes causing free fatty acids to be imported to MM cells by fatty acid transport proteins (FATPs)²⁴³. Transfer of mitochondria from bone marrow mesenchymal stem cells to MM cells increases MM cell OXPHOS²⁴⁴. This figure is adapted from Marques-Mourlet *et al.* 2023²²⁰.

To increase the capacity of energy storage during caloric excess, adipocytes increase in size, in a phenomenon called hypertrophy. Although increases and decreases in adipocyte size based on the nutrition state of the organism is normal, excessive and prolonged adipocyte hypertrophy is often a sign for adipocyte dysfunction and leads to system-wide changes due to an altered adipocyte secretome. Although hypertrophic adipocytes have an increased capacity to store lipids, it is insufficient to contend with the extracellular excess of free fatty acids (**FFAs**). The excess of FFAs induces local lipotoxicity from increases in oxidative and endoplasmic reticulum (**ER**) stress and can have system effects as well^{245,246}. The increase in size of adipocytes prevents oxygen from diffusing across the adipose tissue, resulting in a hypoxic microenvironment^{247–249}. Together, adipocyte hypertrophy, hypoxia, oxidative and ER stress contribute to the increase in the secretion of adipokines and cytokines as well as the differentiation of new adipocytes^{250,251}. An increase in local pro-inflammatory cytokines resulting from adipocyte secretion, necrosis and lysis leads to immune cell recruitment and chronic inflammation, perpetuating adipocyte dysfunction^{252,253}. When compared to healthy patients, obese individuals also have increased leptin, fasting glucose, TGs, inflammatory markers and insulin concentrations, and decreased high-density lipoproteins (**HDLs**) in their serum and higher oxidized low-density lipoproteins (**LDL**)²¹⁹. Together, these factors can lead to additional morbidities including T2DM and cardiovascular disease. Interestingly, there is a subpopulation of obese patients that have an increase in fat mass but lack the risk of metabolic dysfunctions and cardiovascular disease, known as metabolically healthy obese patients²¹⁹. For the

purposes of this dissertation, obesity will refer to the metabolically dysfunctional population.

Impaired insulin signaling is at the heart of why T2DM patients fail to regulate their blood sugar and is intimately linked with obesity²⁰⁹. Insulin signaling activates two major pathways through phosphorylation of insulin receptor substrates (**IRSs**) on tyrosine residues: (1) the PI3K-AKT and (2) MAPK pathways²⁵⁴. While the PI3K-AKT pathway regulates glucose uptake and suppresses gluconeogenesis, the MAPK pathway interacts with PI3K-AKT to regulate cell growth and differentiation. Insulin signaling is negatively regulated by phosphorylation of serine residues on IRS1 by kinases such as I kappa B kinase beta (**IKKB**) and C-jun-N-terminal kinase (**JNK1**)²⁵⁴. Interestingly, ER stressors from FFA signal through endoplasmic reticulum to nucleus signaling 1 (**ERN1**) to activate both IKK and JNK pathways, contributing to insulin resistance. Additionally, blood glucose remains higher in obese individuals due to *GLUT4* expression in adipocytes being downregulated by the induction of ER stress²⁵⁵. The negative effects of inflammation are further perpetuated by the recruitment of adipose tissue macrophages (**ATMs**).

Activated stress pathways found in obesity drive the expression of chemokines like C-C motif chemokine ligands 2, 8 and 5 (**Ccl2**, **Ccl8**, **Ccl5**), and chemokine receptors (e.g. **Ccr2** and **Ccr5**), which help recruit macrophages to the dysfunctional tissue^{252,256}. ATMs form crown-like structures around the stressed adipocytes in order to clear debris and excess FFAs²⁵². The recruited ATMs secrete both anti-inflammatory (interleukin-10 (**IL-10**) and IL-1) and pro-inflammatory and pro-MM, TNFA, IL-6 and IL-1B cytokines, suggesting they can serve both a protective and harmful role in obesity²³⁷.

However, the inflammation caused by ATMs causes further adipocyte dysfunction and impaired insulin signaling, leading to the manifestation of chronic low-grade inflammation.

Given the intersection between fatty acids (**Figure 4**) in MM with respect to obesity and MM cell interactions with BMAds, there is a promising potential in researching how fatty acid metabolism (**Figure 5**) contributes to MM cell proliferation, survival, and drug resistance.

1.6. Acyl-CoA Synthetase Long Chain (ACSL) Isozyme Family in Cancer

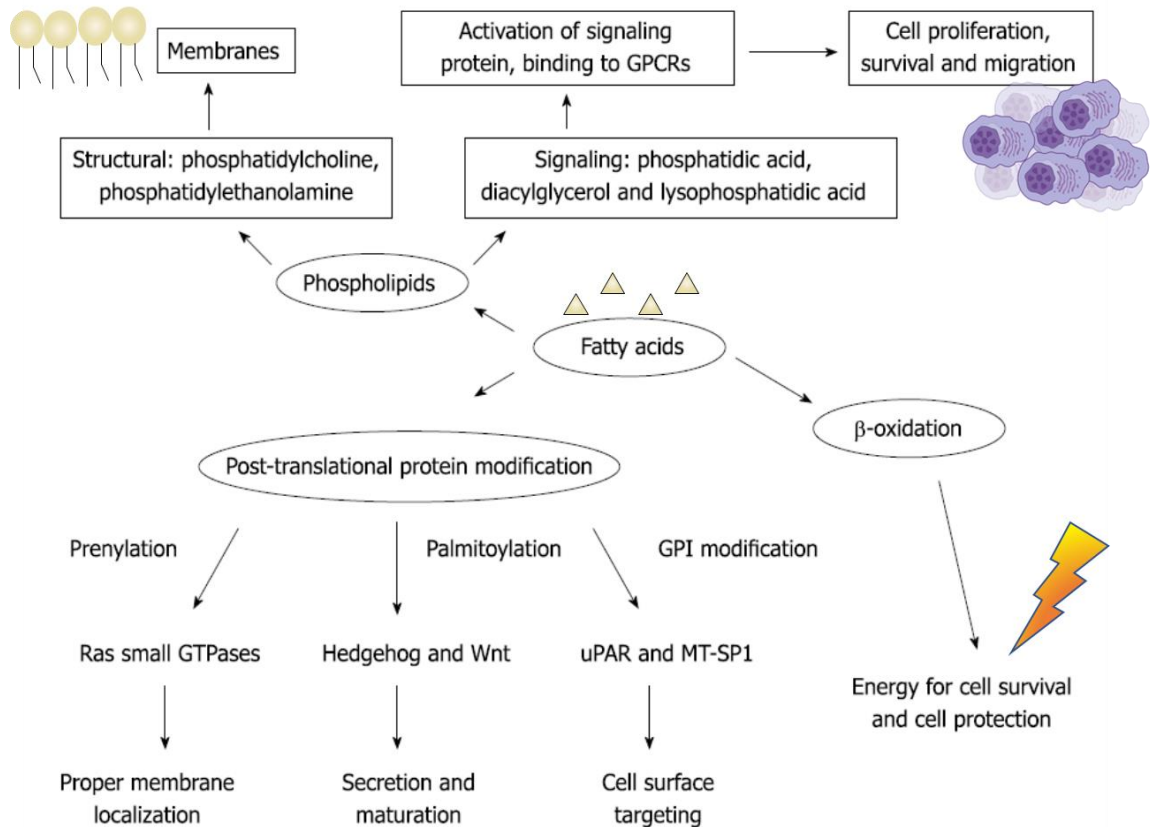


Figure 4 Fatty Acids have Diverse Cellular Functions

Fatty acids are important for cellular energy generation, membrane localization, secretion and maturation, cell membrane structure and are key signaling molecules that support cell proliferation and survival. G-protein coupled receptors (GPCRs), membrane type serine protease 1 (MT-SP1), Urokinase-type plasminogen activator-receptor (uPAR). Adapted from Zhang *et al.* 2012²⁵⁷.

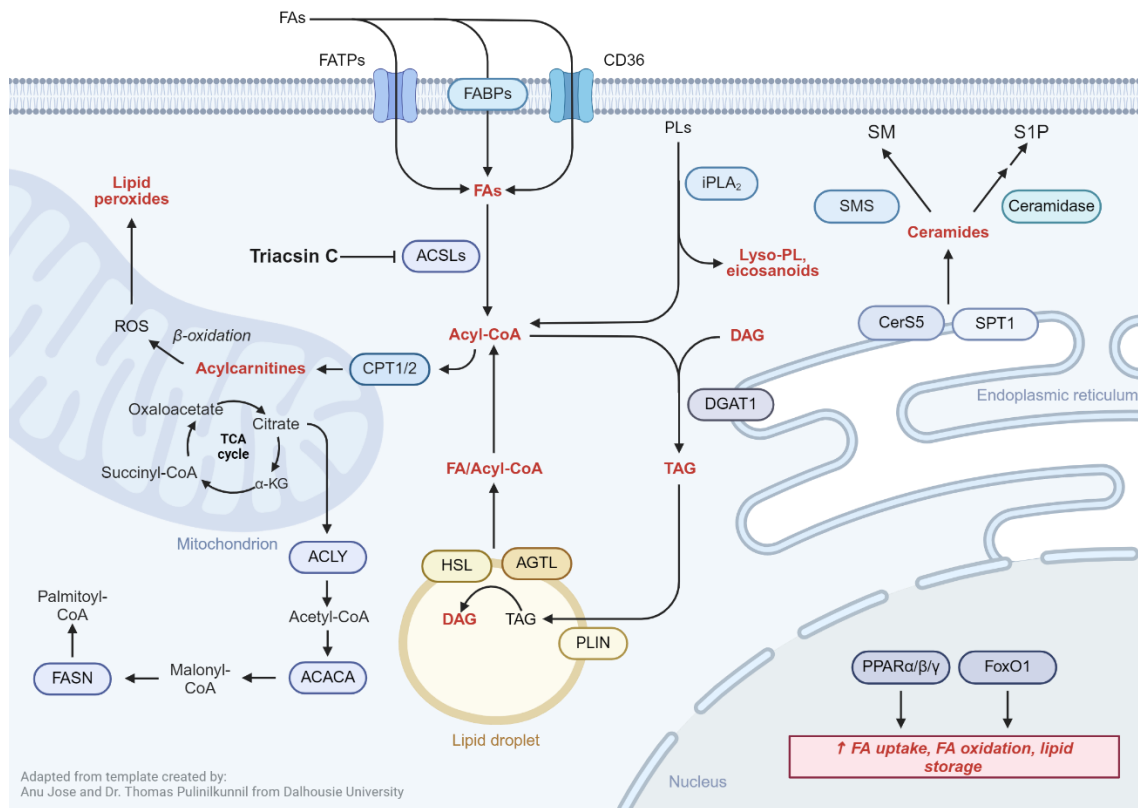


Figure 5 General Fatty Acid Metabolism

Fatty acids (FAs) can enter through the cell through fatty acid binding proteins (FABPs), fatty acid transport proteins (FATPs) and cluster of differentiation 36 (CD36). Long-chain fatty acids (8-20 carbons long) are activated by the acyl-CoA synthetase long-chain family (ACSLs) so they can be metabolized catabolically or anabolically. The activity of the ACSLs can be inhibited by a small molecule competitive inhibitor, Triacsin C. FA acyl-CoAs are converted to acylcarnitines in the mitochondria through carnitine palmitoyl transferase 1/2 where they undergo β -oxidation (fatty acid oxidation) to support energy generation and the tricarboxylic acid cycle. As a byproduct of OXPHOS and β -oxidation, reactive oxygen species (ROS) are generated and can react with lipid and form lipid peroxides. Alternatively, FA acyl-CoAs can be processed into the long-term FA storage molecule, triacylglycerols (TAGs) by the action of diacylglycerol acyltransferases ligating diacylglycerols (DAGs) with the FA acyl-CoAs. Perilipin (PLINs) proteins form the structural basis to for lipid droplets, the organelle that stores TAGs. TAGs are mobilized back into FA acyl-CoAs by hormone sensitive lipase (HSL) and adipose triglyceride lipase (ATGL). Serine palmitoyltransferase 1 (SPT1) and ceramide synthase 5 (CERS5) coordinate with other enzymes to produce ceramides, key signaling and structural lipids. Ceramides can be catabolized into sphingomyelins (SMs) or sphingosine-1-phosphate (S1P), important for phospholipid and cell signaling, respectively. Calcium-independent phospholipases (iPLAs) hydrolyze phospholipids (PLs) to lysophospholipids and eicosanoids (derived from FAs), which are key signaling molecules. FAs can be synthesized from the conversion of tricarboxylic acid (TCA) cycle-derived citrate to acetyl-CoA by ATP citrate lyase (ACYL). Acetyl-CoA is further processed by acetyl-CoA carboxylase (ACACA) to form malonyl-CoA, the substrate fatty acid synthase (FASN) uses to form palmitoyl-CoA¹¹⁶. This figure was made with Biorender.com

Recent work on other cancers shows promise for targeting members of the acyl-coenzyme A long chain synthetase (ACSL) family of proteins (**Figure 6; Table 3**), which activates long-chain fatty acids (saturated and unsaturated FAs with chain lengths of 8–22 carbons) into fatty acyl-CoA esters, which can then be used for catabolic or anabolic metabolism²⁵⁸. Although there is not a crystal structure of The catalytic activity of rat ACSL1 can be completely inhibited by mutation or acetylation of Lys676 in the C-terminus of the protein²⁵⁹. System-level analyses of ACSLs across cancer types have revealed that ACSL expression and their role as oncogenes or tumor suppressors are heterogeneous and cancer-type dependent²⁶⁰. While ACSL1 has been shown to support the proliferation of both colorectal cancer (**CRC**) and breast cancer (**BC**) cell lines, evidence supports ACSL1 as a tumor suppressor in non-squamous cell lung carcinoma (**NSCLC**) cells^{260,261}. Additionally, ACSL1 and ACSL4 support invasion of CRC, prostate cancer, and quadruple-negative BC cells^{262–265}. In estrogen receptor-positive BC, ACSL4 has been shown to modulate drug efflux pumps to support chemotherapy resistance²⁶³. ACSLs also regulate metabolism in a cancer type-specific manner. In CRC, overexpression of *ACSL1* and *ACSL4* resulted in enhanced glycolysis²⁶¹, while ACSL3 regulates FAO in BC and NSCLC in opposite directions, while supporting proliferation in both cancers^{266,267}. Therefore, it is critical to study the role of ACSLs in a cancer specific manner.

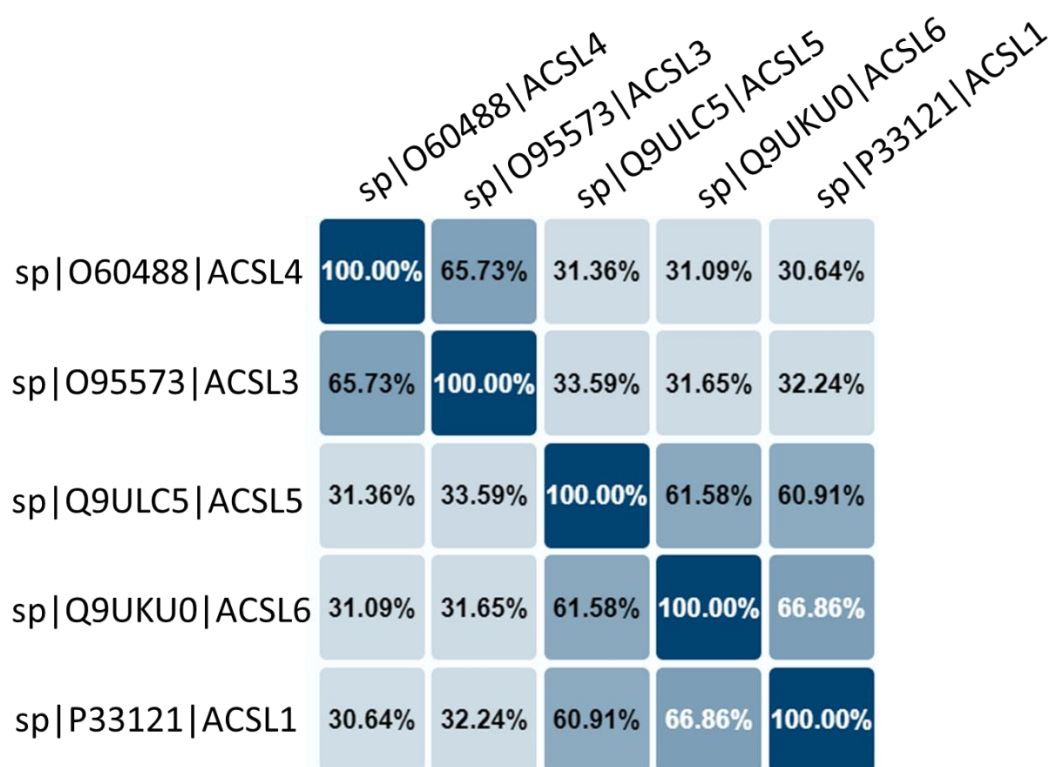


Figure 6 Human ACSL Isozyme Family Protein Homology
 Clustal Omega protein alignments of the human ACSL family isozymes with their associated UniProt accession numbers²⁶⁸. Darker colors represent greater primary amino acid homology. ACSL4 and 3 share 65.7% homology while ACSL6 and 1 are 66.86% homologous. This figure was made through <https://www.uniprot.org/align> through Clustal Omega.

Table 3. ACSL Isozyme Family Function and Regulation²⁵⁸

Protein Name	Tissue Expression*	Subcellular Localization**	Substrate Preference	Cellular Functions	Transcriptional Regulators
ACSL1	Liver Heart Adipose Tissue Muscle	ER Mitochondria	16-18 Carbon Saturated FAs 16-20 Carbon Unsat. FAs	FAO TAG Synthesis Ferroptosis Cardiolipin Synthesis	SREBP (+) NF-κB (+) PKC-SIRT6 (+) BRD4-PPARα (+) HBXIP-SP1 (+)
ACSL3	Brain Prostate	ER Mitochondria Lipid Droplets	16:0 (Palmitic Acid)	FAO TAG Synthesis Oxidative Stress	FGF19 (+) LxR (+) PPARγ,δ (+) CREBP-1C (+) OCT1-AR (+)
ACSL4	Adrenal Gland Ovary Testis Brain	ER Mitochondria Peroxisomes	20-carbon PUFAs (eg, Arachidonic Acid, EPA)	Ferroptosis Glycolysis FAO	STAT3 (-) AR (-) YAP (+) SHP2 (+) SP1 (+) CREB (+)
ACSL5	Intestines Liver Skeletal Muscle	ER Mitochondria Lipid Droplets	16-18 Carbon FAs (16:0, 18:0, 18:2)	FAO WNT Signaling Apoptosis Ceramide Synthesis	Estrogen Receptor (+) HNF4 (+) SREBP1-c (+) PPARα,γ (+) ERK-OM (+)
ACSL6	Brain Bone Marrow Muscle	ER Mitochondria Peroxisomes	22:6 (Docosahexaenoic Acid)	FA Synthesis OXPHOS Glycolysis	PPARγ (+) SREBP1-c(+)

Table 3 ACSL Isozyme Family Function and Regulation

*Tissues in which is the gene in question is highly enriched **It has been shown that ACSL subcellular localization and function is tissue- and cell type-dependent²⁶⁹. (+)/(-) is representative of positive or negative regulation (respectively) of the ACSL isozyme by the protein listed.

ACSLs play important roles in the development of lymphoid hematological malignancies. In a retrospective study of leukemia patients, *ACSL6* expression was positively correlated with overall survival, suggesting that *ACSL6* may be a tumor suppressor in leukemia²⁶⁰. In that analysis, of all ACSLs, only *ACSL4* was shown to be overexpressed in myeloma cells relative to control tissues²⁶⁰. Zhang *et al.* also reported that *ACSL4* was overexpressed in primary MM cells and supported MM cell proliferation, possibly involving the c-Myc/sterol regulatory element binding protein (SREBP) axis²⁷⁰. These investigators also showed that *ACSL4* expression in MM cells was positively correlated with their sensitivity to ferroptosis, an iron-dependent form of cell death²⁷⁰. Despite these studies, the contribution of the ACSL family to MM cell fitness remains largely unaddressed.

1.7. Triacsin C and Cancer

Triacsin C (TriC) is an alkenyl-N-hydroxytriazene bacterial metabolite and a competitive inhibitor of the FA-binding domain of ACSLs²⁷¹. Biochemical inhibition of ACSLs from rat liver homogenates found the concentrations of TriC required for 50% inhibition to be 8.7 μM ²⁷². Similarly, in enzymatic activity studies using rat recombinant ACSL1 and ACSL4, the IC_{50} values for TriC were found to be ~4–6 μM ²⁷³ while importantly, rat ACSL5 activity was found to be insensitive to TriC²⁷³. TriC's effectiveness may be species specific, as TriC inhibited the growth of human BC cells and human intestinal cells, where *ACSL5* is highly expressed^{274,275}. TriC also has been shown to inhibit viability of acute myeloid leukemia (AML) cell lines and primary cells (in

part by inducing apoptosis), synergized with other anti-AML therapies, and showed no toxicity to healthy donor CD34+ cord blood cells in the dose range tested (up to 16 μ M, 48 hours)²⁷⁶. TriC has been shown to effectively inhibit the growth of human breast cancer cells²⁷⁵, while in acute myeloid leukemia (AML), TriC treatment inhibits cellular viability and synergizes with other anti-AML therapies²⁷⁶. In endometrial cancer, TriC decreases survival, an effect that is enhanced by the addition of omega-3 FA docosahexaenoic acid (DHA)²⁷⁷. TriC also induces apoptosis in glioma cells and synergizes with the apoptosis inducer etoposide, causing substantial cytotoxicity in glioma cells both *in vitro* and *in vivo*²⁷⁵.

If readers are interested in 3D models of adipose tissue models of disease, please find what I have written on the topic here²⁷⁸.

2. CHAPTER 2: MATERIALS AND METHODS

2.1. Cancer Dependency Map Analysis

The gene essentiality scores (Chronos scores) ²⁷⁹ for a modified list of the Hallmark Fatty Acid Metabolism genes (GSEA M5935 <https://www.gseamsigdb.org>, (Table 14) in 21 human MM cell lines from the Cancer Dependency Map (DepMap) dataset (<https://depmap.org/portal/download/>) were reported. Modifications were made to Hallmark Fatty Acid Metabolism Gene List via addition of other genes within the same family. For example, ACSL1, ACSL4 and ACSL5 are in the original data set but ACSL3 and ACSL6 are not. Therefore, ACSL3 and ACSL6 were added to provide a more comprehensive list of genes associated with fatty acid metabolism. Chronos scores are calculated from a high-throughput clustered regularly interspaced short palindromic repeats (**CRISPR**)/CRISPR-associated protein 9 (**Cas9**) genetic screen in cancer cell lines. Cell lines of interest stably expressing Cas9 were transduced with lentiviruses containing four short guide RNAs (sgRNAs) against each gene. Chronos scores are an integration of sgRNA cutting efficiency, proliferation rate, and correcting for copy number that are assessed over multiple timepoints as the cell lines of interest proliferate²⁷⁹. Essential genes are designated with a value of -1 and the Chronos score of a query gene is relative to -1²⁷⁹. Human MM cell line gene and protein expression data were downloaded from the Cancer Dependency Map/Cancer Cell Line Encyclopedia (Expression 22Q2_Public)²⁸⁰.

2.2. Cell Lines and Culture Conditions

MM.1S (ATCC), RPMI-8226 (ATCC), and OPM-2 (DSMZ) cells, as well as green fluorescent protein (GFP) and luciferase-expressing MM.1S (MM.1S^{gfp+/luc+}), MM.1R (MM.1R^{gfp+/luc}) and HL-60^{mCherry+/luc+} (an AML cell line, referred in the rest of the text as HL-60) cell lines (**Table 4**) were obtained and cultured as previously described²⁸¹ in RPMI-1640 basal media supplemented with 10% (15% for U266B1 cells) fetal bovine serum (FBS, VWR) with 1% PSA (Penicillin, Streptomycin and Amphotericin B, ThermoFisher Scientific, Cat # 15240112) at a cell density of 4.1×10^5 cells/mL in tissue culture-treated T-75 flasks (VWR)²⁸¹. Cells were cultured at 37 °C at 5% CO₂, unless otherwise stated. MM.1S^{gfp+/luc+} cells were used for experiments involving MM.1S cells unless otherwise stated. Human myeloma cell lines were authenticated by subjecting genomic DNA isolated with the QIAamp DNA Mini Kit (Qiagen), and short tandem repeat (STR) analysis was performed with the CLA IdentiFiler™ Plus PCR Amplification Kit (ThermoFisher Scientific) and sequenced on an ABI SeqStudio Genetic Analyzer (ThermoFisher Scientific) according to the manufacturer's protocol through the Vermont Integrative Genomics Resource at the University of Vermont. STR profiles (**Table 5**) were compared between the experimental results and the reference using the Cellosaurus STR Similarity Search tool with the Tanabe algorithm, scoring only non-empty markers and excluding amelogenin (CLASTR v1.4.4, Swiss Institute of Bioinformatics).

Table 4. Human MM and AML Cell Lines Used

Human Cell Lines (Origin)	Genetic Alteration and Frequency in Patients (%)	Sex, Age (Years)
MM.1S ^{gfp/luc} (Ghobrial Lab) ²⁸² And MM.1S (ATCC)	t(12;14)(q32;q23) MAF overexpression (~25%) ^{282,283} KRAS; pGly12A TRAF3; pVal536_Asn545del	Female (42)
MM.1R ^{gfp/luc}	t(12;14)(q32;q23) MAF overexpression (~25%) KRAS; pGly12A TRAF3; pVal536_Asn545del	Female (42)
OPM-2 (DSMZ) ²⁸⁴	t(4;14), 1q21+, FGFR3; p.Lys650Glu mutation (15%) ^{57,66,68}	Female (56)
RPMI-8226, ²⁸⁵	1q21+, KRAS; p.Gly12Ala mutation ²⁸⁵ (21%) ⁶⁸	Male (61)
U266B1 (ATCC)	BRAF; p.Lys601Asn MSH6; p.Gly141Asp TP53; p.Ala161Thr TRAF3; p.Lys550LeufsX3 ²⁸⁶	Male (53)
HL-60 ^{mCherry/luc} ²⁸⁷ (Ghobrial Lab, this is an AML cell line)	TP53 Deletion CDKN2A; p.Arg80Ter, pPro94Leu NRAS; p.Gln61Leu	Female (36)

ATCC = American Type Culture Collection, DSMZ= German Collection of Microorganisms and Cell Cultures

2.3. Assessment of Single Nucleotide Variants (SNVs) via Sanger sequencing

Primers were designed with ExonPrimer accessed via the UCSC Genome Browser to target the genomic regions encoding SNVs relevant to cell line authentication including exons 1 and 2 of *CDKN2A*, exon 3 of *NRAS*, and the sequence encoding Arginine 175 in *TP53* (**Table 13**). For PCR amplification of genomic regions to target cell line-specific variants, cells were thawed and allowed to equilibrate in culture for 1 week, prior to counting. For each sample tested, 1×10^6 cells were collected in a pellet prior to genomic DNA isolation with Qiagen DNeasy Blood and Tissue Kit (Qiagen, Cat. No. 69504) per the manufacturer's instructions. Amplicon size was

confirmed by gel electrophoresis prior to isolation of DNA by QIAquick PCR Purification Kit (Qiagen, Cat. No 28104). 10ng of DNA was combined with the forward primer from each PCR pair and submitted for Sanger sequencing at the Vermont Integrative Genomics Resource. This method was written and performed by Heather Fairfield Campbell.

2.4. Assessment of predicted deletion on chromosome 17 by gel electrophoresis

Two primer sets were designed to target the region of chromosome 17 predicted to be deleted in HL-60 cells (Table 13). The predicted deletion on chromosome 17 was estimated using the CNV & Expression data for HL-60 from the Catalogue Of Somatic Mutations in Cancer (COSMIC) database. The UCSC Genome Browser was used to obtain genomic sequences in these regions and Primer3 was used to design primer sets on both the proximal and distal end of the predicted deletion. This method was written and performed by Heather Fairfield Campbell.

2.5. Primary Human Bone Marrow Mesenchymal Stem Cell Isolation

Deidentified and Institutional Review Board (IRB)-approved bone marrow biopsies from iliac crests of non-MM patients were physically dissociated with a serological pipette. Dulbecco's Modified Eagle Medium (DMEM, Corning, Cat. No. 10-101-CV) + 10% FBS +1% PSA was added to resuspend and the suspension was applied to a 0.7 µm filter (Corning Inc, Cat. No. 352350) to remove debris. The eluate containing human BM mesenchymal stem cells (hMSCs) and other cell types in the BM, was seeded onto tissue culture-treated T-180 flasks (VWR, Cat. No. 10062-864 and

cultured at 37 °C at 5% CO₂, allowed to adhere for one week and for to any residual red blood cells to lyse. Media was changed once per week. Upon reaching 90% confluence, cells were washed with phosphate buffered saline (**PBS**, Invitrogen Cat. No. 14040), incubated with 0.25% trypsin (Invitrogen, Cat. No. 25200) at 37 °C for 5-10 minutes. The trypsin was neutralized with DMEM +10% FBS and 1% antibiotic and antimycotic and cells were centrifuged for 5 minutes at 200 x g. The supernatant was removed and cells were resuspended in fresh DMEM +10% FBS and 1% antibiotic and antimycotic and plated into new tissue culture treated flasks at a density of 9,000 cells per cm².

Table 5 Primary Human Donor Information

Patient ID	Diagnosis	Sex	Race	Age (Years)	Median Age [95%CI]	BMI	Median BMI [95% CI]	Experiment
R16-0403	OsA	F	White	65	67.0 [60.3, 73.6]	25.4	28.5 [14.9, 42.1]	MM.1S + BMAAd Pre- exposure TriC
R17-0040	Hip OsA	M	White	69		30.28		MM.1S + BMAAd Pre- exposure TriC
R18-0075	Hip OsA	M	White	73		26.77		HL-60 Co- Culture 3 and 7 days (Gene Expression), Lipid Droplet Content and Fatty Acid Transfer
R19-2370	Hip OsA	F	White	65		42.61		MM.1S + BMAAd Pre- exposure TriC
R20-9000	MM	F	White	56	75.0 [54.9, 95.0]	20.43	22.4 [18.4, 26.4]	Primary MM + RealTime- Glo
R24-0125	MM	F	White	79		22.47		Primary MM + RealTime- Glo
R24-0553	MM	M	White	75		33.05		Primary MM + RealTime- Glo

OsA=Osteoarthritis, CI=Confidence Interval, BMI=Body Mass Index

2.6. Human Bone Marrow Adipocyte Differentiation

This protocol is adapted from Mauney *et al.* 2005 *Biomaterials* and Sekiya *et al.* 2004 *Journal of Bone Mineral Research*^{288,289}. 1×10^5 hMSCs were plated per well in 6-well dishes in DMEM +10% FBS + 1% antibiotic and antimycotic and allowed to adhere for seven days. Media was gently removed by aspiration and washed with PBS and replaced with adipogenic differentiation media: DMEM/F12 (Invitrogen, Cat. No.10565) +10% FBS + 1% antibiotic and antimycotic with 1 μ M insulin (Millipore-Sigma, I9278) 500 μ M 3-Isobutyl-1-methylxanthine (**IBMX**, Millipore-Sigma, Cat. No. I7018), 50 μ M indomethacin (Millipore-Sigma, Cat. No. I7378), 1 μ M dexamethasone (Millipore-Sigma, Cat. No. D8893). Adipogenic media was changed every seven days for a total of twenty-one days. Upon differentiation, adipocytes were maintained in DMEM/F12 + 10% FBS and 1% antibiotic and antimycotic.

2.7. Fluorescent Fatty Acid Transfer Assay Between hBMAds and HL-60 Cells in Transwells

1.5×10^4 hMSCs were differentiated into BMAds as above in 24-well tissue culture-treated plates and were gently washed three times with 0.2% fatty acid-free bovine serum albumin (BSA, ThermoFisher, Cat. No. AAJ6494422) dissolved in PBS to remove exogenous fatty acids. BMAds were then incubated with a fluorescent fatty acid, 10 μ M BODIPYTM 500/510 C₁,C₁₂ (ThermoFisher Scientific, Cat. No. D3823) for 4 hours in serum-free DMEM + 1% antibiotic and antimycotic at 37 °C with 5% CO₂. Labeled BMAds were then washed with 0.2% fatty acid-free BSA/PBS to remove excess extracellular label and were then cocultured with (5.0×10^4) HL-60 in 6.5 mm transwell

inserts with a 0.4 μm pore (Corning, Cat. No. 3470) for a 24-well plate for 6 days in RPMI-1640 basal media supplemented with 10% FBS and 1% antibiotic-antimycotic, this media was present in both compartments of the transwell. After 6 days of co-culture HL-60 cells were lifted from the transwells by pipetting up and down and seeded onto poly-D-lysine-coated glass bottom dishes, centrifuged for 5 minutes at 200 x g. The media was carefully removed and cells were incubated with 10% neutral buffered formalin (VWR, Cat. No. 89370-094) for 20 minutes at room temperature. Fixed HL-60 cells were then washed 3 times with PBS and counterstained with 0.3 $\mu\text{g}/\text{mL}$ of 4',6-diamidino-2-phenylindole (**DAPI**, 365 nm excitation/465 nm emission) and visualized using a 40x objective on a Leica DMI 6000b. This experiment was done once and with one human donor.

2.8. Bone Marrow Adipocyte and HL-60 Transwell Co-culture

1.5×10^4 hMSCs were either differentiated into BMAds as above in 24-well tissue culture- treated plates or seeded in parallel and cultured in DMEM + 10% FBS and 1% PSA. 5×10^4 HL-60 cells were seeded into the apical portion of a 6.5 mm transwell insert with a 0.4 μm pore size in RPMI-1640 +10% FBS + PSA. The media in the basolateral portion of the chamber was removed and replaced with RPMI-1640 +10% FBS + 1% PSA and the co-culture was incubated for either 3 or 7 days at 37 °C at 5% CO₂. For the 7-day timepoint, 3 days post-seeding the HL-60 cells, spent media on the bottom chamber was removed and replaced with fresh RPMI-1640 +10% FBS + 1% PSA. Fresh media equal to 50% to the total volume in the apical portion of the transwell was added (this equated to 500 μL) and co-culture was continued till the 7-day timepoint.

HL-60 cells were collected at each timepoint and processed for RNA extraction (see protocol below).

2.9. Magnetic Activated Cell Sorting of CD138 (Syndecan-1)-Positive Cells from Primary Multiple Myeloma Patients

Deidentified IRB-approved BM aspirates of MM patients were transferred to a 5 mL round-bottom tube (Corning Cat. No. 352058) and centrifuged for 5 mins at 200 x g. The EasySep™ Human PE Positive Selection (Stem Cell Technologies, Cat. No. 18551) was used for this protocol. The supernatant was removed and the pellet was resuspended in 500 µL of FACS buffer (PBS + 2% FBS + 1 mM ethylenediaminetetraacetic acid (**EDTA**)). FcR blocker was added to a final concentration of 50 µg per mL and an anti-CD138-PE conjugated antibody (Biolegend, Cat. No. 356504) in a 1:300 dilution and samples were incubated on ice for 3 hours (usually 15 minutes) under light protected conditions. Samples were washed 3 times with FACS buffer and PE selection solution (Stem Cell Technologies, Cat. No. 18151) was added 1:100 and incubated for 15 minutes at room temperature. Samples were mixed by pipetting up and down and EasySep™ Magnetic Nanoparticles (Stem Cell Technologies, Cat. No. 18150) were added 1:200 and incubated for 10 minutes at room temperature. FACS buffer was added 4 volumes of FACS buffer:1 volume of sample and each sample was subject to a 5 minute incubation at room temperature using the EasySep™ magnet (Stem Cell Technologies, Cat. No. 18000). The pellet (CD138 positive fraction) and supernatant were retained for measuring cellular redox potential with RealTime Glo as described below with both the CD138 positive and negative fractions were plated for experiments.

2.10. Miltenyi Magnetic Activated Cell Sorting of CD138 (Syndecan-1)-Positive Cells from Primary Multiple Myeloma Patients

Deidentified IRB-approved BM aspirates of MM patients were transferred to a 50 mL centrifuge tube (Avantor, Cat. No. 525-1075) through a 70 µm cell strainer (VWR, Cat. No. 76327-100) and centrifuged for 5 mins at 200 x g. The MACSprep™ Multiple Myeloma CD138 MicroBeads protocol was used for the following positive selection (Miltenyi Biotec, Cat. No. 130-111-744). The supernatant was removed and to lyse red blood cells, the pellet was resuspended in an equal volume of ACK lysis buffer (Lonza, Cat. No. 10-548E). After 10 minutes of incubation at room temperature, RPMI-1640 +10% FBS + 1% PSA was added 3 volumes of media: 1 volume of sample to halt the lysis. The cells were pelleted by centrifugation and resuspended in 50 µL MACSprep Multiple Myeloma CD138 MicroBeads for every 1 mL of pelleted cells. The cells and MicroBeads were thoroughly mixed and then incubated for 15 minutes at room temperature. Two 20 µL aliquots were removed to serve as the no-stain and pre-stain standards. The multi stand magnetic column (Miltenyi Biotec, Cat. No. 009039) was assembled and MACS Buffer (BSA, EDTA, and 0.09% azide, Miltenyi Biotec, Cat. No. 130-091-221) was eluted through the column into a waste beaker as preparation. The cells were passed through a 30 µm filter (Miltenyi Biotec, Cat. No. 130-041-407) and the eluate was saved as the negative fraction. The column was rinsed twice with 2 mL MACSQuant Buffer to ensure all CD138(-) cells passed through the column. The column was removed from the separator and flushed with 4 mL MACSQuant Buffer to collect the CD138(+) cell fraction. Flow Cytometry with an APC-anti-human CD138 Syndecan-1 antibody (BioLegend, Cat. No. 352308) was used to confirm viability and selection of the cells. Patients R24-0125 and R24-0553 were subjected to this protocol.

Note that R24-0124 had two additional 10-minute incubations with Red Blood Cell Lysing Buffer Hybri-Max (Sigma-Millipore, Cat. No. R7757) which led to a decrease in viability and compromised the results of the experiment. Also, for the the R24-0124 sample 3.2×10^5 cells were plated for the RealTime-Glo experiments due to a mathematical error, instead of the standard, 1.6×10^5 cells per well. For the R12-0124 sample, 2×10^5 cells per well (in a tissue culture-treated 24 well plate) from the CD138(+) and CD138(-) fractions were treated with TriC or vehicle for 24 h. Cells were scrapped and transferred to 1.5 mL tubes and centrifuged for 5 minutes at $200 \times g$ at 4°C . The supernatant was removed and samples were washed with 500 μL cold PBS twice. Samples were resuspended in 200 μL RLT Plus Lysis buffer (Qiagen Cat. No. 1053393) and flash frozen with liquid nitrogen and stored at -80°C . These samples have not been processed further for RNA isolation.

2.11. Triacsin C Treatment

Triacsin C (TriC) was purchased from Cayman Chemical (Ann Arbor, Michigan, USA). MM.1S^{gfp+/luc+}, MM.1R^{gfp+/luc+}, OPM-2, RPMI-8226, U266B1 and HL-60 cells were seeded into either tissue culture-treated white bottom 96 well plate (4.3×10^4 cells per well), tissue culture treated 24 well plates (1×10^5 cells per well), tissue culture-treated 6-well dishes (4.81×10^5 cells per well), or tissue culture-treated T-25 flasks (2×10^6 cells per flask; Avantor/VWR, Cat. No. 10861-568) under the growth conditions described above. MM cells were treated with TriC or dimethyl sulfoxide (DMSO, vehicle). Samples were collected at 24-hour intervals and subjected to functional analyses below.

2.12. Myeloma Cell Quantification, Viability and Apoptosis

For quantification and viability testing, MM cells were collected and resuspended in RPMI-1640 +10% FBS + 1% PSA, and diluted 1:2 in 0.4% Trypan Blue. Viable and non-viable cells were counted using a hemocytometer. To characterize apoptosis, MM cells were collected, washed 3 times with Cell Staining Buffer (BioLegend, Cat. No. 420201) and stained with APC-Annexin V (1:20, BioLegend Cat. no. 640920), DAPI (0.004 µg/ mL, ThermoFisher Scientific, Cat. No. D1306) in Annexin V Binding Buffer (BioLegend, Cat. no. 422201) for 15 min at room temperature). For all flow cytometric TriC analyses, a minimum of 1×10^4 events were collected per sample on a MACSQuant Analyzer (Miltenyi Biotec) and analyzed using FlowJo v.10 (Becton, Dickinson & Company, Ashland, OR).

2.13. Bioluminescent Assays Measuring Cell Viability

CellTiter-Glo (Promega, Cat. No. G7570) relies on the oxidation of luciferin, an ATP-dependent reaction as a proxy for cell viability and is a terminal assay because it requires cell lysis. 1.6×10^3 cells of either human or MM or AML cell lines of interest were plated in tissue culture-treated white flat bottom 96 well plates and subject to the experimental conditions of interest. At the timepoint of interest, CellTiter Glo reagent was added in equal volume to the total volume in the 96 well of interest, mixed well and incubated for 10 minutes at room temperature. Samples were read on a GLOMAX plate reader (Promega). Alternatively, at the timepoints of interest 357 µg /mL of D-luciferin (Invitrogen, Cat. No. L2912) was added to wells, mixed well then incubated for 10 minutes and read with a GLOMAX plate reader. This method was only utilized with cell lines expressing luciferase (MM.1S^{gfp/luc} or HL-60^{mCherry/luc}). The integration time for all luminescent readings was 0.5 seconds.

2.14. RealTime-Glo™ MT Cell Viability Assay to Measure Cellular Redox Potential

The RealTime-Glo MT Cell Viability assay (Promega, Cat. No. G9711) relies on the luciferin-based substrate to be reduced intracellularly before binding to NanoLuc® luciferase as a proxy for cellular redox potential. NanoLuc® and MT Cell Viability Substrate were added to the wells 1:1000, simultaneously with pharmacological inhibitors or vehicle controls, immediately after cells of interest were seeded for an experiment in tissue culture-treated white flat bottom 96 well plates as described previously, unless otherwise noted. Samples are incubated for 10 minutes at room temperature under light-protected conditions and luminescence was read on a GLOMAX plate reader (Promega). Samples were incubated at 37 °C at 5% CO₂ and luminescence was read longitudinally at designated time points up to 96 hours. Media alone was used for background subtraction.

2.15. Intracellular Characterization of BAX Protein

MM.1S cells were washed three times with Cell Staining Buffer (BioLegend) and then fixed in 1x Fixation Buffer (4% paraformaldehyde, BioLegend). Cells were washed 3 times with Cell Staining Buffer and stained with either Alexa Fluor (AF) 488 mouse anti-human BAX antibody (0.5 µg/mL, BioLegend, Cat. No. 633603) or AF488 Mouse IgG1 κ isotype control (5 µg/mL, BioLegend, Cat. No. 400129) in 1x Intracellular Staining Permeabilization Wash Buffer (Perm/Wash, BioLegend, Cat. No. 421002) for 15 min at room temperature. Cells were washed 2 times in 1x Perm/Wash buffer and resuspended in Cell Staining Buffer (BioLegend) prior to flow cytometry analysis. A total of 2x10⁴ events were collected using a MACSQuant (Miltenyi Biotec) and analyzed

using FlowJo v10.6.1. Data are presented as the mean fluorescence intensity (MFI) of the FITC-H channel within the FSC-A and SSC-A gates.

2.16. Myeloma Cell Cycle and Ki-67 Staining

MM cells were washed three times with Cell Staining Buffer (BioLegend) and fixed in 1x Fixation Buffer (4% paraformaldehyde, BioLegend). Cells were washed three times with Cell Staining Buffer and stained with Alexa Fluor 647 anti-human Ki-67 antibody (1:100) and DAPI (0.5 µg/mL) respectively in 1x Intracellular Staining Permeabilization Wash Buffer (BioLegend). The cells were resuspended in cell staining buffer (BioLegend, Cat. No. 420201) prior to flow cytometry using a MACSQuant Analyzer (Miltenyi Biotec).

2.17. Flow Cytometric Characterization of Mitochondrial Number/Mass, Mitochondrial Membrane Potential, and Mitochondrial Superoxide Levels

MM cells were washed three times with Cell Staining Buffer (BioLegend) and resuspended in their respective cell culture media with 100 nM MitoTracker Green (Invitrogen, Cat. No. M7514), and incubated for 30 min at 37 °C. Cells were washed three times with cell staining buffer and resuspended in Cell Staining Buffer (BioLegend) prior to flow cytometry using a MACSQuant Analyzer (Miltenyi Biotec). To characterize mitochondrial membrane potential, MM cells were washed three times with Cell Staining Buffer (BioLegend) and resuspended in tetramethylrhodamine ethyl ester (TMRE) buffer (Cayman Chemicals) containing 100 nM TMRE (Cayman Chemicals, Cat. no. 701310) and incubated for 30 min at 37 °C. Cells were pelleted and resuspended in TMRE buffer and subjected to flow cytometry on a MACSQuant Analyzer (Miltenyi Biotec). For mitochondrial superoxide measurements, ATCC MM.1S cells were washed three times

with cell staining buffer (BioLegend) and stained with 5 μM MitoSOXTM Red (Invitrogen, Cat. No. M36008) in Hank's balanced salt solution with calcium and magnesium (HBSS/Ca²⁺/Mg²⁺, Gibco, 14025-092) for 10 min at 37 C. Cells were washed three times with warm HBSS/Ca²⁺/Mg²⁺ and resuspended in HBSS/Ca²⁺/Mg²⁺ before analysis by flow cytometry.

2.18. Cellular Metabolic Analysis

5x10⁶ MM.1S^{gfp+/luc+} cells were treated with DMSO or 1.00 μM TriC for 24 hours in T-25 flasks (Avantor/VWR; Cat. no. 10861-568). Cells were then harvested, centrifuged, and resuspended in XF DEM media (pH 7.4; Agilent, Cat # 103575-100) containing 1mM sodium pyruvate, 10mM glucose and 2mM glutamine prior to plating on Seahorse XF 96 PDL-coated plates (Agilent, Cat # 103730-100) at a density of 75,000 cells/well per the manufacturer's instructions. Mitochondrial function was determined using a Mitochondrial Stress Test on the Seahorse XFe96 analyzer (Agilent Technologies), as previously described²⁸¹. Cells were also analyzed for total, mitochondrial, and glycolytic ATP production rates using a Seahorse XF ATP Production Rate Assay according to the manufacturer's instructions. The data presented here are representative of at least three independent experiments with ≥ 24 wells per treatment.

2.19. Acyl-CoA Synthetase Long-chain Activity Assay

This protocol (**Figure 7**) was adapted from Nchoutmboube *et al.* (2013) and Castillo *et al.* 2020^{290,291}. MM.1S cells were plated in 6 well dishes (4.81x10⁵ cells/well) in RPMI+0.5% Fatty Acid (FA) Free BSA + 1% PSA and incubated with 0.5 μM BODIPY FL C₁₆ (4,4-Difluoro-5,7-Dimethyl-4-Bora-3a,4a-Diaza-s-Indacene-3-Hexadecanoic Acid, ThermoFisher, D3821) at 37 C for 2 hours. The cells were incubated with TriC or DMSO

for 2 hours, collected and washed 3x with 0.2% FA-free BSA/PBS (ThermoFisher Scientific, Cat. No. AAJ6494422) to remove excess label. Cells were resuspended in 8.5% Sucrose + 0.5 μ M EDTA + 10 mM Tris Buffer (pH 8.0) + 0.1% Triton X-100 and incubated at room temperature for 25 min. Lysates were centrifuged for 10 min at 14,000 \times g, and the supernatant was transferred to fresh tubes. Heptane was added to the supernatant (1 volume of supernatant: 6 volumes of n-heptane), shaken at 1,300 rpm for 10 min, and centrifuged for 5 min at 12,000 \times g. n-Heptane was removed using a pipette, and the aqueous layer was subsequently extracted with n-heptane three more times. The aqueous layer was read on a black 96-well plate (Corning, Cat No. 3603, 475 nm /500-525 nm, excitation/emission). n-Heptane (Cat. no. 34873) was purchased from Millipore Sigma (Burlington, MA, USA).

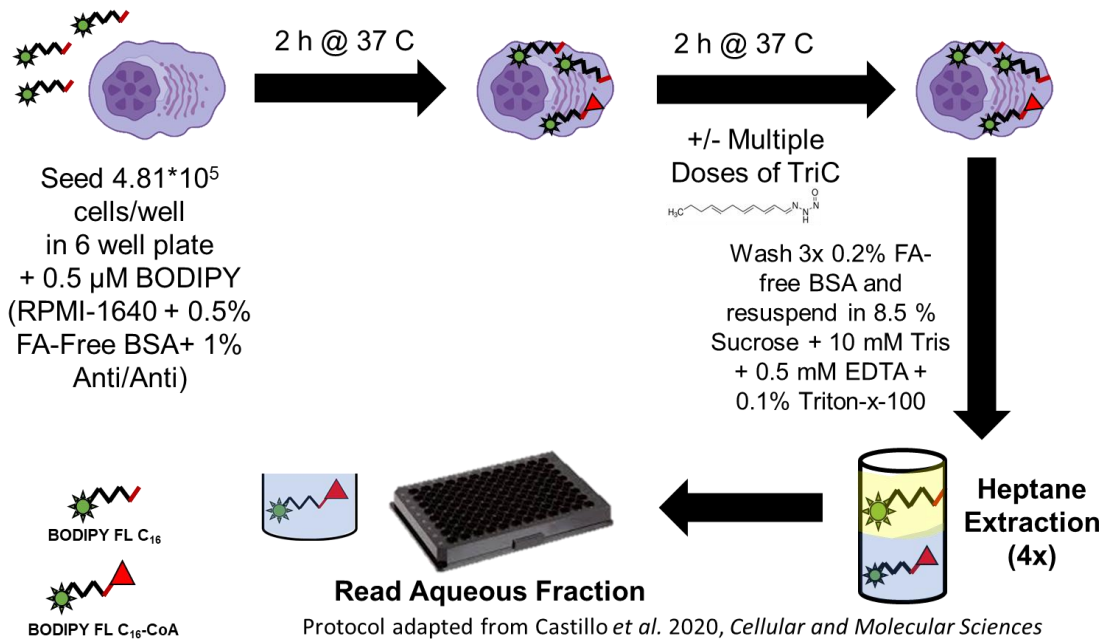


Figure 7. General Live Cell ACSL Activity Assay- BODIPY FL C16 (4,4-Difluoro-5,7-Dimethyl-4-Bora-3a,4a-Diaza-s-Indacene-3-Hexadecanoic Acid) Roswell Park Memorial Institute Medium

(RPMI), Fatty Acid (FA), Bovine Serum Albumin (BSA) Antibiotic/Antimycotic (Anti/Anti), Ethylenediaminetetraacetic acid (EDTA)

2.20. Total mRNA extraction and quantitative real-time polymerase chain reaction (qRT-PCR)

Total RNA was harvested in QIAZOL and prepared using the Qiagen miRNEASY Kit with DNase On-column digestion (Qiagen, Hilden, Germany), according to the manufacturer's protocol. mRNA was quantified and tested for quality and contamination using a Nanodrop 2000 (ThermoFisher Scientific) and subjected to quality control minimum standards of $260/230 > 2.0$ and $260/280 > 1.8$ before downstream applications. For qPCR, cDNA was synthesized using MultiScribe reverse transcriptase (High-Capacity cDNA, Applied Biosciences, ThermoFisher Scientific) according to the manufacturer's instructions using 500 ng of total RNA. Relative transcript expression was determined using SYBR Master Mix (Bio-Rad, Hercules, CA) and thermocycling reactions on a CFX-96 or Opus system (Bio-Rad) using 500 ng of cDNA. Target transcripts (**Supplementary Tables 1, 2**) were normalized to *TATA-box binding protein (TBP)* using the $2^{-\Delta\Delta Ct}$ method. Data were analyzed using Bio-Rad CFX Manager 3.1.

2.21. RNA Sequencing Sample Preparation and Analysis

A total of 5×10^6 MM.1S^{gfp+/luc+} cells were seeded in T-25 flasks (Avantor/VWR, Cat. No. 10861-568) and treated with the vehicle (DMSO) or 1.00 μ M TriC for 24 h. Replicates were defined as MM.1S^{gfp+/luc+} cells of the same passage grown in parallel. After 24 hours, RNA was isolated using a Qiagen RNeasy Plus Mini Kit (Qiagen, Hilden, Germany) Cat. no. 74136), according to the manufacturer's protocol. Samples were evaluated on Bioanalyzer BA2100 RNA pico chips and quantified using the Qubit HS DNA reagent. Sequence libraries were prepared with the Takara Pico V2 library prep using 6 ng of total RNA and sequenced with an Illumina HiSeq 1500/2500. RNA

sequence data was analyzed using the nf-core/rnaseq pipeline v3.9^{292,293} using the Nextflow workflow manager v22.10.2²⁹⁴. Raw reads were subjected to quality checking and reporting (FastQC v0.11.9/ MultiQC v1.13²⁹⁵; and low quality sequence (Phred score <20) using Trim Galore v 0.6.7²⁹⁶ were removed. Reads were aligned to the *Homo sapiens* hg38 reference genome using STAR v2.7.10a²⁹⁷ and SAMtools v1.15.1²⁹⁸. Read counts were quantified using SALMON v1.5.2²⁹⁹, and DESeq2 v1.28.0³⁰⁰ was used to identify differentially expressed genes using a cut-off value of ($\log_2(\text{FC}) > |1|$, q-value < 0.05) using the Wald test and adjusted for multiple testing using the Benjamini and Hochberg method. Gene ontology enrichment analysis was performed using the Enrichr package and STRINGv11, with a high confidence score cutoff of 0.70.

2.22. Sample Preparation for Mass Spectrometry Proteomics of TriC treated MM.1S cells

MM.1S^{gfp+/luc+} cells treated with vehicle (DMSO) or 1.00 or 2.00 μM triacsin C for 48 hours. Cells were collected and washed 3x with cold PBS and flash frozen. Cells were solubilized in ice-cold RIPA buffer and DNA sheared using a probe-tip sonicator (Branson Ultrasonifier 250, Branson Ultrasonic Corporation, Danbury, CT, 3 \times 10 seconds). Each sample was then centrifuged (14,000 \times g) at 4°C and the supernatant collected. 100 μg of protein was taken from each sample and reduced using 5 mM TCEP (tris(2-carboxyethyl)phosphine hydrochloride; Strem Chemicals, Newburyport, MA). The reaction was allowed to proceed for 20 minutes at 56°C and alkylated for 30 minutes in the dark with 10 mM iodoacetamide at room temperature (G-Biosciences, St. Louis, MO). Protein was precipitated at -20°C with ethanol and pellets were washed twice with ice-cold ethanol and each sample was incubated overnight at 37°C in 100

mM ABC containing 1 mM CaCl₂ and trypsin (Sequencing grade, modified, Promega Co, Madison, WI). Digested proteins were evaporated and each sample freed from salts and buffers by solid-phase extraction on C18 resin using cartridges prepared in-house. Briefly, for each sample a C18 StageTip was prepared according to the procedure originally-reported³⁰¹. 4 mg octadecyl-derivatized silica (SiliaSphere PC, C18 monomeric, 25 µm particles, 90 Å pore size, SiliCycle Inc., Québec City, Canada) suspended in LC-MS-grade isopropanol (Honeywell, Morris Plains, NJ) was added to each tip. Each cartridge was then equilibrated and samples purified according to the StageTip protocol referenced above. Purified peptides were eluted directly into autosampler vials to be used on the LC-MS instrumentation using 100 µL elution buffer and solvent was removed by vacuum centrifugation. Each sample was then resuspended in a volume of sample load solvent [5% formic acid (Optima grade, Thermo Fisher Scientific) and 4% acetonitrile (both water and acetonitrile were LC-MS-grade, Honeywell)] to yield an approximate concentration of 1 µg/µL peptides.

2.23. Mass Spectrometry Proteomics of TriC-treated MM.1S Cells

Chromatography, mass spectrometry, and data analysis were performed as previously described³⁰². See supplementary methods for more details. Briefly, sample separations performed in tandem with mass spectrometric analysis were performed on an Eksigent NanoLC 425 nano-UPLC System (Sciex, Framingham, MA) in direct-injection mode with a 5 µL sample loop made in-house. Fractionation was performed on a reverse-phase nano HPLC column (Acclaim PepMap 100 C18, 75 µm × 150 mm, 3 µm particle, 120 Å pore). Analysis was performed in positive ion mode on a TripleTOF 5600 quadrupole time-of-flight (QTOF) mass spectrometer (Sciex, Framingham, MA).

Protein identification was performed using Protein Pilot software (Sciex, Version 5.0.2) running the Paragon algorithm. Data was searched against a human proteome database from the Uniprot website (UP000005640) with cysteines modified (iodoacetamide). A target false-discovery rate of 0.05 was the threshold for downstream analysis with a minimum of 95% confidence was used as a threshold for peptide identification as calculated by Protein Pilot. Relative quantification was performed using the SWATH processing microApp in the Sciex PeakView software and t-tests and principal component analyses were completed for treatment datasets using Sciex MarkerView software; significantly different proteins were determined via t-test ($p < 0.05$). Ingenuity pathway analysis (QIAGEN) was used to identify if proteins of interest had an association with a pathway of interest using a right-tailed Fisher's Exact Test between 1 μM TriC-treated MM.1S^{gfp/luc} relative to vehicle and between 2 μM TriC-treated MM.1S^{gfp/luc} relative to vehicle. A Z-score statistic was used to make a prediction on the activation status of pathways of interest. Briefly, the expression ((Log₂(Fold-Change)) of significantly differentially expressed proteins is compared to the canonical activated state of a pathway and if a molecule in that pathway is in agreement with the canonical activation status it receives a score of +1, if has the opposite expression what is expected it receives a score of -1. The scores of all molecules involved in the pathway are summed and divided by the square root of the total number of molecules in the pathway. If the score is positive then the pathway is predicted to be activated and a negative number is associated with a deactivated prediction.

2.24. Lipofectamine-based Transfection of Short-Interfering RNAs (siRNAs) Against *DGAT1*

Desiccated SMART pool ON-TARGET siRNAs against *Homo sapiens DGAT1* or a Non-Targeting Control (Dharmacon, See Table 6 for sequence and ordering information) were resuspended in 60 mM KCl (Millipore-Sigma, Cat. No. P5405), 6 mM HEPES-pH 7.5 (4-(2-hydroxyethyl)-1-piperazineethanesulfonic acid, Millipore-Sigma, Cat. No. H9897) and 0.2 mM MgCl₂ (Millipore-Sigma, Cat. No. M2393) in RNase-free water to a concentration of 100 μM. 5x10⁵ HL-60^{mCherry/luc} cells were plated in tissue culture-treated 6-well plates in RPMI-1640 +10% FBS +1% PSA. Lipofectamine™ RNAiMAX (ThermoFisher Scientific, Cat. No. 13778075) and Opti-MEM™ (ThermoFisher Scientific, Cat. No. 31985062) and were added together in a 1:10 volume to volume ratio with siRNAs at a final concentration of 0.025 μM and allowed to incubate at room temperature for 5 minutes. siRNA-Lipofectamine complexes were then added dropwise to their respective wells. Opti-MEM™ and Lipofectamine™ RNAiMAX alone was also added to control for lipofectamine-related toxicity. Cells were incubated at 37 °C at 5% CO₂ for 24 and 72 hours, upon which cells were collected for downstream analyses.

Table 6. Human DGAT1 Short-Interfering RNA Sequences

Gene Target & Organism	Target Sequence 5'-3'	Dharmacon Catalog Number	Dharmacon Reference Number
<i>DGAT1</i> <i>Homo sapiens</i>	5'-CUU GAG CAA UGC CCG GUU A-3'	J-003922-05	SO-2812174G
<i>DGAT1</i> <i>Homo sapiens</i>	5'-CAA UAG CCG UCC UCA UGU A-3'	J-003922-06	SO-2812174G
<i>DGAT1</i> <i>Homo sapiens</i>	5'-UCA AGG ACA UGG ACU ACU C-3'	J-003922-07	SO-2812174G
<i>DGAT1</i> <i>Homo sapiens</i>	5'-GCU GUG GUC UUA CUG GUU G-3'	J-003922-08	SO-2812174G
<i>PPIB</i> <i>Homo sapiens</i>	5'-ACA GCA AAU UCC AUC GUG U-3'	D-001820-01-20	SO-2821851G
Non-Targeting Pool	<ol style="list-style-type: none"> 1. 5'-UGG UUU ACA UGU CGA CUAA-3' 2. 5'-UGG UUU ACA UGU UGU GUG A-3' 3. 5'-UGG UUU ACA UGU UUU CUG A-3' 4. 5'-UGG UUU ACA UGU UUU CCU A-3' 	D-001810-10-20	SO-2812174G

2.25. Dicer-Substrate Short Interfering RNA-Mediated Knockdown of ACSL3

Double-stranded Dicer-substrate short interfering RNAs (DsiRNAs) targeted against *Homo sapiens ACSL3* were ordered from Integrated DNA Technologies as part of their TriFECTa® Kit. FBS and RPMI-1640 basal media were warmed to 37 °C prior to processing samples. 3×10^6 HL-60^{mCherry/luc} cells were washed twice in warm RPMI-1640 basal media to remove excess FBS. Samples were resuspended in 150 µL of RPMI-1640 basal media and activated recombinant streptolysin O (SLO, Abcam, Cat. No. ab63978) was added (to a final 10 U per mL), and DsiRNAs against *ACSL3* or a non-targeting sequence was added to the cells. Samples were incubated for 5 minutes at 37 °C with 5% CO₂, mixed by vortexing gently and incubated for an additional 5 minutes at 37 °C with 5% CO₂. 1.5 volumes of FBS was added to the samples and incubated for 30 minutes at 37 °C at 5% CO₂ to inactivate the SLO. Cells were then seeded into a tissue culture-treated 24 well plate in RPMI-1640 and 10% FBS at 37 °C at 5% CO₂ for 48 hours. Cells were then processed for RNA extraction as described above. See Table 7 for more information.

Table 7. Human ACSL3 Double-Stranded Dicer-Substrate RNA Sequences

Gene Target & Organism	Predicted Targeted Transcripts	Reagent Name	Target Sequence 5'-3'
<p>ACSL3</p> <p><i>Homo sapiens</i></p>	<p>NM_203372 (Exon 5)</p> <p>NM_004457 (Exon 6)</p>	<p>Hs.Ri.ACSL3. 13.1</p>	<p>Sense Strand:</p> <p>5'- GACCAACAUCAUUACUAGUAAAAGAA- 3'</p> <p>Anti-sense Strand:</p> <p>5'- UUCUUUACUAGUAAUGAUGUUGGUC AC-3'</p>
<p>ACSL3</p> <p><i>Homo sapiens</i></p>	<p>NM_203372 (Exon 16)</p> <p>NM_004457 (Exon 17)</p>	<p>Hs.Ri.ACSL3. 13.2</p>	<p>Sense Strand:</p> <p>5'- ACUUGUCAGUAUGAGAAUUUUUCTG -3'</p> <p>Anti-sense Strand:</p> <p>5'- CAGAAAAAUUCUCAUACUGACAAGUA C-3'</p>
<p>ACSL3</p> <p><i>Homo sapiens</i></p>	<p>NM_203372 (Exon 3)</p> <p>NM_004457 (Exon 4)</p>	<p>Hs.Ri.ACSL3. 13.3</p>	<p>Sense Strand:</p> <p>5'- CCAUCUACCAUGAAGCUAAAACATA- 3'</p> <p>Anti-sense Strand:</p> <p>5'- UAUGUUUUAGCUUCAUGGUAGAUGG UU-3'</p>

Table 7 Continued			
<i>Non-Targeting</i>		Qiagen	Sense strand:
		AllStars	5'-
		Negative	GCAAGCUGACCCUGAAGUUCAUTT-
		Control siRNA	3',
<i>Homo sapiens</i>		AlexaFluor647	Anti-sense strand: 5'-
			AUGAACUUCAGGGUCAGCUUGCCG-
			3'

2.26. Addition of Exogenous Oleic Acid to HL-60 Cells

This protocol was adapted from Than *et al.* 2003³⁰³. 1×10^5 HL-60 cells were plated in tissue culture-treated 24 well plates in RPMI-1640 + 2% fatty acid-free BSA and 1% PSA and incubated at 37 °C at 5% CO₂ for 6 hours. Oleic acid (**OA**, Millipore Sigma, O1008-5G, originally resuspended in 100% ethanol at a concentration of 400 mM) was diluted 1:10 in RPMI-1640 + 2% fatty acid-free BSA to a concentration of 40 mM. To conjugate OA to BSA, samples were emulsified by sonicating for 25 seconds on power level 2. OA-BSA samples were incubated at 55 °C and shaken at 600 RPM in an Eppendorf Thermomixer R for 20 minutes (or until the solution is translucent). OA-BSA was filter sterilized using a Leur-locked 0.2 µm filter on a 5 mL syringe. Conjugating the OA to the BSA takes ~1 hour, allowing buffer time for the cells to be sufficiently serum-starved to facilitate uptake of the OA-BSA. Either OA-BSA or the vehicle (RPMI-1640 +2% fatty acid-free BSA +1% PSA + equal volumes of ethanol found in the OA-BSA) was added to the cells in the 24 well dishes and incubated at 37 °C at 5% CO₂ till the designated timepoints upon which downstream analyses were performed.

2.27. Triacsin C and Oleic Acid Co-treatment

1x10⁵ HL-60 cells were plated in tissue culture-treated 24 well plates in RPMI-1640 + 2% fatty acid-free BSA and 1% PSA and incubated at 37 °C at 5% CO₂ for 2 hours. Cells were then incubated with 300 μM of OA-BSA (as described above) for 18 hours in RPMI-1640 +1% FBS + 1% PSA. Cells were then treated with 1.0 μM TriC or vehicle (DMSO) for 24 hours in RPMI-1640 + 1% FBS + 1% PSA and subjected to downstream analyses.

2.28. Measuring Intracellular Neutral Lipids with Flow Cytometry

Cells of interest were collected and washed 3 times with 4% fatty acid-free BSA/PBS and fixed with 10% NBF for 30 minutes at room temperature. Samples were washed 3 times with PBS and cells were resuspended in 2 μM BODIPY 493/503 (4,4-Difluoro-1,3,5,7,8-Pentamethyl-4-Bora-3a,4a-Diaza-s-Indacene, ThermoFisher, Cat. No. D3922) and incubated for 45 minutes at 37 °C at 5% CO₂. Samples were washed 2 times with PBS and run on a MACSQuant (Miltenyi) for flow cytometric analysis in PBS.

2.29. Diacylglycerol Acyltransferase Inhibitor Treatment

1.6x10³ HL-60, ATCC MM.1S or RPMI-8226 cells were plated in tissue culture-treated white flat bottom 96 well plates and treated with inhibitors against DGAT1 (DG1i, A-922500, Cayman Chemical, Cat. No. 10012708), DGAT2 (DG2i, PF-06424439, Cayman Chemical, Cat. No. 17680), a combination of the two DGAT inhibitors, or vehicle (DMSO) for 48 h. At the timepoint of interest, CellTiter-Glo reagent was added in equal volume to the total volume in the 96 well of interest, mixed well and incubated for 10 minutes at room temperature. Samples were read on a GLOMAX plate reader (Promega). The integration time for the luminescent readings was 0.5 seconds.

2.30. Data Availability Statement

Raw and normalized RNA-Seq data are available from the Gene Expression Omnibus database (GSE252929). Mass spectrometry data are available in the PRIDE database, PXD049304.

2.31. Statement Regarding the Use of Human Samples

This work uses human mesenchymal stem cells from healthy human donors in order to differentiate into bone marrow adipocytes. Additionally, primary MM patient samples are used. Through an approved Institutional Review Board protocol, the Reagan lab receives deidentified samples from the Maine Medical Center Biobank, that only contain information about the patient's sex, body mass index and age. The Maine Medical Center Biobank is accredited by the College of American Pathologists (CAP) and follows the National Cancer Institute Best Practices for Biorepositories and the International Society of Biological and Environmental Repositories. Given that these samples are *ex vivo*, the identity of these patients remains unknown and we are not testing clinical outcomes of the patients; the use of human mesenchymal stem cells from these donors does not qualify as human subjects research. We are grateful for the generosity of all the patients who offered their informed consent and part of themselves through the hard work of the Maine Medical Center Biobank to help push our research forward.

2.32. Statistical Analysis

All graphs were created using GraphPad Prism (v9 or above); statistical significance was determined using One-way or Two-way ANOVA with Tukey's, Šídák's, or Dunnett's multiple comparisons tests, Student's t-test, or Welch's test unless

otherwise stated. Data represent the mean \pm standard deviation, unless otherwise noted. Significance is indicated as: *, $p < 0.05$; **, $p < 0.01$; ***, $p < 0.001$; **** $p < 0.0001$.

3. CHAPTER 3: RESULTS

3.1. Identity of Presumed OPM-2^{mCherry/Luc} Line as HL-60^{mCherry/Luc} Cells

Until April 2022, it was assumed by our lab that the cell line labeled OPM-2^{mCherry/luc} was the OPM-2 myeloma cell line. However, cell authentication by short-tandem repeat profiling was done and suggested up to 97.67% homology to the acute myeloid leukemia cell line HL-60 (**Table 8**). To further investigate the identity of the cell line deemed “Mislabelled OPM-2 cells”, Sanger sequencing and PCR was used to assess SNVs characteristic of wild type OPM-2 cells which include mutations in *CDKN2A*, *NRAS*, and *TP53*. The Sanger sequencing and PCR to confirm the mislabeled cells were done by Heather Fairfield Campbell and the figures and results related to these data with exception of 3.1B-C were the product of her hard work. These data are being included to provide more context to this occurrence.

Table 8. Short-Tandem Repeat Profiling Results of HL-60^{mCherry/luc} Cell Line

Accession	Name	N° Markers	% Similarity	Amel	CSF1PO	D2S1338	D3S1358	D5S818	D7S820	D8S1179	D13S317	D16S539	D18S51	D19S433	D21S11	FGA	Penta D	Penta E	TH01	TPOX	vWA
NA	Query	NA	NA	X	13,14	17	16	12	11,12	12,13	8,11	11	14,15	14	29,30	22			7,8	8,11	16
CVCL_A794	HL-60(TB)	14	97.67%	X	13,14	17	16	12	11,12	12,13	8,11	11	14,15	14	29,30	22			7,8	8,11	16
CVCL_0002 <i>Best</i>	HL-60	14	95.45%	X	13,14	17	16	12	11,12	12,13	8,11	11	14,15	14	29,30	22,24	10,12	13	7,8	8,11	16
CVCL_0002 <i>Worst</i>	HL-60	14	85.00%	X	13,14	17	16	12	11,12	13	8,11	11	14	14	30	22,24	10,12	13,14	8	8,11	16
CVCL_WZ17	HL-60 DeltaF508-CF	12	95.00%	X	13,14		16	12	11,12	12,13	8,11	11	14,15		29,30	22,24	10,12	13,14	7,8	8,11	16
CVCL_2945	HL60RG	11	86.49%	X	13,14			12	11,12	12,13	8,11	11	14,15		30	21,22,24			8	8,11	16
CVCL_9921	ch-2879	11	71.43%	X		17	16	12	11,12	12		8,9	12	14	30,32,2	22			8	10,11	16
CVCL_UN03	ICCSiCi006-A	8	68.97%	X,Y	10,12			11,12	11,12		8,11	9,13			30,31,2				7,9,3	8,11	16
CVCL_F328	IST-MELA-16	8	68.97%	X,Y	12,13			12,13	11,12		11,12	10,13,14			29,30				6,7	8	16,18
CVCL_UN08	ICCSiCi002-A	8	66.67%	X	12			12	9,12		8,11	11			29,30				9,9,3	8,11	16
CVCL_UC20	LM-MEL-5a	8	66.67%	X,Y	11			12	10,11		10,11	9,13			29,30				7	8,11	14,16

Every column proceeding the % similarity column are designations of short-tandem repeats. Blue squares are the query (“mislabelled OPM-2” matches to HL-60 cells).

3.2. Mutations present in mislabeled cells in the CDKN2A gene are largely consistent with HL-60 cells

The Cellosaurus database suggests HL-60 has a termination codon at amino acid position 80 (R80*). Primers were designed to examine the SNVs in *CDKN2A* with PCR and Sanger Sequencing. In the mislabeled “OPM-2” cells, Sanger sequencing confirmed the presence of the single nucleotide change of C to T in *CDKN2A*, resulting in the introduction of a premature termination codon at position 80, consistent with predictions in HL-60 cells (Figure 1B, orange box and arrows). DSMZ OPM-2 cells contained the reference variant (C) at this locus, while ATCC HL-60 cells also contained the predicted SNV (T). We identified a variant (R29*) in mislabeled “OPM-2” that was detected in our Sanger sequencing data as well. This variant was not present in either control cell line, and likely represents a spontaneous mutation arising over time in this cell line. We also amplified and sequenced the region of *CDKN2A* with a predicted SNV in OPM-2 cells and confirmed the presence of the predicted C to T change in DSMZ OPM-2 cells as a heterozygous variant, with the reference allele C present in both ATCC HL-60 and our cells of interest (**Figure 8A**, green box and star). In summary, the cells in question (mislabeled “OPM-2”) contain a homozygous mutation in *CDKN2A* consistent with HL-60 cells and do not contain the mutation predicted in OPM-2 cells. They also contain a new heterozygous variant in *CDKN2A* which is not present in either control cell line.

3.3. Mutations present in mislabeled cells in the NRAS gene are consistent with HL-60 cells

Sanger sequencing also confirmed the predicted A to T SNV in HL-60 cells in NRAS was present in both our mislabeled cells and the HL-60 cells sampled, while the DSMZ OPM-2 cells were unchanged at this locus (Figure 8B).

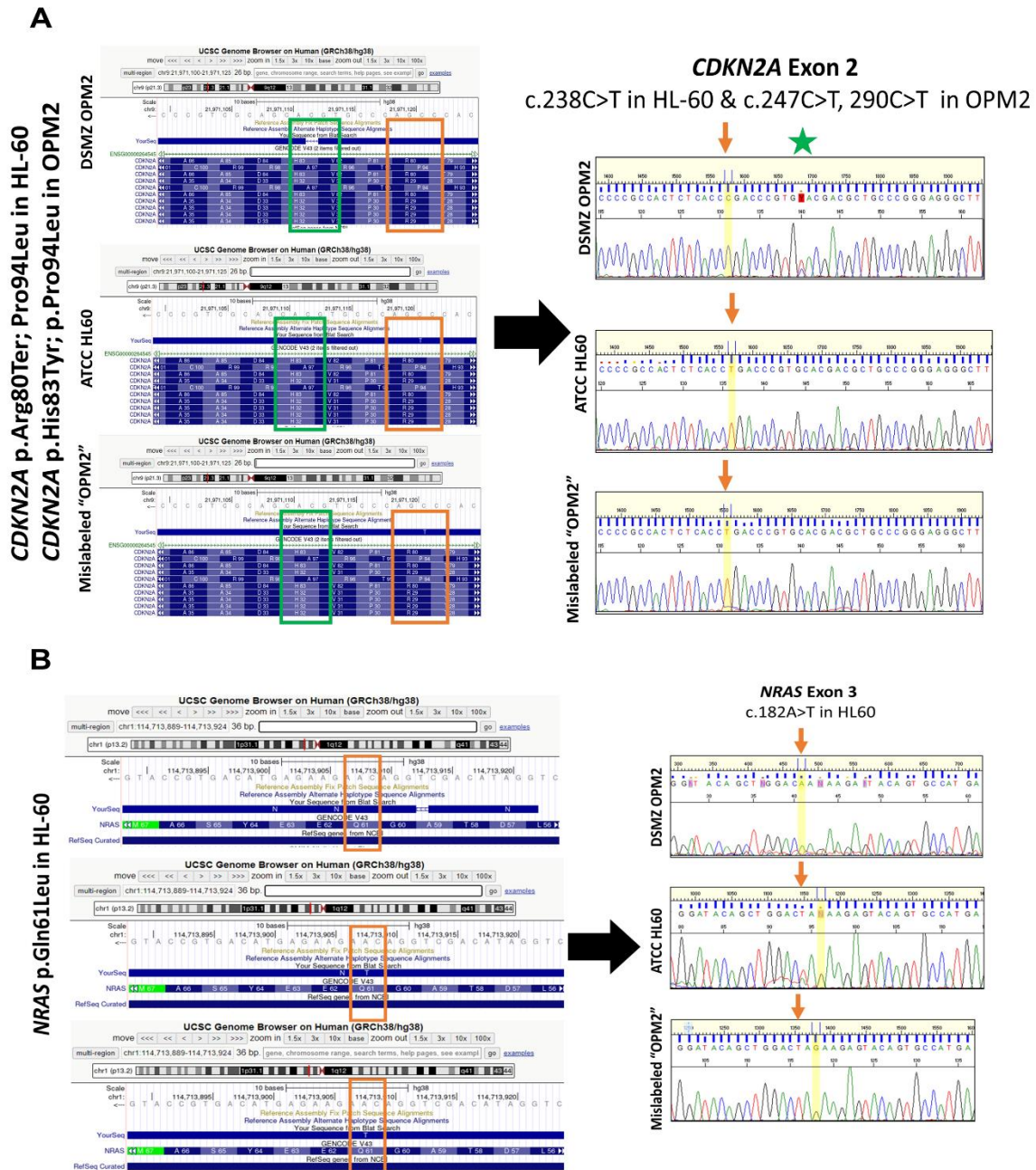


Figure 8. Confirmation of OPM-2 and HL60 Cell Identity

A-B) Sanger Sequencing results for control cell lines (DSMZ OPM2, ATCC HL-60) and mislabeled cells (Mislabeled "OPM2") in reference to the University of California

Santa Cruz (UCSC) database (left panels) with the amino acids/nucleotides in question highlighted with orange squares and arrows for HL-60 predicted variants and green squares/green star for OPM-2 predicted variants. Chromatograms for Sanger sequencing data represented (right panels). Variants in A) *CDKN2A* and B) *NRAS*

3.4. Mutations present in mislabeled cells in the *TP53* gene are consistent with HL-60 cells

Both HL-60 and OPM-2 cell lines contain mutations in *TP53*: HL-60 cells have a deletion encompassing the entirety of the gene while OPM-2 cells are predicted to have an SNV resulting in a missense mutation that should not affect the expression of the transcript. The *TP53* missense mutation predicted to be present in OPM-2 cells was not present in Sanger sequencing for additional samples (**Figure 9A**). The predicted G to A change was only present in DSMZ OPM-2 cells, and not in ATCC HL-60 or our mislabeled “OPM2” cells.

In an attempt to investigate a potential deletion on Chromosome 17 in mislabeled cells that would be consistent with HL-60 cells, we used two primer pairs to amplify regions of the genome predicted to be adjacent to the structural variant characteristic of HL-60 cells (**Figure 9B-C**). In DSMZ OPM-2 cells, we observed amplification of a product of the correct predicted size (176 bp) in intact chromosome 17 near the predicted proximal end of the deletion in HL-60 cells. However, in the Mislabeled OPM2 and HL-60 cells, no product was produced suggesting that at least one primer was unable to anneal in the absence of this genomic sequence, consistent with a deletion. Similarly, the predicted product (185 bp) for the distal end of the deletion was amplified in DSMZ OPM-2 cells, but not in HL-60 or our mislabeled cells (**Figure 9D**). Combined,

these data suggest that a genomic deletion encompassing *TP53* is present in our cells of interest, consistent with genomic aberrations in HL-60 AML cells.

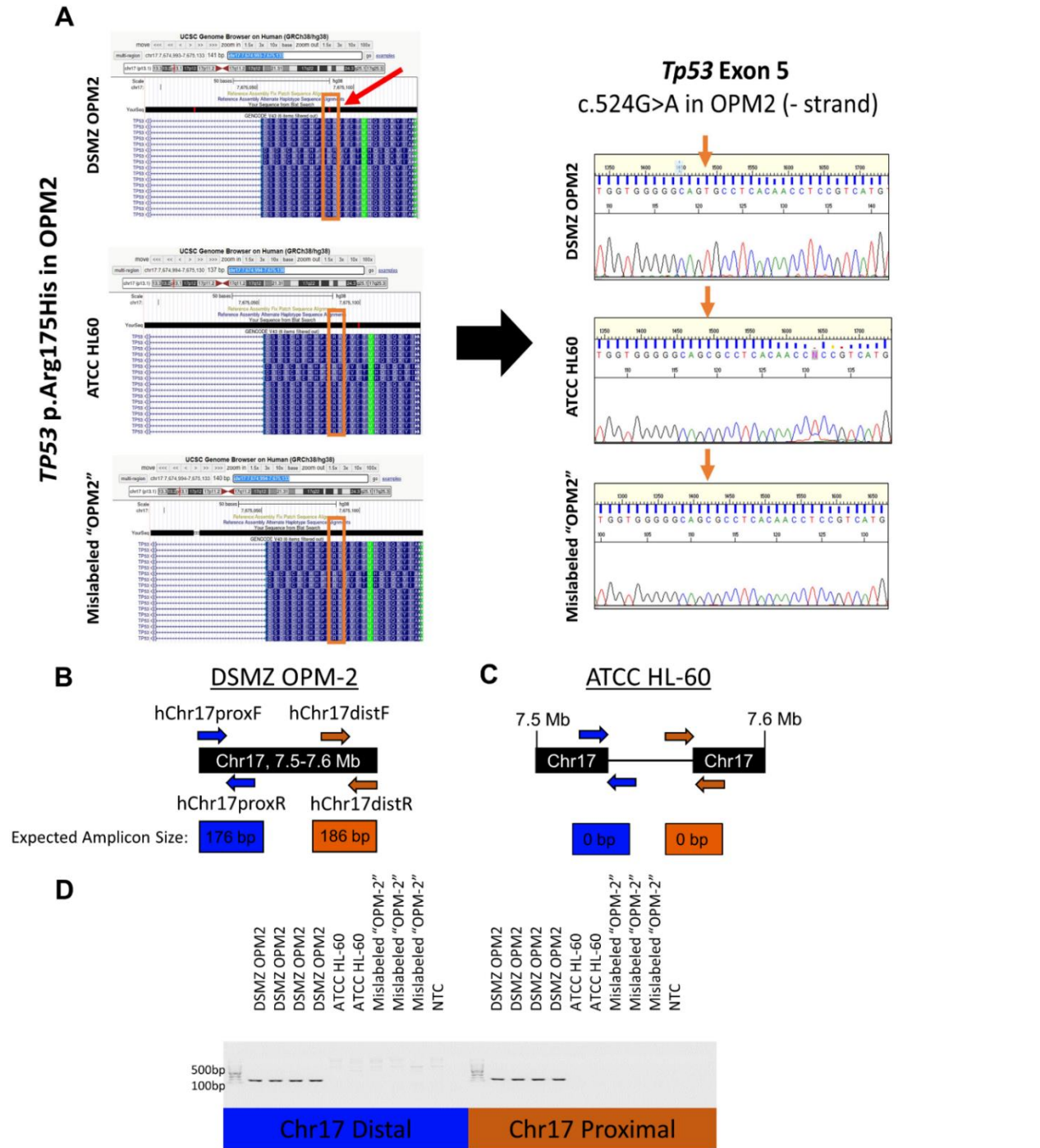


Figure 9. OPM-2 and HL-60 Related Genotyping Regarding TP53
A) Sanger Sequencing results for control cell lines (DSMZ OPM2, ATCC HL-60) and mislabeled cells (Mislabeled "OPM2") in reference to the UCSC database (left panels)

with the amino acids/nucleotides in question highlighted with orange squares and arrows for HL-60 predicted variants and green squares/green star for OPM-2 predicted variants. Chromatograms for Sanger sequencing data represented (right panels) for variants in *TP53* were examined. B-C) Graphical representation of the PCR design to assess the large structural predicted in HL-60 cells was examined with PCR and gel electrophoresis. Primers directed to the proximal (blue arrows) and distal (orange arrows) ends of the predicted deletion on chromosome 17 (Chr17) with the associated sizes of their amplicons in B) DSMZ OPM-2 and C) ATCC HL-60 cells. Arrows are in the 5'-3' orientation with the arrowhead being the 3' end of the primer. Mb = mega bases D) In multiple samples for all three cell lines, the predicted deletion in HL-60 cells in Chromosome 17 was examined with PCR and gel electrophoresis. NTC: No template control lane; the darkest band in the ladder represents a 500 bp product, the bottom band is 100 bp.

3.5. Conclusions

In summary, cells we previously identified as “OPM-2^{mCherry/luc}” were almost certainly HL-60 cells. The data presented here demonstrate high scores for STR agreement between the mislabeled cells and HL-60 cell lines. We specifically examined variants in *CDKN2A*, *NRAS*, and *TP53* reported in the Cellosaurus database and present additional evidence that the cells in question are in fact HL-60 cells. The cells in question also do not express *TP53*, and likely contain a large deletion on chromosome 17 deleting this gene, consistent with the HL-60 genotype. Our PCR and gel electrophoresis data demonstrate proper amplification of both the proximal and distal regions of this chromosomal segment in DSMZ OPM-2 cells, no amplification in ATCC HL-60 and similar lack of amplification in the mislabeled cells. Interestingly, primers targeting the genomic region encoding arginine 175 in *TP53*, which is predicted to be changed to histidine in OPM-2 cells, were able to amplify in all samples tested which may confirm the presence of a complex rearrangement in HL-60 cells.

3.6. Inhibition of the Acyl-CoA Synthetase Family with Triacsin C in Multiple Myeloma and Acute Myeloid Leukemia Cell Lines

3.6.1. Pharmacological Inhibition of the Long-Chain Acyl-CoA Synthetase (ACSL) Family Decreases Multiple Myeloma Cell Proliferation and Survival

To test the hypothesis that fatty acid metabolism supports MM proliferation and survival, we investigated the fitness of genes within the Hallmark Fatty Acid Metabolism gene set (Molecular Signature Database: M5935)³⁰⁴ in a CRISPR/Cas9 genome-wide screen in a diverse set of human myeloma cell lines within the Cancer Dependency Map (DepMap)²⁷⁹. We observed that 4 of the 5 human acyl-CoA synthetase long chain family members (ACSL) had negative Chronos scores, with *ACSL3* and *ACSL4* being among the top 25% most essential fatty acid metabolism genes in MM cells (**Figure 9A**). These data suggest that *ACSL1*, *ACSL3*, *ACSL4* and *ACSL5* are supportive of human myeloma cell proliferation. To understand the landscape of the ACSL gene and protein expression in MM cell lines, we again consulted the DepMap. We found that the average gene expression of *ACSL1*, 3, 4 and 5 ranged from 3.78-5.19 transcripts per million (TPM) +1, with *ACSL3* having the highest average expression in the family and *ACSL6* having the lowest (0.05 TPM+1) (**Figure 11A**). DepMap ACSL protein expression data of 6 human myeloma cell lines showed varied expression of each ACSL family member between each cell line (**Figure 15B**).

Triacsin C (TriC), a small molecule inhibitor against ACSL1,3,4 and 5²⁷², was used to test the hypothesis that the ACSL family supports MM cell fitness. To determine the IC₅₀ of TriC and a rational dose range for subsequent experiments, we measured total cellular ACSL activity using a novel fluorescent live cell assay adapted from protocols in the literature^{290,291}. To determine the optimal length of FA to assess ACSL activity, we incubated HL-60 cells with either a fluorescent 12-carbon (BODIPY FL C₁₂) or 16-carbon (BODIPY FL C₁₆) fatty acid analog for 2 hours at 37 °C then extracted with n-

heptane, to separate the product (BODIPY FL C₁₆) and the substrate (BODIPY FL C₁₆-CoA). We observed the BODIPY FL C₁₆ yielded nearly 3-fold higher fluorescent values in the aqueous fraction relative to the BODIPY FL C₁₂ carbon alternative, and therefore the 16-carbon fatty acid substrate was used (**Figure 10A**). To determine the rate of BODIPY FL C₁₆ uptake, ATCC MM.1S cells were incubated with BODIPY FL C₁₆ at 37 °C and flow cytometry was used to measure the mean fluorescent intensity after 0.5, 1.5 and 3.0 hours of incubation as a proxy for BODIPY FL C₁₆ cellular uptake. We found a positive correlation between incubation time and fluorescent signal with a maximum signal after 3.0 hours of incubation with a rate of 98.18 fluorescent units per hour (**Figure 10B**). 2 hours of initial incubation was chosen because the additional 2 hours of TriC would be sufficient to allow enough substrate to enter the cell. To measure the IC₅₀ of TriC, ATCC MM.1S were incubated with a BODIPY FL C₁₆ for 2 hours, challenged with various doses of triacsin C for 2 hours and subjected to n-heptane extraction to separate the product (BODIPY FL C₁₆) and the substrate (BODIPY FL C₁₆-CoA). HL-60 cells were subject to a similar protocol but with an incubation time for the substrate and TriC for 3 h. We found the IC₅₀ of TriC was 3.66 μM [0.02, 10.1 μM 95% confidence intervals] in ATCC MM.1S cells and 2.66 μM [0.0,9.3 μM 95% confidence intervals] in HL-60 cells (**Figure 11C, 10C**). To test the hypothesis that ACSL family inhibition by TriC would decrease MM cell proliferation and survival, human MM cell lines (MM.1S, MM.1R, RPMI-8226, OPM-2 and U266B1) were treated with doses of TriC (0.0366-6.00 μM) for up to 72 hours and subjected to trypan blue staining to assess cell viability. Significant differences in MM cell viability were first observed after 48 hours of TriC treatment with most human MM cells responding with a dose-dependent decrease in

viability (average EC₅₀: 1.88 μM), except for U266B1 cells (EC₅₀: 8.56 μM) (**Figure 11C**). To determine if there would be compensatory changes in ACSL expression by TriC, we assessed the gene expression of the ACSL family after treating MM.1S cells with 1 and 2 μM TriC for 48 hours by qRT-PCR. We observed significant increases in transcript levels of *ACSL1* and *ACSL3* in response to TriC treatment in MM.1S cells and variable expression (**Figure 15D**). We used RealTime Glo (RT-Glo) to measure the redox potential of HL-60 cells treated with TriC. HL-60 cells treated with TriC had a dose-dependent decrease in luminescence (**Figure 16A**).

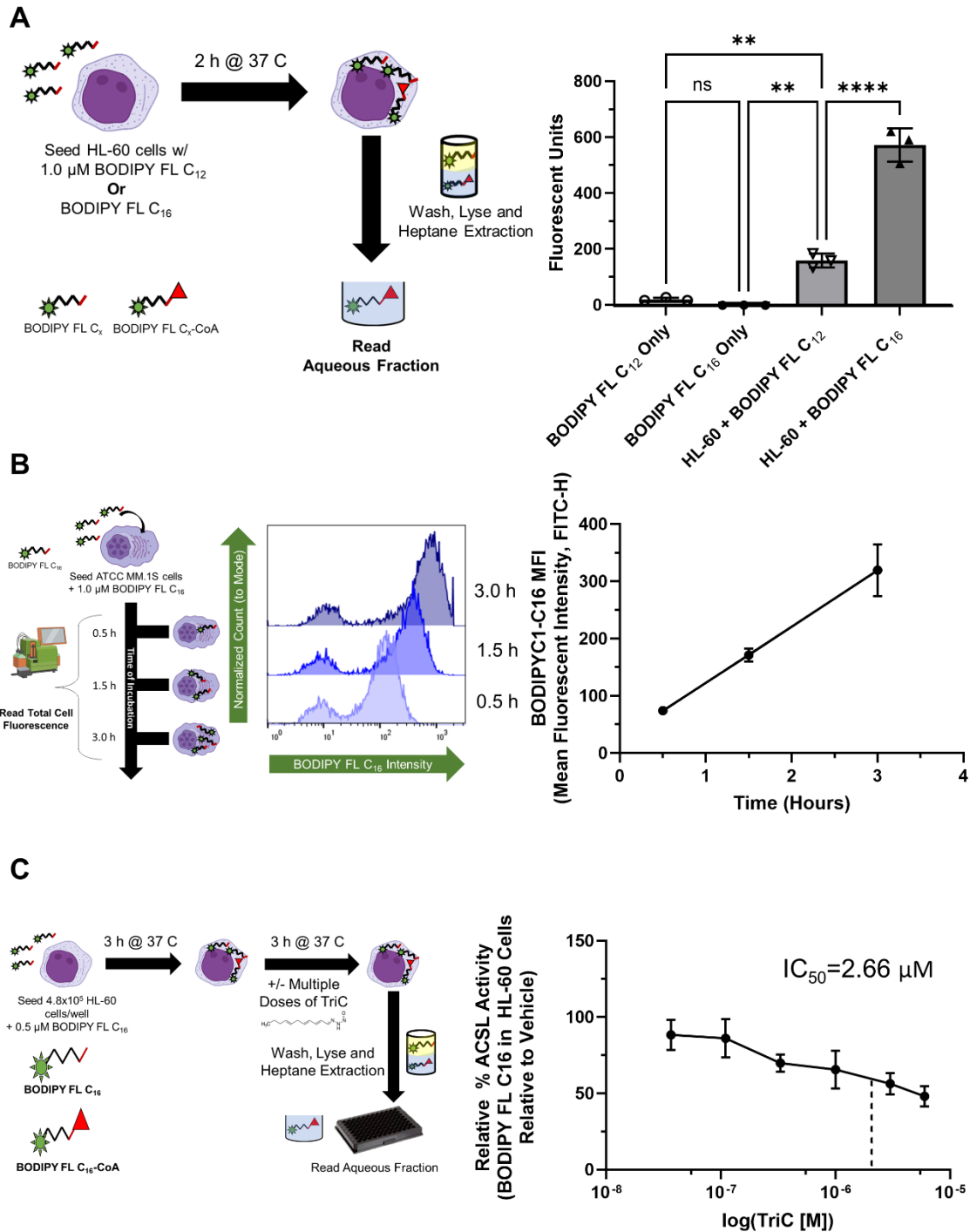


Figure 10. Optimization of Live Cell Activity Assay with HL-60 and ATCC MM.1S Cells-
A) HL-60 cells were seeded in 6 well dishes and incubated with either 1.0 μM BODIPY FL C₁₂ or C₁₆ for 2 hours at 37 $^{\circ}\text{C}$. Cells were washed with fatty acid(FA)-free BSA and resuspended in STE Buffer +0.1% Triton-x100 and subject to an n-heptane extraction, the organic fraction was the read to quantify the amount of BODIPY FL-CoA product was produced. n=3 **B)** ATCC MM.1S cells were seeded in 6 well dishes and incubated with 1.0 μM BODIPY FL C₁₆ for 0.5, 1.5 and 3.0 hours at 37 $^{\circ}\text{C}$. At each timepoint cells

were washed with FA-Free BSA and total fluorescence was read via flow cytometry. n=3 C) HL-60 cells were seeded in 6 well dishes and incubated with either 1.0 μ M BODIPY FL C₁₂ or C₁₆ for 3 hours at 37 °C then challenged with multiple doses of TriC for 3 hours. Cells were then washed with FA-Free BSA and resuspended in STE Buffer +0.1% Triton-x100 and subject to an n-heptane extraction, the organic fraction was the read to quantify the amount of BODIPY FL-CoA product was produced. EC₅₀ values were calculated using Non-linear regression (four parameter, variable slope) n=3.

The cell counting data revealed a decrease in viability upon TriC treatment. To determine if the effects of TriC were cytostatic or cytotoxic, we measured MM cell proliferation via Ki-67 staining, cell cycle (DAPI; **Figure 11E, 12**), and apoptosis by Annexin V/DAPI staining, and by measuring BAX protein levels for 72 hours at 24-hour intervals. At 48 hours, 3 μ M TriC decreased Ki-67 positivity in MM.1S, U226B1, OPM-2 and RPMI-8226 cells compared to vehicle (**Figure 11F, 15E-F**). We observed batch-dependent effects of TriC in these experiments due to unknown differences between batches (**Figure 14**). Interestingly, treatment with 1 and 3 μ M TriC for 48 hours significantly decreased the percentage of cells in G₁ and G₂/M phases and increased the population of sub-G₁ MM.1S, OPM-2, and RPMI-8226 cells. As sub-G₁ cells are associated with DNA degradation, these data suggest that TriC induces DNA fragmentation but not cell cycle arrest (**Figure 11E, 13A-B 15G-H**). We observed a similar decrease in the percentage of G₁, S and G₂/M and increase in Sub-G₁ in HL-60 cells treated with TriC for 24 hours and 48 hours (**Figure 16E-F**). Consistent with the MM cell data, apoptotic cells [Annexin V(+), DAPI(+)] increased (7-12% total apoptosis) in a dose-dependent manner at both 48 and 72 hours post-TriC treatment in MM.1S and OPM-2 cells (**Figure 9F**). Moreover, we observed a dose-dependent increase in the key apoptotic protein BAX in MM.1S cells treated with TriC for 48 and 72 hours (**Figure 11G; Figure 13B**). Taken together, these data demonstrate that TriC treatment

decreases the viability and proliferation of human MM cell lines after 48 hours of treatment and is characterized by an increase in the percentage of sub-G₁ cells, increases in Annexin V/DAPI-positive cells, and the apoptosis-related protein BAX. HL-60 cells show a similar response to TriC as the human MM cell lines with increases in the percentage of sub-G₁, and an induction of apoptosis.

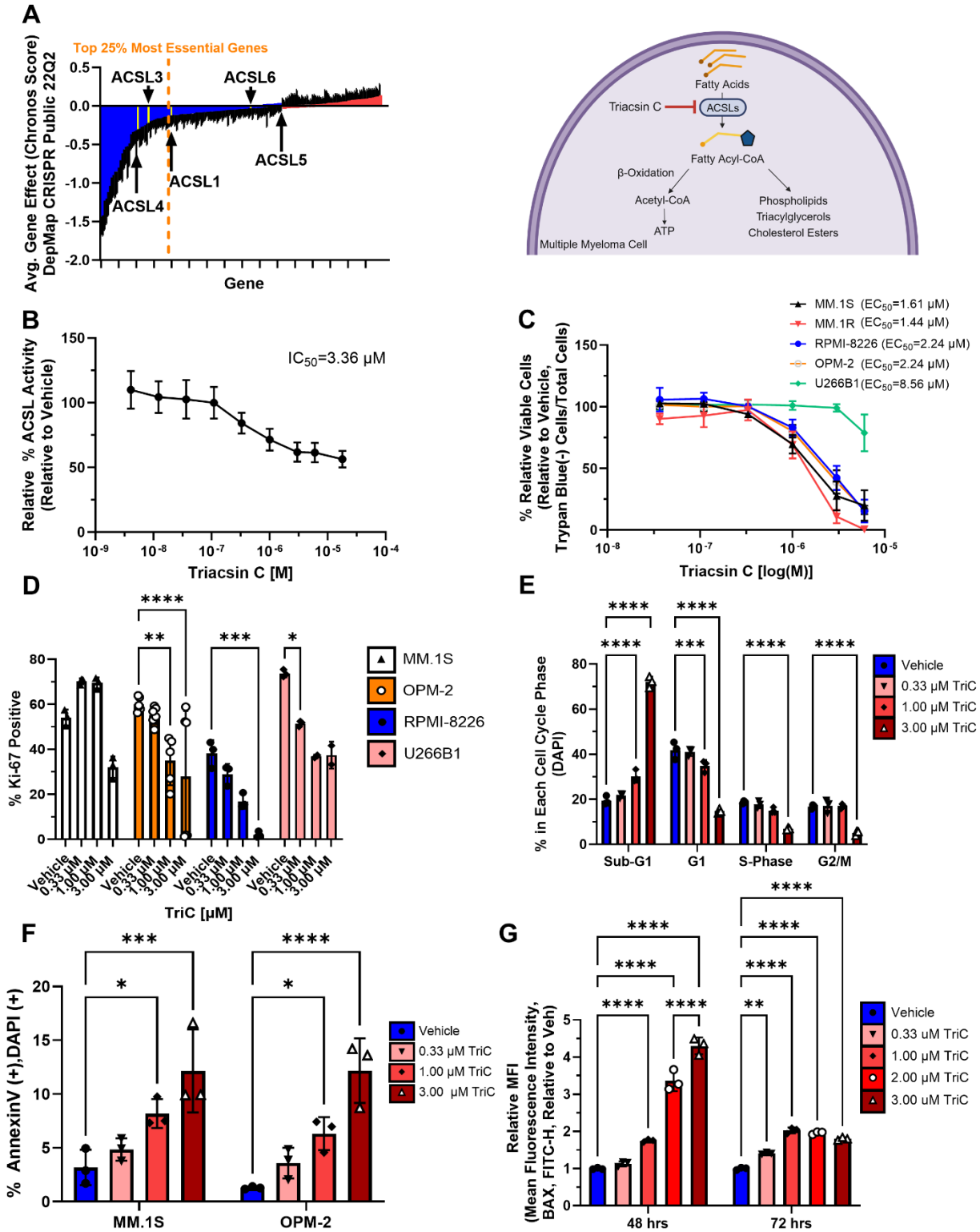


Figure 11. Targeting the ACSLs using Triacsin C Inhibits Myeloma Cell Proliferation and Survival-
A) Hallmark Fatty Acid Metabolism genes from Gene Set Enrichment Analysis (M5935) displayed as the average gene fitness (Chronos Score) data from the Cancer Dependency Map of 21 human myeloma cell lines. Blue bars represent targets of

interest with average Chronos scores < 0.0 (myeloma cell growth fitness defect upon CRISPR knockout), while red bars are Chronos scores >0.0 . Schematic was made with Biorender.com and adapted from Tang *et al.* 2018, *Oncology Letters*³⁰⁵; ACSL family members are highlighted in yellow. B) ACSL activity relative to vehicle treated cells of ATTC MM.1S cells treated with various doses of triacsin C (TriC) for 2 hours C) MM.1S, MM.1R, RPMI-8226, OPM2 and U266B1 cells were incubated with various doses of TriC for 48 hrs and stained with Trypan Blue to quantify viable cells/mL. EC₅₀ values were calculated using Non-linear regression (four parameter, variable slope) in GraphPad Prism v9.4.1. n=3 D) Proliferation of human MM cell lines MM.1S, OPM-2, RPMI-8226 and U226B1 cells treated with various doses of TriC for 48 hrs and stained with AF647 anti-human Ki67 (% positive); n=2-6. E) Cell cycle distribution of MM.1S cells treated with various doses of TriC for 48 hrs and stained with DAPI; n=3. F) Apoptosis assay using Annexin V/DAPI staining of MM.1S, U266B1 and OPM2 cells treated with various doses of TriC for 48 hrs; n=3. G) Intracellular BAX (AF488 mouse anti-human BAX antibody) levels in MM.1S cells treated with various doses of TriC for 48 hrs; data displayed as FITC-H MFI; n=3 . Statistics Significance determined via two-way ANOVA with: Tukey's multiple comparison test (E-F), Dunnett's multiple comparison test (D) or Šídák's multiple comparisons test (G) All data are mean \pm StDev, *p<0.05, **p<0.01, ***p<0.001 ****p<0.0001.

A

Ki-67

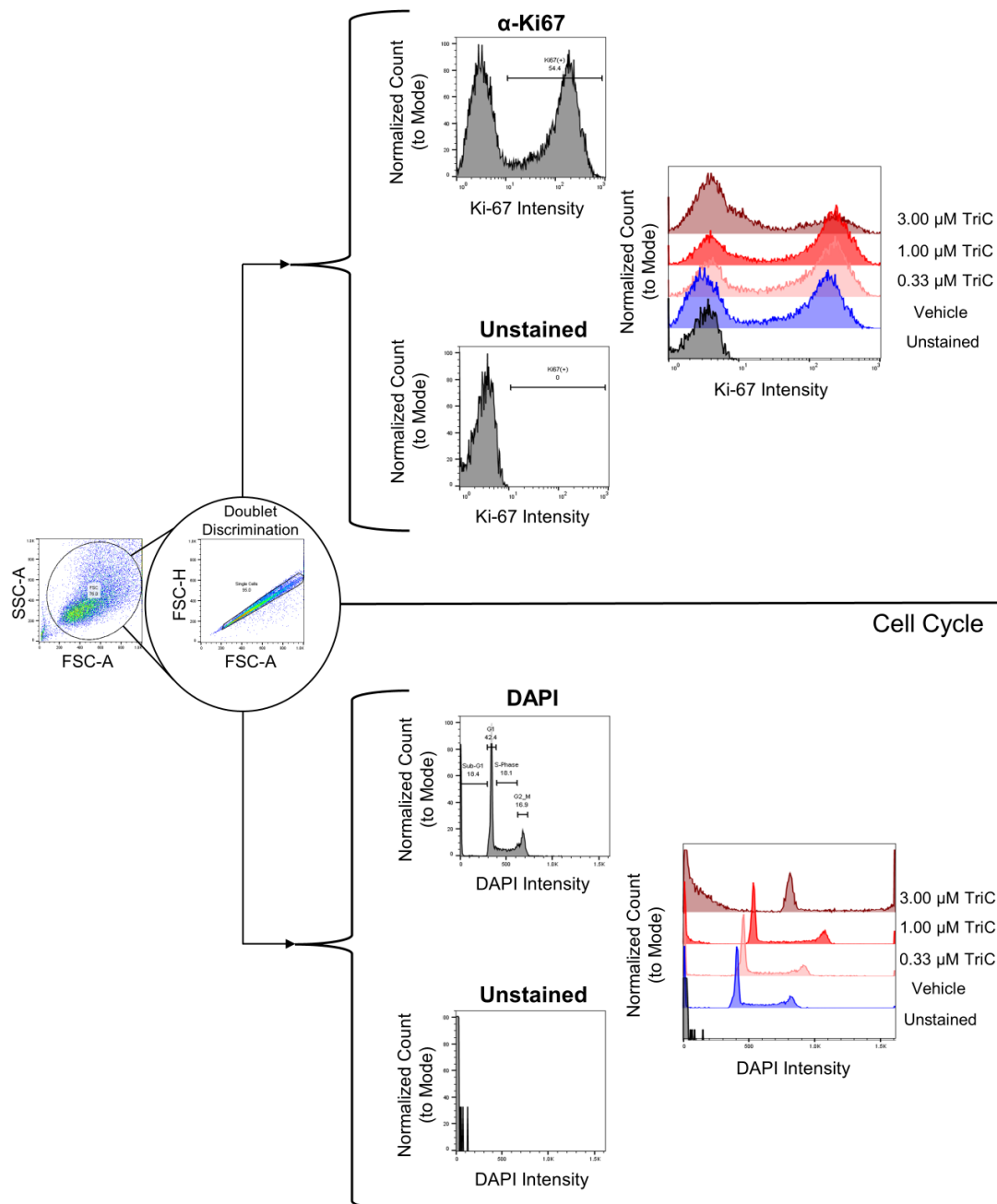
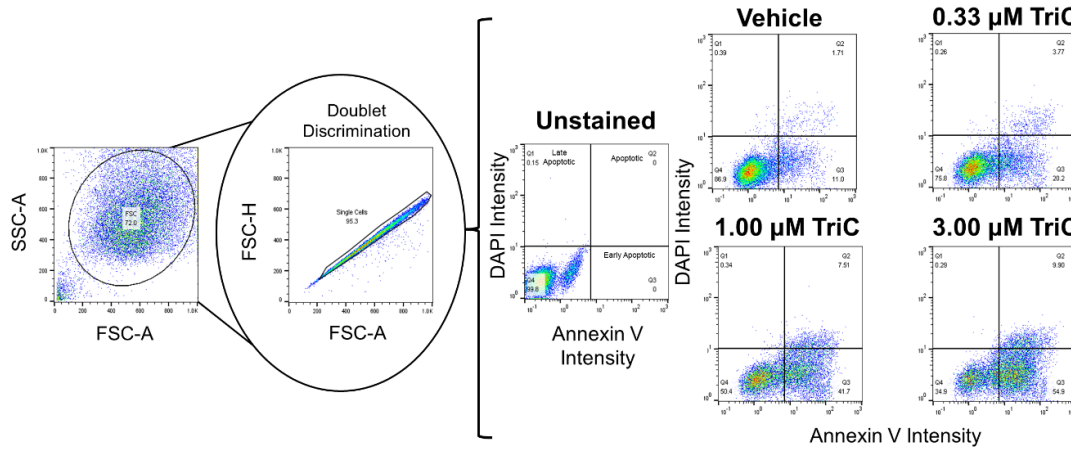


Figure 12. Gating Strategies for Ki-67 and Cell Cycle Distribution

A) Representative Ki-67 and cell cycle distribution flow cytometry plots depicting the gating strategies in MM.1S cells treated with various concentrations of TriC for 48 hours. An initial gate was made in the FSC-A vs. SSC-A and doublets were excluded comparing the FSC-A vs. FSC-H. In the same sample, both DAPI and Ki-67-AF647 was analyzed, positive populations were identified by comparing stained and unstained samples. Representative histograms of Ki-67 (top) and DAPI staining (bottom) depicting fluorescent intensities vs. normalized counts (to the mode) for various concentrations of TriC. A minimum of 10,000 events were collected.

A

Annexin-V and DAPI



B

BAX

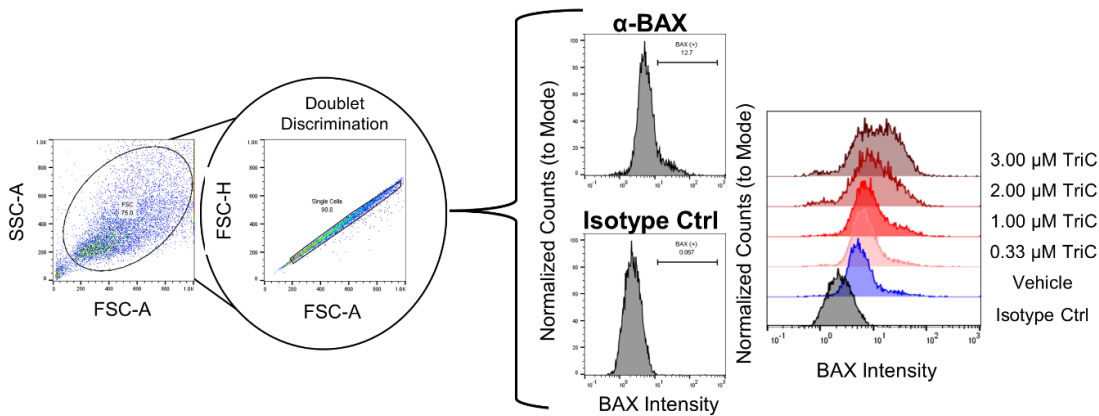


Figure 13. Gating Strategies for Apoptosis and BAX Staining
A) Representative Apoptosis assay (Annexin V/DAPI) flow cytometry plots depicting the gating strategies in MM.1S cells treated with various concentrations of TriC for 48 hours. An initial gate was made in the FSC-A vs. SSC-A and doublets were excluded comparing the FSC-A vs. FSC-H. Within the single cell gate, positive populations were identified by comparing stained and unstained samples. Representative flow plots depicting fluorescent intensities of Annexin V vs. DAPI for various concentrations of TriC. A minimum of 10,000 events were collected. B) Representative BAX protein flow cytometry plots gated with a similar strategy as above, however positive signal was identified by comparing AF488 anti-BAX stained samples to AF488 Isotype control stained samples. A minimum of 10,000 events were collected.

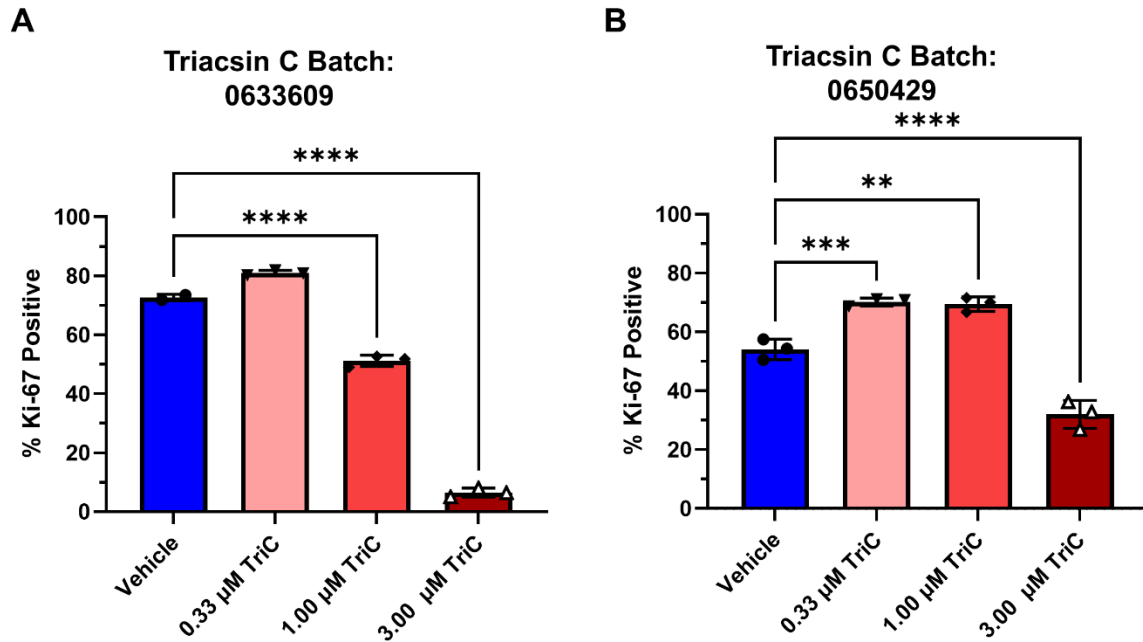


Figure 14. Triacsin C has Batch-Dependent Effects on Ki-67 Levels-
A&B) Proliferation of human MM cell lines MM.1S cells treated with various doses of TriC for 48 hrs and stained with AF647 anti-human Ki67 (% positive) from two different batches, denoted by the specific batch numbers see above their respective graphs. n=3 Significance determined via One-way ANOVA with Statistics: Dunnet's multiple comparison test. Data are the mean \pm StDev, * $p < 0.05$, ** $p < 0.01$, * $p < 0.001$ **** $p < 0.0001$.**

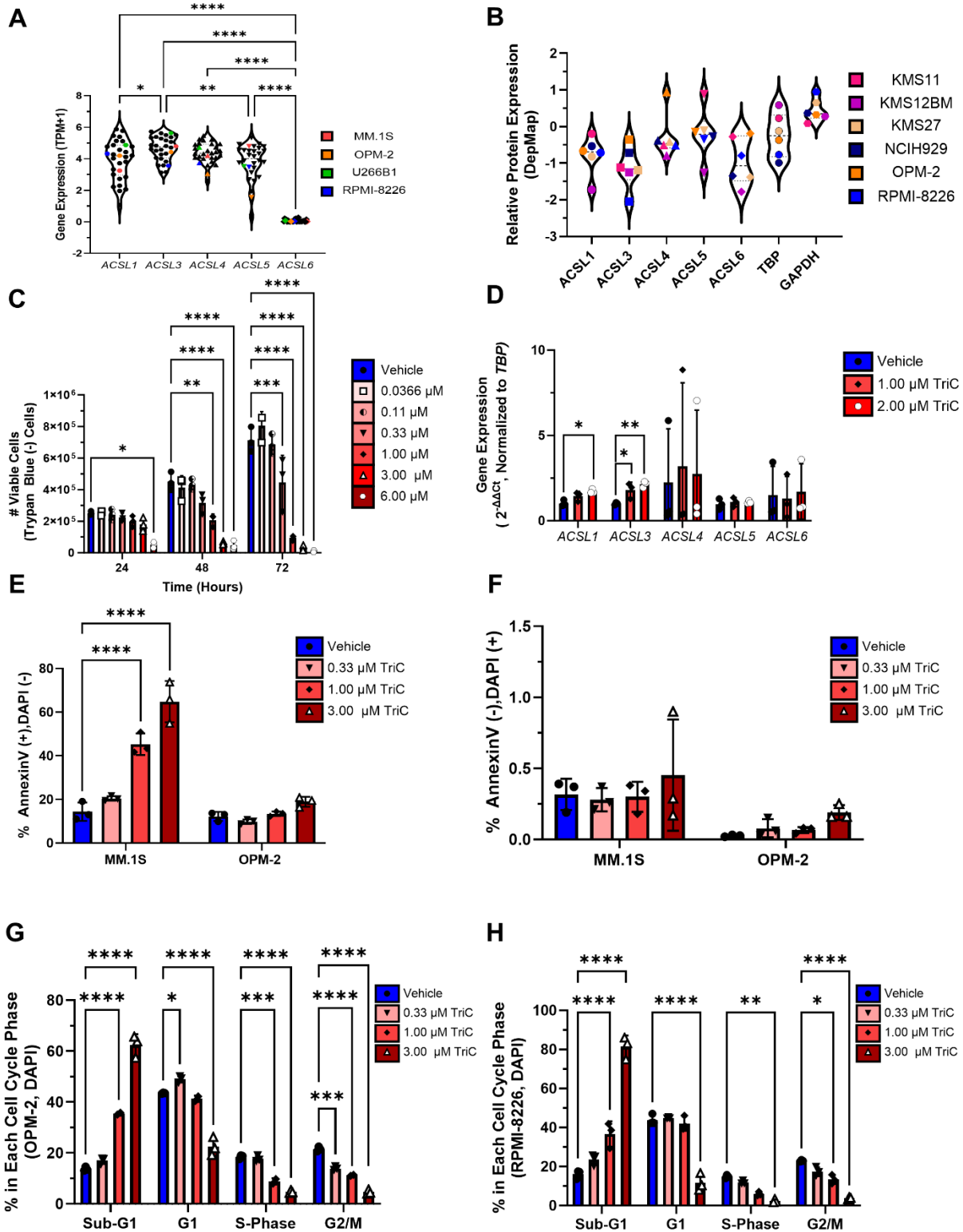


Figure 15. ACSL Gene and Protein Expression, Early and Late Apoptosis and Cell Cycle Distribution of OPM-2 and RPMI-8226 Cells Treated with TriC-
A) ACSL family member gene expression (transcripts per million+1 (TPM+1) in 30 human myeloma cell lines from the Cancer Dependency Map/Cancer Cell Line

Encyclopedia. Cell lines used in this study are highlighted in color with all other cell lines are in black. B) Relative protein expression of the ACSL family and the house keeping proteins Tata-box binding protein (TBP) and glyceraldehyde-3-phosphate dehydrogenase (GAPDH) of 6 human myeloma cell lines from the Cancer Dependency Map/Cancer Cell Line Encyclopedia. C) Expression of the ACSL family members in MM.1S cells treated with vehicle, 1, or 2 μ M triacin C for 48 hours; assessed by qRT-PCR; n=3. D-E) Apoptosis (Annexin V-APC/DAPI) data for MM.1S, U266B1 and OPM2 treated with various doses of TriC for 48 hrs; n=3. Statistics: Panels C, E-H, Two-way ANOVA with Tukey's multiple comparisons test. D) One-way ANOVA with Dunnet's multiple comparisons test. Data are mean \pm StDev, *p<0.05, **p<0.01, ***p<0.001 ****p<0.0001.

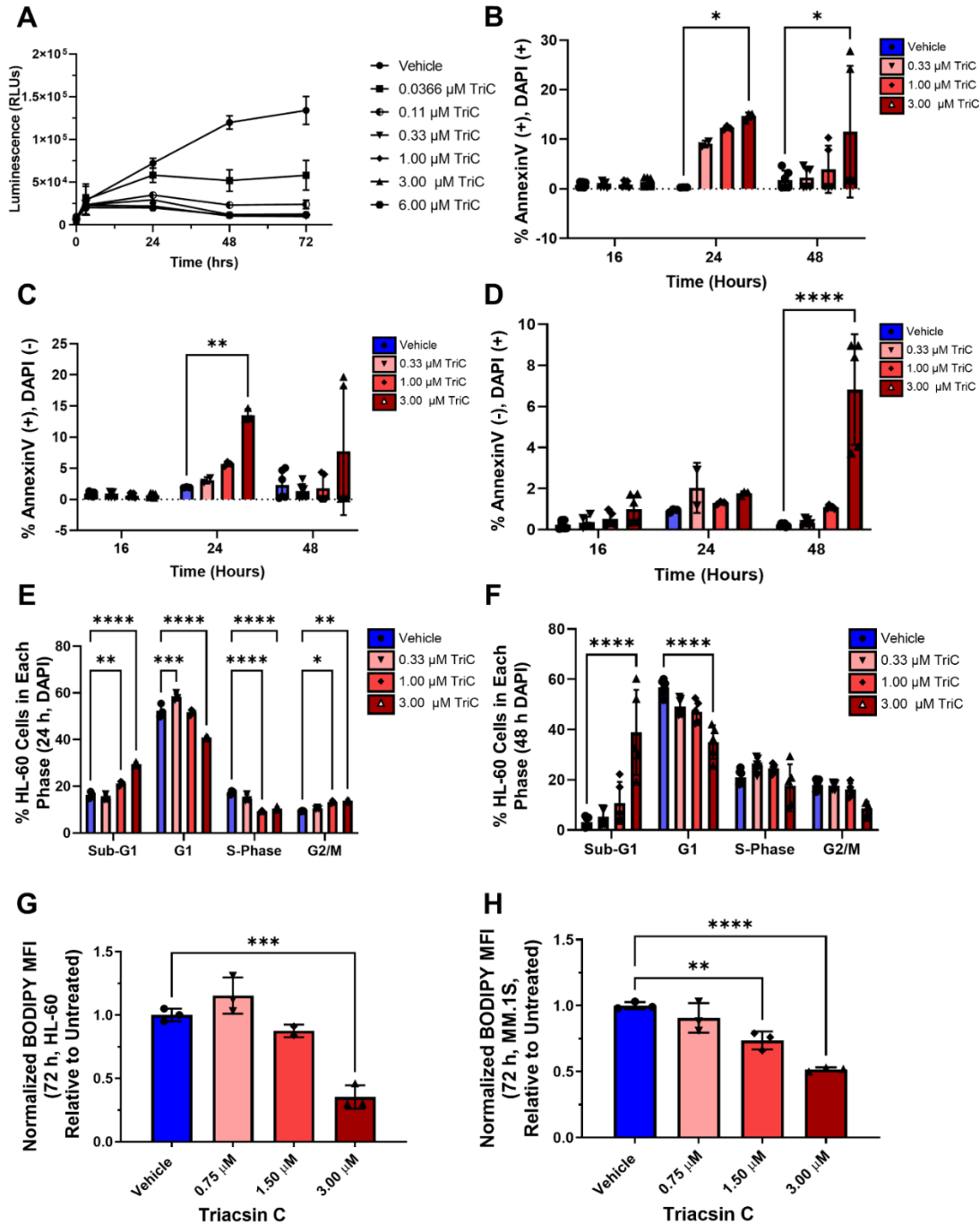


Figure 16. Triacsin C Decreases HL-60 Redox Potential, Survival and Lipid Droplets-
A) RealTime-Glo measurement of cellular redox potential of HL-60 cells treated with TriC over 72 hours **B-D)** Apoptosis (Annexin V-APC/DAPI) data for HL 60 cells treated with various doses of TriC for 16, 24, or 48 h; n=3. **E-F)** Cell cycle distribution of HL-60 cells treated with various doses of TriC for 24 and 48 hours (respectively), and stained with DAPI; n=3. **G-H)** HL-60 or H) MM.1S cells were treated with various doses of TriC for 72 hours and stained with BODIPY FL or BODIPY 581/591 C11, respectively and mean fluorescence intensity (MFI) was measured by

flow cytometry. One-way ANOVA with Tukey's multiple comparisons test. Data are mean \pm StDev, * $p < 0.05$, ** $p < 0.01$, *** $p < 0.001$ **** $p < 0.0001$.

3.6.2. Triacsin C Induces Transcriptional Changes in MM.1S Cells Associated with Cell Death and the Integrated Stress Response

To investigate the mechanism underlying TriC toxicity in MM cells, MM.1S cells were treated *in vitro* with vehicle or 1 μ M TriC for 24 hours and subjected to RNA-seq analysis. Transcripts for each sample were aligned to the *Homo sapiens* GRCh38 genome, which included 12,772 protein-coding genes, all of which passed the read mapping and quality parameters (**Figure 19A-D**). Principal component analysis and comparison of Euclidean distances between samples showed that the transcriptomes of vehicle- and TriC-treated cells were distinct (**Figure 17A and Figure 19A**). Between TriC and vehicle-treated MM.1S cells, DESeq2 analysis revealed 208 differentially expressed genes (DEGs; $\log_2(\text{FC}) > |1|$, $\text{padj} < 0.05$)³⁰⁰ which included 167 upregulated and 41 downregulated genes (**Figure 17B**). Enrichr was used to identify significantly enriched pathways within the 208 DEGs. Significant pathways of interest in both the Reactome³⁰⁶ and KEGG³⁰⁷ pathways of upregulated DEGs included: Cellular Response to Stress, ATF4 Activation in Response to Endoplasmic Reticulum Stress, Ferroptosis, and Apoptosis (**Figure 15C-D, Tables 17-18**). Search Tool for the Retrieval of Interacting Genes/Proteins (STRING v.12) was used to facilitate an understanding of the general interaction between the DEGs. 3 nodes were calculated using k-means clustering and the labels "Integrated Stress Response and Cell Death" (red), "Fatty acid and One-Carbon Metabolism" (yellow) and "Amino Acid and Arachidonic Acid Metabolism" (blue) were used to reflect generalized GO terms within each cluster (**Figure 18**). Reactome and KEGG pathways enriched among the significantly downregulated genes in TriC-treated cells were Aryl Hydrocarbon Receptor Signaling

and POU5F1 (OCT4), SOX2, and NANOG activated genes related to proliferation (**Figure 19E-F, Tables 25-26**).

Gene overrepresentation analysis suggests that TriC activates EIF2AK3-EIF2S1-ATF4 signaling and cell death pathways and negatively regulates proliferation. Indeed, we observed significantly increased gene expression of *EIF2AK3* (3.2-fold) and *ATF4* (4.2-fold) and a trend of increased expression in a number of its downstream targets, such as *PPP1R15A* (5.6-fold), *TRIB3* (6.7-fold) and the pro-apoptotic *DDIT3* (13.7-fold) in MM.1S cells treated with 1 μ M TriC relative to vehicle-treated cells. Furthermore, there was a significant increase in a key gene in another arm of the ER stress pathway, *ERN1* after 24 hours of treatment with 1 μ M TriC in MM.1S cells. There were no significant changes in gene expression of other kinases that activate EIF2S1, *EIF2AK1* or *EIF2AK4* (**Figure 17E**). In addition to EIF2AK3-EIF2S1-ATF4 activation, a gene associated with mitigating ferroptosis, *SLC3A2*, (4.0-fold) was significantly increased, with a trending increase in gene expression of the related *SLC7A11*. Additionally, the pro-ferroptotic genes, *HMOX1* (1.8-fold) had significantly increased expression and *CHAC1* (13.9-fold) had an increasing trend in gene expression upon TriC treatment (**Figure 17F**). Moreover, the key tumor suppressor *CDKN1A* (2.9-fold) was significantly increased in TriC-treated MM.1S cells, with *TP53* levels remaining unchanged (**Figure 17G**). There was a significant ($p < 0.05$) increase in genes involved in fatty acid metabolism, such as *ACACA* (2.3-fold), *SCD1* (5.0-fold), and the cholesterol transporter *ABCG1* (14.2-fold) with a trending increase in the rate-limiting enzyme for cholesterol biosynthesis, *HMGCS1* (**Figure 17H**). Interestingly, there was a decrease in the gene expression of metastasis-associated, *RAC1* (*PAK6*, 0.5-fold), and oncogenic RAS

pathways (*RASA4B*, 0.2-fold) (**Figure 19F**). Thus, these data show that MM.1S cells treated with TriC for 24 hours have a transcriptional profile associated with ATF4 activation, apoptosis, ferroptosis, and negative regulation of cell cycle progression.

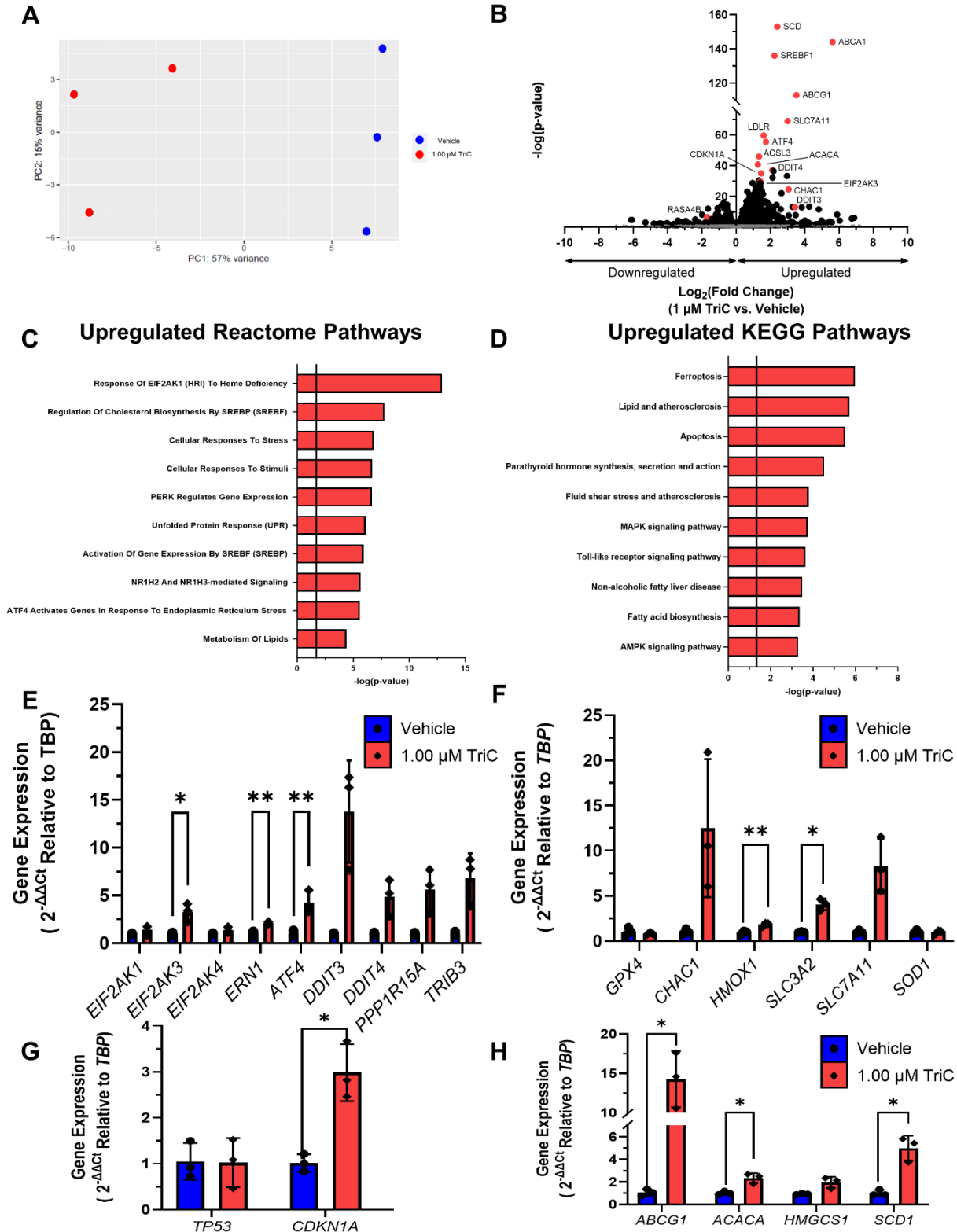


Figure 17. Triacsin C Treatment of MM.1S Cells Induces Transcriptional Changes Associated with Cell Death and the Integrated Stress Response

A) Transcriptional profiles of MM.1S cells treated with vehicle (DMSO) or 1 μ M TriC for 24 hours as assessed by PCA of RNA-Seq data. **B)** Differentially expressed

transcripts derived from RNA-seq of MM.1S cells treated with vehicle (DMSO) or 1 μ M TriC for 24 hours. C-D) Reactome and KEGG pathways (respectively) enriched in the significantly upregulated transcripts in 1 μ M TriC treated MM.1S as determined via Enrichr. E-H) Expression of genes related to *ATF4* signaling (E), ferroptosis (F) *TP53* signaling (G) and fatty acid metabolism (H) relative to *TBP* in MM.1S cells treated with vehicle or 1 μ M TriC for 24hrs; n=3. Statistics: Significance was tested in panels 2E-H with an unpaired Student's t-test or Welch's t-test. All data are mean \pm StDev, *p<0.05, **p<0.01, ***p<0.001 ****p<0.0001.

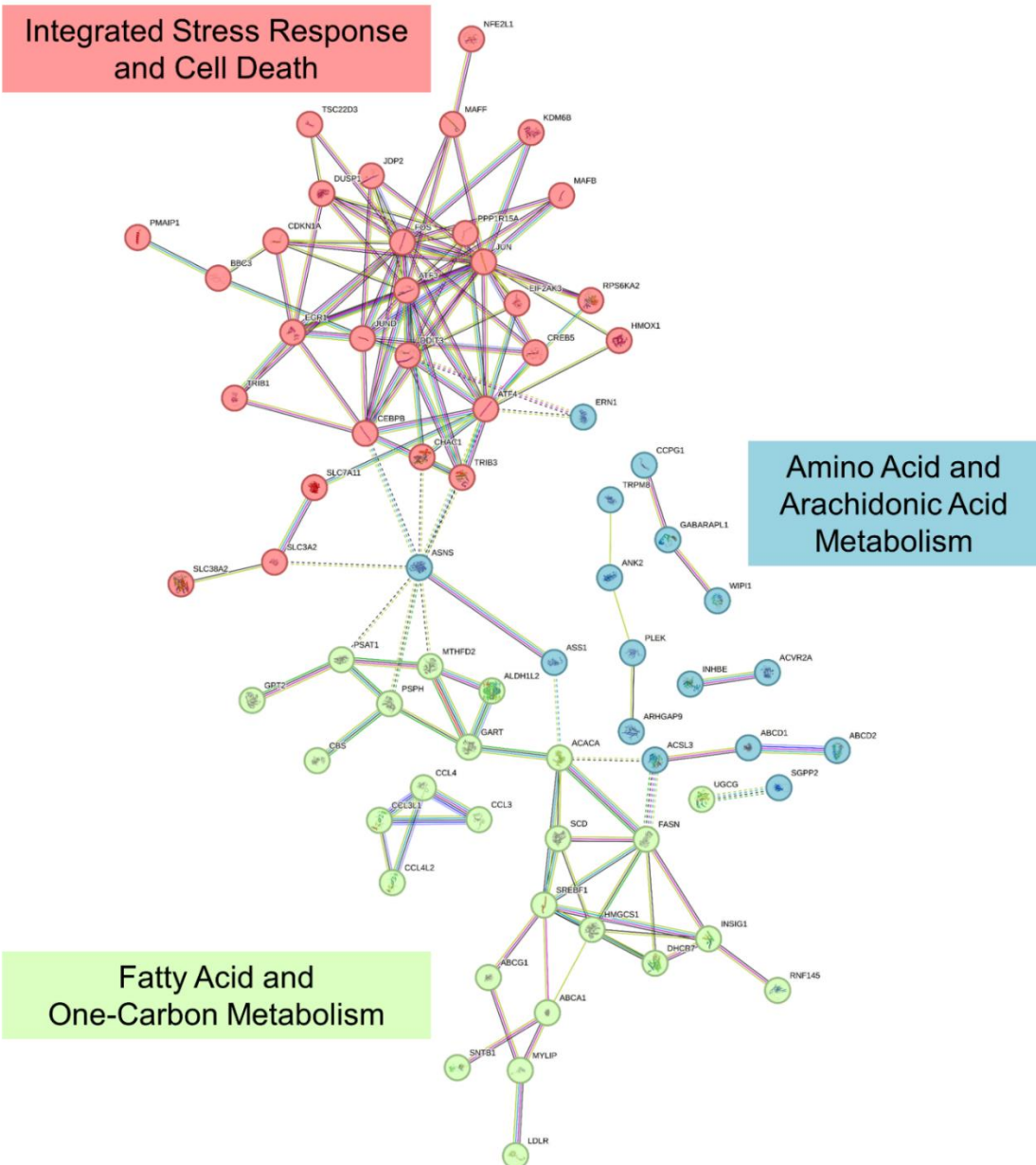


Figure 18. Significantly Upregulated Transcripts in MM.1S Cells Treated with TriC for 24 hours Search Tool for the Retrieval of Interacting Genes/Proteins (STRING v 12.0) diagram of the significantly upregulated, differentially expressed genes identified by RNA-Seq in MM.1S cells treated with 1 μ M TriC. The STRING parameters used were a stringency of 0.7 (high confidence) and k-means clustering with 3 nodes.

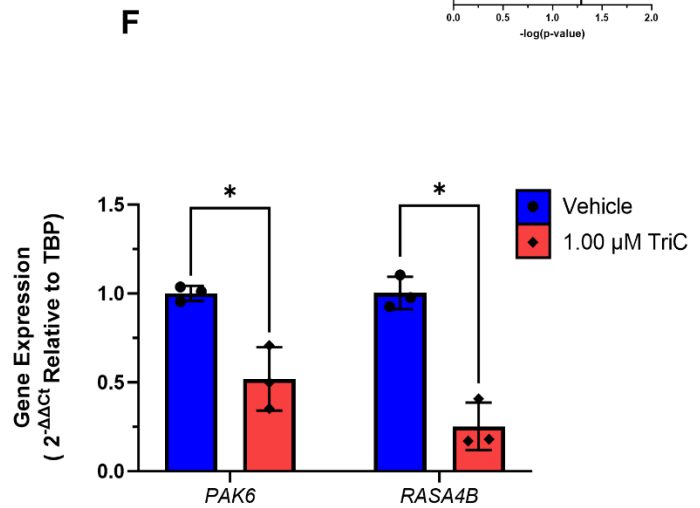
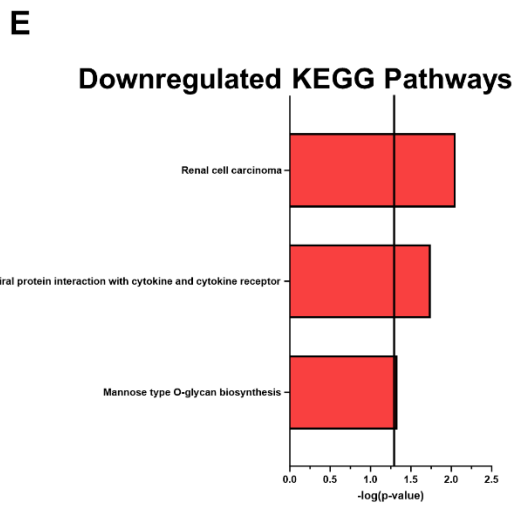
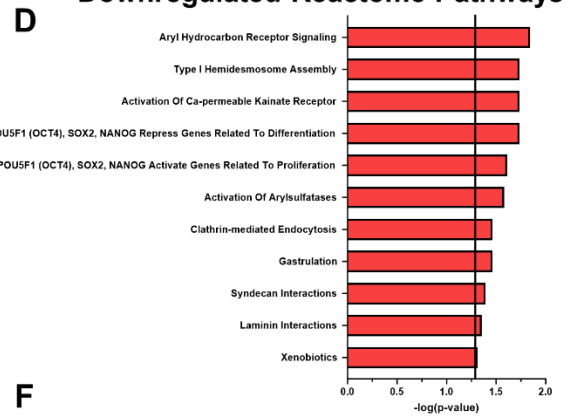
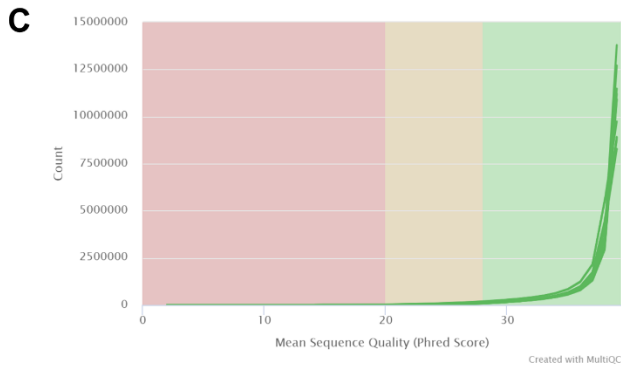
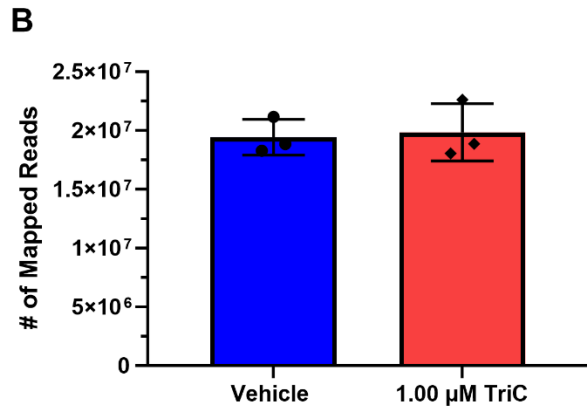
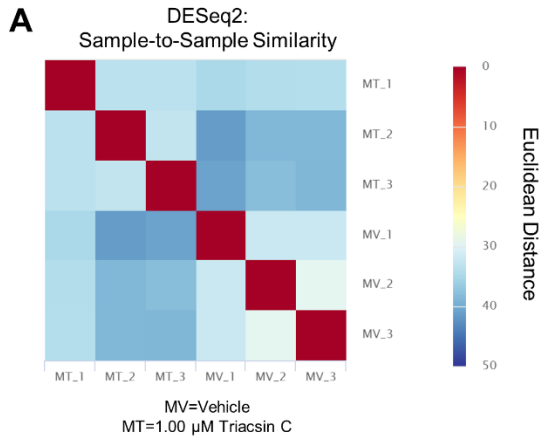


Figure 19. Quality Control Parameters for RNA-Sequencing of TriC-Treated MM.1S Cells and Downregulated Pathways

A) RNA-Seq sample-to-sample similarity as displayed via Euclidean distances of the transcriptional profiles of MM.1S cells treated either with vehicle (DMSO, MV) or 1 μ M triacsin C (TriC; MT) were calculated with DESeq2. Numbers associated with conditions designate different replicates. B) The number of reads mapped for MM.1S cells treated either with vehicle (DMSO) or 1 μ M TriC after 24hrs. Reads were aligned to the *Homo sapiens* hg38 reference genome using STAR v2.7.10a and SAMtools v1.15.1, read counts were quantified using SALMON v1.5.250. C) The mean sequence quality (Phred Score) for each sample and their associated read counts are displayed for MM.1S cells treated either with vehicle (DMSO) or 1 μ M triacsin for 24 hrs. Raw reads were subjected to quality checking and reporting (FastQC v0.11.9/ MultiQC v1.13⁴⁶; and low quality sequence (Phred score <20) using Trim Galore v 0.6.7⁴⁷ were removed. D-E) Reactome and KEGG Pathways (respectively) associated with the significantly downregulated transcripts in 1 μ M triacsin C treated MM.1S cells as assessed with Enrichr. F) Gene expression of significantly downregulated genes in the RNA-seq in MM.1S cells treated with vehicle or 1.00 μ M triacsin C for 24hrs by qRT-PCR. Values are relative to *TBP*, n=3. Statistics: Unpaired Student's t-test or Welch's t-test. All data are mean \pm StDev, *p<0.05, **p<0.01, *p<0.001 ****p<0.0001**

3.6.3. Triacsin C Treatment Induces Proteomic Changes Associated with Mitochondrial Dysfunction and Reactive Oxygen Species Detoxification in MM.1S Cells

To identify global protein changes induced by TriC treatment, we treated MM.1S cells with 1 μ M TriC, 2 μ M TriC, or vehicle for 48 hours and subjected them to sequential window acquisition of all theoretical fragment ion spectra (SWATH)³⁰⁹ mass spectrometry. The proteome of each treatment group was well-defined and functionally distinct from that of the other treatments, as assessed by PCA (Figure 3.13A). Of the approximately 1,580 total proteins detected in TriC-treated MM.1S cells, 167 and 614 differentially expressed proteins were detected in the 1 and 2 μ M TriC-treated cells, respectively. The majority of differentially expressed proteins in both TriC treatments decreased (81.4% and 61.7%, 1 μ M, and 2 μ M, respectively) relative to vehicle-treated control cells (Figure 20B-C, Supp. Table 8). The canonical pathway features in the Ingenuity Pathway Analysis³¹⁰ revealed six shared pathways among MM.1S cells treated for 48 hours with both TriC doses, including: phagosome maturation, protein

ubiquitination, FAT10 signaling, mitochondrial dysfunction, oxidative phosphorylation, and EIF2 signaling (Figure 18D, E). Interestingly, mitochondrial function and EIF2 signaling were predicted to be activated, while oxidative phosphorylation was likely inactivated (Z score $\geq |2|$) based on the differential protein expression of both the 1 μ M and 2 μ M TriC conditions compared to the vehicle (Figure 20D-E). Within the six shared dysregulated pathways, 39 differentially expressed proteins were common to both TriC doses tested in MM.1S (Figure 20F, Supp. Table 8), and these were significantly enriched for Biological Processes (identified using Enrichr) in two major categories: reactive oxygen species metabolism (SOD1, PRDX1, 2, 5, and 6) and mitochondrial electron transport (COX6B1, COX5A and COX7A2) (Figure 20G). Indeed, qRT-PCR gene expression of COX5A, a subunit of Complex IV, was significantly decreased in MM.1S cells treated with TriC for 48 hours, with similar but non-significant trends for decreased expression of COX6B1 and ATP5ME (Figure 20H). Taken together, these data show that 48 hours of TriC treatment induces proteomic changes associated with decreases in mitochondrial dysfunction, oxidative stress, protein ubiquitination EIF2 signaling, with increases in proteins associated with fatty acid oxidation like CPT1A and ribosomal subunits.

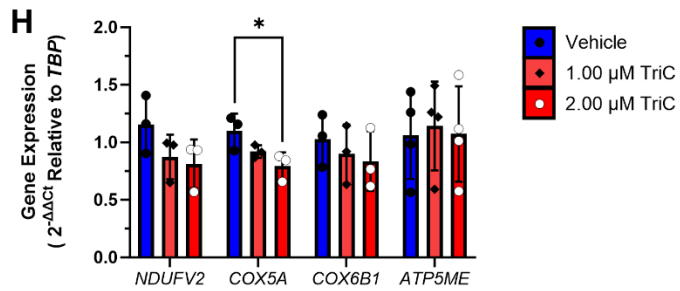
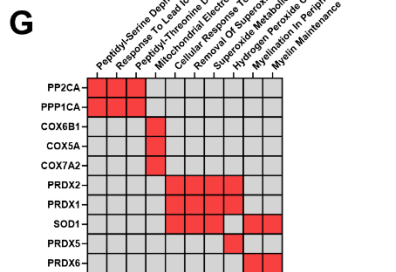
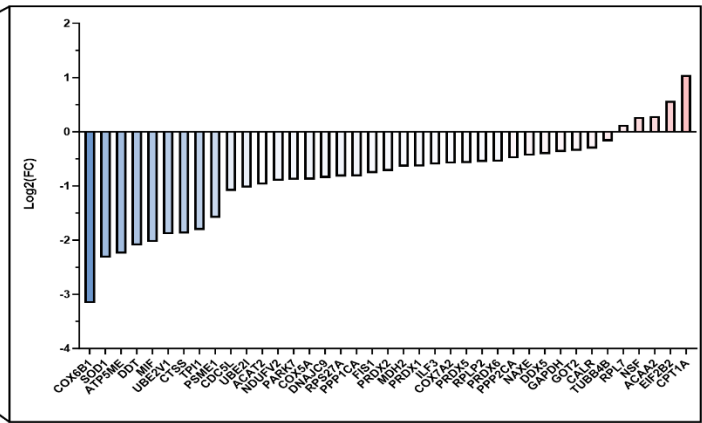
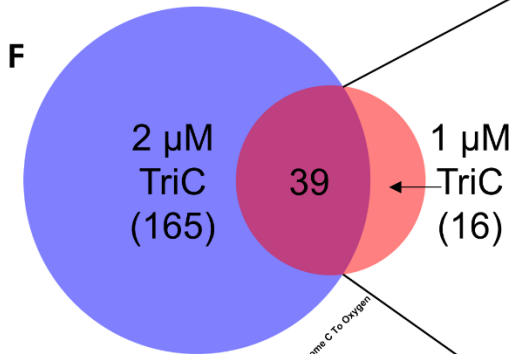
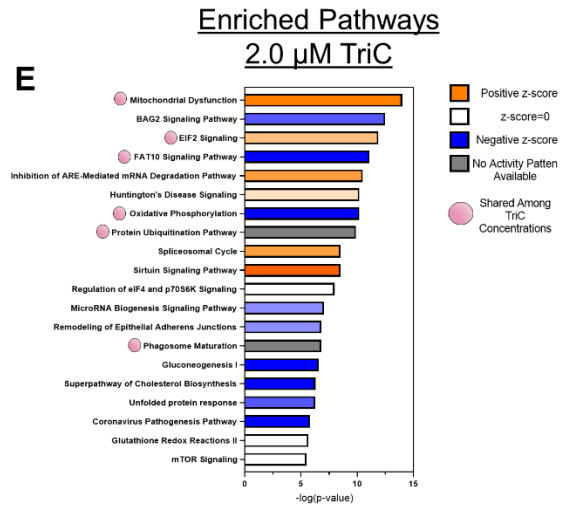
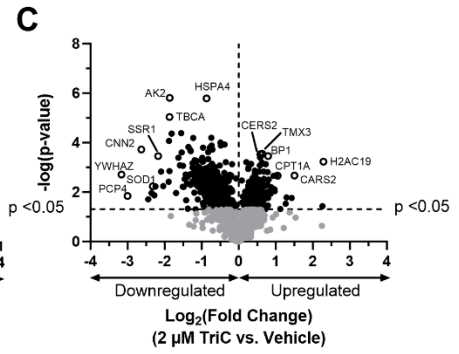
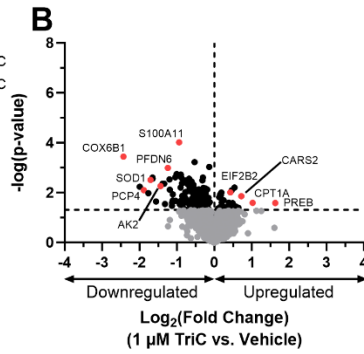
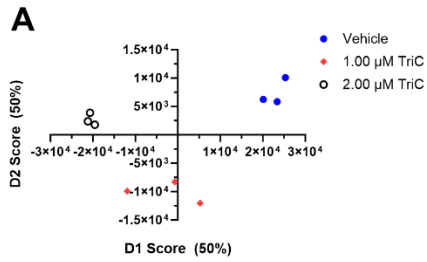


Figure 20. Triacsin C Treatment of MM.1S Cells Induces Proteomic Changes Associated with Mitochondrial Dysfunction and Reactive Oxygen Species

A) Proteomic profiles of MM.1S cells treated with Vehicle (DMSO, blue filled circles), 1 μ M (red diamonds) or 2 μ M (open black circles) TriC as assessed by principal component analysis. **B-C)** Aberrantly expressed proteins in MM.1S cells treated for 48hrs w/ either 1 or 2 μ M TriC **D-E)** Top 20 enriched pathways in MM.1S cells treated with 1 and 2 μ M TriC, respectively, identified using Ingenuity Pathway Analysis with their associated $-\log(p\text{-value})$. **F)** DeepVenn depiction of the number of significantly changed proteins among the shared significantly changed pathways identified by IPA between 1 μ M TriC (red, 16 unique proteins) and 2 μ M TriC (blue, 165 unique proteins) with a total of 39 shared proteins (purple). The $\log_2(\text{fold change})$ is depicted for the 39 shared proteins among MM.1S^{gfp+/luc+} treated for 48 hrs with 1 or 2 μ M TriC. **G)** Gene ontology (GO) enrichment for GO Biological Process of the 39 shared dysregulated proteins between MM.1S cells treated with 1 μ M and 2 μ M TriC treated for 48 hrs as assessed by Enrichr. A selection of proteins with common aberrant expression in the presence of both TriC doses are depicted here with red boxes indicating association between the protein and the GO term; gray boxes indicate no association. **H)** Expression of genes related to oxidative phosphorylation in MM.1S cells treated with vehicle or 1 μ M TriC for 24hrs, as assessed by qRT-PCR; n=3. Statistics: Student's t-test to identify differentially expressed proteins (B-C) and a right-tailed Fisher's exact test was used to identify significantly associated proteins in a given pathway in Ingenuity pathway analysis (D-E) Two-way ANOVA with Šidák's multiple comparisons test (H) and). All data are mean \pm StDev, *p<0.05, **p<0.01, ***p<0.001 ****p<0.0001.

3.6.4. Triacsin C Treatment Negatively Impacts Multiple Myeloma Cell Metabolism and Mitochondrial Function in MM.1S and HL-60 Cells

Given that TriC-treated MM.1S cells exhibited changes in mitochondria-related pathways (oxidative phosphorylation and mitochondrial dysfunction), we aimed to test the hypothesis that TriC impairs MM cellular metabolism and mitochondrial function. To assess the effect of TriC on MM cellular metabolism, we treated MM.1S cells with 1 μ M TriC (MM.1S-TriC) for 24 hours and then subjected the cells to mitochondrial stress measurements (**Figure 20A**). MM.1S-TriC cells had significantly reduced basal, maximal, and ATP-dependent mitochondrial respiration and proton leakage (**Figures 20A-B**). Interestingly, in parallel samples, we observed a significant 21.27% decrease in total ATP production rates attributable to a 57.3% decrease in mitochondrial ATP production rates, with no significant compensatory increase in glycolytic ATP production

rates in MM.1S-TriC compared to MM.1S-Veh (**Figure 20C**). To understand the contribution of fatty acid oxidation to MM cell respiration, ATCC MM.1S cells were subjected to the same mitochondrial stress test mentioned above with or without TriC but were treated with etomoxir, (Eto) a CPT1 inhibitor 30 minutes prior to the first reading (**Supp. Figure 6.1**). MM.1S-Eto cells had significantly reduced basal, maximal and ATP-linked respiration. MM.1S-TriC + Eto cells had significantly reduced basal and ATP-linked respiration relative to vehicle and TriC-treated cells alone. Intriguingly, MM.1S-TriC and MM.1S-TriC +Eto treated cells had significantly increased spare respiratory capacity. Taken together, these data demonstrate that TriC has profound effects on mitochondrial ATP production rates that reduce cellular respiration in MM.

To test whether TriC alters mitochondrial biogenesis, total mitochondria were quantified by flow cytometry using MitoTracker Green staining (**Figure 19D**). TriC-treated MM.1S cells exhibited a dose-dependent decrease in the relative mean fluorescence intensity (MFI) of total mitochondria in MM.1S-TriC vs. MM.1S-Veh cells after 24 hours, but not at 48 or 72 hours of treatment. MM.1S cells treated with either 1 μ M or 2 μ M TriC after 48 hours showed significant increases in gene expression of the key mitochondrial biogenesis gene *PPARGC1B* relative to vehicle-treated cells, as assessed by qRT-PCR (**Figure 19E**). These data suggest that there is a decrease in total mitochondrial number after 24 hours of treatment with triacsin C in MM.1S cells, but that this decrease was recovered over time. We next tested the mitochondrial membrane potential of MM.1S cells treated with TriC at 24-hour intervals for a total of 72 hours using tetramethylrhodamine ethyl ester (TMRE). Consistent with the proteomic enrichment of mitochondrial dysfunction, we observed a dose-dependent decrease in

the relative MFI of TMRE in MM.1S-TriC vs. MM.1S-Veh after 24 and 48 hours of treatment. These data suggest that TriC induces mitochondrial dysfunction through the loss of mitochondrial membrane potential (**Figure 19F**).

Mitochondrial dysfunction is often associated with an increase in oxidative stress. Coupled with our observation that the reactive oxygen species metabolism was an enriched biological process in the shared proteins among 1 and 2 μ M TriC-treated MM.1S cells, we predicted that TriC-treated MM cells would exhibit increased ROS. Interestingly, MM.1S cells treated with TriC showed an initial decrease in mitochondrial superoxide by MitoSOX Deep Red staining MFI after 24 hours of TriC treatment. However, treatment for 48 and 72 hours resulted in a dose-dependent increase in the mitochondrial superoxide levels (**Figure 21G**). Taken together, TriC-treated MM cells showed compromised oxygen consumption, mitochondria-derived ATP production rates, decreased mitochondrial mass and mitochondrial membrane potential, and increased production of superoxide.

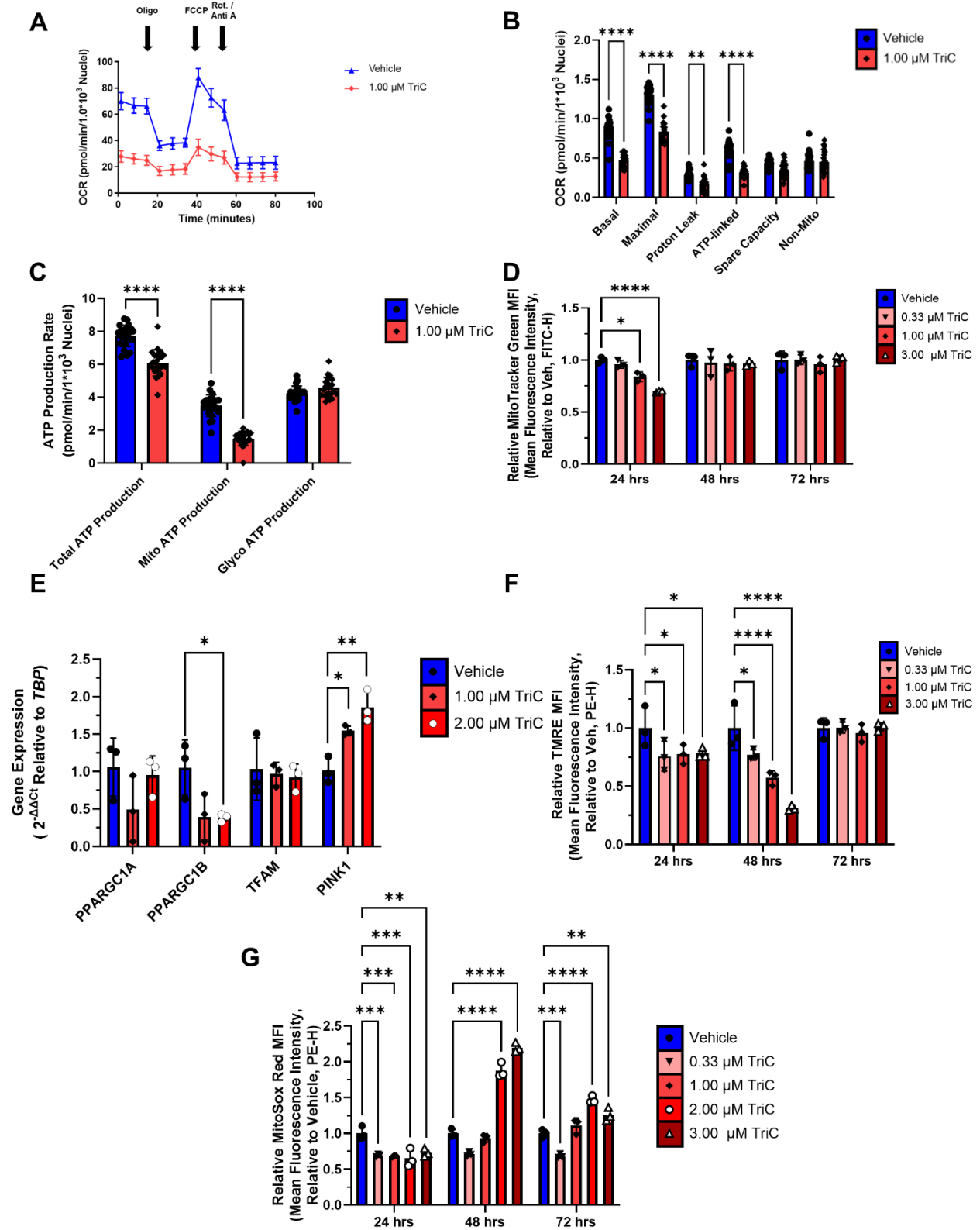


Figure 21. Triacin C Induces Mitochondrial Dysfunction in MM Cells

A-B) Cellular respiration (oxygen consumption rate, OCR) in MM.1S cells treated with 1 μM triacin C (TriC) for 24 hours and subjected to a Mitochondrial Stress test.

Values are normalized to the number of nuclei. Data are representative of 3 independent experiments. Oligo=oligomycin (Complex V inhibitor), FCCP (carbonyl cyanide p-trifluoro methoxyphenylhydrazine, proton gradient uncoupler), Rot/Anti A=Rotentone/antimycin A (Complex I and III inhibitors, respectively). C) Total, Glycolytic, and Mitochondrial ATP Production Rates in MM.1S cells treated with 1 μ M TriC. D) Number/Mitochondrial Mass assessed with MitoTracker Green in MM.1S cells treated with TriC for 24, 48 and 72 hrs; n=3. E) Expression of genes related to mitochondrial biogenesis MM.1S cells treated with vehicle, 1.00 or 2.00 μ M triacsin C for 48 hours; n=3. Statistics: Assessment of mitochondrial integrity in MM.1S cells were treated with TriC for 24, 48 and 72 hrs with TMRE staining; n=3. F) Mitochondrial superoxide quantification (MitoSox Deep Red) in MM.1S cells treated with TriC for 24, 48 and 72 hrs; n=3. Statistics: Two-way ANOVA with Tukey's multiple comparison test used throughout except for 4E, where a One-way ANOVA with Dunnett's multiple comparisons test was used. Data are mean \pm StDev *p<0.05, **p<0.01, ***p<0.001 ****p<0.0001.

3.7. Exploration of the Role of Lipid Droplets in Human Multiple Myeloma and Acute Myeloid Leukemia Cell Lines

This section will aim to provide data to investigate the following: 1) the kinetics of lipid droplets under nutrient-rich conditions *in vitro*, 2) methods of negatively and positively modulating lipid droplets, 3) how modulation of lipid droplets alters the response of HL-60 cells to TriC treatment, and 4) the contributions of the rate-limiting enzymes to lipid droplet formation (DGAT1 and 2) to the viability of MM and AML cell lines.

3.7.1. Defining and Modulating the Lipid Droplet Landscape in MM and AML Cell Lines

Triacsin C has been shown to modulate lipid droplets and we were motivated to explore the contributions of lipid droplets in TriC-induced toxicity in MM and AML cell lines. To understand the dynamics of lipid droplets as HL-60 cells grow *in vitro*, HL-60 cells were sampled at 5, 24, 48 and 72 hours in culture with nutrient-rich media, stained with the fluorescent neutral lipid dye, BODIPY 493/503 and measured by flow cytometry. We observed a significant change in BODIPY 493/503 MFI between 5 and 48 hours in culture. Interestingly, we observed a significant decrease in BODIPY signal between 48

and 72 hours. (Figure 22A-B). These data suggest that either lipid droplet number or size increases after 48 hours in culture and sharply decline thereafter in HL-60 cells.

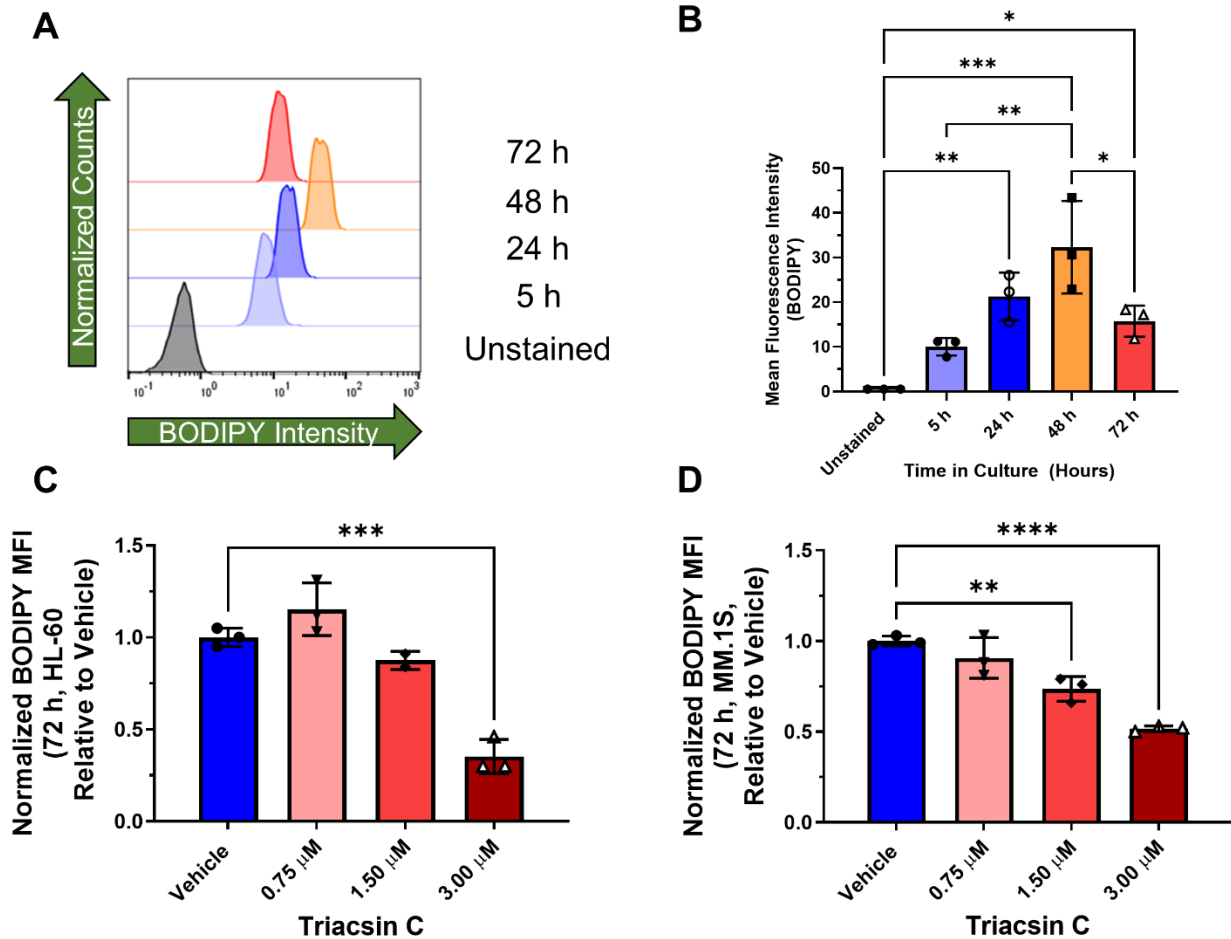


Figure 22. Total Intracellular Neutral Lipids are Dynamic in HL-60 Cells and Can be Decreased by Triacsin C Treatment

A) Representative histograms of HL-60s stained with the fluorescence neutral lipid dye BODIPY 493/503 with B) the mean fluorescence intensity of the BODIPY signal quantified using flow cytometry C&D) HL-60 or MM.1S cells, respectively, were treated with TriC for 72 hours and stained with BODIPY 493/503 to quantify total intracellular neutral lipids by flow cytometry. n=3 Statistics: A One-way ANOVA with Tukey's multiple comparison test was used. Data are mean \pm StDev *p<0.05, **p<0.01, ***p<0.001 ****p<0.0001.

To test if TriC would decrease the total amount of neutral lipids, HL-60 and ATCC MM.1S cells were treated with various doses of TriC for 72 hours, collected and stained with BODIPY 493/503. We found that 3.0 μ M TriC significantly decreased BODIPY 493/503 MFI in both HL-60 and MM.1S cells, with a significant decrease with 1.5 μ M

TriC only occurring in MM.1S cells (**Figure 22C-D**). These data demonstrate that TriC reduces lipid droplets in both HL-60 and MM.1S cell lines.

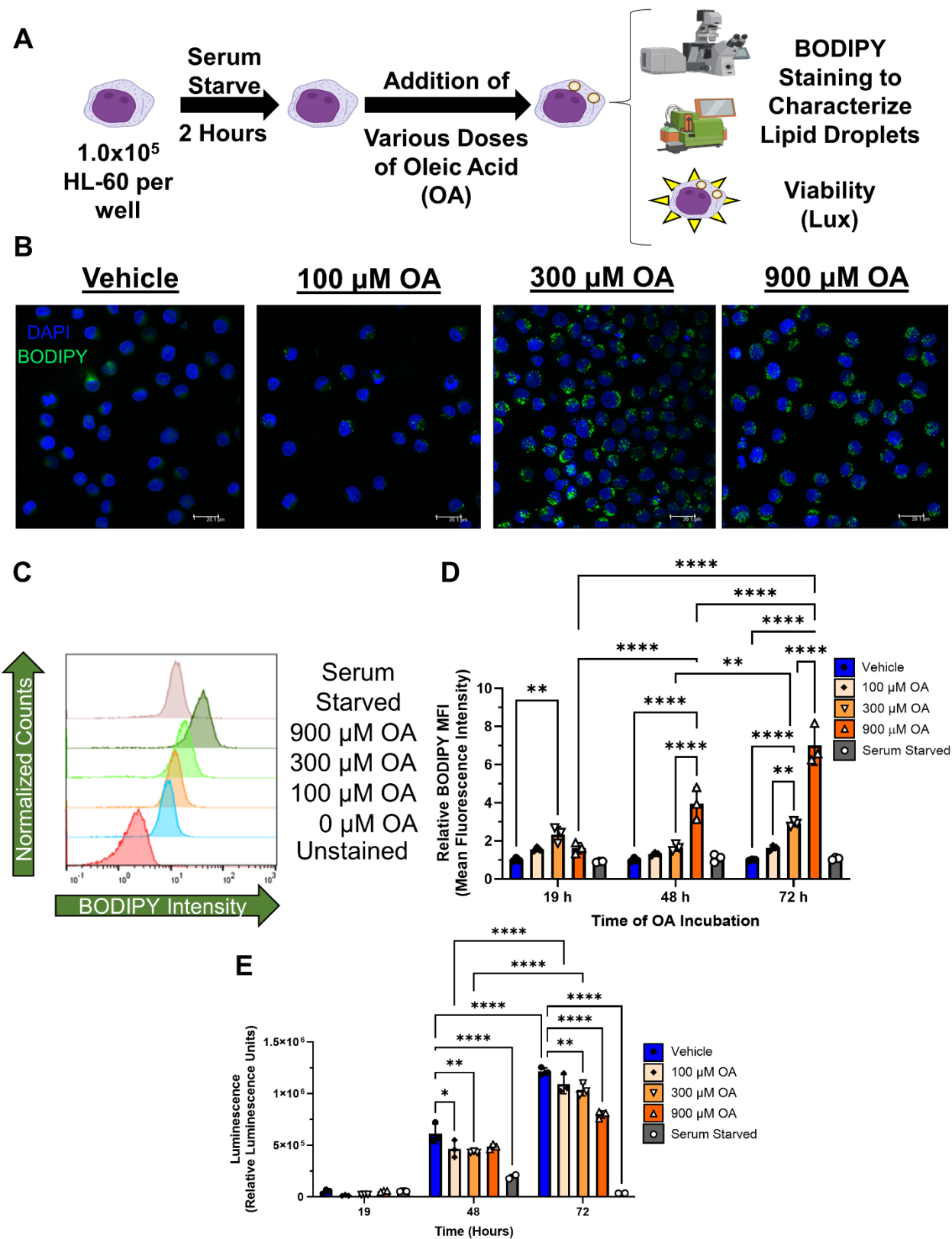


Figure 23. Exogenous Oleic Acid Increases Lipid Droplets and Decreases HL-60 Cell Viability
A) Experimental schematic of the addition of exogenous oleic acid to HL-60 cells. **B)** Representative micrographs of HL-60 cells stained with DAPI (blue, nuclei) and 2 μM

BODIPY 493/503 (green, neutral lipids) incubated with various doses of oleic acid (OA) after 19 hours and imaged using a 40x objective on a Leica DMI 6000b. Scale bar =20.1 μm . C,D) Parallel HL-60 samples were stained with 2 μM BODIPY 493/503 and MFI was measured using flow cytometry (MACSQUANT, Miltenyi) after 19, 48 and 72 hours of incubation with OA. E) Luciferin was added to parallel HL-60 samples and luminescence was read on a GLOMAX plate reader (Promega) as a proxy for cell viability after incubation of OA for 19, 48 and 72. Note, the HL-60 cells constitutively express luciferase. n=3 Statistics: A Two-way ANOVA with Tukey's multiple comparison test was used. Data are mean \pm StDev *p<0.05, **p<0.01, ***p<0.001 ****p<0.0001.

To attempt to increase the amount of lipid droplets in HL-60 cells, oleic acid (OA,18:1) was added to serum starved HL-60 cells and total lipid droplet content and cell viability was measured after 19, 48 and 72 hours of incubation *in vitro* by fluorescence microscopy, flow cytometry and using the ATP-dependent oxidation of luciferin as a proxy for cell viability (**Figure 23A**). Both qualitatively and quantitatively, we observed a dose-dependent increase in lipid droplets by fluorescence microscopy and measuring BODIPY 493/503 MFI by flow cytometry (**Figure 23B-D**). The kinetics of the flow cytometry data revealed significant time-dependent increases in BODIPY 493/503 MFI between 48 and 72 hours in both the 300 and 900 μM doses of OA. (**Figure 23C-D**). The luminescence data showed that HL-60 cells were able to proliferate with the addition of OA but there was a significant decrease in luminescence with concentrations of OA \geq 300 μM relative to vehicle-treated cells (**Figure 23E**). These data suggest that OA may exerts a negative, concentration-dependent effect on HL-60 cell number, ATP production, or proliferation. Additionally, these experiments provided a rationale to use 300 μM OA for future experiments because it significantly increased the total neutral lipids and was less detrimental to cell viability at later timepoints.

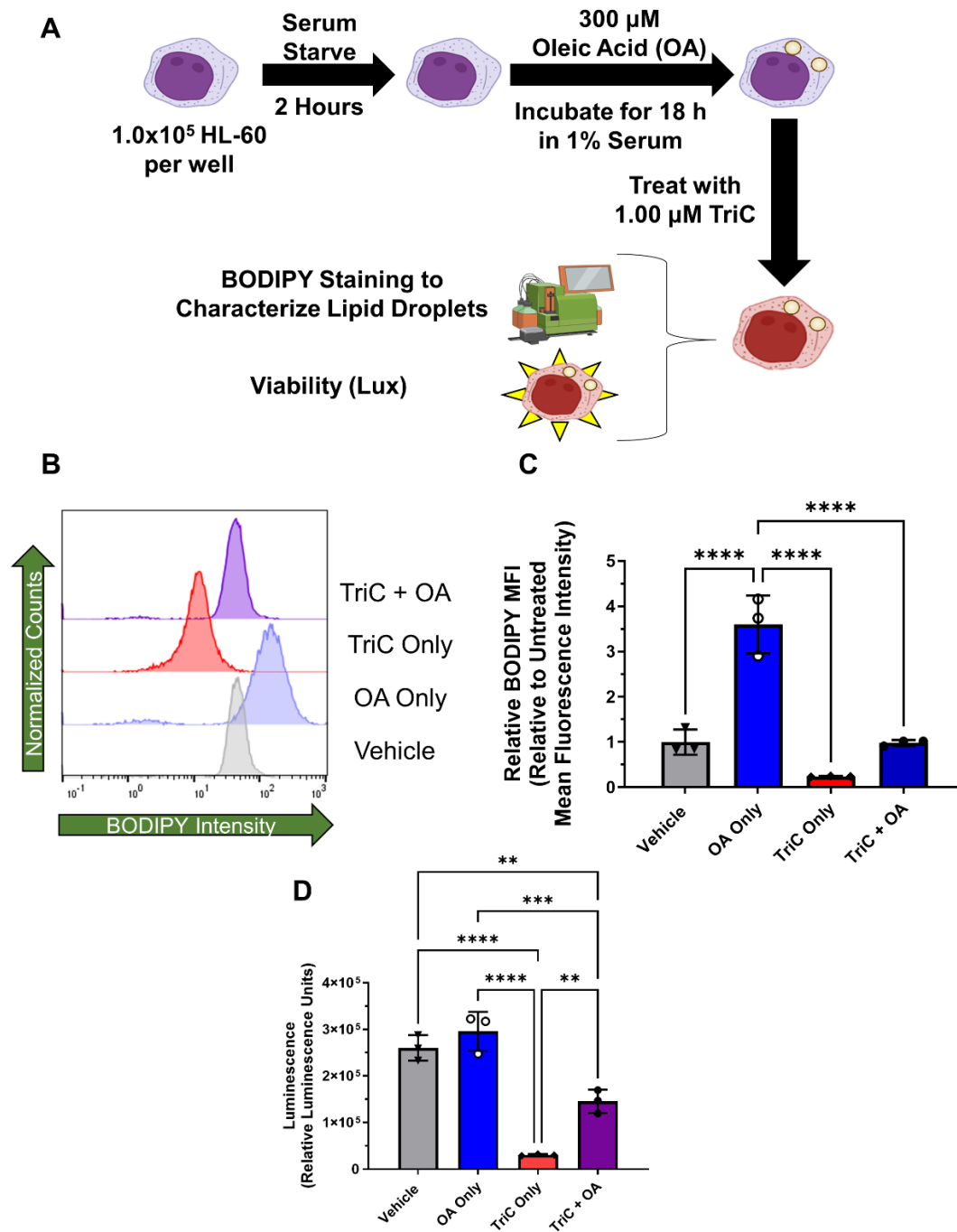


Figure 24. Exogenous Oleic Acid May Confer Minor Protection Against TriC-Induced Changes in HL-60 Cell Viability

A) Schematic of the experimental design of HL-60 cells incubated with 300 μM oleic acid (OA) then subsequently treated with 1.00 μM Triacsin C for 24 hours. **B,C)** HL-60 cells were collected after preexposure to OA and 24 hour treatment with either

vehicle or TriC and total neutral lipids were measured by staining with 2 μM BODIPY 493/503 and measuring the MFI by flow cytometry (MACSQUANT, Miltenyi) and in parallel D) luciferin was added to the HL-60 cells and luminescence was measured at the 24 hour-post TriC timepoint on a GLOMAX plate reader (Promega) as a proxy for cell viability. n=3 Statistics: A two-way ANOVA with Tukey's multiple comparison test was used. Data are mean \pm StDev * $p < 0.05$, ** $p < 0.01$, *** $p < 0.001$ **** $p < 0.0001$.

If mobilized, triacylglycerols within lipid droplets can be processed either catabolically or anabolically. Therefore, it was hypothesized that the presence of lipid droplets could rescue the effects of ACSL family inhibition by TriC by providing the substrates necessary for fatty acid metabolism. To test this hypothesis, total neutral lipids and cell viability was assessed in serum-starved HL-60 cells incubated with 300 μM OA for 18 hours and then challenged with 1.00 μM TriC for 24 hours (**Figure 24A**). Consistent with similar experiments performed in this work, OA alone significantly increased BODIPY 493/503 MFI and TriC decreased BODIPY 493/503 MFI (**Figure 24B-C**). Although there was an increasing trend of BODIPY 493/503 MFI in HL-60 cells treated with OA and TriC compared to TriC alone, there was not a significant difference between those groups (**Figure 24B-C**). Under these conditions, a decrease in luminescence as a proxy for cell viability was not observed in HL-60 cells incubated with OA alone (**Figure 24D**). Furthermore, HL-60 cells pretreated with OA then challenged with TriC had significantly increased luminescence compared to cells treated with TriC alone, but lower than that of cells treated with OA alone (**Figure 24D**). These data suggest that in the presence of TriC, lipid droplets either do not continue to form after the 18 hour incubation period or that lipid droplets are utilized upon TriC treatment- either method could contribute to the decreases in BODIPY 493/503 detected. They also suggest that exogenous OA or increased lipid droplets have the potential to protect from TriC-induced decreases in ATP or cell viability.

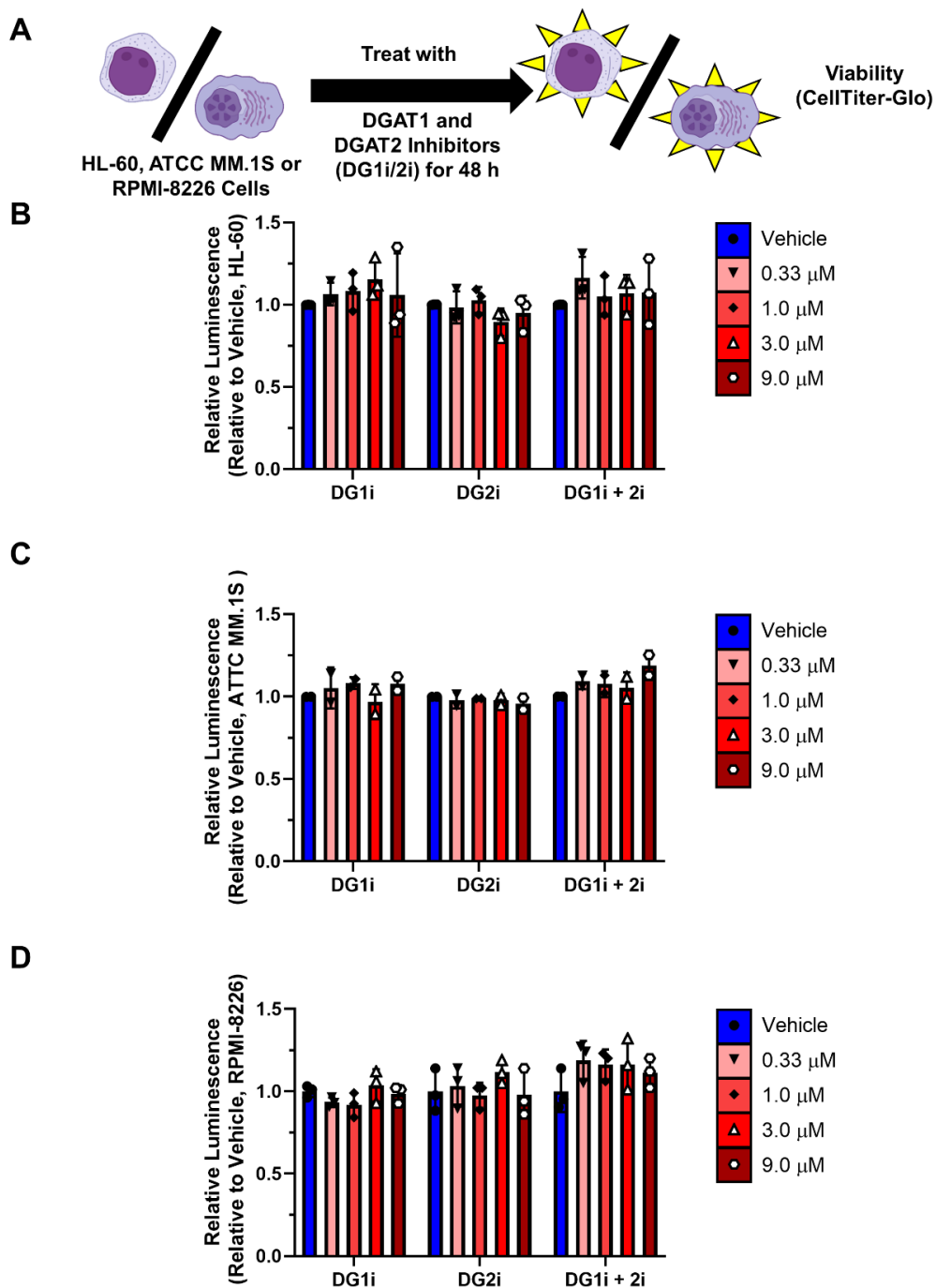


Figure 25. Pharmacological Inhibition of DGAT1/2 for 48 Hours Does Not Change HL-60, MM.1S and RPMI-8226 Cell Viability

A) Experimental schematic showing HL-60, ATCC MM.1S and RPMI-8226 cells treated with vehicle, inhibitors against DGAT1 (DG1i, A-922500, Cayman Chemical), DGAT2 (DG2i, PF-06424439, Cayman Chemical) or a combination of the two DGAT inhibitors (DG1i + 2i). B-D) CellTiter-Glo was added to HL-60 (B), ATCC MM.1S (C) and RPMI-8226 (D) cells were treated with various doses of DGAT1, DGAT2 or a combination of

the two inhibitors (concentrations of both inhibitors were equal to the value displayed (e.g. 3.0 μ M DG1i +2i = 3.0 μ M A-922500 + 3.0 μ M PF-06424439). n=3 Statistics: A two-way ANOVA with Tukey's multiple comparison test was used. Data are mean \pm StDev

To test the hypothesis that lipid droplet formation supports the viability of hematological malignancies, we used pharmacological inhibitors against the rate-limiting enzymes) for lipid droplet formation (diacylglycerol acyltransferases, DGATs) in an attempt to specifically deplete lipid droplets in HL-60, ATCC MM.1S and RPMI-8226 cells (**Figure 25A**). No significant changes in ATP/viability (as measured by CellTiter-Glo) were detected in HL-60, ATCC MM.1S and RPMI-1640 cells treated with inhibitors against DGAT1 (DG1i), DGAT2 (DG2i) or a combination of the two DGAT inhibitors (DG1i + 2i) for 48 hours (**Figure 25B-D**). These data suggest that lipid droplets may not support viability of HL-60, MM.1S or RPMI-8226 cells under basal media conditions *in vitro*.

3.7.2. Efforts to Knockdown ACSL3 and DGAT1 Expression Levels by RNA Interference

To characterize the individual contributions of the ACSL family with respect to the toxicity we observed in both human MM and AML cell line(s) treated with TriC, HL-60 cells were treated with double-stranded RNA duplexes targeting human *ACSL3* or a non-targeting control. Streptolysin O was used to permeabilize the plasma membrane to allow the RNA duplexes to enter the cells and proceed to be processed by the RNA-induced silencing complex (RISC) to eventually bind to target mRNAs and degrade them³⁰⁸. *ACSL3* was chosen as an initial target for preliminary knockdown as it was predicted to be an essential ACSL isozyme in MM cells through our initial DepMap screen (**Figure 15A**) and it is more highly expressed than *ACSL4*. We did not observe

any knockdown of *ACSL3* or any upregulation in *ACSL1* or *ACSL4* upon transfection of RNA duplexes against *ACSL3* (**Figure 26A**).

Transfection of si*DGAT1* by lipid nanoparticles showed a 75% knockdown of *DGAT1* after 24 hours (**Figure 24B**). The magnitude of knockdown was transient, as there was a significant 25% reduction in *DGAT1* levels and no significant decrease after 72 hours (**Figure 26B**). Although preliminary, these data show promise that *DGAT1* levels can be effectively knocked down by siRNAs, albeit only within the first 24 hours.

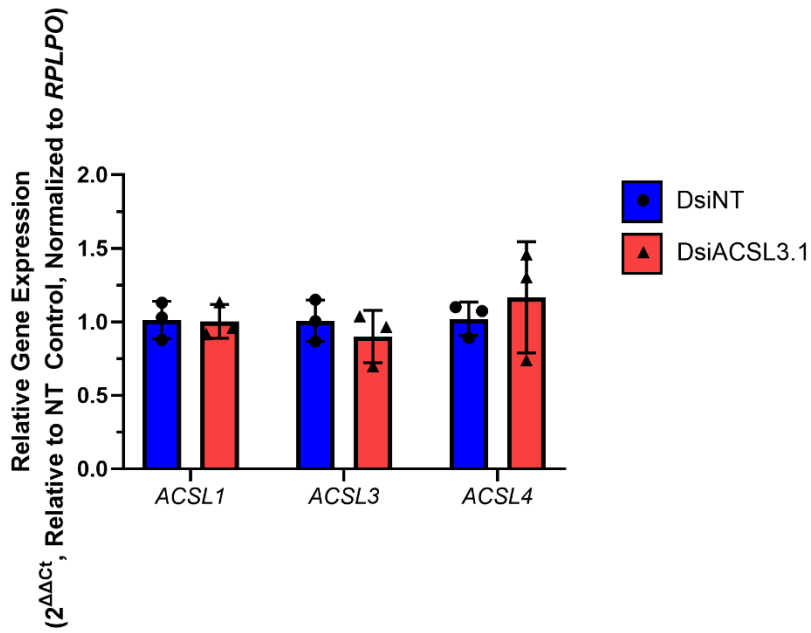
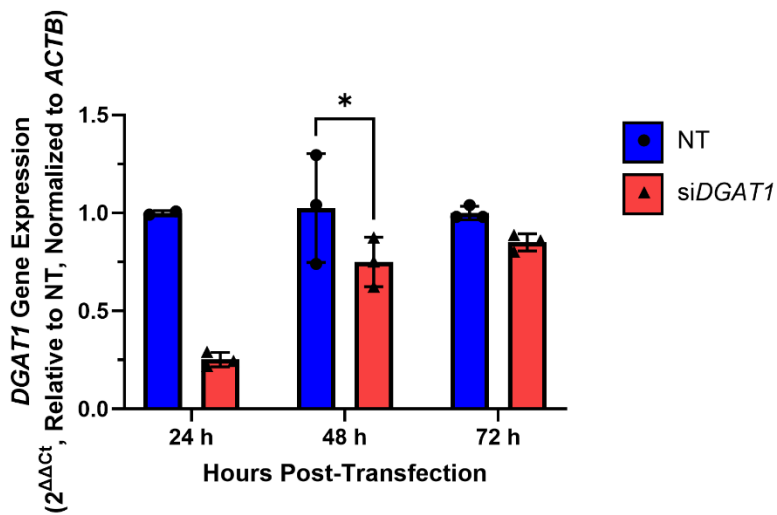
A**B**

Figure 26. Delivery of siRNAs Targeting ACSL3 and DGAT1 in HL-60 Cells

A) HL-60 cells were transfected with an RNA duplex directed against *ACSL3* or a non-targeting (NT) sequence mediated by transient pore-formation by streptolysin O and the gene expression of *ACSL1, 3 and 4* was assessed by qRT-PCR and normalized to *RPLPO*. Values are relative to NT controls. n=3 **B)** *DGAT1* gene expression from qRT-PCR of HL-60 cells were transfected with either a non-targeting siRNA or siRNAs against *DGAT1* using a lipid nanoparticle-based approach with Lipofectamine

RNAiMax (ThermoFisher) for 24, 48 and 72 h. n=2-3 Statistics: A two-way ANOVA with Tukey's multiple comparison test was used. Data are mean \pm StDev.

3.8. Characterizing Bone Marrow Adipocyte-Dependent Modulation of Fatty Acid Metabolism in HL-60 and MM.1S Cells

3.8.1. Development of Fatty Acid Transfer Assay Between Bone Marrow Adipocytes and HL-60 Cells

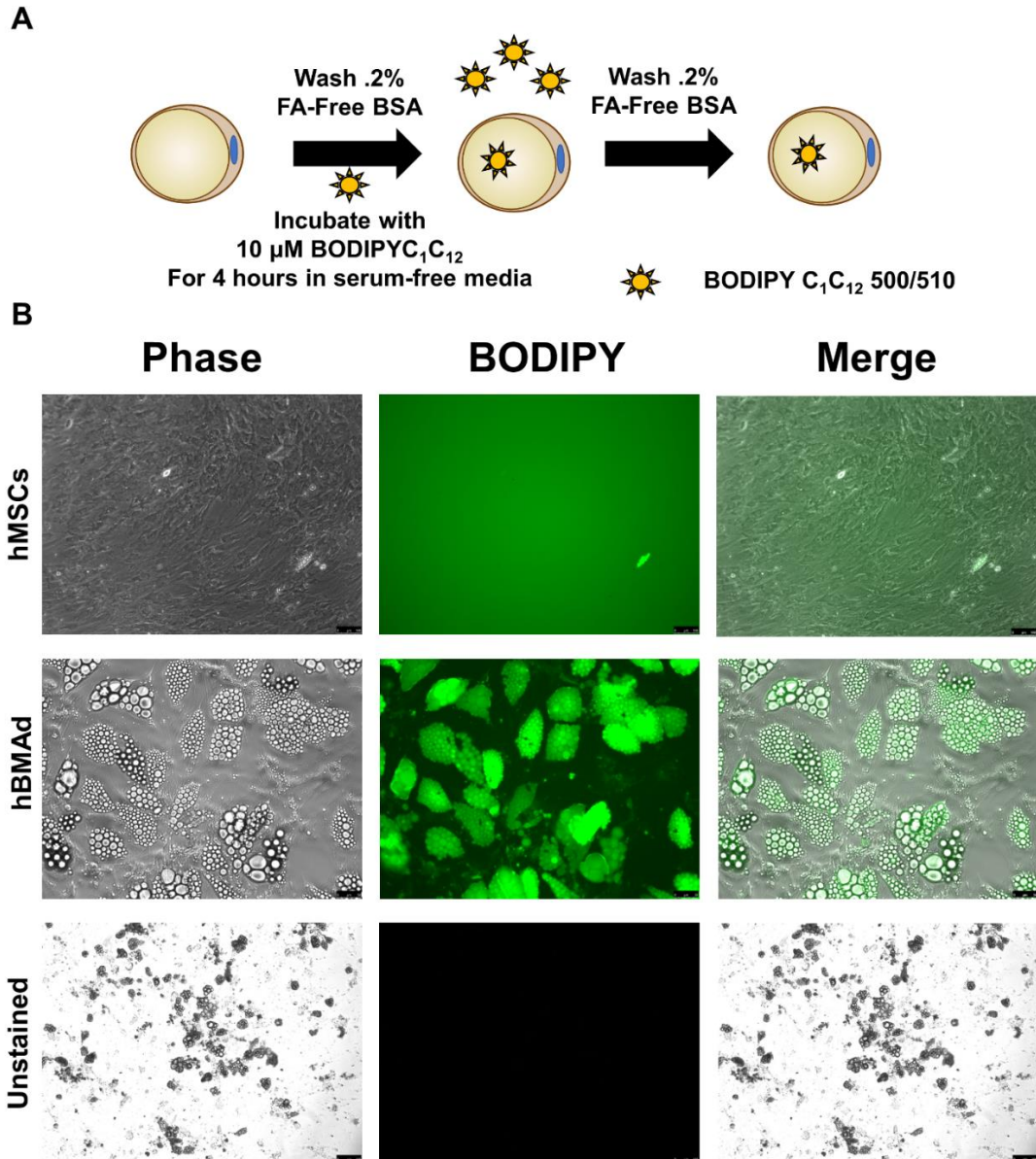


Figure 27. Human Bone Marrow Adipocytes Take Up a 12-Carbon Fluorescent Fatty Acid
 A) Experimental schematic where human bone marrow adipocytes (hBMAd) or human mesenchymal stem cells (hMSCs) were first washed with fatty acid-free bovine serum albumin (FA-free BSA) then incubated with 10 μ M BODIPY C₁ C₁₂ for four hours, washed again in FA-free BSA and imaged. B) Representative of

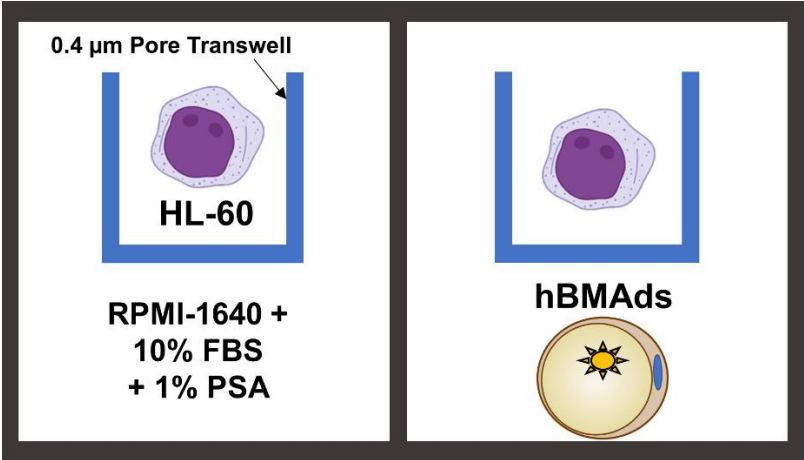
micrographs of hMSCs, hBMAds or unstained hBMAds in phase, in the green channel (525 nm/50 nm) and a merge of phase and the green channel on a Leica DMI 6000b. The scale bars for the hMSCs and the unstained conditions are 100 μ m while the hBMAds are 50 μ m. n=1 donor (R18-0075)

Having established that modulation of fatty acid metabolism via TriC treatment has a negative effect on malignant hematological cells, we next investigated the relationship between MM cells and one of the key sources of FAs in the bone marrow microenvironment: the bone marrow adipocyte (BMAAd). Studies have shown that BMAds are in close contact with MM cells and support MM proliferation, survival and drug resistance^{231,309,310}. Experiments running concurrently with those described in this thesis, the results which have since been published²²⁹, suggest that MM causes BMAAd to shrink through an unknown mechanism. Therefore, we hypothesized that hematological cancer cells were inducing lipolysis in BMAAd and those previously stored fatty acids were transferred to malignant cells. To test this, we developed a fluorescent-based fatty acid transfer assay where a 12-carbon fatty acid with a BODIPY tag (BODIPY C₁ C₁₂) was incubated in hBMAds or hMSCs (**Figure 27A**). As expected, we observed a qualitative increase in fluorescent fatty acid uptake by hBMAAd compared to hMSCs (**Figure 27B**). These data demonstrate that BODIPY C₁ C₁₂ is readily transported into hBMAds in a four-hour time frame.

To test if fluorescent fatty acids in BMAAd could transfer to HL-60 cells, HL-60s were cultured in transwell membranes alone or co-cultured with BMAds labeled with BODIPY C₁ C₁₂ for 6 days (**Figure 3.21A**). We observed that 30% of the HL-60 cells had fluorescent BODIPY C₁ C₁₂ label after 6 days in transwell co-culture as opposed to no observable label in the HL-60 cells alone (**Figure 28B-D**) These data demonstrate that

fluorescent fatty acids are able to transfer from hBMADs to HL-60 cells in a contact-independent manner.

A



 BODIPY C₁₂ 500/510

HL-60 Alone

HL-60 + hBMADs

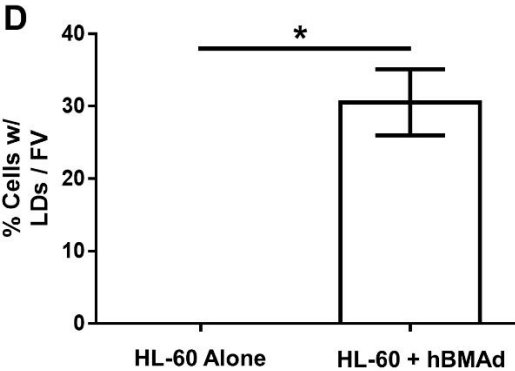
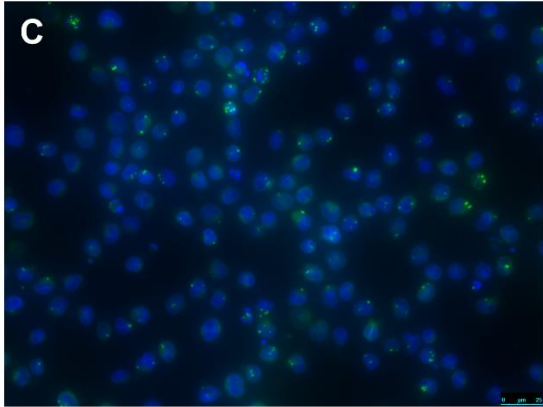
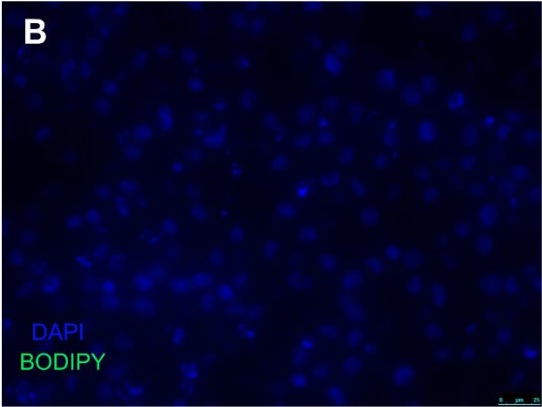


Figure 28. Fluorescent Fatty Acids Transfer from Human Bone Marrow Adipocytes to HL-60 Cells in a Contact-Independent Manner

Experimental schematic of 7-day transwell cultures of HL-60 cells alone or co-cultured with BMAds incubated with 10 μ M BODIPY C₁ C₁₂. B,C) Representative micrographs of merges of the blue (450 nm/ 40 nm, DAPI, nuclei) and green (525 nm/50 nm, BODIPY C₁ C₁₂) channels imaged on a Leica DMI 6000b with a 40x objective. Scale bars are 25 μ m. N= 1 donor (R18-0075) D) Quantification of percentage of cells with lipid droplets per field of view (FV). Statistics: Student's t-test *p<0.05.

3.8.2. Characterization of hBMAd and hMSC-dependent Changes in Lipid Droplets in HL-60 Cells

Since we previously observed that HL-60 and MM.1S cells have a basal amount of lipid droplets in culture (**Figure 20**), we aimed to test whether hBMAds and hMSCs altered the amount of lipid droplets in HL-60 cells in a contact-independent manner. To test this hypothesis, HL-60 cells were cultured alone or in transwells with hBMAds or hMSCs for 7 days and stained with BODIPY 493/503 to measure lipid droplets (**Figure 29A**). Interestingly, relative to HL-60 cells alone, HL-60 cells co-cultured with either BMAds or hMSCs had a significantly decreased percentage of HL-60 cells with lipid droplets (**Figure 29B-E**). Given that we observed changes in the number of lipid droplets in HL-60 cells co-cultured with hBMAds and hMSCs, we quantified the gene expression of the rate-limiting enzymes to lipid droplet formation, *DGAT1* and *DGAT2* after 3 and 7 days of transwell co-culture. We detected a trending increase in *DGAT1* at both timepoints and a trending increase in *DGAT2* levels after 3 days of co-culture and a trending decrease after 7 days (**Figure 30A-D**), although these results did not reach significance. Lipid droplets have been shown to negatively regulate ER stress³¹¹⁻³¹³, therefore we measured levels of *ATF4*, a major transcriptional regulator of cellular stress and normal ER function, and one gene it regulates, *DDIT3*, which is associated with terminal ER stress (**Figure 30E-F**). We found that HL-60 cells co-cultured with hBMAds for 7 days had significantly decreased *ATF4* expression, with a trending decrease in

DDIT3 (Figure 30E-F). We did not see any significant changes in *ATF4* or *DDIT3* expression levels in HL-60 cells co-cultured with hMSCs after 7 days (Figure 28D-E).

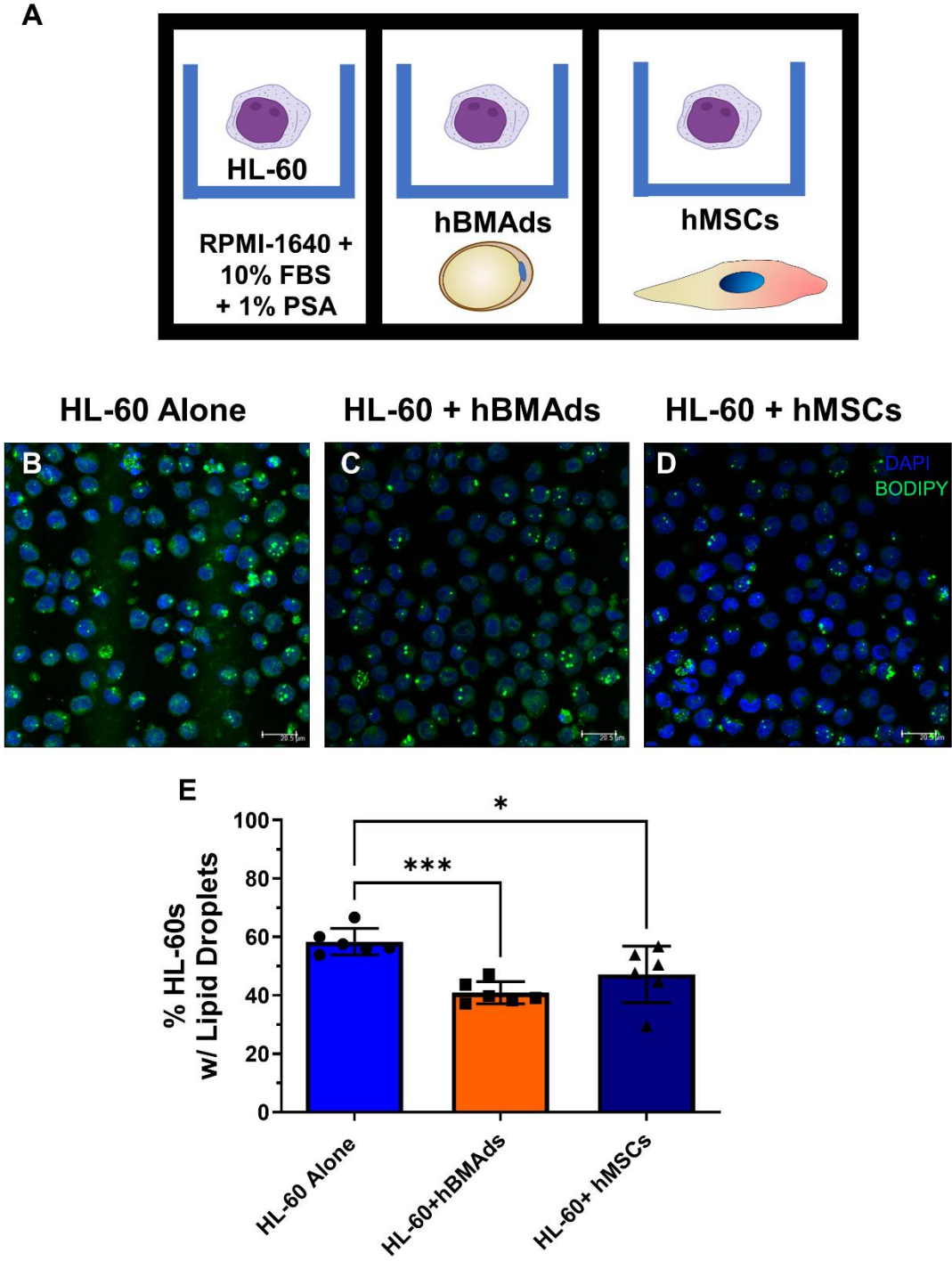
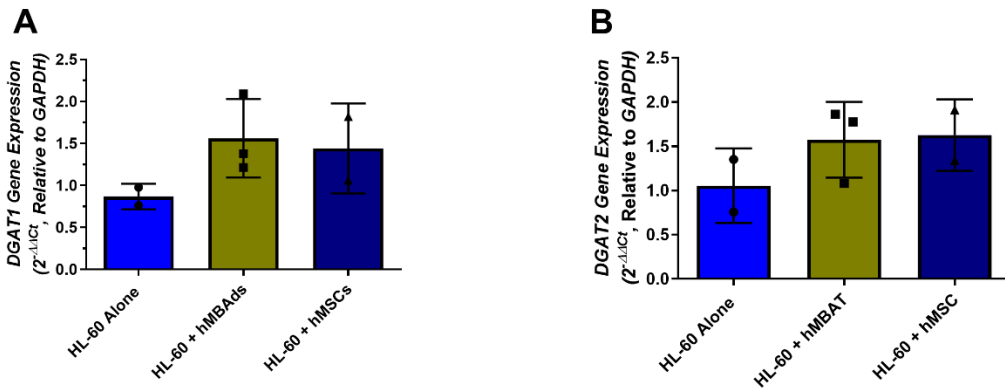


Figure 29. The Percentage of HL-60 Cells with Lipid Droplets Decreases in Co-Culture with either hBMAds or hMSCs

A) Experimental schematic of 7-day transwell cultures of HL-60 cells alone or co-cultured with BMAds or hMSCs. B-D) Representative micrographs of merges of the blue (450 nm/ 40 nm, DAPI, nuclei) and green (525 nm/50 nm, BODIPY 493/503 channels imaged on a Leica DMI 6000b with a 40x objective. Scale bars are 20.5 μ m. n=1 donors D) Quantification of percentage of cells with lipid droplets, individual values depicted are technical replicates of 2 different human donors. Statistics: A one-way ANOVA with Tukey's multiple comparison test was used. Data are mean \pm StDev *p<0.05, **p<0.01, *p<0.001 ****p<0.0001.**

3 Days of Transwell Co-Culture



7 Days of Transwell Co-Culture

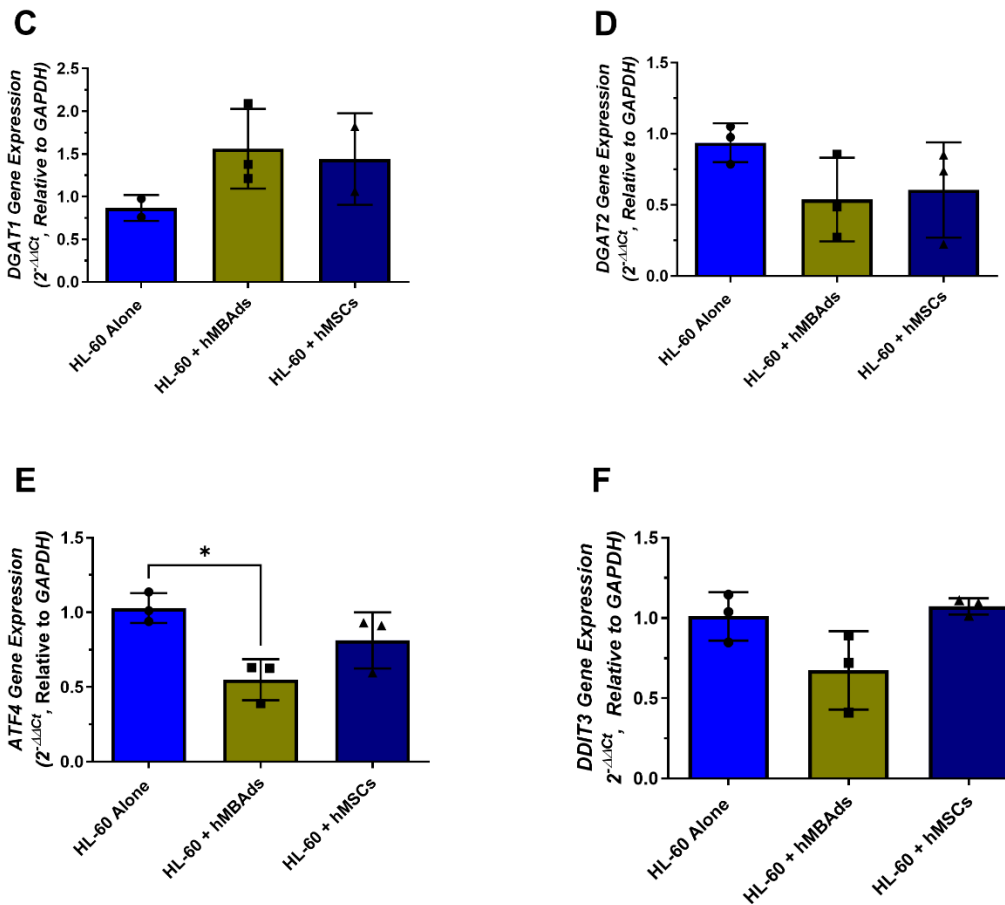
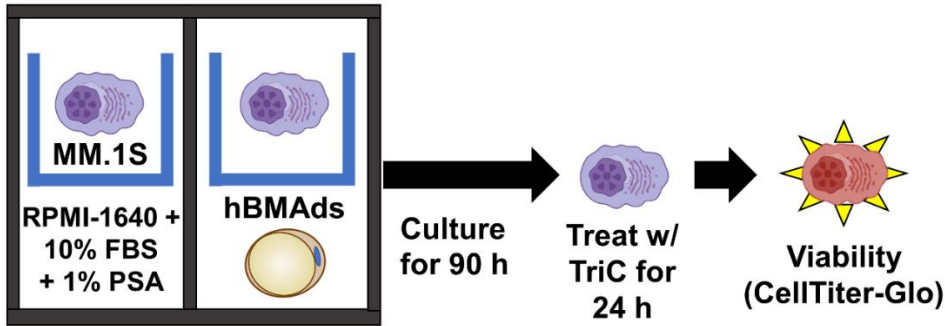


Figure 30. hMBAd and hMSCs Do Not Alter HL-60 Cell Gene Expression of DGAT1 or DGAT2
A) *DGAT1* and **B)** *DGAT2* gene expression (qRT-PCR, normalized to *GAPDH*) of HL-60 cells alone, co-cultured in transwells with either hMBAdIs or hMSCs for 3 days. n=1 donor (R18-0075). **C)** *DGAT1*, **D)** *DGAT2*, **E)** *ATF4*, and **F)** *DDIT3* gene expression (qRT-PCR, normalized to *GAPDH*) of HL-60 cells alone, co-cultured in transwells with either hMBAdIs or hMSCs for 7 days. n=1 donor (R18-0075). Statistics: One-way

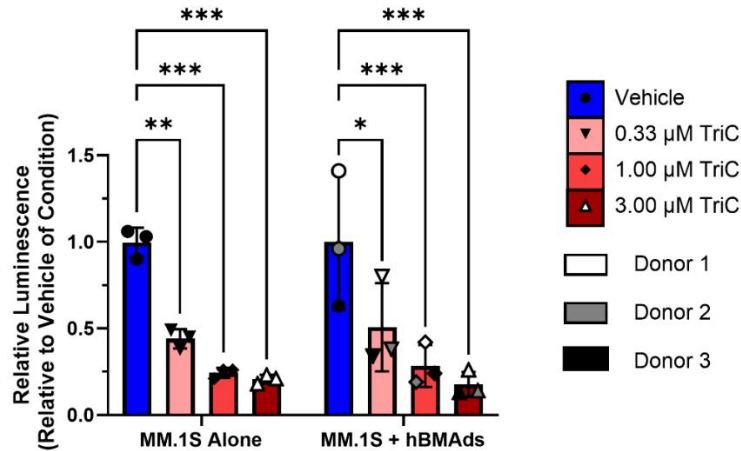
ANOVA with Tukey's multiple comparison test was used. Data are mean \pm StDev
 $*p < 0.05$, $**p < 0.01$, $***p < 0.001$, $****p < 0.0001$.

3.8.3. MM.1S Cells Pre-exposed to BMAds in Transwells Are Sensitive to Triacsin C Treatment

A



B



C

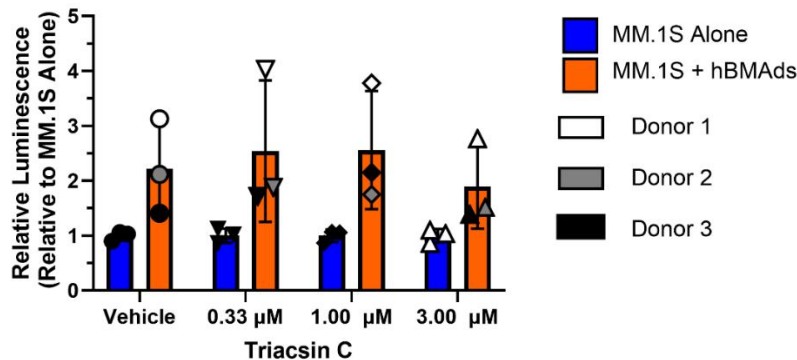


Figure 31. MM.1S Cells Pre-exposed to hBMAds Are Sensitive to TriC Treatment
 A) Experimental schematic of measuring the viability (by Cell-Titer-Glo) in HL-60 cells cultured alone or co-cultured with BMAds for 90 hours then challenged with various doses of TriC for 24 hours. B) Relative luminescence values to each

respective condition's vehicle. n=3 donors (R16-0403, R17-0040, R19-2370). and C) Relative luminescence values to match doses in the MM.1S alone condition. n=3 donors. Statistics: Two-way ANOVA with Tukey's multiple comparison test was used. Data are mean \pm StDev *p<0.05, **p<0.01, ***p<0.001 ****p<0.0001.

Having observed an ability for malignant hematological cells to uptake lipids from BMAds, and a negative impact of inhibition of fatty acid metabolism via TriC treatment, we next asked whether BMAds alter the response of ATCC MM.1S cells to TriC. ATCC MM.1S cells were cultured alone or co-cultured with BMAds in transwell membranes for 90 hours (3.75 days), then challenged with various doses of TriC for 24 hours at which point MM.1S viability was assessed by CellTiter-Glo (**Figure 31A**). We observed a significant dose-dependent decrease in luminescence in TriC treated cells in both MM.1S cells grown alone and pre-exposed to BMAds in transwells relative to each condition's respective vehicle (**Figure 31B**). Upon comparing doses across conditions (MM.1S alone versus pre-exposure to BMAds) we observed an increasing trend in luminescence in MM.1S cells pre-exposed to BMAds (**Figure 31C**). These data suggest that paracrine signaling between BMAds and MM.1S cells for 90 hours increases MM cell number (consistent with prior reports) but does not confer any protection against TriC.

4. CHAPTER 4: DISCUSSION

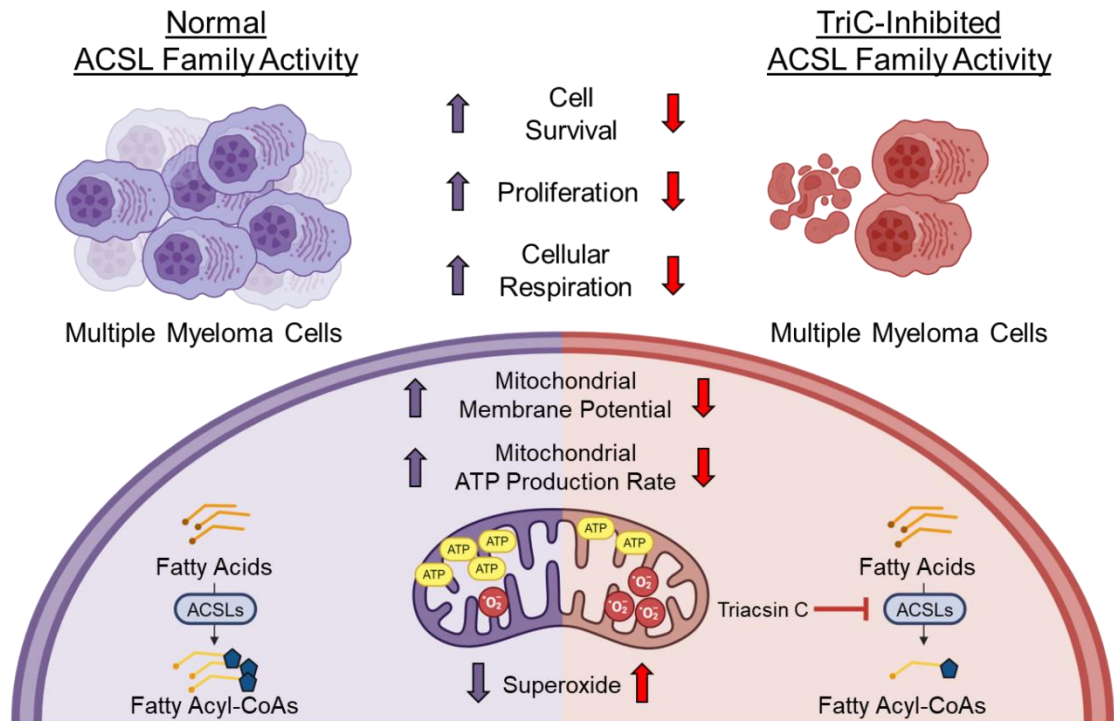


Figure 32. Summary of Phenotypes of Triacsin C Treatment
Triacsin C inhibition of the acyl-CoA synthetase long chain (ACSL) family decreases multiple myeloma cell survival, proliferation and reduces mitochondrial respiration and membrane potential.

4.1. Major Findings of Triacsin C Phenotypes in MM and AML Cell Lines

There has been accumulating evidence for the potential for targeting the long-chain fatty acyl-CoA synthetase family in cancer²⁵⁸, however, studies in MM have been limited to ACSL4²⁷⁰. In this study, we found within the Cancer Dependency Map's genome-wide CRISPR/Cas9 screen, that the majority of long-chain acyl-CoA synthetase family members are supportive of human MM cell fitness. Congruent with the hypothesis that the ACSL family is supportive of MM cell proliferation and survival, we showed that pharmacological inhibition of the ACSL family with TriC in human MM cell lines decreased MM cell viability, proliferation, and induced apoptosis starting after 48 hours of treatment. These results are consistent with reports of TriC treatment decreasing viability in human breast cancer³¹⁴, Burkitt's lymphoma³¹⁵ and endometrial³¹⁶

cell lines and initiating apoptosis in human TP53-mutant lung, colon and brain cancer cell lines³¹⁷. Interestingly, while most of the MM cell lines tested were TP53 mutants, MM.1S (TP53^{WT}) cells were sensitive to TriC treatment, suggesting that either TriC toxicity in MM cells is independent of TP53 status or the toxicity occurs via multiple mechanisms (**Figure 32**).

We initially found that human myeloma cells exhibit basal expression of *ACSL1*, *ACSL3*, *ACSL4*, and *ACSL5*, with minimal expression of *ACSL6*, suggesting that broad targeting by pharmaceutical methods could be successful. Future studies with TriC in MM could test the EC₅₀ in non-malignant plasma cells to provide evidence that toxicity of targeting the ACSL family is specific to MM cells (see Chapter 5 for more details). In our studies, we found that the human MM cells tested were similarly sensitive to TriC, with EC₅₀ values ranging from 1.44 μ M (MM.1R) to 8.56 μ M (U266B1). Importantly, cells treated with 1 μ M TriC exhibited significantly higher levels of apoptosis and a shift from active cell cycle phases into sub-G1 compared to vehicle-treated cells, suggesting that inhibition of the ACSLs in myeloma may be a plausible therapeutic target.

4.2. Possible Explanations of Why U226B1 Cell Viability is Unchanged after 48 h of TriC Treatment

Given the higher EC₅₀ in U266B1 cells treated with TriC, it is possible that there could be a molecular sub-type of MM cells that are intrinsically resistant to the effects of ACSL family inhibition. Compared to the other cell lines used in this study, U226B1 cells have the highest gene expression of *ACSL1*, *ACSL3* and *ACSL4* and it is possible that the doses that were tested were not sufficient to inhibit ACSL activity. Although U266B1 cells did not have a defect in viability after 48 hours of TriC treatment like the other cell lines tested, U266B1 cells treated with TriC after 48 hours had a significant decrease in

Ki-67 (+) cells at 0.33 μ M TriC. Additional experiments for the higher doses of TriC must be done to determine statistical significance. This suggests that U266B1 respond similarly to TriC when compared to the other cell lines used in this study. Furthermore, U266B1 cells have a longer average doubling time (an average of the doubling times in the literature and the from the biorepositories ATCC and DSMZ) of 90.5 hours compared to an average doubling time of the other MM cell lines of 61.8 hours. Therefore, the metabolic demands for either catabolic or anabolic fatty acid metabolism may be staggered relative to the faster proliferating cell lines that were tested. These observations warrant further investigation of how TriC affects U266B1 viability after 72 h. U266B1 cells are cultured in 15% FBS and therefore the increased activation of key survival pathways could help ameliorate the effects of TriC. Also, the increased amount of BSA could bind the lipophilic TriC, lowering the effective concentration of TriC. However, there is no direct evidence that TriC binds to BSA. Measuring the viability of MM cell lines treated with TriC in different concentrations of FBS could help address this unanswered question.

Table 9. Double Times of Cell Lines Used in this Work

Cell Line	Doubling Time (h) in Literature	Doubling Time (h) from ATCC/DSMZ	Average Doubling Time (h)
------------------	--	---	----------------------------------

U266B1 ³¹⁸	126*	55	90.5
MM.1S ³¹⁹	80	72	76
OPM-2 ^{284,319}	36, 50	55	47
RPMI-8226 ³¹⁹	60	65	62.5
HL-60 ^{319,320}	16, 28	40	28

*This was an average of the reported range in the literature of 108-144 hours

4.3. The Mutational Landscape of U266B1 Cells Does Not Provide a Clear Explanation of the Lack of a Viability Response to TriC

A mutation in the DNA mismatch repair protein, mutS homolog 6 (MSH6, p.Gly141Asp), is the only mutated gene that is unique to U266B1 cells compared to the cell lines tested. The mutation is in the proline-tryptophan-tryptophan-proline (**PWWP**) domain, a domain that binds to histone 3 on trimethylated Lys-36 (**H3K36me3**) to direct MSH6 to chromatin³²¹. The functional implications of this mutation are unclear but based on the amino acid changes, it is possible that these residues are phosphorylated and subject to changes in function.

We also observed a compensatory increase in *ACSL1* and *ACSL3* gene expression (and *ACSL3* protein expression by mass spectrometry) in response to TriC. Therefore, the inhibition of ACSL activity by TriC is decreased by the increase *ACSL1* and *ACSL3* expression. The upregulation of *ACSL1* and *ACSL3* in response to TriC

suggests that they are functionally important, which is corroborated by the DepMap data that identified them as MM-supportive. To exclude the possibility of TriC-dependent off-target effects and address concerns of compensation from ACSL isozymes after TriC treatment, we propose that future studies use genetic approaches to knockdown or knockout all ACSL isozymes, as well as each ACSL isozyme individually in MM cells; see Chapter 5 for more details. It should be noted that the proteomics only detected ACSL3 and ACSL4. Given that the ACSL family are transmembrane proteins, it is possible that the other ACSL family members are more resistant to the solubilization techniques used to isolate total protein. While all the ACSLs are localized on the mitochondria and therefore rule out membrane composition influencing solubilization, the abundance of the ACSLs on different organelles in MM cells is unknown. Additionally, the individual ACSLs may physically interact with unique proteins that could affect their solubilization and sites available for proteolytic cleavage.

To start to understand why MM cells upregulate *ACSL1* and *ACSL3*, it is important to understand how they are regulated. Both *ACSL1* and *ACSL3* gene expression are regulated by the PPAR family, with *ACSL1* being regulated by both PPARA and PPARG and *ACSL3* regulated by PPARD and PPARG^{258,322–324}. *ACSL1* is also regulated by sterol regulatory element binding protein (**SREBP**), NFκB, protein kinase C (PKC), hepatitis B interaction protein (**HBXIP**) and bromodomain-containing protein (**BRD4**)²⁵⁸. *ACSL3* has been shown to be regulated by carbohydrate-response-element-binding protein (**CREBP**)-1C, octamer transcription factor 1, and liver x receptors (LxR also known as nuclear receptor subfamily 1 group H member 2, NR1H) and fibroblast growth factor 19 (**FGF19**)^{258,325,326}. In MM.1S cells treated with 1.0 μM

TriC, we observed significant increases in gene expression of *ABCG1*, *ACACA*, *FASN* and *SCD1* that were found under the GO enrichment of pathways such as “Activation of Gene Expression by SREBF”, “NR1H2 And NR1H3-mediated Signaling” and “Metabolism of Lipids”. Taken together, these data suggest that there is activation of the PPAR family, SREBP and CREBP-related signaling with TriC treatment. Interestingly, *FASN*, *SCD1* and *ACACA* are activated by ATF4 and X-box binding protein 1 spliced (XBP1s)³²⁷. EIF2AK3/EIFS1 signaling activates SREBP transcription, while another arm of the unfolded protein response, ERN1, activates both CEBPB, CEPBD and PPARG³²⁷. The ISR-induced, DDIT3, also induces the expression of CEBPA and CEBPB³²⁷. It has also been shown in hepatocytes that induction of ER stress by tunicamycin specifically induced the expression of ACSL3³²⁸. Taken together, these data suggest that the upregulation of fatty acid metabolism genes, including *ACSL1* and *ACSL3*, in TriC-treated cells could be induced by ER stress / the ISR.

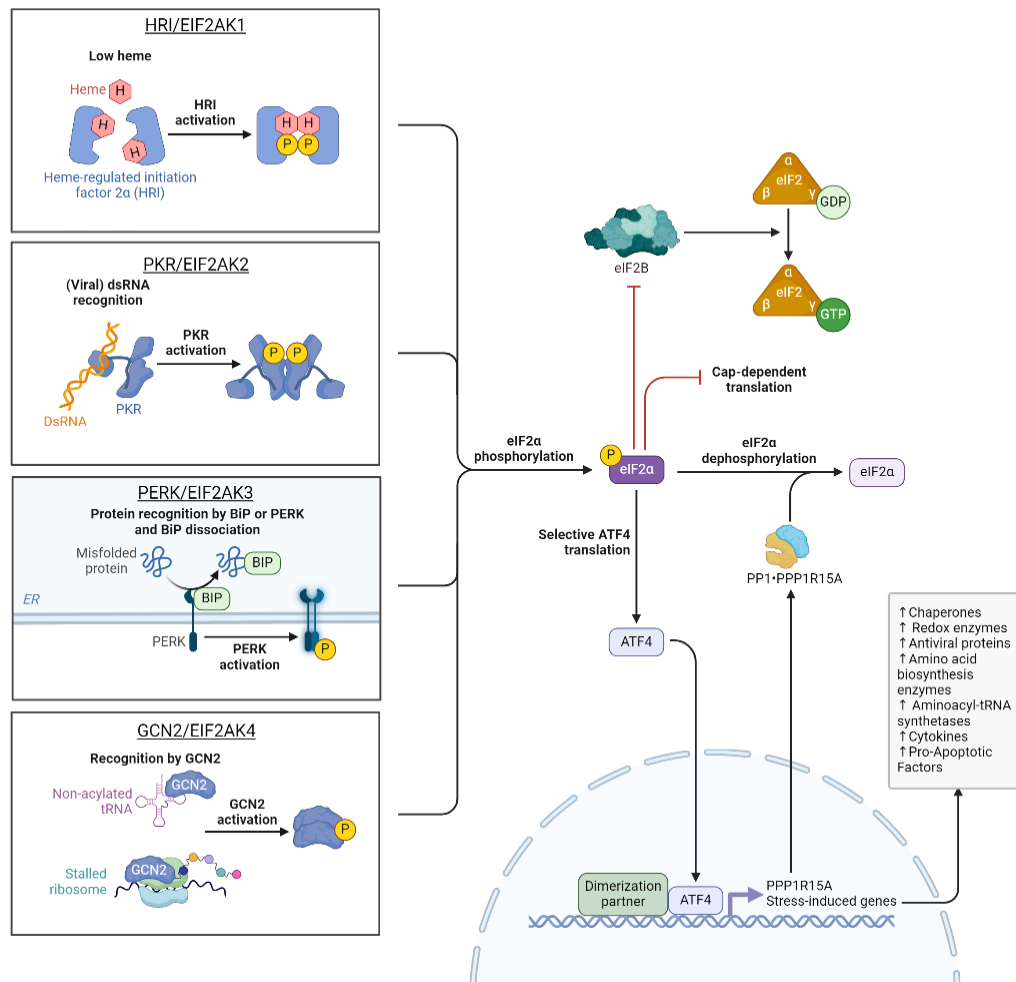


Figure 33. The Integrated Stress Response Signaling

The integrated stress response (ISR) is adaptive cellular mechanism to respond to endoplasmic reticulum (ER), stress, nutrient deprivation, oxidative stress and hypoxia and mitochondrial stress^{329–331}. The ISR is activated by the phosphorylation of eukaryotic translation initiation factor 2 subunit alpha (EIF2S1 or eIF2α) at serine 51 and suppresses global translation and cell survival and upon chronic or severe activation initiates apoptosis^{332,333}. Phosphorylation status of EIF2S1 is dependent on four kinases that respond to distinct stressors: 1) eukaryotic translation initiation factor 2 alpha kinase 1, also known as Heme Regulated Initiation Factor 2α (EIF2AK1 or HRI) is activated by low cytoplasmic levels of heme, 2) EIF2AK2, also known as Protein Kinase R (PKR) is activated by double stranded RNA (usually associated with viruses) 3) EIF2AK3, also known as Protein Kinase RNA-Like ER Kinase (PERK) binds to misfolded proteins in its dimerized form and 4) EIF2AK4 also known as General Control Nonderepressible 2 (GCN2) is activated by non-acylated tRNAs^{329,332}. Although phosphorylated EIF2S1 inhibits global translation, a key transcription factor, Activating Transcription Factor 4 (ATF4) is regulates a cohort of genes that are ultimately selectively translated in response to the stressor³²⁹. The integrated stress response is a compelling target in cancers, including MM^{88,332,334}.

A variety of different mechanisms of action have been shown or suggested for TriC's effects in other cells, including reducing key survival pathways (p38/MAPK³³⁵, NFκB³³⁵), PPARγ³³⁶ and increasing Bax-induced caspase activation²⁷⁵. In MM.1S cells treated with 1 μM TriC, we observed a dose-dependent increase in BAX intracellular protein levels at 48 hours, with sustained levels at 72 hours of treatment. After 24 hours of TriC treatment, MM.1S cells had a robust transcriptional and metabolic response consistent with the decreased viability, proliferation and apoptosis observed at later timepoints. Indeed, many pro-apoptotic genes downstream of the ATF4-eIF2S1 pathway³³⁷ such as *DDIT3* and *TRIB3*, were significantly upregulated upon TriC treatment (**Figures 33 and 34**) Two upstream activators of ATF4- eIF2S1(also known as eIF2A) pathway; PERK/EIF2AK2 and HRI/EIF2AK1 signaling were enriched with TriC treatment. Interestingly, activation of ATF4 via PERK/EIF2AK2 or HRI/EIF2AK1 has been shown to induce apoptosis in AML³³⁸ and MM^{339,340}. Depending on the magnitude and duration of the stressor, the ISR can support both cell survival to mitigate stress or induced apoptosis³³². The transcriptional profile of TriC-treated MM.1S cells showed both pro-survival and pro-apoptotic after 24 hours. However, examination of the proteomics of MM.1S cells treated with 1 μM TriC for 48 hours showed a significant decrease in proteins that promote protein folding: prefoldin subunit 2 and 6 (**PFDN2,6**), DnaJ homolog subfamily C member 9 (DNAJC9), chaperonin containing T cell complex protein 1 subunit 3,4,8 (CCT3, 4 and 8). Additionally, components of the proteasome including: proteasome activator complex subunit 1 (**PSME1**) and 26S proteasome regulatory subunit 6B (**PSMC4**) were significantly decreased. These data suggest at least two possibilities: 1) proteins are sufficiently

folded and these protein folding chaperones are no longer required, or 2) due to the loss of these proteins, there is an abundance of misfolded proteins and therefore, further activation of the ISR leading to a pro-apoptotic pathway. Myeloma cells have an abundance of misfolded proteins due to their increased secretory capacity and rely on the proteasome and protein folding chaperones to function^{88,341}. In conjunction with our data showing decreased viability, proliferation, and induction of apoptosis after 48 hours of TriC treatment, the latter is most likely occurring. As discussed in Chapter 5, it is important to test the activation status of the ISR and state of misfolded proteins in TriC-treated MM cells.

TriC treatment for 24 hours also significantly reduced MM.1S cell basal, maximal, and total ATP production rate due to a reduction in mitochondrially-derived ATP. We observed a decrease in mitochondrial number and mitochondrial membrane potential after 24 hours, therefore it is unclear if the reduction of MM.1S cellular respiration and ATP production rate is definitively due to reduced mitochondria and/or compromised mitochondrial function. Our observation of suppressed superoxide at 24 hours is consistent with an antioxidant transcriptional response with *NFE2L1* and *HMOX1* being significantly increased after TriC treatment.

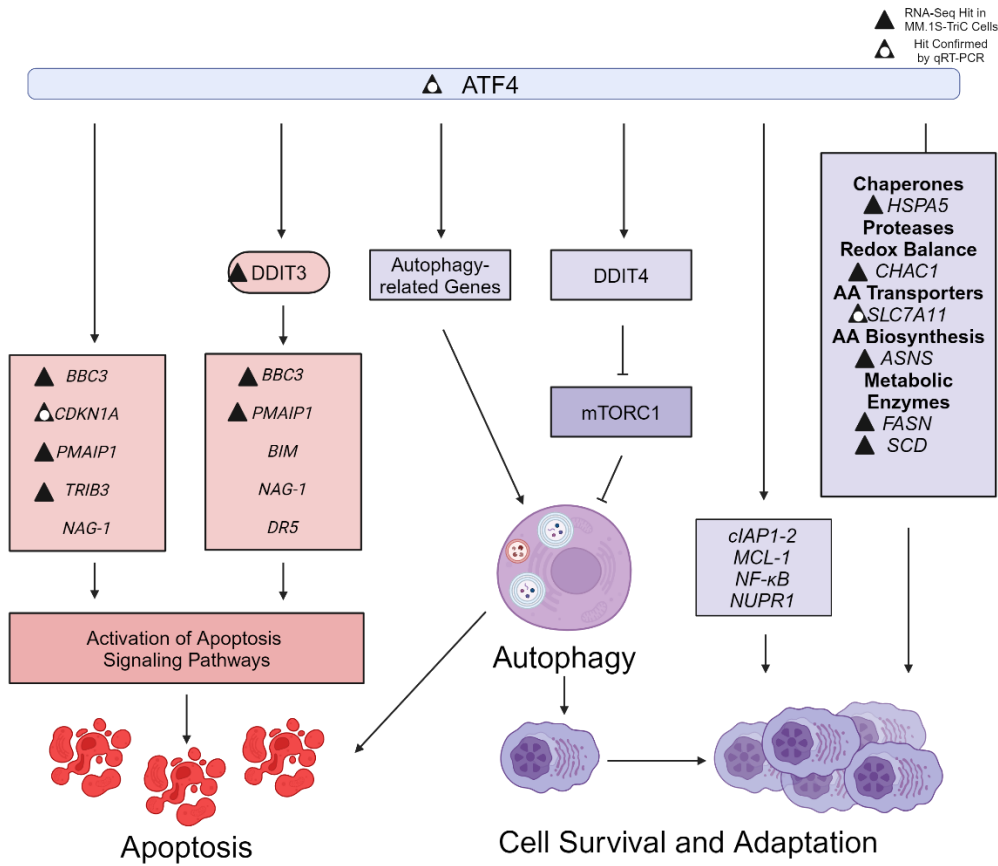


Figure 34. ATF4-Regulated Transcripts Support Both Cell Survival and Apoptosis
 Adapted from Tian et al. 2021, *Frontiers in Pharmacology*³³²

As loss of mitochondrial function is associated with the production of superoxide, the subsequent increase in mitochondrial superoxide after 48 hours of TriC treatment aligns with the proteomics data at the same timepoint that showed proteins in the electron transport chain such as *NDUFV2*, *COX5A*, *COX6B1*, and *ATP5ME* were significantly downregulated in TriC treated MM.1S cells. However, only *COX5A* gene expression was significantly down, suggesting that a post-translational-dependent mechanism may regulate these critical proteins. Taken together, these data suggest that TriC induces mitochondrial dysfunction and the integrated stress response.

The kinetics of the response of MM cell lines to TriC are important to understanding TriC-induced toxicity. MM.1S cells treated with TriC exhibited

mitochondrial dysfunction and a transcriptional profile aligned with the integrated stress response, ferroptosis, and apoptosis at the 24-hour timepoint. By 48 hours, significant decreases in viability and induction of apoptosis were detected in these cells as assessed by functional assays and mass spectrometry proteomics, demonstrating the signaling events triggered by TriC treatment occur within the first 24 hours, with maximum effects on cell viability occurring thereafter. A common denominator among these cellular pathways is the mitochondrion. Although the ACSL isozyme family are localized in various organelles, mitochondrion is shared amongst them all (See **Table 3**).

4.4. Mitochondrial-Derived Signals that Activate the Integrated Stress Response

Having detected an enrichment in HRI/EIF2AK1 molecules combined with dysfunctional mitochondria in MM.1S cells treated with TriC, it is likely that mitochondrial-derived signals are activating the integrated stress response (**ISR**). Interestingly, it has been shown by two independent groups that the mitochondrial protease, overlapping proteolytic activity with m-AAA protease 1 (**OMA1**), cleaves the mitochondrial protein DAP3 binding cell death enhancer (**DELE1**)^{342,343}. Cleaved DELE1 accumulates in the cytoplasm and activates HRI/EIF2AK1 and in turn, activates the ISR^{342,343}.

There is evidence that other signals from mitochondria can activate the ISR and specific ETC defects have distinct metabolites that activate different kinases upstream of EIF2S1³⁴⁴. Inhibition of the ETC in myoblasts increased cytosolic NADH/NAD⁺ ratios which inhibited aspartate synthesis, and therefore, asparagine levels, ultimately activating GCN2/EIF2AK2 because of amino acid starvation³⁴⁴. We observed an

upregulation in a number of genes involved in amino acid metabolism in MM.1S cells treated with TriC for 24 h that are critical for nucleotide synthesis, like serine, glycine and aspartate. This included genes involved in serine biosynthesis: phosphoserine aminotransferase (**PSPH**), phosphoserine aminotransferase (**PSAT1**). Serine can be processed by serine hydroxymethyltransferase 1 (**SHMT1**) to form glycine, which then can be used for purine synthesis³⁴⁵. Additionally, asparagine synthase (**ASNS**), which catalyzes the formation of asparagine from aspartate, was upregulated in MM.1S cells treated with TriC for 24 hours. It is possible that the TriC-induced mitochondrial dysfunction we observed inhibited the TCA cycle, and therefore critical biosynthetic precursors for amino acids like alpha-ketoglutarate and oxalacetate are depleted. Given that TriC has deleterious effects on OXPHOS, measuring NADH/NAD⁺ ratios, aspartate levels and measuring GCN2/EIF2AK2 phosphorylation upon ACSL inhibition may provide evidence for activation of the GCN2/EIF2AK2 arm of the ISR.

The upregulation of genes and proteins related to catabolic FA metabolism may also suggest that there is a dire need to produce essential acetyl-CoA for critical anabolic and catabolic cellular processes. We observed that inhibition of the rate-limiting enzyme in FAO, CPT1A for 30 minutes in MM.1S cells decreased basal, maximal and ATP-linked respiration, suggesting that MM cells use FAs as an energy source. There were significant increases in CPT1A and the very long-chain specific acyl-CoA dehydrogenase (**ACADVL**), an enzyme that catalyzes the first step of beta oxidation by converting an acyl-CoA to a trans- Δ^2 -enoyl-CoA¹¹⁶ in the proteomics of MM.1S cells treated with TriC for 48 hours. Given TriC decreases mitochondrial ATP production rate, the upregulation of genes involved in FAO may be a compensatory

mechanism to account for a depletion of ATP and TCA intermediates. Studies using isotope-labeled glucose, fatty acids and glutamine in MM cells treated with TriC would provide invaluable insight into substrate utilization preferences and deficiencies that may be exploited to induce MM cell death or defects in proliferation. Additionally, given that CPT1 is an AMPK-regulated gene and we observed decreased ATP production rates, the activation of AMPK should be investigated.

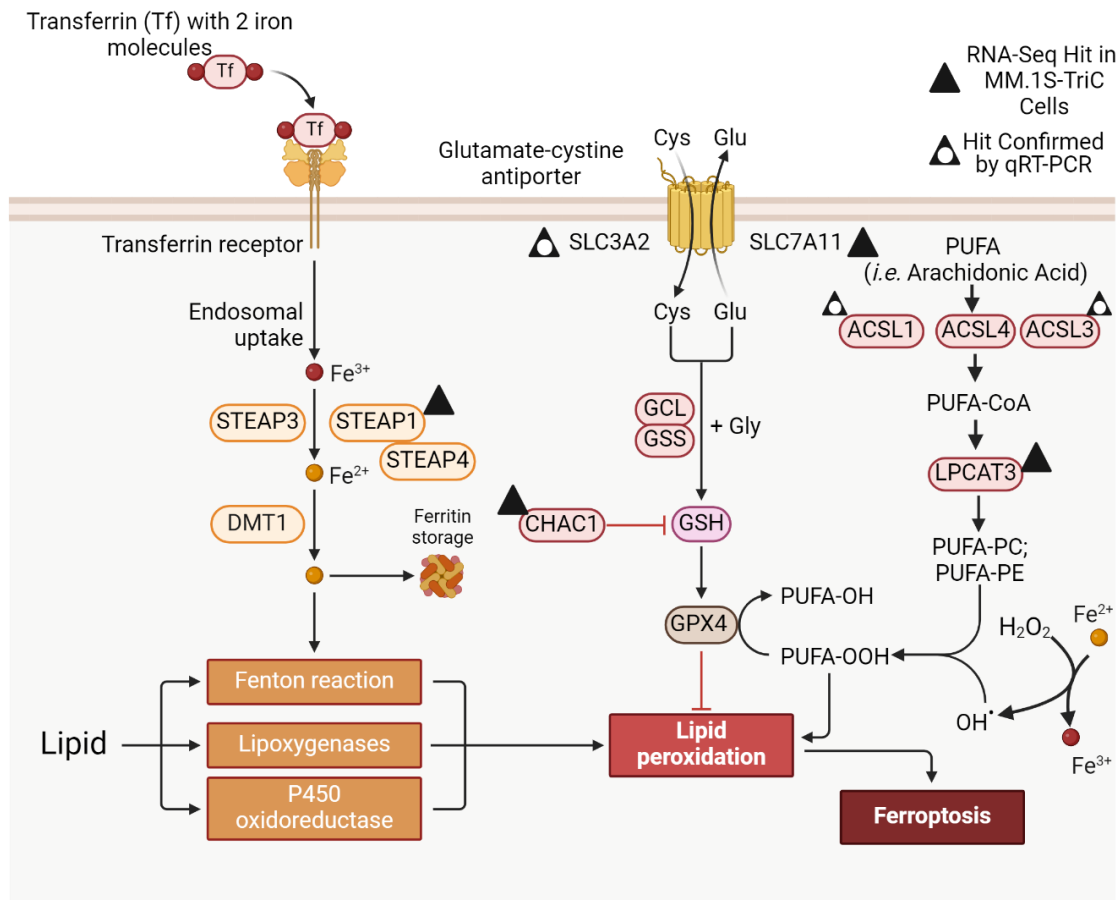


Figure 35. Triacsin C Upregulates Transcripts Associated with Ferroptosis
 Adapted from template made with Biorender.com by Gaia Lugano. Transferrin (Tf), Ferric iron (Fe^{3+}) Ferrous Iron (Fe^{2+}), Six transmembrane epithelial antigen of the prostate (STEAP) family members: STEAP 1, STEAP3, STEAP4, Divalent metal reporter 1 (DMT1), Cysteine (Cys), Glutamic acid (Glu), Glycine (Gly), Solute carrier family 3 member 2 (SLC3A2), Solute carrier family 7 member 11 (SLC7A11),

Glutamate-cysteine ligase (GCL), Glutathione synthetase (GSS), ChaC glutathione specific gamma-glutamylcyclotransferase 1 (CHAC1), Glutathione (GSH), glutathione peroxidase 4 (GPX4), Polyunsaturated fatty acid (PUFA), PUFA-coenzyme A (PUFA-CoA), PUFA-phosphatidylcholine (PUFA-PC), PUFA-phosphatidylethanolamine (PUFA-PE), PUFA hydroperoxides (PUFA-OOH), PUFA-alcohol (PUFA-OH), lysophosphatidylcholine acyltransferase 3 (LP3CAT), Hydrogen peroxide (H₂O₂), hydroxy radicals (OH[•])

4.5. The ACSL Family, Triacsin C and Ferroptosis

In our data, “Ferroptosis and Lipid/atherosclerosis” were among the top upregulated KEGG pathways in MM cells treated with 1 μ M TriC, as assessed by RNA-Seq.

Additionally, metabolism of lipids was enriched in the upregulated genes, suggesting that pathways modulating or responding to lipid species within TriC-treated MM cells are activated. While we did observe modest increases in apoptosis in response to 1 μ M TriC treatment, it is possible that other mechanisms of cell death, like ferroptosis, are playing a role in the decreased cell viability we observed.

Ferroptosis is a unique form of regulated necrosis that is triggered by the peroxidation of lipids by sources of ROS from lipoygenases like NADPH oxidase activator 1 (**NOXA1**), the ETC, or from hydroxy radicals (**OH[•]**) or hydroperoxyls (**HOO[•]**) derived from Fenton reactions³⁴⁶ (**Figure 35**). Cells are protected from ferroptosis by the protein glutathione peroxidase 4 (**GPX4**), which utilizes the antioxidant glutathione (**GSH**) to reduce phospholipid and cholesterol hydroperoxides (e.g. **PUFA-OOH**)³⁴⁶ and inhibition of GPX4 by the small inhibitor, RSL3, induces ferroptosis³⁴⁷. The action of GPX4 is supported by the glutamate-cystine antiporter, system X_c⁻ (**Sxc-**). Sxc- is composed of solute carrier family 3 member 2 (**SLC3A2**) and solute carrier family 7 member 11 (**SLC7A11**). Sxc- imports cystine, an important precursor to glutathione biosynthesis³⁴⁸. Inhibition of Sxc- by the small molecule erastin induces ferroptosis³⁴⁷. The gene expression of both components of the Sxc- complex were upregulated in

TriC-treated MM.1S cells by RNA-Seq, and upregulation of *SLC3A2* was confirmed by qRT-PCR. However, pro-ferroptotic *CHAC1*, which degrades glutathione, and lysophosphatidylcholine acyltransferase 3 (***LPCAT3***), were significantly upregulated in MM.1S cell treated with TriC for 24 hours, relative to vehicle cells. Combined, these findings provide mixed evidence that TriC treatment induces ferroptosis in MM.1S cells, but the modulated expression of all these components suggests the response to lipid peroxidation is likely a factor in TriC-mediated cellular phenotypes.

Indeed, members of the ACSL family have previously been connected to ferroptosis in a variety of cell types. ACSL4 is a major contributor to promoting ferroptosis because it preferentially processes PUFAs such as arachidonic acid which are sensitive to oxidation by ROS³⁴⁹. Recently, ACSL4 expression was shown to be positively correlated with sensitivity to ferroptosis in MM²⁷⁰, and ACSL4 levels were positively regulated by mitogen activated kinase (**MAPK**)-Extracellular signal-regulated kinase (**ERK**) kinase (**MEK**) / ERK1/2. They also correlated ACSL4 levels to c-Myc and SREBP protein levels²⁷⁰, suggesting a role for MAPK regulation of ACSL4, a connection that may be related to findings in our data. This will be discussed in later sections.

The composition of intracellular fatty acids can modulate pro-survival or cell death pathways. A variety of linolenic acids (18:2), especially α -eleostearic acid (α -ESA), have been shown to have tumor suppressive properties in multiple cancer cell lines from lung carcinoma (A549) colonic adenocarcinoma (DLD-1), hepatic carcinoma (HepG2) to AML (HL-60)^{350,351}. Recently, in triple negative breast cancer cell lines, ACSL1 was implicated in promoting ferroptosis after the addition of α -ESA by incorporating it into the acyl-chains of TAGs of lipid droplets³⁵². Given that ACSL1 preferentially binds linolenic

acid and that linolenic acid is preferentially incorporated into CLs, α -ESA also incorporates into CLs and cause increased ROS.

In clear cell renal cell carcinoma, knockdown of ACSL3 decreased proliferation and lipid droplet formation but increased resistance to ferroptosis induction, showing that ACSL3 contributes to ferroptosis, and is supportive of clear cell renal cell carcinoma³⁵³. Taken together, the literature suggests that ACSL1, ACSL3 and ACSL4 confer sensitivity to ferroptosis and understanding their expression and mechanism of action could inform clinical practice, as treatment with small molecule ferroptosis-inducers or certain fatty acids like α -ESA may be effective. Our data suggest that ferroptosis is occurring on a transcriptional level, but more functional studies are required to support that hypothesis. It is possible that the increase in ROS caused by TriC oxidizes the presumed increased pool of free fatty acid in the cytosol due to their inability to be conjugated with CoA.

In myeloma, Panaroni *et al* showed that high doses of arachidonic acid (25 μ M or greater *in vitro*, or 0.5 μ g/kg in a severe combined immunodeficiency disease (**SCID**)-MM.1S xenograft mouse model) decreased MM cell number and proliferation. The toxicity of arachidonic acid was ablated *in vivo* by ferrostatin, a ferroptosis inhibitor that scavenges alkoxyl radicals, and to a lesser degree by antioxidants like ibuprofen (an inhibitor of the cyclooxygenases, that convert arachidonic acid to prostaglandins)²⁴³. Interestingly, lower doses of arachidonic acid *in vitro* were shown to be tumor supportive. Addition of linoleic acid *in vitro* only significantly increased mouse MM cell viability at 0.5 and 6.5 μ M. When we treated HL-60 cells with OA (18:1), we saw a

decrease in viability, which may suggest that ferroptosis was occurring and that the toxicity of FAs is dependent on chain length and saturation status.

During the course of this work, a study was published showing that MM cells induce lipolysis of healthy and MM patient BMAds, and BMAd-derived FAs are transferred to MM cells mediated by the fatty acid transport protein (**FATP**) family²⁴³. These data support our observation of BMAd-derived FA transfer to HL-60 cells in transwell co-culture. Interestingly, Morris *et al.* showed that lipid droplets formed in the presence of conditioned media from BMAds had no effect on MM cell line viability²²⁶. Of note, the formation of lipid droplets was either cell line or species-dependent (the human JJN-3 were lipid droplet positive while the mouse 5TGM1 lacked lipid droplets) suggesting heterogeneity in FA metabolism or lipid droplet accumulation among MM cell lines. There may be intra-cell line heterogeneity of fatty acid metabolism as well, given that 50% of the JJN-3 cells they used and 60% of the HL-60 cells we used had lipid droplets. The fatty acid composition of BMAds may not be toxic or immediately afford an increase in ATP production (viability), therefore it may be low in arachidonic acid. Characterization of the fatty acid composition of BMAds using ¹⁴C-tagged fatty acids and how those are metabolized by MM or AML cells would inform how they are being utilized and how BMAds alter MM/AML FA metabolism.

4.6. Triacsin C, ROS Detoxification and Connections with TriC-Associated Transcriptome

We observed a significant decrease of mitochondrial superoxide upon TriC treatment after 24 hours. This could be due to a few mechanisms that are not mutually exclusive: (1) decreased mitochondrial number by defects in biogenesis, (2) mitophagy of damaged mitochondria, (3) decreased ETC activity, and (4) active detoxification of

ROS. We did observe a decrease in mitochondrial number after 24 hours but that needs to be further confirmed by isolating mitochondria, counting them, and observing their morphology, which is directly related to their function. We did observe a significant decrease in the positive regulator of mitochondrial biogenesis, *PPARGC1B* but not *PPARGC1A* or their upstream regulator *TFAM*. *PINK1*, an indicator of mitophagy, was significantly increased by TriC-treatment after 48 hours. Investigation of these genes and proteins at the 24 hour timepoint would help test the hypothesis that mitophagy may be responsible for the decrease in ROS and/or mitochondrial number at 24 hours.

ROS detoxification in the mitochondrion is performed mainly by SOD2, while SOD1 also regulates ROS, but is more widely dispersed throughout the cell. Intriguingly, *SOD2* expression is significantly decreased in MM patients compared to normal BM plasma cells, and is inversely correlated with the rate of myeloma cell proliferation³⁵⁴. This suggests that mitochondrial superoxide and perhaps ROS are myeloma supportive. *SOD2* levels were not significantly changed in the RNA-Seq data of MM.1S-TriC treated cells for 24 hours, but it is possible that basal *SOD2* expression is sufficient to reduce the levels of mitochondrial superoxide produced after 24 hours of TriC treatment. Monitoring *SOD2* levels and activity of the enzyme throughout the course of TriC treatment would help elucidate the superoxide dynamics. The increase of mitochondrial superoxide after 48 and 72 hours of TriC treatment with decreases in SOD1 protein levels (by mass spectrometry) in MM.1S cells suggests that ROS detoxification is insufficient at those time points. *SOD1* is regulated by NFκB, activator protein 1 complexes 1 and 2 (AP-1, AP-2), specificity protein 1 (**Sp1**), and CCAAT-enhancer-binding protein (C/EBP)^{355,356}. In other disease models, SOD1 has been tied

to regulation of the pro-myeloma NFκB pathway^{357,358}. Proteomics of TriC-treated MM.1S cells showed SOD1 was amongst the most downregulated proteins in TriC-treated cells. Our RNA-Seq data showed gene expression of an inhibitor of NFκB signaling, NFκB inhibitor zeta (***NFKBIZ***) was significantly upregulated. These data show a possible connection between TriC-induced ROS and inactivation of NFκB signaling that may lead to decreased proliferation. However, further assessment of NFκB signaling and SOD1 on a protein level must be done to test this hypothesis, as ROS can both activate and inhibit NFκB signaling³⁵⁹. The mitogen-activated protein kinase (MAPK) pathway is another important signaling pathway that is regulated by ROS.

4.7. TriC and Mitogen-Activated Protein Kinase Signaling

“MAPK Signaling” was a significantly enriched KEGG pathway in our RNA-Seq data and had both activators (*JUN*, *FOS*, and ribosomal protein S6 kinase A2 (***RPS6KA2***)) and inhibitors (dual specificity phosphatase (***DUSP1***, *DUSP10* and *DUSP16*)). The components of the AP-1 complex, *JUN* and *FOS*, were upregulated in our RNA-Seq data of TriC-treated MM.1S cells. AP-1 (also known as JNK) signaling is a downstream arm of the mitogen-activated protein kinase (MAPK) pathway³⁶⁰. Upon stimulation by receptor tyrosine kinases (RTKs) and/or ROS, an activating phosphorylation cascade of RAS, Raf oncogene (***RAF***), and MAPK-Extracellular signal-regulated kinase (ERK) kinase (MEK) occurs. MEK then activates AP-1, ERK1/2 and mitogen-activated protein kinase 14 (p38/MAPK14)³⁶⁰. Activated ERK1/2 can activate cAMP response element-binding protein (CREB) to induce *FOS* transcription, and activate tumor supportive transcription factors such as NFκB and transcriptional regulator Myc-like (c-Myc)³⁶⁰. *CREB5* was the most upregulated (5.88-fold) transcript in

TriC-treated MM.1S cells relative to vehicle treated cells in our RNA-Seq data. These data suggest that MAPK signaling is activated. However, the expression of the *DUSPs* also shows that MAPK signaling may be decreased. *DUSP10* dephosphorylates p38/MAPK14³⁶⁰. p38/MAPK14 can activate the tumor suppressor tumor protein p53 (**TP53**), which negatively regulates cell cycle progression. Although we did not observe changes in *TP53* expression, its downstream effector *CDKN1A* was significantly increased. These data suggest that TriC-induces a transcriptional program that promotes both proliferation and cell cycle arrest. Consistent with negative regulation of MAPK signaling, it has been previously shown that macrophages treated with TriC had decreased p38/MAPK14 and JNK signaling³⁶¹. The role of TriC-induced ROS in the regulation of MAPK, NFκB and AP-1 signaling requires further investigation due to the various ways these pathways can be activated.

4.8. The Potential Implications of Triacsin C Use and Approved Therapies for Multiple Myeloma and Acute Myeloid Leukemia

Combination therapies in MM is standard practice due to the development of drug resistance, and it is critical to identify new therapeutic combinations. TriC has been shown to synergize with other drugs such as etoposides²⁷⁵, and a combination of anti-metabolites and alkylating agents³⁶² in glioma and colorectal cancer. TriC has been shown to reduce lipid droplets³⁶³, and lipid droplets have been identified in colorectal cancer as a mechanism of drug resistance³⁶². Therefore, TriC treatment in combination with other standard myeloma treatments such as dexamethasone or proteasome inhibitors may show promise. Additionally, MM cell Complex I and II activity is positively correlated to the sensitivity of the BCL2 inhibitor, venetoclax³⁶⁴. Hence, MM.1S cells treated with TriC may be sensitive to venetoclax treatment because we observed

decreased mitochondrial ATP production and decreased expression of subunits of Complex I and IV. In AML, it has been shown that AMPK-PERK-ATF4 activation also confers sensitivity to venetoclax treatment by repressing oxidative phosphorylation³³⁸, therefore future studies could test if a similar mechanism is occurring in MM. Interestingly, low levels of ATF4 and ATF3 are positively correlated with poorer outcomes in myeloma patients treated with bortezomib and dexamethasone³⁶⁵. Combined with the fact that bortezomib induces a terminal unfolded protein response⁸⁸, the induction of ATF4 and ATF3 gene expression by TriC may push MM cells closer to the apoptotic threshold³⁶⁶. Elucidating the mechanisms of how the ACSL family is tied to mitochondrial function and the ISR response could identify novel treatments for MM. Taken together, targeting the ACSL family in combination with existing clinical therapeutics could reveal promising synergies.

4.9. Experimental Limitations

4.9.1. ACSL Homology to Luciferase

A consideration with respect to any assay that used luciferase, is the homology of the ACSL family to click beetle luciferase^{367,368}. Due to this homology, it is possible that TriC also binds and inhibits luciferase. A dose curve of TriC and luciferase and luciferin could elucidate if this is true. This was a one reason why Trypan Blue staining was used to assess viability. There are other higher-throughput ways to assess viability like propidium iodide staining.

***n vitro* Culture Conditions**

Nutrients under cell culture conditions *in vitro* are in excess and under normoxia. The bone marrow microenvironment is dynamic and the lower concentrations of oxygen

have major implications in cellular metabolism^{312,369}. Experiments assessing FA metabolism of MM within the bone marrow microenvironment, would better inform the outcome of possible therapeutic interventions.

4.9.3. Triacsin C is a Pan-ACSL Small Molecule Inhibitor

As mentioned before, we cannot elucidate the individual contributions of the ACSL family with this inhibitor. Due to their different preferences of FA and cellular localizations, it is possible that TriC has a bias with respect to which ACSL isozyme family member it targets. Genetic approaches targeting the individual ACSL members will be discussed in the future directions. Additionally, we observed batch-dependent effects of TriC, which could account for the variability we saw. Most experiments (besides the Ki-67 and BAX protein at 48 hours) were done with the same lot between biological replicates. Determining the half-life of TriC in culture through mass spectrometry or nuclear magnetic resonance (**NMR**) would inform our kinetics experiments. Despite using doses close to the IC_{50} , it is also unclear if TriC has off-target effects. Additionally, we cannot make clear assessment on whether the addition of OA was protective of TriC-induced toxicity in HL-60 cells because the OA was in culture simultaneously with TriC. TriC is a competitive inhibitor of the ACSLs, and the OA may have outcompeted TriC. Although the data presented here point to exciting avenues of future research, the mechanism of TriC-induced toxicity is still unknown and true mechanistic studies are required.

4.9.4. Limited Number of Donors

Experiments with hMSCs or BMAds were mainly with 1 donor. Human samples have a high amount of heterogeneity due to genetic and environmental factors, therefore, more donors must be used to make conclusive claims.

4.9.5. RNA Interference Experimental Design

The experiment regarding dsRNA-mediated knockdown of *ACSL3* was flawed in both execution and design. The NT dsRNA is conjugated to AlexaFluor(AF)-647, meaning it can act as a proxy for transfection efficiency. However, AF-647 fluorescence was not assessed in this experiment and therefore it is unclear if the lack of knockdown is due to a poor efficiency by the dsRNA construct or poor transfection efficiency. In the future, both the NT and the targeted interfering RNA constructed should be fluorescently tagged so they have the same lipophilic properties to be directly compared. Transfection efficiency can be measured with either flow cytometry, fluorescence microscopy or a fluorometer.

4.10. Summary of Conclusions and Significance

We identified the ACSL family of proteins (excluding ACSL6) as supportive of a MM.1S, MM.1R, OPM-2, RPMI-8226 cells. U266B1 appeared to be resistant to TriC treatment. Treating MM cell lines with TriC, a small molecule inhibitor against ACSL1, 3, 4 and 5 caused decreases in proliferation and viability, increases in cell death (apoptosis), and induction of mitochondrial superoxide at longer times of incubation (48 hours or more). Proliferation, viability, and survival did not change after 24 hours of TriC treatment but MM.1S cells exhibited compromised cellular respiration, decreased mitochondrial membrane potential, and decreased number of mitochondria at this time. Transcriptional assessment by RNA-Seq suggested that there was activation of the integrated stress response, the cell death pathways apoptosis and ferroptosis, and

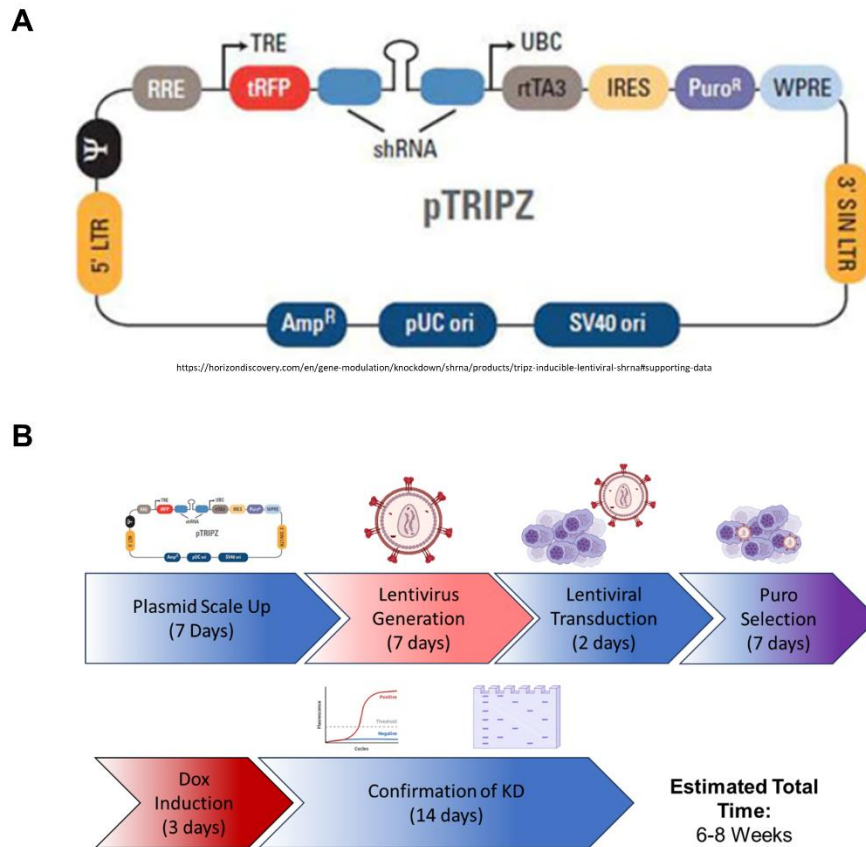
factors that both negatively and positively regulate the MAPK pathway. GO overrepresentation analysis of the proteomics of MM.1S cells treated with TriC for 48 hours showed a proteome that had increased mitochondrial dysfunction, significant changes in proteins related to ubiquitination and the proteome. The terms within the mitochondrial dysfunction were components of the ETC from complexes I, III, IV and V; however, gene expression of parallel samples only showed a significant change in *COX5A*, a complex III subunit. We observed that TriC also modestly induces apoptosis and negatively impacts cell viability in the AML cell line, HL-60. More studies must be done to test the hypothesis that the ACSL family may be a target in both MM and AML.

Further studies of the role of the ACSL family may reveal unique metabolic vulnerabilities in MM, and novel biological phenomenon such as the role of fatty acid metabolism in communication between the mitochondrion, the endoplasmic reticulum and the nucleus regarding bioenergetic status and cellular stress. These insights may translate to new therapies in the field of hematological oncology and have the potential to improve the survival rate and quality of life of MM patients.

5. CHAPTER 5: UNANSWERED QUESTIONS AND FUTURE DIRECTIONS

5.1. Genetic Targeting of the ACSL Family

The transfection of MM cells with traditional lipid nanoparticles is very inefficient and transient. For a more efficient system that is stable and affords temporal flexibility, shRNAs targeted against *ACSL 1*, 3 and 4 have been ordered from Horizon Discovery (Dharmacon). The shRNAs are in the pTRIPZ vector, a second-generation lentiviral vector with the shRNA and turboRFP (red fluorescent protein (**tRFP**) under a tetracycline responsive element (**TRE**) regulating a minimal Cytomegalovirus (**CMV**) promoter. Therefore, the expression of both the shRNA and tRFP can be induced by tetracycline or its analogs (*i.e.* doxycycline). Other notable features are a puromycin resistance cassette so that puromycin can be used a means of selecting transduced cells. The pMD2.G and psPAX will be used as the envelope and packaging plasmids. Upon knockdown, viability, proliferation, survival and ACSL activity should be assessed (**Figure 36**) After these are made, they should be the primary tool to study the role of the ACSL family in MM cells *in vitro* and *in vivo*. See Table 10 for more information about the target sequence.



pTRIPZ vector Map and B) The overview of the experimental procedure on lentiviral transduction

5.2. Confirmation of Activation of the Integrated Stress Response

There is strong transcriptional evidence that TriC treatment activates the p-EIFS1-ATF4 pathway in MM cells, however evidence on the protein level must be gathered to test the hypothesis the ISR is activated. First, ATF4 nuclear localization should be determined in the presence and absence of TriC. If there is ATF4 nuclear localization, it is indicative of ATF4 activation. The next experimental step would be assessing protein levels of ATF4 and EIFS1(EIF2A) and phosphorylated EIFS1 (p-EIFS1 or p-EIF2A) in the presence and absence of TriC. Tunicamycin can be used as a positive control for p-EIF2³³⁷. These data may be sufficient for reviewer comments but

the protein levels and their phosphorylation statuses of all the kinases that can activate the ISR should be determined in the presence of TriC. They are EIF2AK1-4.

The composition of phospholipid membranes influences the state of cellular ISR. Indeed, PUFAs have been shown to induce activate EIF2AK3/PERK and ERN1/IRE1 α ^{370,371}. Therefore, understanding the lipid profile upon ACSL family inhibition would provide insight into whether the transcriptional profile consistent with the ISR. One family of lipids are the mitochondrial specific cardiolipins (CLs), that have a compelling connections with oxidative stress, mitochondrial function and the ISR, all of which are key pathways associated with TriC treatment.

There is evidence in the literature that ACSLs alter mitochondrial function. Additionally, mitochondria from mouse cardiac tissue from global *Acs/1* knockouts showed decreased responsiveness to ADP stimulation and decreased ATP production³⁷². Furthermore, isolated mouse cardiac mitochondria from *Acs/1* knockouts had decreased expression of *taffazin*, (**Taz**) a phospholipid-lysophospholipid transacylase responsible for maturation of cardiolipins (**CLs**), a phospholipid species predominantly found in the mitochondrial inner membrane³⁷². A brief overview of the details of cardiolipin biosynthesis remodeling and cellular functions will be provided below. CLs are critical for mitochondrial bioenergetics, intrinsic apoptotic signaling, and mitophagy³⁷³. The following section will attempt to rationally interweave the data in this work and in the literature to build a speculative model that postulates that TriC changes the composition of CL species in mitochondria and induces ETC dysfunction, causing a loss of ATP production and generation of ROS. The mitochondrial stress signal is

transduced to activate the ISR, chronic activation leads to slower cell cycle progression and cell death by both apoptosis and ferroptosis.

Lipids are a widely diverse group of biomolecules that could all be altered by the inhibition of the ACSL family. Indeed, even in the mitochondrion there are various classes of phospholipid besides cardiolipins (**CL**) including: phosphatidylcholine (**PC**), phosphatidylethanolamine (**PE**), phosphatidylinositol (**PI**), phosphatidylserines (**PS**) and phosphatidic acid (**PA**). However, CLs have a clear functional connection between the phenotypes we observed upon TriC treatment in MM and AML cell lines. To understand the proposed model above, background of CL biosynthesis and remodeling, CL regulation of bioenergetics, as well as the relationship between CLs, ROS, and activation of apoptosis, ferroptosis, and the ISR, is required.

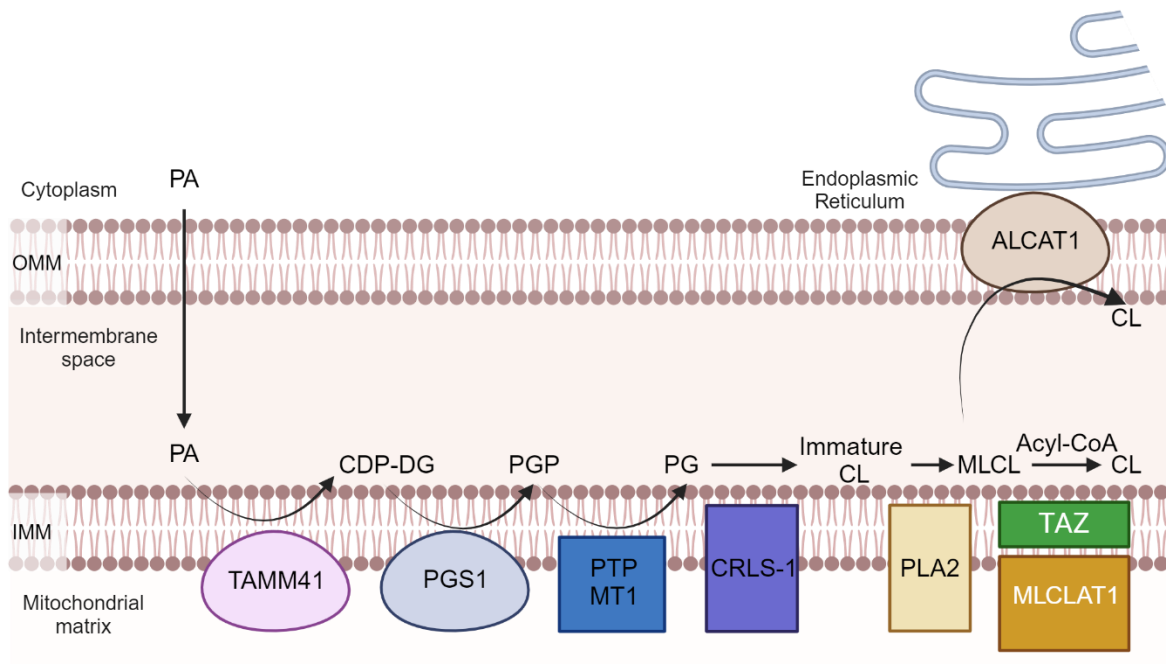


Figure 37. Cardiolipin Biosynthesis and Remodeling

This figure is adapted from Ahmadpour *et al.* 2020 *Int. J. of Mol. Sciences*³⁷³. CL biosynthesis is initiated by phosphatidic acid (PA) entering the IMM and being processed to cytidine diphosphate(CDP)-diacylglycerol (CDP-DG) by the CDP-DG synthase, TAMM41³⁷⁴. CDP-DG is then

converted to phosphatidylglycerol phosphate (PGP) by the phosphatidylglycero-phosphate synthase, PGS1, by transferring a phosphatidyl group to a molecule of glycerol-3-phosphate (G3P)³⁷⁵. A phosphate on PGP is cleaved by phosphatidylglycerophosphate phosphatase 1 (PTPMT1) to form phosphatidylglycerol (PG). CL biosynthesis concludes with PG being converted to immature CL by cardiolipin synthase 1 (CRLS1)³⁷⁶. Immature CLs are characterized by variably sized saturated acyl chains and asymmetry with respect to the glycerol head group³⁷⁷. Immature CLs require remodeling to be functional. CL maturation involves cleaving of the fatty acyl chains on immature CLs by phospholipase A2 (PLA2) to form monolysocardiolipin (MLCL) and then a series of acyl-CoA transferases in the IMM by monolysocardiolipin acyltransferase 1 (MLCLAT1) and TAZ^{378,379} that have preferences for linoleic acid (18:2)³⁸⁰. TAZ transfers an acyl group from a PE or PC in the membrane to form mature cardiolipin^{378,379}. The acyl-CoA:lysocardiolipin acyltransferase (ALCAT1) located on endoplasmic reticulum-mitochondria associated membranes (ER MAMs), remodels cardiolipins upon oxidative stress^{381,382}. Made with Biorender.com

5.3. Cardiolipin Biosynthesis and Remodeling

Enriched in the IMM where it is synthesized, CLs are type of phospholipid consisting of two phosphatidyl moieties bound to a glycerol head group (**Figure 37**). Each phosphatidyl group is bound to two esterified fatty acyl chains bridged by a glycerol group, these symmetrical halves help form a cone-like shape³⁸³. While we hypothesize that cardiolipin accumulation is involved in TriC toxicity, expression of genes and proteins involved in CL biosynthesis or remodeling were not significantly changed in either the RNA-Seq or proteomics data of MM.1S cells. However, it is possible that TriC treatment modulates CL composition, as one of the most important functions that mature CLs perform is regulating bioenergetics, and this was found to be aberrant in TriC-treated MM cells.

5.4. Regulation of Bioenergetics by Cardiolipins

CLs physically interact with key components of the ETC such as Complex I Complex III, IV and ADP/ATP carrier (**AAC**)^{384–386}. CLs are required for the formation of supercomplexes or respirasomes between the ETC complexes by physically bringing individual ETC complexes in closer proximity, ultimately increasing the efficiency of electron transfer^{387–389}. Given our data showing that MM.1S cells treated with TriC for 24 hours had decreased respiratory parameters, it is possible that a depletion or change

in CL composition could disrupt the formation of respirasomes. Interestingly in neurons, knockdown of a critical component of complex I, NDUFS1 caused a decrease of complex I to form respirasomes and led to decreased oxygen consumption and increased mitochondrial ROS³⁹⁰, however the mechanism of how ROS is produced due to a lack of respirasome formation is unknown. We observed a significant increase in mitochondrial superoxide in TriC-treated MM.1S cells after 48 hours and 72 hours relative to vehicle treated cells. The effect of ROS on CL and downstream will be discussed in the context of apoptosis, ferroptosis and activation of the ISR.

5.5. Oxidized Cardiolipins Are a Signal of Mitochondrial Stress and Activate Apoptosis and the ISR

Cytochrome C is a key component in the ETC and serves multiple cellular functions including regulating oxidative stress and apoptosis³⁹¹. Cytochrome c (**Cyt C**) has peroxidase activity and is able to scavenge electrons from superoxide to regenerate oxygen, thus acting as an antioxidant³⁹², a process that is promoted through interactions with CLs through two distinct mechanisms³⁹³. Cyt c interacts with the phosphate head group of CL, which promotes the electron transfer and peroxidase activity of Cyt cand when CLs migrate from the IMM to the OMM during apoptosis, the unsaturated acyl chain interacts with Cyt c to promote peroxidase activity^{394,395}. Oxidation of CLs in the proximity of Cyt c peroxidase activity causes the release of Cyt c from the IMM to the cytosol, promoting apoptosis³⁹⁶. Oxidation of CL can be driven by ROS species, generating reactive aldehydes like 4-hydroxy-trans-2-nonenal (**4-HNE**), a signaling molecule that has been shown to upregulate HMOX1 and activate the PERK-EIFS1-ATF4 and the ATF6 pathways of the unfolded protein response ³⁹⁷. Addition of 4-HNE on PC12, a neuron-like cell line, caused activation of ERK, JNK and p38/MAPK14 and

the downstream NFE2L2, a key protein in the response to oxidative stress³⁹⁷. Inhibition of p38/MAPK with SB203580 upon 4-HNE treatment reduced HMOX1 upregulation and induced the pro-apoptotic ISR-induced transcripts: *DDIT3*, *BBC3*, and *TRIB3*³⁹⁷. Consistent with these results, TriC-treated MM.1S cells also had significantly upregulated *HMOX1*, *DDIT3*, *BBC3* and *TRIB3* and induced apoptosis, making a compelling connection between 4-HNE and TriC-induced ACSL inhibition in MM cells. CL may have a possible connection with regulating the activation of HRI/EIFA2K1 arm of the ISR. In neurons, it has been shown OMA1 binds CL in complex with the prohibitin (**PHB**) complex³⁹⁸. They show that the PHB complex promotes OMA1 turnover but do not directly test that that CL are necessary for the PHB regulation of OMA1 levels in the mitochondrion and would be a novel experimental pursuit to investigate. These data would show a direct role of CL in the OMA1-DELE-HRI/EIF2AK1 arm of the ISR.

5.6. Triacsin C Drug Synergy Studies

Proteasome inhibitors like bortezomib and the BCL-2 antagonist venetoclax have anti-MM effects. To test how TriC treatment alters the response to these therapeutic agents, dose curves of each drug alone and in combination will be done in a high-throughput manner by assessing changes in viability by propidium iodide staining and assessing redox potential with RealTime-Glo. These data will add more clinical relevance to the existing data. If the ISR is indeed activated by TriC, ISR-related factors should be examined in this context as well (**Figure 38**).

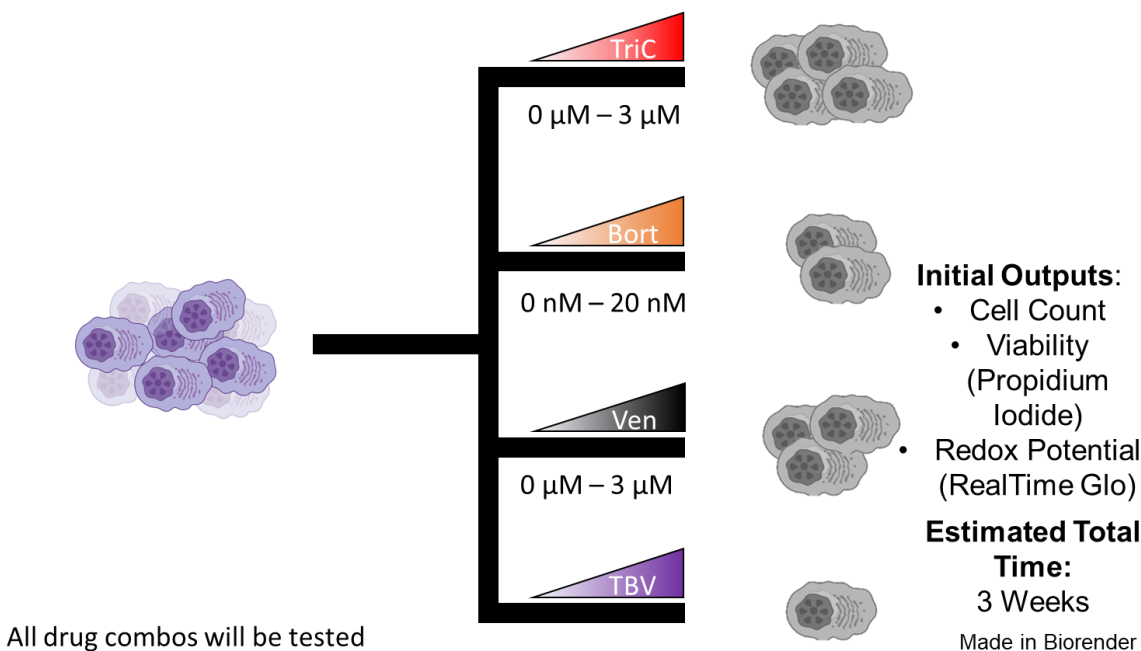




Figure 38. Potential Combination Treatments to Test in Myeloma
 TriC:Triacsin C Bort:Bortezomib, Ven:Venetoclax, TBV: TriC + Bortezomib+Venetoclax.

5.7. Treatment of MM Mouse Models with Triacsin C

To further develop the promise of targeting the ACSL family in MM cells, Triacsin C should be used to treat myeloma murine models. Triacsin C has been shown to be efficacious in combination with etoposide, a topoisomerase inhibitor, in a subcutaneous mouse model of glioma using the U251 cells²⁷⁵. Additionally, at a dose of 10 mg/kg via oral gavage, TriC showed decreases in the percentage of aortic lesions and the area of those lesions in a LDLR^{-/-} C57BL/6 mouse³⁹⁹; they did not report any deleterious side-effects in these mice due to TriC treatment. Finally, TriC was delivered intraperitoneally (IP) in a colorectal cancer mouse model using CT26 cells in BALB/c mice to reduce lipid droplets prior to fluorouracil and oxaliplatin treatment³⁶². These studies suggest that TriC is safe and could be efficacious to reduce tumor burden in MM mouse models.

Given our *in vitro* data, we hypothesize that TriC will reduce tumor burden relative to vehicle treated cells. There are multiple routes of delivery of TriC reported in the literature, therefore we will test oral gavage and IP routes of delivery. Briefly, MM.1S^{gfp/luc} cells will be injected intravenously into SCID-Beige mice (Charles River). 24 hours later mice will begin treatments either daily by oral gavage or IP 3 times per week. On average it takes 14 days for MM.1S cells to be detectable by bioluminescent imaging (BLI). BLI is the reading of bioluminescence from the luciferase expressing MM.1S cells after injections of luciferin (luciferase substrate). Tumor burden will be quantified 1-2times per week and mice will be sacrificed upon meeting the body conditioning score threshold (**BCS** ≤2) or when there is evidence of hindlimb paralysis as assessed by early paralysis detection (**EPD**) monitoring.

A

Strain (male and female) MM cell line n=15/ treatment group	Day 0	Day 1	Day 14	Day 21
SCID-Beige mice GFP+Luc+ MM.1S	Inoculation with tumor cells Max: 5x10 ⁶ 	Daily Triacsin C treatment via oral gavage starts (Max Dose: 35 mg/kg) 	Bioluminescent Imaging starts (2-3x weekly)	Mice monitored for stress and tumor ulceration. Euthanized as necessary according to body conditioning score or hindlimb paralysis

B


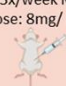
Strain (male and female) MM cell line n=15/ treatment group	Day 0	Day 1	Day 14	Day 21
SCID-Beige mice GFP+Luc+ MM.1S	Inoculation with tumor cells Max: 5x10 ⁶ 	Triacin C Treatment via Intraperitoneal Injection starts (3x/week M,W,F), Max dose: 8mg/ kg) 	Bioluminescent Imaging starts (2-3x weekly)	Mice monitored for stress and tumor ulceration. Euthanized as necessary according to body conditioning score or hindlimb paralysis

Figure 39. Triacsin C in MM Mouse Models
Made with elements from Biorender.com

5.8. Treating Primary MM Cells with Triacsin C

Understanding if TriC has a similar phenotype in primary human MM cells is critical to establishing the efficacy of targeting the ACSL family or ACSL-related pathways in MM. Given that processing MM cells from patient samples is a very rare occurrence (~2 per year), only preliminary results have been collected over the course of this thesis which are summarized below; further exploration and analyses are required.

Primary deidentified patient samples were provided by the MaineHealth Biobank and processed in the Reagan Laboratory. We had the privilege to isolate primary MM cells from patients (R20-9000, R24-0125 and R24-0553 using MACS to sort CD138-expressing (CD138(+)) cells; CD138 is a plasma cell-specific marker (Figure 40 and Table 10)^{400,401}. RealTime-Glo was then used to measure the redox potential of the isolated cells, per the manufacturer's instructions.

Table 10 CD138(+) Yield from Primary MM Patient Bone Marrow Aspirates

Patient Sample ID	Sample Volume (mL)	CD138(+) Cells	Median CD138(+) Cells [95% CI]	CD138(+) cells/mL	Median CD138(+) Cells/mL [95% CI]
R20-9000	12	9.52x10 ⁶	3.49x10 ⁶ [0, 9.04x10 ⁶]	7.93x10 ⁵	3.71x10 ⁵ [0, 7.68x10 ⁵]
R24-0125	3	4.45x10 ⁵		1.48x10 ⁵	
R24-0553	3	5.10x10 ⁵		1.70x10 ⁵	

CI=Confidence Interval

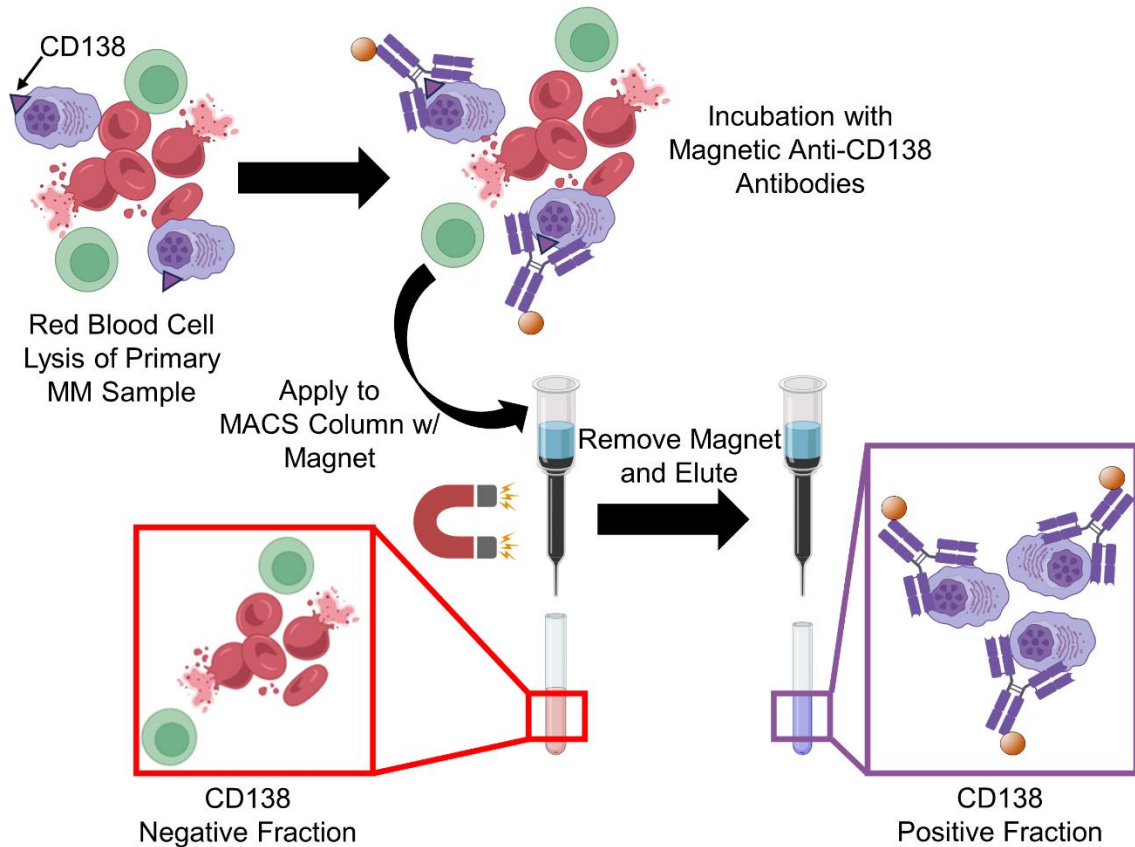


Figure 40. Magnetic Activated Cell Sorting (MACS) of Primary MM Cells

Bone marrow aspirates from primary MM patients are subjected to red blood cell lysis then are incubated with magnetic-conjugated antibodies against CD138. The cell mixture is then applied to the MACS column in the presence of a magnetic field to retain the CD138(+) fraction in the column while the CD138(-) fraction is the flowthrough. A new collection tube is placed under the MACS column, the magnetic field is removed and the column is washed to elute the purified CD138(+) fraction.

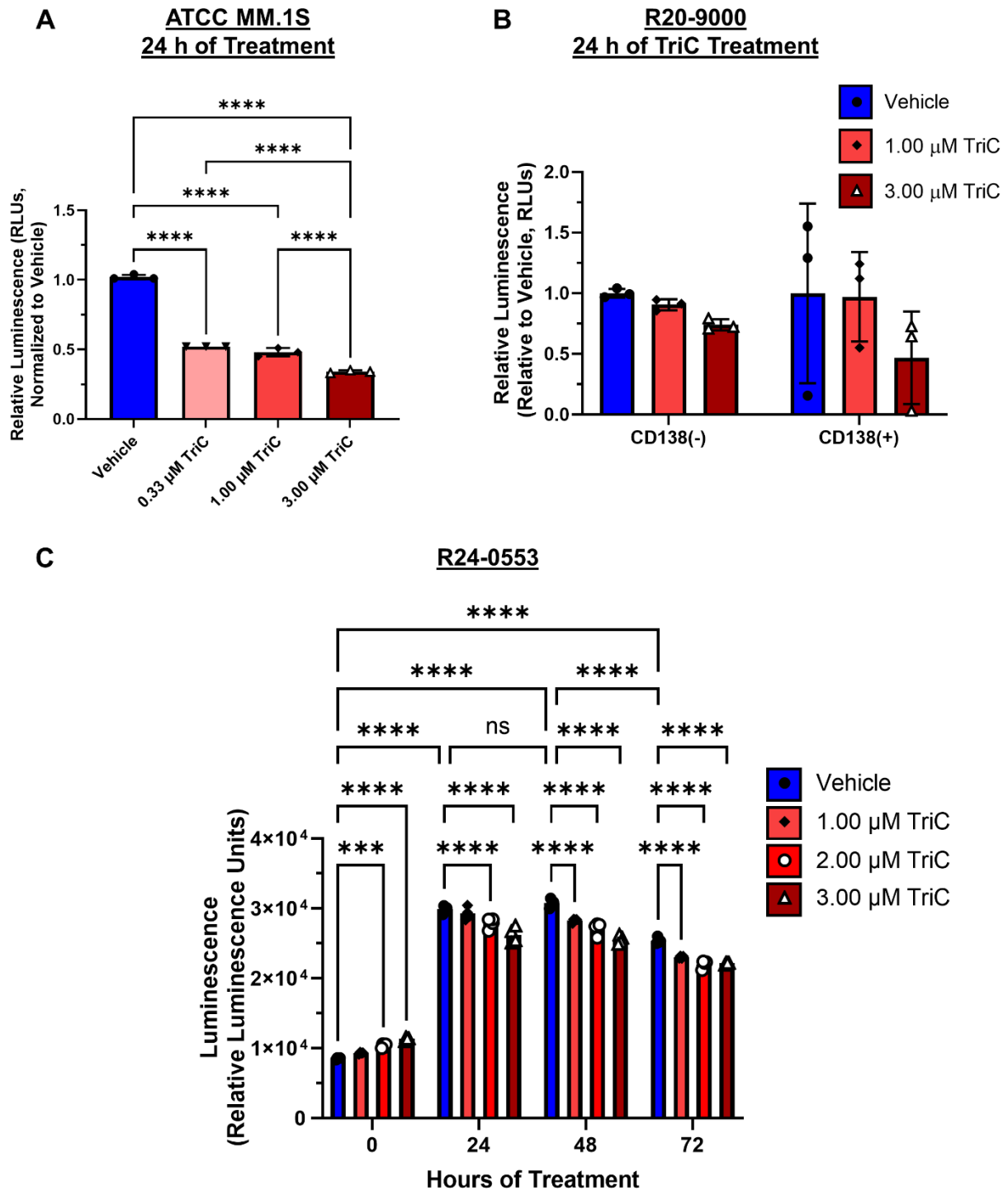


Figure 41. Triacsin C Treatment of Primary MM Cells

A) ATCC MM.1S cells were treated with various doses of Triacsin C (TriC) for 24 hours and redox potential was quantified with RealTime-Glo (RTG; Promega). B) Bone marrow aspirates from a multiple myeloma patient (R20-9000) were processed and subjected to magnetic activated cell sorting (Stem Cell Technologies), selecting for CD138 (+) cells. Each fraction was plated with RealTime-Glo and TriC to monitor redox potential after 24 hours. n = 3 technical replicates. C) similar to panel B but

with a separate donor (R24-0553), additional treatment times (0, 24, 48 and 72 hours) and using the Miltenyi MACS system n =4 technical replicates. Statistics: Data are mean +/- standard deviations One-way ANOVA with Tukey's multiple comparisons test. *p<0.05, **p<0.01, ***p<0.001 ****p<0.0001.

The three primary MM samples yielded a median 3.49×10^6 total cells [95% CI: 0, 9.04×10^6] (**Table 10**). Bone marrow aspirates are typically around 3 mL, however the R20-9000 sample was a total of 12 mL and had a higher concentration of CD138(+) cells compared to the other samples (**Table 10**) The median CD138(+) cells across the three primary MM samples was 3.71×10^5 [95% CI: 0, 7.68×10^5] (**Table 10**). Given that R20-9000's volume and CD138(+) yield appear to be an outlier, it may be safer to expect $\sim 5 \times 10^5$ CD138(+) cells given the median yield between R24-0125 and R24-0553 is 4.78×10^5 CD138(+) cells. Mariah Farrell and Heather Fairfield Campbell collected, processed, and plated the experiment for R20-9000 in March of 2020. Their dedication to their craft, colleagues and myeloma patients is appreciated, especially in backdrop of a time of extreme uncertainty. Michelle Karam and Heather Campbell isolated and executed the experiment for R24-0553. Edward Jachimowicz assisted with the MACS sorting for R24-0125 and R24-0553. The processing of the primary MM sample, R24-0125 produced a CD138+ fraction with reduced viability (as assessed by size and granularity with flow cytometry). This is likely due to excessive repetition of the red blood cell lysis step and future studies using patient samples should strictly follow the parameters this process as primary cells are sensitive to prolonged exposure to the lysis buffer. For these reasons, the RTG data for this patient sample has not been included.

When treated with TriC for 24 hours, ATCC MM.1S cells have significantly decreased redox potential as measured by RealTime-Glo at 0.33, 1.0 and 3.0 μM TriC

(**Figure 41A**). We did not observe significant changes in RealTime-Glo luminescence from R20-9000 CD138 (-) or CD138 (+) cells treated with TriC for 24 h (**Figure 41B**). However, there was a trending decrease in the 3.0 μM . In another patient sample, R24-0553, CD138(+) cells treated with 2.0 and 3.0 μM TriC for 24 hours had significantly lower RealTime-Glo luminescence relative to vehicle-treated cells (**Figure 41C**). Also, CD138(+) cells treated with 1.0, 2.0 and 3.0 μM after both 48 and 72 h had significantly decreased RealTime-Glo luminescence compared to vehicle-treated cells (**Figure 41C**). RealTime-Glo expression was stable between 24 and 48 h in vehicle-treated cells but significantly decreased from 48 to 72 h, suggesting a decrease in redox potential after longer times in culture (**Figure 41C**). The short culture time *ex vivo* is common among many primary human cells, especially with MM because they lack essential growth factors provided by the microenvironment. It should be noted that the TriC used in the experiment with R24-0553 was from Millipore-Sigma (Cat. No. T4540), which is different from the rest of the experiments presented in this work.

The limited amount of CD138(+) cells consistently collected should also be considered in future studies, as well as characterizing the purity of the MACS sort with CD138 fluorescent labeling and flow cytometry. To further explore the efficacy of TriC treatment in patient samples, additional RealTime-Glo experiments should be conducted with more donors to establish an overall effect. Apoptosis assays should also be conducted as well as investigating genes of interest which appear to be modulated with TriC treatment and have been highlighted in the findings of this thesis (members of the ETC, and components of the ISR).

The data from R24-0553, combined with a trending negative response in R20-9000 suggest that TriC has a modest negative impact on the redox potential of CD138(+) cells derived from a MM patient. It is promising to see a similar response of primary MM cells from a donor and the MM.1S cell line, however these studies require samples from additional donors to make conclusions, especially given the varied response between R20-9000 and R24-0553. Whether this effect is observed in samples from additional patients, and whether this reduction in redox potential is directly linked to cell death in these cells should be one of the critical next steps of this work.

5.9. ACSLs, SREBP Signaling and MYC

Reports in hepatocellular carcinoma and MM related suggests that there is crosstalk between ACSL4 and ERK to stabilize MYC and activate the SREBP pathway^{270,402}. Given that we observed significant decreases in proteins related to ubiquitination like ubiquitin conjugating enzyme E2 V1 (**UBE2V1**) in TriC-treated MM.1S cells for 48 h in our proteomics data, observed increased *SREBPF* gene expression after 24 h of TriC treatment in MM.1S cells and have evidence of MAPK-related transcription, it would be interesting to test if TriC treatment alters MYC protein levels. Work in our lab has shown that the FABP family decreases MYC protein levels, so there may be a shared mechanism of fatty acid metabolism-related genes modulating the stability of this critical oncogene²⁸¹.

5.10 The ACSL-Adenylate Kinase Connection

One of the most significantly downregulated proteins in MM.1S cells treated with TriC for 48 h was adenylate kinase 2 (**AK2**). AK2 is a mitochondrial protein responsible for high energy phosphate transfer of mitochondrial ADP to form ATP. In many cancers,

it has been shown that this mitochondrial-derived ATP drives the conversion of glucose to lactate and therefore drives unregulated cellular energy usage⁴⁰³ and is usually accompanied by overexpression of hexokinase 2, and pyruvate kinase M2 the first and last enzymes in glycolysis⁴⁰³. Consequently, ADP is not converted to AMP, and the depleted AMP pool represses AMPK signaling. Repression of AMPK results in increased cell cycle progression and AMPK-regulated anabolic metabolism⁴⁰³. It has been shown that MM cells with the t(4;14) translocation (associated with a poorer prognosis) are dependent on AK2 due to overexpression of the histone methyltransferase, nuclear receptor binding SET domain protein 2 (**NSD2**) disruptions in the parallel ATP-generating creatine kinase pathway by driving S-adenosylmethionine away from creatine kinase⁴⁰⁴. Knockdown of AK2 in t(4;14) MM cell lines resulted in increased apoptotic-related proteins caspase 3 and BIM and impeded protein folding⁴⁰⁴. Paradoxically, knockdown of AK2 in in t(4;14) MM cells concurrent decreased protein levels of ATF4, DDIT3, XBP1s, suggesting that AK2 has a role in regulating the ER stress/ISR⁴⁰⁴ that may be independent from inducing cell death. There is not direct evidence but it is postulated that AK2-derived ATP can be utilized by proteins that aid in protein folding⁴⁰⁴. Additionally, they showed that AK2 knockdown in in t(4;14) MM cells had decreased NADP/H levels which ultimately led to replicative stress by the depletion of deoxyribonucleic acids. A suppression of AK2 in TriC-treated MM.1S cells would drive ADP to AMP formation to activate AMPK leading to repression of the cell cycle and anabolic processes. Our observations of decreased proliferation may be consistent with AMPK activation, but we also observed increases in key anabolic fatty acid metabolism genes like *FASN* and *ACACA*, suggesting that these genes may have been

upregulated in an AMPK-independent manner. Given the unknown status of AMPK activation upon TriC treatment in MM cells, it is critical to assess AMPK activation via phosphorylation of ACACA at Ser79. MM.1S cells treated with TriC may be attempting to compensate for the loss of mitochondrial-derived ATP by redirecting energy generation to other pathways like glycolysis. Paradoxically, MM.1S cells treated with TriC for 48 hours had increased HK2 but decreased PKM and triosephosphate isomerase (**TPI1**) which is responsible for the interconversion of glycerol-3-phosphate (**G3-P**) and dihydroxyacetone phosphate (**DHAP**). This suggests that glucose utilization is being directed to G3P and DHAP, which are important precursors for fatty acid metabolism and nucleotide synthesis. Taken together, our data suggests a strong rationale to further investigate the connection between the ACSL family and AK2.

6. BIBLIOGRAPHY

1. Siegel RL, Giaquinto AN, Jemal A. Cancer statistics, 2024. *CA. Cancer J. Clin.* 2024;74(1):12–49.
2. Bertazzi PA, Zocchetti C, Guercilena S, et al. Dioxin Exposure and Cancer Risk: A 15-Year Mortality Study after the “Seveso Accident.” *Epidemiology.* 1997;8(6):.
3. LeMasters GK, Genaidy AM, Succop P, et al. Cancer Risk Among Firefighters: A Review and Meta-analysis of 32 Studies. *J. Occup. Environ. Med.* 2006;48(11):.
4. Padala SA, Barsouk A, Barsouk A, et al. Epidemiology, Staging, and Management of Multiple Myeloma. *Med. Sci. (Basel, Switzerland).* 2021;9(1):1–14.
5. Birmann BM, Giovannucci E, Rosner B, Anderson KC, Colditz GA. Body mass index, physical activity, and risk of multiple myeloma. *Cancer Epidemiol. Biomarkers Prev.* 2007;16(7):1474–1478.
6. Marinac CR, Birmann BM, Lee I-M, et al. Body mass index throughout adulthood, physical activity, and risk of multiple myeloma: a prospective analysis in three large cohorts. *Br. J. Cancer.* 2018;(March):1.
7. Marinac CR, Suppan CA, Giovannucci E, et al. Elucidating Under-Studied Aspects of the Link Between Obesity and Multiple Myeloma: Weight Pattern, Body Shape Trajectory, and Body Fat Distribution. *JNCI cancer Spectr.* 2019;3(3):pkz044.
8. SEER*Explorer: An interactive website for SEER cancer statistics [Internet]. *Surveill. Res. Program, Natl. Cancer Inst.* .
9. Ozsan GH, Dispenzieri A. Serum free light chain analysis in multiple myeloma and plasma cell dyscrasias. *Expert Rev. Clin. Immunol.* 2011;7(1):65–73.
10. Kyrtsolis MC, Vassilakopoulos TP, Kafasi N, et al. Prognostic value of serum free light chain ratio at diagnosis in multiple myeloma. *Br. J. Haematol.* 2007;137(3):240–243.
11. Landgren O, Kyle RA, Pfeiffer RM, et al. Monoclonal gammopathy of undetermined significance (MGUS) consistently precedes multiple myeloma: A prospective study. *Blood.* 2009;113(22):5412–5417.
12. Rajkumar SV. Updated Diagnostic Criteria and Staging System for Multiple Myeloma. *Am. Soc. Clin. Oncol. Educ. B.* 2016;36:e418–e423.
13. Kyle RA, Therneau TM, Rajkumar SV, et al. Prevalence of monoclonal gammopathy of undetermined significance. *N. Engl. J. Med.* 2006;354(13):1362–1369.

14. Kyle RA, Rajkumar SV. Monoclonal gammopathy of undetermined significance and smouldering multiple myeloma: Emphasis on risk factors for progression. *Br. J. Haematol.* 2007;139(5):730–743.
15. Bladé J, Rosiñol L, Cibeira MT, de Larrea CF. Pathogenesis and progression of monoclonal gammopathy of undetermined significance. *Leukemia.* 2008;22(9):1651–1657.
16. Kyle RA, Durie BGM, Rajkumar S V., et al. Monoclonal gammopathy of undetermined significance (MGUS) and smoldering (asymptomatic) multiple myeloma: IMWG consensus perspectives risk factors for progression and guidelines for monitoring and management. *Leukemia.* 2010;24(6):1121–1127.
17. Lakshman A, Vincent Rajkumar S, Buadi FK, et al. Risk stratification of smoldering multiple myeloma incorporating revised IMWG diagnostic criteria. *Blood Cancer J.* 2018;8(6):.
18. Mateos MV, Kumar S, Dimopoulos MA, et al. International Myeloma Working Group risk stratification model for smoldering multiple myeloma (SMM). *Blood Cancer J.* 2020;10(10):.
19. Rajkumar SV, Merlini G, San Miguel JF. Haematological cancer: Redefining myeloma. *Nat. Rev. Clin. Oncol.* 2012;9(9):494–496.
20. Mateos M-V, Hernández M-T, Giraldo P, et al. Lenalidomide plus Dexamethasone for High-Risk Smoldering Multiple Myeloma. *N. Engl. J. Med.* 2013;369(5):438–447.
21. Rajkumar SV, Kumar S, Lonial S, Mateos MV. Smoldering multiple myeloma current treatment algorithms. *Blood Cancer J.* 2022;12(9):1–7.
22. Rasche L, Angtuaco EJ, Alpe TL, et al. The presence of large focal lesions is a strong independent prognostic factor in multiple myeloma. *Blood.* 2018;132(1):59–66.
23. Usmani SZ, Mitchell A, Waheed S, et al. Prognostic implications of serial 18-fluoro-deoxyglucose emission tomography in multiple myeloma treated with total therapy 3. *Blood.* 2013;121(10):1819–1823.
24. Lonial S, Anderson KC. Association of response endpoints with survival outcomes in multiple myeloma. *Leukemia.* 2014;28(2):258–268.
25. Burwick N, Sharma S. Glucocorticoids in multiple myeloma: past, present, and future. *Ann. Hematol.* 2019;98(1):19–28.
26. Stahn C, Buttgerit F. Genomic and nongenomic effects of glucocorticoids. *Nat. Clin. Pract. Rheumatol.* 2008;4(10):525–533.
27. Bera S, Greiner S, Choudhury A, et al. Dexamethasone-induced oxidative stress enhances myeloma cell radiosensitization while sparing normal bone marrow hematopoiesis. *Neoplasia.* 2010;12(12):980–992.

28. Liu W, Zhao Z, Na Y, et al. Dexamethasone-induced production of reactive oxygen species promotes apoptosis via endoplasmic reticulum stress and autophagy in MC3T3-E1 cells. *Int. J. Mol. Med.* 2018;41(4):2028–2036.
29. Moreau P, Attal M, Hulin C, et al. Bortezomib, thalidomide, and dexamethasone with or without daratumumab before and after autologous stem-cell transplantation for newly diagnosed multiple myeloma (CASSIOPEIA): a randomised, open-label, phase 3 study. *Lancet (London, England)*. 2019;394(10192):29–38.
30. Durie BGM, Hoering A, Sexton R, et al. Longer term follow-up of the randomized phase III trial SWOG S0777: bortezomib, lenalidomide and dexamethasone vs. lenalidomide and dexamethasone in patients (Pts) with previously untreated multiple myeloma without an intent for immediate autologous stem . *Blood Cancer J.* 2020;10(5):.
31. Moreau P, Masszi T, Grzasko N, et al. Oral Ixazomib, Lenalidomide, and Dexamethasone for Multiple Myeloma. *N. Engl. J. Med.* 2016;374(17):1621–1634.
32. Dimopoulos MA, Špička I, Quach H, et al. Ixazomib as Postinduction Maintenance for Patients With Newly Diagnosed Multiple Myeloma Not Undergoing Autologous Stem Cell Transplantation: The Phase III TOURMALINE-MM4 Trial. *J. Clin. Oncol. Off. J. Am. Soc. Clin. Oncol.* 2020;38(34):4030–4041.
33. Stewart AK, Rajkumar SV, Dimopoulos MA, et al. Carfilzomib, lenalidomide, and dexamethasone for relapsed multiple myeloma. *N. Engl. J. Med.* 2015;372(2):142–152.
34. Dimopoulos MA, Goldschmidt H, Niesvizky R, et al. Carfilzomib or bortezomib in relapsed or refractory multiple myeloma (ENDEAVOR): an interim overall survival analysis of an open-label, randomised, phase 3 trial. *Lancet. Oncol.* 2017;18(10):1327–1337.
35. Dimopoulos M, Quach H, Mateos M-V, et al. Carfilzomib, dexamethasone, and daratumumab versus carfilzomib and dexamethasone for patients with relapsed or refractory multiple myeloma (CANDOR): results from a randomised, multicentre, open-label, phase 3 study. *Lancet (London, England)*. 2020;396(10245):186–197.
36. Moreau P, Mateos M-V, Berenson JR, et al. Once weekly versus twice weekly carfilzomib dosing in patients with relapsed and refractory multiple myeloma (A.R.R.O.W.): interim analysis results of a randomised, phase 3 study. *Lancet. Oncol.* 2018;19(7):953–964.
37. Voorhees PM, Kaufman JL, Laubach J, et al. Daratumumab, lenalidomide, bortezomib, and dexamethasone for transplant-eligible newly diagnosed multiple myeloma: The GRIFFIN trial. *Blood.* 2020;136(8):936–945.

38. Dimopoulos MA, San-Miguel J, Belch A, et al. Daratumumab plus lenalidomide and dexamethasone versus lenalidomide and dexamethasone in relapsed or refractory multiple myeloma: Updated analysis of POLLUX. *Haematologica*. 2018;103(12):2088–2096.
39. Mateos MV, Sonneveld P, Hungria V, et al. Daratumumab, Bortezomib, and Dexamethasone Versus Bortezomib and Dexamethasone in Patients With Previously Treated Multiple Myeloma: Three-year Follow-up of CASTOR. *Clin. Lymphoma, Myeloma Leuk*. 2020;20(8):509–518.
40. Facon T, Kumar S, Plesner T, et al. Daratumumab plus Lenalidomide and Dexamethasone for Untreated Myeloma. *N. Engl. J. Med*. 2019;380(22):2104–2115.
41. Lokhorst HM, Plesner T, Laubach JP, et al. Targeting CD38 with Daratumumab Monotherapy in Multiple Myeloma. *N. Engl. J. Med*. 2015;373(13):1207–1219.
42. Lonial S, Dimopoulos M, Palumbo A, et al. Elotuzumab Therapy for Relapsed or Refractory Multiple Myeloma. *N. Engl. J. Med*. 2015;373(7):621–631.
43. Dimopoulos MA, Dytfeld D, Grosicki S, et al. Elotuzumab plus Pomalidomide and Dexamethasone for Multiple Myeloma. *N. Engl. J. Med*. 2018;379(19):1811–1822.
44. Grosicki S, Simonova M, Spicka I, et al. Once-per-week selinexor, bortezomib, and dexamethasone versus twice-per-week bortezomib and dexamethasone in patients with multiple myeloma (BOSTON): a randomised, open-label, phase 3 trial. *Lancet (London, England)*. 2020;396(10262):1563–1573.
45. Cavo M, Gay F, Beksac M, et al. Autologous haematopoietic stem-cell transplantation versus bortezomib-melphalan-prednisone, with or without bortezomib-lenalidomide-dexamethasone consolidation therapy, and lenalidomide maintenance for newly diagnosed multiple myeloma (EMN02/HO95): a mul. *Lancet. Haematol*. 2020;7(6):e456–e468.
46. Lonial S, Lee HC, Badros A, et al. Belantamab mafodotin for relapsed or refractory multiple myeloma (DREAMM-2): a two-arm, randomised, open-label, phase 2 study. *Lancet. Oncol*. 2020;21(2):207–221.
47. Raje N, Berdeja J, Lin Y, et al. Anti-BCMA CAR T-Cell Therapy bb2121 in Relapsed or Refractory Multiple Myeloma. *N. Engl. J. Med*. 2019;380(18):1726–1737.
48. Munshi NC, Anderson LDJ, Shah N, et al. Idecabtagene Vicleucel in Relapsed and Refractory Multiple Myeloma. *N. Engl. J. Med*. 2021;384(8):705–716.
49. Rajkumar SV, Harousseau JL, Durie B, et al. Consensus recommendations for the uniform reporting of clinical trials: Report of the International Myeloma Workshop Consensus Panel 1. *Blood*. 2011;117(18):4691–4695.
50. Bhatt P, Kloock C, Comenzo R. Relapsed/Refractory Multiple Myeloma: A Review of Available Therapies and Clinical Scenarios Encountered in Myeloma Relapse. *Curr. Oncol*. 2023;30(2):2322–2347.

51. Kumar S, Paiva B, Anderson KC, et al. International Myeloma Working Group consensus criteria for response and minimal residual disease assessment in multiple myeloma. *Lancet. Oncol.* 2016;17(8):e328–e346.
52. Altieri A, Chen B, Bermejo JL, Castro F, Hemminki K. Familial risks and temporal incidence trends of multiple myeloma. *Eur. J. Cancer.* 2006;42(11):1661–1670.
53. Broderick P, Chubb D, Johnson DC, et al. Common variation at 3p22.1 and 7p15.3 influences multiple myeloma risk. *Nat. Genet.* 2012;44(1):58–61.
54. Chubb D, Weinhold N, Broderick P, et al. Common variation at 3q26.2, 6p21.33, 17p11.2 and 22q13.1 influences multiple myeloma risk. *Nat. Genet.* 2013;45(10):1221–1225.
55. Weinhold N, Johnson DC, Rawstron AC, et al. Inherited genetic susceptibility to monoclonal gammopathy of unknown significance. *Blood.* 2014;123(16):2513–2517.
56. Vo JN, Wu YM, Mishler J, et al. The genetic heterogeneity and drug resistance mechanisms of relapsed refractory multiple myeloma. *Nat. Commun.* 2022;13(1):1–13.
57. Walker BA, Wardell CP, Murison A, et al. APOBEC family mutational signatures are associated with poor prognosis translocations in multiple myeloma. *Nat. Commun.* 2015;6:.
58. Zhan F, Huang Y, Colla S, et al. The molecular classification of multiple myeloma. *Blood.* 2006;108(6):2020–2028.
59. Walker BA, Wardell CP, Johnson DC, et al. Characterization of IGH locus breakpoints in multiple myeloma indicates a subset of translocations appear to occur in pregerminal center B cells. *Blood.* 2013;121(17):3413–3419.
60. Keats JJ, Reiman T, Maxwell CA, et al. In multiple myeloma, t(4;14)(p16;q32) is an adverse prognostic factor irrespective of FGFR3 expression. *Blood.* 2003;101(4):1520–1529.
61. Shaughnessy J, Gabrea A, Qi Y, et al. Cyclin D3 at 6p21 is dysregulated by recurrent chromosomal translocations to immunoglobulin loci in multiple myeloma. *Blood.* 2001;98(1):217–223.
62. Hanamura I, Iida S, Akano Y, et al. Ectopic expression of MAFB gene in human myeloma cells carrying (14;20) (q32;q11) chromosomal translocations. *Japanese J. Cancer Res.* 2001;92(6):638–644.
63. Hurt EM, Wiestner A, Rosenwald A, et al. Overexpression of c-maf is a frequent oncogenic event in multiple myeloma that promotes proliferation and pathological interactions with bone marrow stroma. *Cancer Cell.* 2004;5(2):191–199.
64. Pawlyn C, Melchor L, Murison A, et al. Coexistent hyperdiploidy does not abrogate poor prognosis in myeloma with adverse cytogenetics and may precede IGH translocations. *Blood.* 2015;125(5):831–840.

65. Chng WJ, Kumar S, VanWier S, et al. Molecular dissection of hyperdiploid multiple myeloma by gene expression profiling. *Cancer Res.* 2007;67(7):2982–2989.
66. Manier S, Salem KZ, Park J, et al. Genomic complexity of multiple myeloma and its clinical implications. *Nat. Rev. Clin. Oncol.* 2017;14(2):100–113.
67. Melchor L, Brioli A, Wardell CP, et al. Single-cell genetic analysis reveals the composition of initiating clones and phylogenetic patterns of branching and parallel evolution in myeloma. *Leukemia.* 2014;28(8):1705–1715.
68. Lohr JG, Stojanov P, Carter SL, et al. Widespread genetic heterogeneity in multiple myeloma: Implications for targeted therapy. *Cancer Cell.* 2014;25(1):91–101.
69. Walker BA, Boyle EM, Wardell CP, et al. Mutational spectrum, copy number changes, and outcome: Results of a sequencing study of patients with newly diagnosed myeloma. *J. Clin. Oncol.* 2015;33(33):3911–3920.
70. Uchiyama H, Barut BA, Chauhan D, Cannistra SA, Anderson KC. Characterization of adhesion molecules on human myeloma cell lines. *Blood.* 1992;80(9):2306–2314.
71. Uchiyama H, Barut BA, Mohrbacher AF, Chauhan D, Anderson KC. Adhesion of human myeloma-derived cell lines to bone marrow stromal cells stimulates interleukin-6 secretion. *Blood.* 1993;82(12):3712–3720.
72. Harmer D, Falank C, Reagan MR. Interleukin-6 Interweaves the Bone Marrow Microenvironment , Bone Loss , and Multiple Myeloma. 2019;9(January):1–15.
73. Morgan GJ, Child JA, Gregory WM, et al. Effects of zoledronic acid versus clodronic acid on skeletal morbidity in patients with newly diagnosed multiple myeloma (MRC Myeloma IX): secondary outcomes from a randomised controlled trial. *Lancet. Oncol.* 2011;12(8):743–752.
74. Silbermann R, Roodman GD. Myeloma bone disease: Pathophysiology and management. *J. Bone Oncol.* 2013;2(2):59–69.
75. Pearse RN, Sordillo EM, Yaccoby S, et al. Multiple myeloma disrupts the TRANCE/osteoprotegerin cytokine axis to trigger bone destruction and promote tumor progression. *Proc. Natl. Acad. Sci. U. S. A.* 2001;98(20):11581–11586.
76. Abe M, Kido S, Hiasa M, et al. BAFF and APRIL as osteoclast-derived survival factors for myeloma cells: a rationale for TACI-Fc treatment in patients with multiple myeloma. *Leukemia.* 2006;20(7):1313–1315.
77. Auziņa D, Beinaroviča I, Janicka-Kupra B, et al. Dickkopf-related protein 1 expression in bone marrow of multiple myeloma patients: correlation with bone disease and plasma cell malignancy type. *Exp. Oncol.* 2020;42(4):285–288.

78. van Bezooijen RL, Roelen BAJ, Visser A, et al. Sclerostin is an osteocyte-expressed negative regulator of bone formation, but not a classical BMP antagonist. *J. Exp. Med.* 2004;199(6):805–814.
79. Kaiser M, Mieth M, Liebisch P, et al. Serum concentrations of DKK-1 correlate with the extent of bone disease in patients with multiple myeloma. *Eur. J. Haematol.* 2008;80(6):490–494.
80. Li B, Shi M, Li J, et al. Elevated tumor necrosis factor- α suppresses TAZ expression and impairs osteogenic potential of Flk-1+ mesenchymal stem cells in patients with multiple myeloma. *Stem Cells Dev.* 2007;16(6):921–930.
81. Teramachi J, Miki H, Nakamura S, et al. Myeloma bone disease: pathogenesis and management in the era of new anti-myeloma agents. *J. Bone Miner. Metab.* 2023;41(3):388–403.
82. McDonald MM, Fairfield H, Falank C, Reagan MR, Reagan MR. Adipose, Bone, and Myeloma: Contributions from the Microenvironment. *Calcif. Tissue Int.* 2017;100(5):433–448.
83. Barbato A, Scandura G, Puglisi F, et al. Mitochondrial Bioenergetics at the Onset of Drug Resistance in Hematological Malignancies: An Overview. *Front. Oncol.* 2020;10(December):1–13.
84. Groll M, Ditzel L, Lowe J, et al. Structure of 20S proteasome from yeast at 2.4Å resolution. *Nature.* 1997;386(April):463–471.
85. Hideshima T, Richardson P, Chauhan D, et al. The proteasome inhibitor PS-341 inhibits growth, induces apoptosis, and overcomes drug resistance in human multiple myeloma cells. *Cancer Res.* 2001;61(7):3071–3076.
86. Lopes UG, Erhardt P, Yao R, Cooper GM. P53-Dependent Induction of Apoptosis By Proteasome Inhibitors. *J. Biol. Chem.* 1997;272(20):12893–12896.
87. Herrmann JL, Briones F, Brisbay S, Logothetis CJ, McDonnell TJ. Prostate carcinoma cell death resulting from inhibition of proteasome activity is independent of functional Bcl-2 and p53. *Oncogene.* 1998;17(22):2889–2899.
88. Obeng EA, Carlson LM, Gutman DM, et al. Proteasome inhibitors induce a terminal unfolded protein response in multiple myeloma cells. *Blood.* 2006;107(12):4907–4916.
89. Palombella VJ, Rando OJ, Goldberg AL, Maniatis T. The ubiquitin-proteasome pathway is required for processing the NF- κ B1 precursor protein and the activation of NF- κ B. Palombella. *Cell.* 1994;78:773.pdf. 1994;78:773–785.
90. Accardi F, Toscani D, Bolzoni M, et al. Mechanism of action of bortezomib and the new proteasome inhibitors on myeloma cells and the bone microenvironment: Impact on myeloma-induced alterations of bone remodeling. *Biomed Res. Int.* 2015;2015:.

91. Lu G, Middleton RE, Sun H, et al. The myeloma drug lenalidomide promotes the cereblon-dependent destruction of ikaros proteins. *Science* (80-). 2014;343(6168):305–309.
92. Krönke J, Fink EC, Hollenbach PW, et al. Lenalidomide induces ubiquitination and degradation of CK1 α in del(5q) MDS. *Nature*. 2015;523(7559):183–188.
93. Ito T, Ando H, Suzuki T, et al. Identification of a primary target of thalidomide teratogenicity. *Science*. 2010;327(5971):1345–1350.
94. Rajkumar SV, Rosiñol L, Hussein M, et al. Multicenter, randomized, double-blind, placebo-controlled study of thalidomide plus dexamethasone compared with dexamethasone as initial therapy for newly diagnosed multiple myeloma. *J. Clin. Oncol. Off. J. Am. Soc. Clin. Oncol.* 2008;26(13):2171–2177.
95. Dimopoulos MA, Chen C, Spencer A, et al. Long-term follow-up on overall survival from the MM-009 and MM-010 phase III trials of lenalidomide plus dexamethasone in patients with relapsed or refractory multiple myeloma. *Leukemia*. 2009;23(11):2147–2152.
96. Rajkumar SV, Jacobus S, Callander NS, et al. Lenalidomide plus high-dose dexamethasone versus lenalidomide plus low-dose dexamethasone as initial therapy for newly diagnosed multiple myeloma: an open-label randomised controlled trial. *Lancet. Oncol.* 2010;11(1):29–37.
97. Leleu X, Attal M, Arnulf B, et al. Pomalidomide plus low-dose dexamethasone is active and well tolerated in bortezomib and lenalidomide–refractory multiple myeloma: Intergroupe Francophone du Myélome 2009-02. *Blood*. 2013;121(11):1968–1975.
98. Miguel JS, Weisel K, Moreau P, et al. Pomalidomide plus low-dose dexamethasone versus high-dose dexamethasone alone for patients with relapsed and refractory multiple myeloma (MM-003): a randomised, open-label, phase 3 trial. *Lancet. Oncol.* 2013;14(11):1055–1066.
99. Richardson PG, Siegel DS, Vij R, et al. Pomalidomide alone or in combination with low-dose dexamethasone in relapsed and refractory multiple myeloma: A randomized phase 2 study. *Blood*. 2014;123(12):1826–1832.
100. de Weers M, Tai Y-T, van der Veer MS, et al. Daratumumab, a Novel Therapeutic Human CD38 Monoclonal Antibody, Induces Killing of Multiple Myeloma and Other Hematological Tumors. *J. Immunol.* 2011;186(3):1840–1848.
101. Overdijk MB, Verploegen S, Bögels M, et al. Antibody-mediated phagocytosis contributes to the anti-tumor activity of the therapeutic antibody daratumumab in lymphoma and multiple myeloma. *MAbs*. 2015;7(2):311–320.
102. Singla A, Kumar S. Current advances in non-proteasome inhibitor-based approaches to the treatment of relapsed/refractory multiple myeloma. *Oncology (Williston Park)*. 2011;25 Suppl 2:32–43.

103. Balasa B, Yun R, Belmar NA, et al. Elotuzumab enhances natural killer cell activation and myeloma cell killing through interleukin-2 and TNF- α pathways. *Cancer Immunol. Immunother.* 2015;64(1):61–73.
104. Mo CC, Yee AJ, Midha S, et al. Selinexor: Targeting a novel pathway in multiple myeloma. *EJHaem.* 2023;4(3):792–810.
105. Povirk LF, Shuker DE. DNA damage and mutagenesis induced by nitrogen mustards. *Mutat. Res. Genet. Toxicol.* 1994;318(3):205–226.
106. Bhatia M, Bonnet D, Kapp U, et al. Quantitative analysis reveals expansion of human hematopoietic repopulating cells after short-term ex vivo culture. *J. Exp. Med.* 1997;186(4):619–624.
107. Goardon N, Marchi E, Atzberger A, et al. Coexistence of LMPP-like and GMP-like leukemia stem cells in acute myeloid leukemia. *Cancer Cell.* 2011;19(1):138–152.
108. Ye M, Zhang H, Yang H, et al. Hematopoietic Differentiation Is Required for Initiation of Acute Myeloid Leukemia. *Cell Stem Cell.* 2015;17(5):611–623.
109. Grimwade D, Walker H, Oliver F, et al. The importance of diagnostic cytogenetics on outcome in AML: Analysis of 1,612 patients entered into the MRC AML 10 trial. *Blood.* 1998;92(7):2322–2333.
110. Meyers J, Yu Y, Kaye JA, Davis KL. Medicare fee-for-service enrollees with primary acute myeloid leukemia: An analysis of treatment patterns, survival, and healthcare resource utilization and costs. *Appl. Health Econ. Health Policy.* 2013;11(3):275–286.
111. Ley TJ, Miller C, Ding L, et al. Genomic and epigenomic landscapes of adult de novo acute myeloid leukemia. *N. Engl. J. Med.* 2013;368(22):2059–2074.
112. Bakhtiyari M, Liaghat M, Aziziyan F, et al. The role of bone marrow microenvironment (BMM) cells in acute myeloid leukemia (AML) progression: immune checkpoints, metabolic checkpoints, and signaling pathways. *BioMed Central*; 2023.
113. Geetha N, Sreelesh KP, Priya MJ, Lali VS, Rekha N. Osteolytic Bone Lesions - A Rare Presentation of AML M6. *Mediterr. J. Hematol. Infect. Dis.* 2015;7(1):e2015017.
114. Nair R, Gupta P, Shanmugam M. Mitochondrial metabolic determinants of multiple myeloma growth, survival, and therapy efficacy. *Front. Oncol.* 2022;12(September):1–19.
115. Rich PR, Maréchal A. The mitochondrial respiratory chain. *Essays Biochem.* 2010;47:1–23.
116. Nelson DL, Cox MM. *Lehninger Principles of Biochemistry.* New York, NY: W.H. Freeman and Company; 2008.

117. Boese AC, Kang S. Mitochondrial metabolism-mediated redox regulation in cancer progression. *Redox Biol.* 2021;42:101870.
118. Nogueira V, Hay N. Molecular pathways: Reactive oxygen species homeostasis in cancer cells and implications for cancer therapy. *Clin. Cancer Res.* 2013;19(16):4309–4314.
119. Dan Dunn J, Alvarez LAJ, Zhang X, Soldati T. Reactive oxygen species and mitochondria: A nexus of cellular homeostasis. *Redox Biol.* 2015;6:472–485.
120. Cheung EC, Vousden KH. The role of ROS in tumour development and progression. *Nat. Rev. Cancer.* 2022;22(5):280–297.
121. Martínez-Reyes I, Chandel NS. Mitochondrial TCA cycle metabolites control physiology and disease. *Nat. Commun.* 2020;11(1):1–11.
122. Bhutia YD, Babu E, Ramachandran S, Ganapathy V. Amino acid transporters in cancer and their relevance to “glutamine addiction”: Novel Targets for the design of a new class of anticancer drugs. *Cancer Res.* 2015;75(9):1782–1788.
123. Warburg O. On the origin of cancer cells. *Science.* 1956;123(3191):309–314.
124. Warburg O. On respiratory impairment in cancer cells. *Science.* 1956;124(3215):269–270.
125. Hanahan D, Weinberg RA. Hallmarks of cancer: The next generation. *Cell.* 2011;144(5):.
126. Wei C, Bajpai R, Sharma H, et al. Development of GLUT4-selective antagonists for multiple myeloma therapy. *Eur. J. Med. Chem.* 2017;139:573–586.
127. Deberardinis RJ, Lum JJ, Hatzivassiliou G, Thompson CB. Review The Biology of Cancer : Metabolic Reprogramming Fuels Cell Growth and Proliferation. 2008;(January):11–20.
128. Jones RG, Thompson CB. Tumor suppressors and cell metabolism : a recipe for cancer growth. 2009;(514):537–548.
129. Hsu PP, Sabatini DM. Essay Cancer Cell Metabolism : Warburg and Beyond. 2008;703–707.
130. Schwartzenberg-bar-yoseph F, Armoni M, Karnieli E. The Tumor Suppressor p53 Down-Regulates Glucose Transporters GLUT1 and GLUT4 Gene Expression. 2004;2(1):2627–2633.
131. Bensaad K, Tsuruta A, Selak MA, et al. TIGAR , a p53-Inducible Regulator of Glycolysis and Apoptosis. 2006;53:107–120.
132. Gavriatopoulou M, Paschou SA, Ntanasis-stathopoulos I, Dimopoulos MA. Metabolic disorders in multiple myeloma. *Int. J. Mol. Sci.* 2021;22(21):.

133. Fantin VR, St-pierre J, Leder P. Attenuation of LDH-A expression uncovers a link between glycolysis , mitochondrial physiology , and tumor maintenance. 2006;(June):425–434.
134. Wang C, Youle RJ. The Role of Mitochondria in Apoptosis *. 2009;95–118.
135. Sharma A, Boise LH, Shanmugam M. Cancer Metabolism and the Evasion of Apoptotic Cell Death. 2019;1–20.
136. Rosen ED, Spiegelman BM. What We Talk About When We Talk About Fat. *Cell*. 2014;156(1–2):20–44.
137. Kozak LP, Koza RA. The Genetics of Brown Adipose Tissue. *Genes Obes*. 2010;94(10):75–123.
138. Giralt M, Villarroya F. White, brown, beige/brite: Different adipose cells for different functions? *Endocrinology*. 2013;154(9):2992–3000.
139. Horowitz MC, Berry R, Holtrup B, et al. Bone marrow adipocytes. *Adipocyte*. 2017;6(3):193–204.
140. Costa RM, Neves KB, Tostes RC, Lobato NS. Perivascular Adipose Tissue as a Relevant Fat Depot for Cardiovascular Risk in Obesity . *Front. Physiol.* . 2018;9:253.
141. Pischon T, Boeing H, Hoffmann K, et al. General and abdominal adiposity and risk of death in Europe. *N. Engl. J. Med*. 2008;359(20):2105–2120.
142. Pou KM, Massaro JM, Hoffmann U, et al. Visceral and subcutaneous adipose tissue volumes are cross-sectionally related to markers of inflammation and oxidative stress: the Framingham Heart Study. *Circulation*. 2007;116(11):1234–1241.
143. McLaughlin T, Lamendola C, Liu A, Abbasi F. Preferential fat deposition in subcutaneous versus visceral depots is associated with insulin sensitivity. *J. Clin. Endocrinol. Metab*. 2011;96(11):E1756-60.
144. Olzmann JA. Dynamics and functions of lipid droplets. *Nat. Rev. Mol. Cell Biol.* .
145. Vaughan M, Berger JE, Steinberg D. Hormone-Sensitive Lipase and Monoglyceride Lipase Activities in Adipose Tissue. *J. Biol. Chem*. 1964;239:401–409.
146. Mitrou P, Raptis SA, Dimitriadis G. Insulin action in morbid obesity: a focus on muscle and adipose tissue. *Hormones (Athens)*. 2013;12(2):201–213.
147. Olson AL. Regulation of GLUT4 and Insulin-Dependent Glucose Flux. *ISRN Mol. Biol*. 2012;2012:856987.
148. Shen W-J, Patel S, Miyoshi H, Greenberg AS, Kraemer FB. Functional interaction of hormone-sensitive lipase and perilipin in lipolysis. *J. Lipid Res*. 2009;50(11):2306–2313.

149. Sakaguchi M, Fujisaka S, Cai W, et al. Adipocyte Dynamics and Reversible Metabolic Syndrome in Mice with an Inducible Adipocyte-Specific Deletion of the Insulin Receptor. *Cell Metab.* 2017;25(2):448–462.
150. Cook KS, Groves DL, Min HYEY, Spiegelman BM. A developmentally regulated mRNA from 3T3 adipocytes encodes a novel serine protease homologue. 1985;82(October):6480–6484.
151. Zhang Y, Proenca R, Maffei M, et al. Positional cloning of the mouse obese gene and its human homologue. 1994;372(DECEMBER):
152. Hotamisligil GS, Shargill NS SB. Adipose Expression of Tumor Necrosis Factor- α : Direct Role in Obesity-Linked Insulin Resistance Author (s): Gökhan S . Hotamisligil , Narinder S . Shargill and Bruce M . Spiegelman Published by : American Association for the Advancement of Science Stab. *Science (80-)*. 1993;259(5091):87–91.
153. Frederich RC, Lowell BB, Flier JS, Lowell BB, Flier JS. Expression of ob mRNA and its encoded protein in rodents . Impact of nutrition and obesity . Find the latest version : Expression of ob mRNA and its Encoded Protein in Rodents. 1995;96(3):1658–1663.
154. Weigle DS, Raymond C, Kuijper JL. Recombinant ob protein reduces feeding and body weight in the ob / ob mouse . Recombinant ob Protein Reduces Feeding and Body Weight in the. 1995;96(4):2065–2070.
155. Krug AW, Ehrhart-Bornstein M. Newly discovered endocrine functions of white adipose tissue: Possible relevance in obesity-related diseases. *Cell. Mol. Life Sci.* 2005;62(12):1359–1362.
156. Minokoshi Y, Kim YB, Peroni OD, et al. Leptin stimulates fatty-acid oxidation by activating AMP-activated protein kinase. *Nature.* 2002;415(6869):339–343.
157. Asilmaz E, Cohen P, Miyazaki M, et al. Site and mechanism of leptin action in a rodent form of congenital lipodystrophy. *J. Clin. Invest.* 2004;113(3):414–424.
158. Kubota N, Terauchi Y, Yamauchi T, et al. Disruption of adiponectin causes insulin resistance and neointimal formation. *J. Biol. Chem.* 2002;277(29):25863–25866.
159. Komuro R, Matsuzawa Y, Nagaretani H, et al. Diet-induced insulin resistance in mice lacking adiponectin/ACRP30. *Nat. Med.* 2002;8(7):731–737.
160. Shibata R, Ouchi N, Ito M, et al. Adiponectin-mediated modulation of hypertrophic signals in the heart. *Nat. Med.* 2004;10(12):1384–1389.
161. Yamauchi T, Kamon J, Ito Y, et al. Cloning of adiponectin receptors that mediate antidiabetic metabolic effects. *Nature.* 2003;423(6941):762–769.
162. Pajvani UB, Du X, Combs TP, et al. Structure-function studies of the adipocyte-secreted hormone Acrp30/adiponectin. Implications fpr metabolic regulation and bioactivity. *J. Biol. Chem.* 2003;278(11):9073–9085.

163. Tsao T-S, Murrey HE, Hug C, Lee DH, Lodish HF. Oligomerization state-dependent activation of NF-kappa B signaling pathway by adipocyte complement-related protein of 30 kDa (Acrp30). *J. Biol. Chem.* 2002;277(33):29359–29362.
164. Tsao T-S, Tomas E, Murrey HE, et al. Role of disulfide bonds in Acrp30/adiponectin structure and signaling specificity. Different oligomers activate different signal transduction pathways. *J. Biol. Chem.* 2003;278(50):50810–50817.
165. Jung SM, Sanchez-Gurmaches J, Guertin DA. Brown Adipose Tissue Development and Metabolism. 2018;1–34.
166. Cypess AM, Lehman S, Williams G, et al. Identification and importance of brown adipose tissue in adult humans. *N. Engl. J. Med.* 2009;360(15):1509–1517.
167. Sacks H, Symonds ME. Anatomical locations of human brown adipose tissue: Functional relevance and implications in obesity and type 2 diabetes. *Diabetes.* 2013;62(6):1783–1790.
168. Enerback S, Jacobsson A, Simpson E, et al. Mice lacking mitochondrial uncoupling protein are cold-sensitive but not obese. [5]-[5].
169. Fedorenko A, Lishko P V., Kirichok Y. Mechanism of fatty-acid-dependent UCP1 uncoupling in brown fat mitochondria. *Cell.* 2012;151(2):400–413.
170. Seale P, Kajimura S, Yang W, et al. Transcriptional Control of Brown Fat Determination by PRDM16. *Cell Metab.* 2007;6(1):38–54.
171. Puigserver P, Wu Z, Park CW, et al. A cold-inducible coactivator of nuclear receptors linked to adaptive thermogenesis. *Cell.* 1998;92(6):829–839.
172. Timmons JA, Wennmalm K, Larsson O, et al. Myogenic gene expression signature establishes that brown and white adipocytes originate from distinct cell lineages. *Proc. Natl. Acad. Sci.* 2007;104(11):4401–4406.
173. Young P, Arch JRS, Ashwell M. Brown adipose tissue in the parametrial fat pad of the mouse. *FEBS Lett.* 1984;167(1):10–14.
174. Guerra C, Koza RA, Yamashita H, Walsh K, Kozak LP. Emergence of brown adipocytes in white fat in mice is under genetic control. Effects on body weight and adiposity. *J. Clin. Invest.* 1998;102(2):412–420.
175. Xue B, Rim J-S, Hogan JC, et al. Genetic variability affects the development of brown adipocytes in white fat but not in interscapular brown fat. *J. Lipid Res.* 2006;48(1):41–51.
176. López-Soriano FJ, Fernández-López JA, Mampel T, et al. Amino acid and glucose uptake by rat brown adipose tissue. Effect of cold-exposure and acclimation. *Biochem. J.* 1988;252(3):843 LP – 849.

177. Scheller EL, Troiano N, Vanhoutan JN, et al. Use of osmium tetroxide staining with microcomputerized tomography to visualize and quantify bone marrow adipose tissue in vivo. *Methods Enzymol.* 2014;537:123–39.
178. Lecka-Czernik B, Moerman EJ, Grant DF, et al. Divergent effects of selective peroxisome proliferator-activated receptor-gamma 2 ligands on adipocyte versus osteoblast differentiation. *Endocrinology.* 2002;143(6):2376–2384.
179. Ackert-Bicknell CL, Shockley KR, Horton LG, et al. Strain-specific effects of rosiglitazone on bone mass, body composition, and serum insulin-like growth factor-I. *Endocrinology.* 2009;150:1330–1340.
180. Yagi M, Arentsen L, Shanley RM, et al. A Dual-Radioisotope Hybrid Whole-Body Micro-Positron Emission Tomography/Computed Tomography System Reveals Functional Heterogeneity and Early Local and Systemic Changes Following Targeted Radiation to the Murine Caudal Skeleton. *Calcif. Tissue Int.* 2014;94(5):544–552.
181. Bolan PJ, Arentsen L, Sueblinvong T, et al. Water–fat MRI for assessing changes in bone marrow composition due to radiation and chemotherapy in gynecologic cancer patients. *J. Magn. Reson. Imaging.* 2013;38(6):1578–1584.
182. Doucette CR, Horowitz MC, Berry R, et al. A High Fat Diet Increases Bone Marrow Adipose Tissue (MAT) But Does Not Alter Trabecular or Cortical Bone Mass in C57BL/6J Mice. *J. Cell. Physiol.* 2015;230(9):2032–7.
183. Bredella MA, Fazeli PK, Daley SM, et al. Marrow fat composition in anorexia nervosa. *Bone.* 2014;66:199–204.
184. Ambrosi TH, Scialdone A, Graja A, et al. Adipocyte Accumulation in the Bone Marrow during Obesity and Aging Impairs Stem Cell-Based Hematopoietic and Bone Regeneration. *Cell Stem Cell.* 2017;20(6):771-784.e6.
185. Chen J, Shi Y, Regan J, et al. Osx-Cre targets multiple cell types besides osteoblast lineage in postnatal mice. *PLoS One.* 2014;9(1):e85161.
186. Ohyama K, Matsumoto Y, Nishimiya K, et al. Increased Coronary Perivascular Adipose Tissue Volume in Patients With Vasospastic Angina. *Circ. J.* 2016;80(7):1653–1656.
187. Folkesson M, Vorkapic E, Gulbins E, et al. Inflammatory cells, ceramides, and expression of proteases in perivascular adipose tissue adjacent to human abdominal aortic aneurysms. *J. Vasc. Surg.* 2017;65(4):1171-1179.e1.
188. Drosos I, Chalikias G, Pavlaki M, et al. Differences between perivascular adipose tissue surrounding the heart and the internal mammary artery: possible role for the leptin-inflammation-fibrosis-hypoxia axis. *Clin. Res. Cardiol.* 2016;105(11):887–900.
189. Ozen G, Daci A, Norel X, Topal G. Human perivascular adipose tissue dysfunction as a cause of vascular disease: Focus on vascular tone and wall remodeling. *Eur. J. Pharmacol.* 2015;766:16–24.

190. Maenhaut N, Van de Voorde J. Regulation of vascular tone by adipocytes. *BMC Med.* 2011;9:25.
191. Miao C-Y, Li Z-Y. The role of perivascular adipose tissue in vascular smooth muscle cell growth. *Br. J. Pharmacol.* 2012;165(3):643–658.
192. Takaoka M, Suzuki H, Shioda S, et al. Endovascular injury induces rapid phenotypic changes in perivascular adipose tissue. *Arterioscler. Thromb. Vasc. Biol.* 2010;30(8):1576–1582.
193. Salgado-Somoza A, Teijeira-Fernández E, Fernández ÁL, et al. Proteomic analysis of epicardial and subcutaneous adipose tissue reveals differences in proteins involved in oxidative stress. *Am. J. Physiol. Circ. Physiol.* 2010;299(1):H202–H209.
194. Imaizumi K. Diet and atherosclerosis in apolipoprotein E-deficient mice. *Biosci. Biotechnol. Biochem.* 2011;75(6):1023–1035.
195. Öhman MK, Luo W, Wang H, et al. Perivascular visceral adipose tissue induces atherosclerosis in apolipoprotein E deficient mice. *Atherosclerosis.* 2011;219(1):33–39.
196. Chang L, Villacorta L, Li R, et al. Loss of perivascular adipose tissue on peroxisome proliferator-activated receptor- γ deletion in smooth muscle cells impairs intravascular thermoregulation and enhances atherosclerosis. *Circulation.* 2012;126(9):1067–1078.
197. Guzik B, Sagan A, Ludew D, et al. Mechanisms of oxidative stress in human aortic aneurysms--association with clinical risk factors for atherosclerosis and disease severity. *Int. J. Cardiol.* 2013;168(3):2389–2396.
198. Boucher JM, Robich M, Scott SS, et al. Rab27a Regulates Human Perivascular Adipose Progenitor Cell Differentiation. 2018;519–530.
199. Kershaw EE, Flier JS. Adipose Tissue as an Endocrine Organ. 2004;89(6):2548–2556.
200. Bråkenhielm E, Cao R, Gao B, et al. Angiogenesis inhibitor, TNP-470, prevents diet induced and genetic obesity in mice. *Circ. Res.* 2004;94(12):1579–1588.
201. Cao Y. Angiogenesis modulates adipogenesis and obesity. *J. Clin. Invest.* 2007;71(9):1–22.
202. Klötting N, Blüher M. Adipocyte dysfunction, inflammation and metabolic syndrome. *Rev. Endocr. Metab. Disord.* 2014;15(4):277–287.
203. Marette A. Mediators of cytokine-induced insulin resistance in obesity and other inflammatory settings. *Curr. Opin. Clin. Nutr. Metab. Care.* 2002;5(4):377–383.
204. Oh DY, Morinaga H, Talukdar S, Bae EJ, Olefsky JM. Increased macrophage migration into adipose tissue in obese mice. *Diabetes.* 2012;61(2):346–354.

205. Berg AH, Scherer PE. Adipose tissue, inflammation, and cardiovascular disease. *Circ. Res.* 2005;96(9):939–949.
206. Lau, D. C.W., Dhillon K, Yan H, Szmitko P, Verma S. Adipokines: molecular links between obesity and atherosclerosis. 2012;(Cvd):
207. Ng M, Fleming T, Robinson M, et al. Global, regional, and national prevalence of overweight and obesity in children and adults during 1980-2013: A systematic analysis for the Global Burden of Disease Study 2013. *Lancet.* 2014;384(9945):766–781.
208. Cawley J, Meyerhoefer C. The medical care costs of obesity: An instrumental variables approach. *J. Health Econ.* 2012;31(1):219–230.
209. Abdullah A, Peeters A, de Courten M, Stoelwinder J. The magnitude of association between overweight and obesity and the risk of diabetes: A meta-analysis of prospective cohort studies. *Diabetes Res. Clin. Pract.* 2010;89(3):309–319.
210. Willett WC, Rimm EB, Flint AJ, et al. Excess Weight and the Risk of Incident Coronary Heart Disease Among Men and Women. *Obesity.* 2009;18(2):377–383.
211. Polednak AP. Estimating the number of U.S. incident cancers attributable to obesity and the impact on temporal trends in incidence rates for obesity-related cancers. *Cancer Detect. Prev.* 2008;32(3):190–199.
212. Groß JP, Nattenmüller J, Hemmer S, et al. Body fat composition as predictive factor for treatment response in patients with newly diagnosed multiple myeloma - subgroup analysis of the prospective GMMG MM5 trial. *Oncotarget.* 2017;8(40):68460–68471.
213. Wallin A, Larsson SC. Body mass index and risk of multiple myeloma: A meta-analysis of prospective studies. *Eur. J. Cancer.* 2011;47(11):1606–1615.
214. Hofmann JN, Moore SC, Lim U, et al. Body mass index and physical activity at different ages and risk of multiple myeloma in the NIH-AARP diet and health study. *Am. J. Epidemiol.* 2013;177(8):776–86.
215. Beason TS, Chang S-H, Sanfilippo KM, et al. Influence of Body Mass Index on Survival in Veterans With Multiple Myeloma. *Oncologist.* 2013;18(10):1074–1079.
216. Teras LR, Kitahara CM, Birmann BM, et al. Body size and multiple myeloma mortality: a pooled analysis of 20 prospective studies. *Br. J. Haematol.* 2014;166(5):667–76.
217. Marinac CR, Birmann BM. Rising cancer incidence in younger adults: is obesity to blame? *Lancet. Public Heal.* 2019;4(3):e119–e120.
218. Serra D, Mera P, Malandrino MI, Mir JF, Herrero L. Mitochondrial fatty acid oxidation in obesity. *Antioxidants Redox Signal.* 2013;19(3):269–284.
219. Engin A. Obesity and Lipotoxicity. 2017.

220. Marques-Mourlet C, Di Iorio R, Fairfield H, Reagan MR. Obesity and myeloma: Clinical and mechanistic contributions to disease progression. *Front. Endocrinol. (Lausanne)*. 2023;14(February):1–13.
221. Khandekar MJ, Cohen P, Spiegelman BM. Molecular mechanisms of cancer development in obesity. *Nat. Rev. Cancer*. 2011;11(12):886–895.
222. Koza RA, Nikonova L, Hogan J, et al. Changes in gene expression foreshadow diet-induced obesity in genetically identical mice. *PLoS Genet*. 2006;2(5):e81.
223. Fehlert E, Wagner R, Ketterer C, et al. Genetic determination of body fat distribution and the attributive influence on metabolism. *Obesity (Silver Spring)*. 2017;25(7):1277–1283.
224. Lehnig AC, Stanford KI. Exercise-induced adaptations to white and brown adipose tissue. *J. Exp. Biol*. 2018;221(Pt Suppl 1):
225. Caers J, Deleu S, Belaid Z, et al. Neighboring adipocytes participate in the bone marrow microenvironment of multiple myeloma cells [11]. *Leukemia*. 2007;21(7):1580–1584.
226. Morris E V., Suchacki KJ, Hocking J, et al. Myeloma Cells Down-Regulate Adiponectin in Bone Marrow Adipocytes Via TNF-Alpha. *J. Bone Miner. Res*. 2019;00(00):1–14.
227. Fairfield H, Falank C, Farrell M, et al. Development of a 3D bone marrow adipose tissue model. *Bone*. 2018;
228. Fairfield H, Costa S, Falank C, et al. Multiple Myeloma Cells Alter Adipogenesis, Increase Senescence-Related and Inflammatory Gene Transcript Expression, and Alter Metabolism in Preadipocytes. *Front. Oncol*. 2021;10(February):1–20.
229. Fairfield H, Dudakovic A, Khatib CM, et al. Myeloma-Modified Adipocytes Exhibit Metabolic Dysfunction and a Senescence-Associated Secretory Phenotype. *Cancer Res*. 2021;81(3):634–647.
230. Li Z, Liu H, He J, et al. Acetyl-CoA Synthetase 2: A Critical Linkage in Obesity-Induced Tumorigenesis in Myeloma. *Cell Metab*. 2021;33(1):78-93.e7.
231. Caers J, Deleu S, Belaid Z, et al. Neighboring adipocytes participate in the bone marrow microenvironment of multiple myeloma cells. *Leukemia*. 2007;21(7):1580–4.
232. Yu W, Cao D-D, Li Q, et al. Adipocytes secreted leptin is a pro-tumor factor for survival of multiple myeloma under chemotherapy. *Oncotarget*. 2016;7(52):86075–86086.
233. Reseland JE, Reppe S, Olstad OK, et al. Abnormal adipokine levels and leptin-induced changes in gene expression profiles in multiple myeloma. *Eur. J. Haematol*. 2009;83(5):460–70.

234. Fowler JA, Lwin ST, Drake MT, et al. Host-derived adiponectin is tumor-suppressive and a novel therapeutic target for multiple myeloma and the associated bone disease. *Blood*. 2011;118(22):5872–82.
235. Olechnowicz SWZ, Weivoda MM, Lwin ST, et al. Multiple myeloma increases nerve growth factor and other pain-related markers through interactions with the bone microenvironment. 2019;(September):1–11.
236. Liu Z, Liu H, Li Y, et al. Adiponectin inhibits the differentiation and maturation of osteoclasts via the mTOR pathway in multiple myeloma. *Int. J. Mol. Med*. 2020;45(4):1112–1120.
237. Zeyda M, Farmer D, Aszmann O, et al. Human adipose tissue macrophages are of an anti-inflammatory phenotype but capable of excessive pro-inflammatory mediator production. *Int. J. Obes*. 2007;31(9):1420–1428.
238. Nedal TMV, Moen SH, Roseth IA, et al. Diet-induced obesity reduces bone marrow T and B cells and promotes tumor progression in a transplantable V κ *MYC model of multiple myeloma. *Sci. Rep*. 2024;14(1):1–7.
239. Kawano M, Hirano T, Matsuda T, et al. Autocrine generation and requirement of BSF-2/IL-6 for human multiple myelomas. *Nature*. 1988;332(6159):83–5.
240. Ge N-L, Rudikoff S. Insulin-like growth factor I is a dual effector of multiple myeloma cell growth. *Blood*. 2000;96(8):2856–2861.
241. Ferlin M, Noraz N, Hertogh C, et al. Insulin-like growth factor induces the survival and proliferation of myeloma cells through an interleukin-6-independent transduction pathway. *Br. J. Haematol*. 2000;111(2):626–634.
242. Qiang YW, Yao L, Tosato G, Rudikoff S. Insulin-like growth factor I induces migration and invasion of human multiple myeloma cells. *Blood*. 2004;103(1):301–308.
243. Panaroni C, Fulzele K, Mori T, Onyewadume C, Raje NS. Multiple Myeloma Cells Induce Lipolysis in Adipocytes and Uptake Fatty Acids through Fatty Acid Transporter Proteins. *Blood*. 2020;136(Supplement 1):41–42.
244. Marlein CR, Piddock RE, Mistry JJ, et al. CD38-driven mitochondrial trafficking promotes bioenergetic plasticity in multiple myeloma. *Cancer Res*. 2019;79(9):2285–2297.
245. Haczeyni F, Barn V, Mridha AR, et al. Exercise improves adipose function and inflammation and ameliorates fatty liver disease in obese diabetic mice. *Obesity (Silver Spring)*. 2015;23(9):1845–1855.
246. Strawford A, Antelo F, Christiansen M, Hellerstein MK. Adipose tissue triglyceride turnover, de novo lipogenesis, and cell proliferation in humans measured with $^2\text{H}_2\text{O}$. *Am. J. Physiol. Endocrinol. Metab*. 2004;286(4):E577-88.
247. Trayhurn P, Wang B, Wood IS. Hypoxia in adipose tissue: A basis for the dysregulation of tissue function in obesity? *Br. J. Nutr*. 2008;100(2):227–235.

248. Kabon B, Nagele A, Reddy D, et al. Obesity Decreases Perioperative Tissue Oxygenation. *Anesthesiology*. 2004;100(2):274–280.
249. Virtanen KA, Lönnroth P, Parkkola R, et al. Glucose Uptake and Perfusion in Subcutaneous and Visceral Adipose Tissue during Insulin Stimulation in Nonobese and Obese Humans. *J. Clin. Endocrinol. Metab.* 2014;87(8):3902–3910.
250. Ozcan U. Chemical Chaperones Reduce ER Stress and Restore Glucose Homeostasis in a Mouse Model of Type 2 Diabetes. *Science (80-.)*. 2006;313(5790):1137–1140.
251. Wang QA, Tao C, Gupta RK, Scherer PE. Tracking adipogenesis during white adipose tissue development, expansion and regeneration. *Nat. Med.* 2013;19(10):1338–1344.
252. Cinti S, Mitchell G, Barbatelli G, et al. Adipocyte death defines macrophage localization and function in adipose tissue of obese mice and humans. *J. Lipid Res.* 2005;46(11):2347–2355.
253. Kanda H, Tateya S, Tamori Y, et al. MCP-1 contributes to macrophage infiltration into adipose tissue, insulin resistance, and hepatic steatosis in obesity. *J. Clin. Invest.* 2006;116(6):1494–1505.
254. Zeyda M, Stulnig TM. Obesity, inflammation, and insulin resistance - A mini-review. *Gerontology*. 2009;55(4):379–386.
255. Miller RS, Diaczok D, Cooke DW. Repression of GLUT4 expression by the endoplasmic reticulum stress response in 3T3-L1 adipocytes. *Biochem. Biophys. Res. Commun.* 2007;362(1):188–192.
256. Huber J, Kiefer FW, Zeyda M, et al. CC chemokine and CC chemokine receptor profiles in visceral and subcutaneous adipose tissue are altered in human obesity. *J. Clin. Endocrinol. Metab.* 2008;93(8):3215–3221.
257. Zhang F. Dysregulated lipid metabolism in cancer. *World J. Biol. Chem.* 2012;3(8):167.
258. Quan J, Bode AM, Luo X. ACSL family: The regulatory mechanisms and therapeutic implications in cancer. *Eur. J. Pharmacol.* 2021;909(July):174397.
259. Frahm JL, Li LO, Grevengoed TJ, Coleman RA. Phosphorylation and Acetylation of Acyl-CoA Synthetase- I. *J. Proteomics Bioinform.* 2011;4(7):129–137.
260. Chen WC, Wang CY, Hung YH, et al. Systematic analysis of gene expression alterations and clinical outcomes for long-chain acyl-coenzyme A synthetase family in cancer. *PLoS One*. 2016;11(5):1–23.
261. Sánchez-Martínez R, Cruz-Gil S, García-Álvarez MS, Reglero G, De Molina AR. Complementary ACSL isoforms contribute to a non-Warburg advantageous energetic status characterizing invasive colon cancer cells. *Sci. Rep.* 2017;7(1):1–15.

262. Sánchez-Martínez R, Cruz-Gil S, de Cedrón MG, et al. A link between lipid metabolism and epithelial-mesenchymal transition provides a target for colon cancer therapy. *Oncotarget*. 2015;6(36):38719–38736.
263. Orlando UD, Castillo AF, Medrano MAR, et al. Acyl-CoA synthetase-4 is implicated in drug resistance in breast cancer cell lines involving the regulation of energy-dependent transporter expression. *Biochem. Pharmacol.* 2019;159(August 2018):52–63.
264. Wu X, Deng F, Li Y, et al. ACSL4 promotes prostate cancer growth, invasion and hormonal resistance. *Oncotarget*. 2015;6(42):44849–44863.
265. Ma Y, Zha J, Yang XK, et al. Long-chain fatty acyl-CoA synthetase 1 promotes prostate cancer progression by elevation of lipogenesis and fatty acid beta-oxidation. *Oncogene*. 2021;40(10):1806–1820.
266. Wright HJ, Hou J, Xu B, et al. CDCP1 drives triple-negative breast cancer metastasis through reduction of lipid-droplet abundance and stimulation of fatty acid oxidation. *Proc. Natl. Acad. Sci. U. S. A.* 2017;114(32):E6556–E6565.
267. Padanad MS, Konstantinidou G, Venkateswaran N, et al. Fatty Acid Oxidation Mediated by Acyl-CoA Synthetase Long Chain 3 Is Required for Mutant KRAS Lung Tumorigenesis. *Cell Rep.* 2016;16(6):1614–1628.
268. Sievers F, Wilm A, Dineen D, et al. Fast, scalable generation of high-quality protein multiple sequence alignments using Clustal Omega. *Mol. Syst. Biol.* 2011;7(539):1–6.
269. Huh JY, Reilly SM, Abu-Odeh M, et al. TANK-Binding Kinase 1 Regulates the Localization of Acyl-CoA Synthetase ACSL1 to Control Hepatic Fatty Acid Oxidation. *Cell Metab.* 2020;32(6):1012-1027.e7.
270. Zhang J, Liu Y, Li Q, et al. ACSL4: a double-edged sword target in multiple myeloma, promotes cell proliferation and sensitizes cell to ferroptosis. *Carcinogenesis*. 2023;44(3):242–251.
271. Igal RA, Wang P, Coleman RA. Triacsin C blocks de novo synthesis of glycerolipids and cholesterol esters but not recycling of fatty acid into phospholipid: evidence for functionally separate pools of acyl-CoA. *Biochem. J.* 1997;324(Pt 2):529.
272. Tomoda H, Kazuaki I, Satoshi O. Inhibition of acyl-CoA synthetase by triacsins. *Biochim. Biophys. Acta (BBA)/Lipids Lipid Metab.* 1987;921(3):595–598.
273. Kim JH, Lewin TM, Coleman RA. Expression and characterization of recombinant rat acyl-CoA synthetases 1, 4, and 5: Selective inhibition by triacsin C and thiazolidinediones. *J. Biol. Chem.* 2001;276(27):24667–24673.
274. Kaemmerer E, Peuscher A, Reinartz A, et al. Human intestinal acyl-CoA synthetase 5 is sensitive to the inhibitor triacsin C. *World J. Gastroenterol.* 2011;17(44):4883–4889.

275. Mashima T, Sato S, Okabe S, et al. Acyl-CoA synthetase as a cancer survival factor: Its inhibition enhances the efficacy of etoposide. *Cancer Sci.* 2009;100(8):1556–1562.
276. Ye W, Wang J, Huang J, et al. ACSL5, a prognostic factor in acute myeloid leukemia, modulates the activity of Wnt/ β -catenin signaling by palmitoylation modification. *Front. Med.* 2023;
277. Chung SH, Lee HH, Kim YS, Song K, Kim TH. Induction of apoptosis in RL95-2 human endometrial cancer cells by combination treatment with docosahexaenoic acid and triacsin C. *Arch. Med. Sci.* 2021;19(2):488–498.
278. Murphy CS, Liaw L, Reagan MR. In vitro tissue-engineered adipose constructs for modeling disease. *BMC Biomed. Eng.* 2019;1:.
279. Dempster JM, Boyle I, Vazquez F, et al. Chronos: a cell population dynamics model of CRISPR experiments that improves inference of gene fitness effects. *Genome Biol.* 2021;22(1):1–23.
280. Ghandi M, Huang FW, Jané-Valbuena J, et al. Next-generation characterization of the Cancer Cell Line Encyclopedia. *Nature.* 2019;569(7757):503–508.
281. Farrell M, Fairfield H, Karam M, et al. Targeting the fatty acid binding proteins disrupts multiple myeloma cell cycle progression and MYC signaling. *Elife.* 2023;12:1–30.
282. Greenstein S, Krett NL, Kurosawa Y, et al. Characterization of the MM.1 human multiple myeloma (MM) cell lines: A model system to elucidate the characteristics, behavior, and signaling of steroid-sensitive and -resistant MM cells. *Exp. Hematol.* 2003;31(4):271–282.
283. Chesi M, Bergsagel PL, Shonukan OO, et al. Frequent dysregulation of the c-maf proto-oncogene at 16q23 by translocation to an Ig locus in multiple myeloma. *Blood.* 1998;91(12):4457–4463.
284. Katagiri S, Yonezawa T, Kuyama J, et al. Two distinct human myeloma cell lines originating from one patient with myeloma. *Int. J. cancer.* 1985;36(2):241–246.
285. Matsuoka Y, Moore GE, Yagi Y, Pressman D. Production of free light chains of immunoglobulin by a hematopoietic cell line derived from a patient with multiple myeloma. *Proc. Soc. Exp. Biol. Med.* 1967;125(4):1246–1250.
286. Keats JJ, Fonseca R, Chesi M, et al. Promiscuous Mutations Activate the Noncanonical NF- κ B Pathway in Multiple Myeloma. *Cancer Cell.* 2007;12(2):131–144.
287. Gallagher R, Collins S, Trujillo J, et al. Characterization of the continuous, differentiating myeloid cell line (HL-60) from a patient with acute promyelocytic leukemia. *Blood.* 1979;54(3):713–733.

288. Mauney JR, Volloch V, Kaplan DL. Matrix-mediated retention of adipogenic differentiation potential by human adult bone marrow-derived mesenchymal stem cells during ex vivo expansion. *Biomaterials*. 2005;26(31):6167–6175.
289. Sekiya I, Larson BL, Vuoristo JT, Cui JG, Prockop DJ. Adipogenic Differentiation of Human Adult Stem Cells from Bone Marrow Stroma (MSCs). *J. Bone Miner. Res.* 2004;19(2):256–264.
290. Nchoutmboube JA, Viktorova EG, Scott AJ, et al. Increased Long Chain acyl-Coa Synthetase Activity and Fatty Acid Import Is Linked to Membrane Synthesis for Development of Picornavirus Replication Organelles. *PLoS Pathog.* 2013;9(6):.
291. Castillo AF, Orlando UD, Maloberti PM, et al. New inhibitor targeting Acyl-CoA synthetase 4 reduces breast and prostate tumor growth, therapeutic resistance and steroidogenesis. *Cell. Mol. Life Sci.* 2020;(0123456789):
292. Patel H, Ewels P, Peltzer A, et al. nf-core/rnaseq: nf-core/rnaseq v3.10.1 - Plastered Rhodium Rudolph. 2023;
293. Ewels PA, Peltzer A, Fillinger S, et al. The nf-core framework for community-curated bioinformatics pipelines. *Nat. Biotechnol.* 2020;38(3):276–278.
294. DI Tommaso P, Chatzou M, Floden EW, et al. Nextflow enables reproducible computational workflows. *Nat. Biotechnol.* 2017;35(4):316–319.
295. Ewels P, Magnusson M, Lundin S, Källner M. MultiQC: Summarize analysis results for multiple tools and samples in a single report. *Bioinformatics.* 2016;32(19):3047–3048.
296. Krueger F, James F, Ewels P, Afyounian E, Schuster-Boeckler B. FelixKrueger/TrimGalore: v0.6.7 - DOI via Zenodo. 2021;
297. Dobin A, Davis CA, Schlesinger F, et al. STAR: Ultrafast universal RNA-seq aligner. *Bioinformatics.* 2013;29(1):15–21.
298. Li H, Handsaker B, Wysoker A, et al. The Sequence Alignment/Map format and SAMtools. *Bioinformatics.* 2009;25(16):2078–2079.
299. Patro R, Duggal G, Love MI, Irizarry RA, Kingsford C. Salmon provides fast and bias-aware quantification of transcript expression. *Nat. Methods.* 2017;14(4):417–419.
300. Love MI, Huber W, Anders S. Moderated estimation of fold change and dispersion for RNA-seq data with DESeq2. *Genome Biol.* 2014;15(12):1–21.
301. Rappsilber J, Mann M, Ishihama Y. Protocol for micro-purification, enrichment, pre-fractionation and storage of peptides for proteomics using StageTips. *Nat. Protoc.* 2007;2(8):1896–1906.
302. Fairfield H, Condruti R, Farrell M, et al. Development and characterization of three cell culture systems to investigate the relationship between primary bone marrow adipocytes and myeloma cells. *Front. Oncol.* 2023;12(January):1–21.

303. Than NG, Sumegi B, Bellyei S, et al. Lipid droplet and milk lipid globule membrane associated placental protein 17b (PP17b) is involved in apoptotic and differentiation processes of human epithelial cervical carcinoma cells. *Eur. J. Biochem.* 2003;270(6):1176–1188.
304. Liberzon A, Birger C, Thorvaldsdóttir H, et al. The Molecular Signatures Database Hallmark Gene Set Collection. *Cell Syst.* 2015;1(6):417–425.
305. Tang YUE, Zhou J, Hooi SC, Jiang YUEM, Lu GUOD. Fatty acid activation in carcinogenesis and cancer development : Essential roles of long - chain acyl - CoA synthetases (Review). 2018;1390–1396.
306. Croft D, Mundo AF, Haw R, et al. The Reactome pathway knowledgebase. *Nucleic Acids Res.* 2014;42(D1):472–477.
307. Kanehisa M, Furumichi M, Sato Y, Kawashima M, Ishiguro-Watanabe M. KEGG for taxonomy-based analysis of pathways and genomes. *Nucleic Acids Res.* 2023;51(D1):D587–D592.
308. Walev I, Bhakdi SC, Hofmann F, et al. Delivery of proteins into living cells by reversible membrane permeabilization with streptolysin-O. *Proc. Natl. Acad. Sci. U. S. A.* 2001;98(6):3185–3190.
309. Liu Z, Xu J, He J, et al. Mature adipocytes in bone marrow protect myeloma cells against chemotherapy through autophagy activation. *Oncotarget.* 2015;6(33):34329–41.
310. Pang J, Shi Q, Liu Z, et al. Resistin induces multidrug resistance in myeloma by inhibiting cell death and upregulating ABC transporter expression. *Haematologica.* 2017;102(7):1273–1280.
311. Velázquez AP, Tatsuta T, Ghillebert R, Drescher I, Graef M. Lipid droplet-mediated ER homeostasis regulates autophagy and cell survival during starvation. *J. Cell Biol.* 2016;212(6):621–631.
312. Qiu B, Ackerman D, Sanchez DJ, et al. HIF2 α -dependent lipid storage promotes endoplasmic reticulum homeostasis in clear-cell renal cell carcinoma. *Cancer Discov.* 2016;5(6):653–667.
313. Welte MA, Gould AP. Lipid droplet functions beyond energy storage. *Biochim. Biophys. Acta - Mol. Cell Biol. Lipids.* 2017;1862(10):1260–1272.
314. Yen MC, Kan JY, Hsieh CJ, et al. Association of long-chain acyl-coenzyme A synthetase 5 expression in human breast cancer by estrogen receptor status and its clinical significance. *Oncol. Rep.* 2017;37(6):3253–3260.
315. Tomoda H, Igarashi K, Cyong JC, Omura S. Evidence for an essential role of long chain acyl-CoA synthetase in animal cell proliferation: Inhibition of long chain acyl-CoA synthetase by triacscins caused inhibition of Raji cell proliferation. *J. Biol. Chem.* 1991;266(7):4214–4219.

316. Chung SH, Lee HH, Kim YS, Song K, Kim TH. Induction of apoptosis in RL95-2 human endometrial cancer cells by combination treatment with docosahexaenoic acid and triacsin C. *Arch. Med. Sci.* 2023;19(2):488–498.
317. Mashima T, Oh-hara T, Sato S, et al. p53-defective tumors with a functional apoptosome-mediated pathway: A new therapeutic target. *J. Natl. Cancer Inst.* 2005;97(10):765–777.
318. Nilsson K. Characteristics of established myeloma and lymphoblastoid cell lines derived from an E myeloma patient: a comparative study. *Int. J. cancer.* 1971;7(3):380–396.
319. Cowley GS, Weir BA, Vazquez F, et al. Parallel genome-scale loss of function screens in 216 cancer cell lines for the identification of context-specific genetic dependencies. *Sci. Data.* 2014;1:1–12.
320. Kajigaya Y, Sasaki H, Ikuta K, et al. [Serum-free culture for leukemia cells]. *Hum. Cell.* 1993;6(1):49–56.
321. Li F, Mao G, Tong D, et al. The histone mark H3K36me3 regulates human DNA mismatch repair through its interaction with MutSa. *Cell.* 2013;153(3):590–600.
322. Martin G, Schoonjans K, Lefebvre AM, Staels B, Auwerx J. Coordinate regulation of the expression of the fatty acid transport protein and acyl-CoA synthetase genes by PPAR α and PPAR γ activators. *J. Biol. Chem.* 1997;272(45):28210–28217.
323. Durgan DJ, Smith JK, Hotze MA, et al. Distinct transcriptional regulation of long-chain acyl-CoA synthetase isoforms and cytosolic thioesterase 1 in the rodent heart by fatty acids and insulin. *Am. J. Physiol. - Hear. Circ. Physiol.* 2006;290(6):2480–2497.
324. Grevengoed TJ, Klett EL, Coleman RA. Acyl-CoA Metabolism and Partitioning. *Annu. Rev. Nutr.* 2014;34(1):1–30.
325. Weedon-Fekjaer MS, Dalen KT, Solaas K, et al. Activation of LXR increases acyl-CoA synthetase activity through direct regulation of ACSL3 in human placental trophoblast cells. *J. Lipid Res.* 2010;51(7):1886–1896.
326. Massafra V, Milona A, Vos HR, Burgering BMT, Van Mil SWC. Quantitative liver proteomics identifies FGF19 targets that couple metabolism and proliferation. *PLoS One.* 2017;12(2):1–18.
327. Han J, Kaufman RJ. The role of ER stress in lipid metabolism and lipotoxicity. *J. Lipid Res.* 2016;57(8):1329–1338.
328. Chang YS, Tsai CT, Huangfu CA, et al. ACSL3 and GSK-3 β are essential for lipid upregulation induced by endoplasmic reticulum stress in liver cells. *J. Cell. Biochem.* 2011;112(3):881–893.
329. Pakos-Zebrucka K, Koryga I, Mnich K, et al. The integrated stress response. *EMBO Rep.* 2016;17(10):1374–1395.

330. Anderson NS, Haynes CM. Folding the Mitochondrial UPR into the Integrated Stress Response. *Trends Cell Biol.* 2020;30(6):428–439.
331. Smyrniak I. The mitochondrial unfolded protein response and its diverse roles in cellular stress. *Int. J. Biochem. Cell Biol.* 2021;133(January):
332. Tian X, Zhang S, Zhou L, et al. Targeting the Integrated Stress Response in Cancer Therapy. *Front. Pharmacol.* 2021;12(September):1–12.
333. Perkins DJ, Barber GN. Defects in Translational Regulation Mediated by the α Subunit of Eukaryotic Initiation Factor 2 Inhibit Antiviral Activity and Facilitate the Malignant Transformation of Human Fibroblasts. *Mol. Cell. Biol.* 2004;24(5):2025–2040.
334. Darawshi O, Muz B, Naamat SG, et al. An mTORC1 to HRI signaling axis promotes cytotoxicity of proteasome inhibitors in multiple myeloma. *Cell Death Dis.* 2022;13(11):1–12.
335. Al-Rashed F, Thomas R, Al-Roub A, Al-Mulla F, Ahmad R. LPS Induces GM-CSF Production by Breast Cancer MDA-MB-231 Cells via Long-Chain Acyl-CoA Synthetase 1. *Molecules.* 2020;25(20):.
336. Yu W, Cao D, Zhou H, Hu Y, Guo T. PGC-1 α is responsible for survival of multiple myeloma cells under hyperglycemia and chemotherapy. *Oncol. Rep.* 2015;33(4):2086–2092.
337. Ohoka N, Yoshii S, Hattori T, Onozaki K, Hayashi H. TRB3, a novel ER stress-inducible gene, is induced via ATF4-CHOP pathway and is involved in cell death. *EMBO J.* 2005;24(6):1243–1255.
338. Grenier A, Poulain L, Mondesir J, et al. AMPK-PERK axis represses oxidative metabolism and enhances apoptotic priming of mitochondria in acute myeloid leukemia. *Cell Rep.* 2022;38(1):110197.
339. Zhong Y, Zhang Y, Wang P, et al. V8 induces apoptosis and the endoplasmic reticulum stress response in human multiple myeloma RPMI 8226 cells via the PERK-eIF2 α -ATF4 signaling pathway. *Oncol. Lett.* 2016;12(4):2702–2709.
340. Burwick N, Zhang MY, de la Puente P, et al. The eIF2-alpha kinase HRI is a novel therapeutic target in multiple myeloma. *Leuk. Res.* 2017;55:23–32.
341. Usmani SZ, Chiosis G. HSP90 inhibitors as therapy for multiple myeloma. *Clin. Lymphoma, Myeloma Leuk.* 2011;11(SUPPL.1):S77–S81.
342. Fessler E, Eckl EM, Schmitt S, et al. A pathway coordinated by DELE1 relays mitochondrial stress to the cytosol. *Nature.* 2020;579(7799):433–437.
343. Guo X, Aviles G, Liu Y, et al. Mitochondrial stress is relayed to the cytosol by an OMA1–DELE1–HRI pathway. *Nature.* 2020;579(7799):427–432.

344. Mick E, Titov D V., Skinner OS, et al. Distinct mitochondrial defects trigger the integrated stress response depending on the metabolic state of the cell. *Elife*. 2020;9:.
345. Saric A, Andreau K, Armand AS, Møller IM, Petit PX. Barth syndrome: From mitochondrial dysfunctions associated with aberrant production of reactive oxygen species to pluripotent stem cell studies. *Front. Genet*. 2016;6(JAN):1–26.
346. Lan H, Gao Y, Zhao Z, Mei Z, Wang F. Ferroptosis: Redox Imbalance and Hematological Tumorigenesis. *Front. Oncol*. 2022;12(January):1–12.
347. Dixon SJ, Lemberg KM, Lamprecht MR, et al. Ferroptosis: An iron-dependent form of nonapoptotic cell death. *Cell*. 2012;149(5):1060–1072.
348. Jyotsana N, Ta KT, DelGiorno KE. The Role of Cystine/Glutamate Antiporter SLC7A11/xCT in the Pathophysiology of Cancer. *Front. Oncol*. 2022;12(February):1–13.
349. Doll S, Proneth B, Tyurina YY, et al. ACSL4 dictates ferroptosis sensitivity by shaping cellular lipid composition. *Nat. Chem. Biol*. 2017;13(1):91–98.
350. Tsuzuki T, Tokuyama Y, Igarashi M, Miyazawa T. Tumor growth suppression by α -eleostearic acid, a linolenic acid isomer with a conjugated triene system, via lipid peroxidation. *Carcinogenesis*. 2004;25(8):1417–1425.
351. Dhar Dubey KK, Sharma G, Kumar A. Conjugated Linolenic Acids: Implication in Cancer. *J. Agric. Food Chem*. 2019;67(22):6091–6101.
352. Beatty A, Singh T, Tyurina YY, et al. Ferroptotic cell death triggered by conjugated linolenic acids is mediated by ACSL1. *Nat. Commun*. 2021;12(1):.
353. Klasson TD, LaGory EL, Zhao H, et al. ACSL3 regulates lipid droplet biogenesis and ferroptosis sensitivity in clear cell renal cell carcinoma. *Cancer Metab*. 2022;10(1):1–17.
354. Hurt EM, Thomas SB, Peng B, Farrar WL. Integrated molecular profiling of SOD2 expression in multiple myeloma. *Blood*. 2007;109(9):3953–3962.
355. Wan XS, Devalaraja MN, St. Clair DK. Molecular Structure and Organization of the Human Manganese Superoxide Dismutase Gene. *DNA Cell Biol*. 1994;13(11):1127–1136.
356. Miao L, St. Clair DK. Regulation of superoxide dismutase genes: Implications in disease. *Free Radic. Biol. Med*. 2009;47(4):344–356.
357. Dimayuga FO, Wang C, Clark JM, et al. SOD1 overexpression alters ROS production and reduces neurotoxic inflammatory signaling in microglial cells. *J. Neuroimmunol*. 2007;182(1–2):89–99.

358. Beni SM, Tsenter J, Alexandrovich AG, et al. CuZn-SOD deficiency, rather than overexpression, is associated with enhanced recovery and attenuated activation of NF- κ B after brain trauma in mice. *J. Cereb. Blood Flow Metab.* 2006;26(4):478–490.
359. Morgan MJ, Liu ZG. Crosstalk of reactive oxygen species and NF- κ B signaling. *Cell Res.* 2011;21(1):103–115.
360. Braicu C, Buse M, Busuioc C, et al. A Comprehensive Review on MAPK: A Promising Therapeutic Target in Cancer. *Cancers (Basel)*. 2019;11(10):.
361. Al-Rashed F, Haddad D, Al Madhoun A, et al. ACSL1 is a key regulator of inflammatory and macrophage foaming induced by short-term palmitate exposure or acute high-fat feeding. *iScience*. 2023;26(7):107145.
362. Cotte AK, Aires V, Fredon M, et al. Lysophosphatidylcholine acyltransferase 2-mediated lipid droplet production supports colorectal cancer chemoresistance. *Nat. Commun.* 2018;9(1):.
363. Fujimoto Y, Itabe H, Kinoshita T, et al. Involvement of ACSL in local synthesis of neutral lipids in cytoplasmic lipid droplets in human hepatocyte HuH7. *J. Lipid Res.* 2007;48(6):1280–1292.
364. Bajpai R, Sharma A, Achreja A, et al. Electron transport chain activity is a predictor and target for venetoclax sensitivity in multiple myeloma. *Nat. Commun.* 2020;11(1):.
365. Narita T, Ri M, Masaki A, et al. Lower expression of activating transcription factors 3 and 4 correlates with shorter progression-free survival in multiple myeloma patients receiving bortezomib plus dexamethasone therapy. *Blood Cancer J.* 2015;5(September):
366. McConkey DJ. The integrated stress response and proteotoxicity in cancer therapy. *Biochem. Biophys. Res. Commun.* 2017;482(3):450–453.
367. Abe T, Fukuyama R, Shimizu N, Toh H, Yamamoto T. Human Long-Chain Acyl-CoA Synthetase : Structure and Chromosomal. 1992;l(1):123–128.
368. McElroy WD, Seliger HE. The Chemistry of Light Emission. *Adv. Enzymol. Relat. Subj. Biochem.* 1963;25:119–166.
369. Hwang HJ, Lynn SG, Vengellur A, et al. Hypoxia Inducible Factors Modulate Mitochondrial Oxygen Consumption and Transcriptional Regulation of Nuclear-Encoded Electron Transport Chain Genes. *Biochemistry.* 2015;54(24):3739–3748.
370. Wei Y, Wang D, Topczewski F, Pagliassotti MJ. Saturated fatty acids induce endoplasmic reticulum stress and apoptosis independently of ceramide in liver cells. *Am. J. Physiol. - Endocrinol. Metab.* 2006;291(2):275–281.

371. Lee SM, Lee SH, Jung Y, et al. FABP3-mediated membrane lipid saturation alters fluidity and induces ER stress in skeletal muscle with aging. *Nat. Commun.* 2020;11(1):1–15.
372. Grevengoed TJ, Martin SA, Katunga L, et al. Acyl-CoA synthetase 1 deficiency alters cardiolipin species and impairs mitochondrial function. *J. Lipid Res.* 2015;56(8):1572–1582.
373. Ahmadpour ST, Mahéo K, Servais S, Brisson L, Dumas JF. Cardiolipin, the mitochondrial signature lipid: Implication in cancer. *Int. J. Mol. Sci.* 2020;21(21):1–16.
374. Tamura Y, Harada Y, Nishikawa SI, et al. Tam41 is a CDP-diacylglycerol synthase required for cardiolipin biosynthesis in mitochondria. *Cell Metab.* 2013;17(5):709–718.
375. Chang SC, Heacock PN, Clancey CJ, Dowhan W. The PEL1 gene (renamed PGS1) encodes the phosphatidylglycerophosphate synthase of *Saccharomyces cerevisiae*. *J. Biol. Chem.* 1998;273(16):9829–9836.
376. Chen D, Zhang XY, Shi Y. Identification and functional characterization of hCLS1, a human cardiolipin synthase localized in mitochondria. *Biochem. J.* 2006;398(2):169–176.
377. Schlame M, Ren M, Xu Y, Greenberg ML, Haller I. Molecular symmetry in mitochondrial cardiolipins. *Chem. Phys. Lipids.* 2005;138(1–2):38–49.
378. Xu Y, Sutachan JJ, Plesken H, Kelley RI, Schlame M. Characterization of lymphoblast mitochondria from patients with Barth syndrome. *Lab. Investig.* 2005;85(6):823–830.
379. Claypool SM, McCaffery JM, Koehler CM. Mitochondrial mislocalization and altered assembly of a cluster of Barth syndrome mutant tafazzins. *J. Cell Biol.* 2006;174(3):379–390.
380. Schlame M, Horvath L, Vigh L. Relationship between lipid saturation and lipid-protein interaction in liver mitochondria modified by catalytic hydrogenation with reference to cardiolipin molecular species. *Biochem. J.* 1990;265(1):79–85.
381. Cao J, Shen W, Chang Z, Shi Y. ALCAT1 is a polyglycerophospholipid acyltransferase potently regulated by adenine nucleotide and thyroid status. *Am. J. Physiol. - Endocrinol. Metab.* 2009;296(4):647–653.
382. Paradies G, Paradies V, Ruggiero FM, Petrosillo G. Oxidative stress, cardiolipin and mitochondrial dysfunction in nonalcoholic fatty liver disease. *World J. Gastroenterol.* 2014;20(39):14205–14218.
383. Schlame M. Cardiolipin synthesis for the assembly of bacterial and mitochondrial membranes. *J. Lipid Res.* 2008;49(8):1607–1620.

384. Pfeiffer K, Gohil V, Stuart RA, et al. Cardiolipin Stabilizes Respiratory Chain Supercomplexes. *J. Biol. Chem.* 2003;278(52):52873–52880.
385. Zhang M, Mileykovskaya E, Dowhan W. Gluing the respiratory chain together: Cardiolipin is required for supercomplex formation in the inner mitochondrial membrane. *J. Biol. Chem.* 2002;277(46):43553–43556.
386. Claypool SM, Oktay Y, Boonthueung P, Loo JA, Koehler CM. Cardiolipin defines the interactome of the major ADP/ATP carrier protein of the mitochondrial inner membrane. *J. Cell Biol.* 2008;182(5):937–950.
387. Enríquez JA. Supramolecular Organization of Respiratory Complexes. *Annu. Rev. Physiol.* 2016;78:533–561.
388. Claypool SM. Cardiolipin, a critical determinant of mitochondrial carrier protein assembly and function. *Biochim. Biophys. Acta - Biomembr.* 2009;1788(10):2059–2068.
389. Mileykovskaya E, Dowhan W. Cardiolipin-dependent formation of mitochondrial respiratory supercomplexes. *Chem. Phys. Lipids.* 2014;179:42–48.
390. Lopez-Fabuel I, Le Douce J, Logan A, et al. Complex I assembly into supercomplexes determines differential mitochondrial ROS production in neurons and astrocytes. *Proc. Natl. Acad. Sci. U. S. A.* 2016;113(46):13063–13068.
391. Hüttemann M, Pecina P, Rainbolt M, et al. The multiple functions of cytochrome c and their regulation in life and death decisions of the mammalian cell: From respiration to apoptosis. *Mitochondrion.* 2011;11(3):369–381.
392. Pereverzev MO, Vygodina T V., Konstantinov AA, Skulachev VP. Cytochrome c, an ideal antioxidant. *Biochem. Soc. Trans.* 2003;31(6):1312–1315.
393. Tuominen EKJ, Wallace CJA, Kinnunen PKJ. Phospholipid-cytochrome c interaction. Evidence for the extended lipid anchorage. *J. Biol. Chem.* 2002;277(11):8822–8826.
394. Petrosillo G, Ruggiero FM, Pistolese M, Paradies G. Reactive oxygen species generated from the mitochondrial electron transport chain induce cytochrome c dissociation from beef-heart submitochondrial particles via cardiolipin peroxidation. Possible role in the apoptosis. *FEBS Lett.* 2001;509(3):435–438.
395. Belikova NA, Vladimirov YA, Osipov AN, et al. Peroxidase activity and structural transitions of cytochrome c bound to cardiolipin-containing membranes. *Biochemistry.* 2006;45(15):4998–5009.
396. Ott M, Zhivotovsky B, Orrenius S. Role of cardiolipin in cytochrome c release from mitochondria. *Cell Death Differ.* 2007;14(7):1243–1247.
397. Lin MH, Yen JH, Weng CY, et al. Lipid peroxidation end product 4-hydroxy-trans-2-nonenal triggers unfolded protein response and heme oxygenase-1 expression in PC12 cells: Roles of ROS and MAPK pathways. *Toxicology.* 2014;315(1):24–37.

398. Anderson CJ, Kahl A, Fruitman H, et al. Prohibitin levels regulate OMA1 activity and turnover in neurons. *Cell Death Differ.* 2020;27(6):1896–1906.
399. Matsuda D, Namatame I, Ohshiro T, et al. Anti-atherosclerotic activity of triacsin C, an Acyl-CoA synthetase inhibitor. *J. Antibiot. (Tokyo).* 2008;61(5):318–321.
400. Draube A, Pfister R, Vockerodt M, et al. Immunomagnetic enrichment of CD138 positive cells from weakly infiltrated myeloma patients samples enables the determination of the tumor clone specific IgH rearrangement. *Ann. Hematol.* 2001;80(2):83–89.
401. Zhan F, Huang Y, Colla S, et al. The molecular classification of multiple myeloma. *Blood.* 2006;108(6):2020–2028.
402. Chen J, Ding C, Chen Y, et al. ACSL4 promotes hepatocellular carcinoma progression via c-Myc stability mediated by ERK/FBW7/c-Myc axis. *Oncogenesis.* 2020;9(4):.
403. Klepinin A, Zhang S, Klepinina L, et al. Adenylate Kinase and Metabolic Signaling in Cancer Cells. *Front. Oncol.* 2020;10(May):1–9.
404. Sobh A, States U, Encinas E, et al. NSD2 drives t (4 ; 14) myeloma cell dependence on adenylate kinase 2 by diverting one-carbon metabolism to the epigenome. 2023;

7. APPENDIX

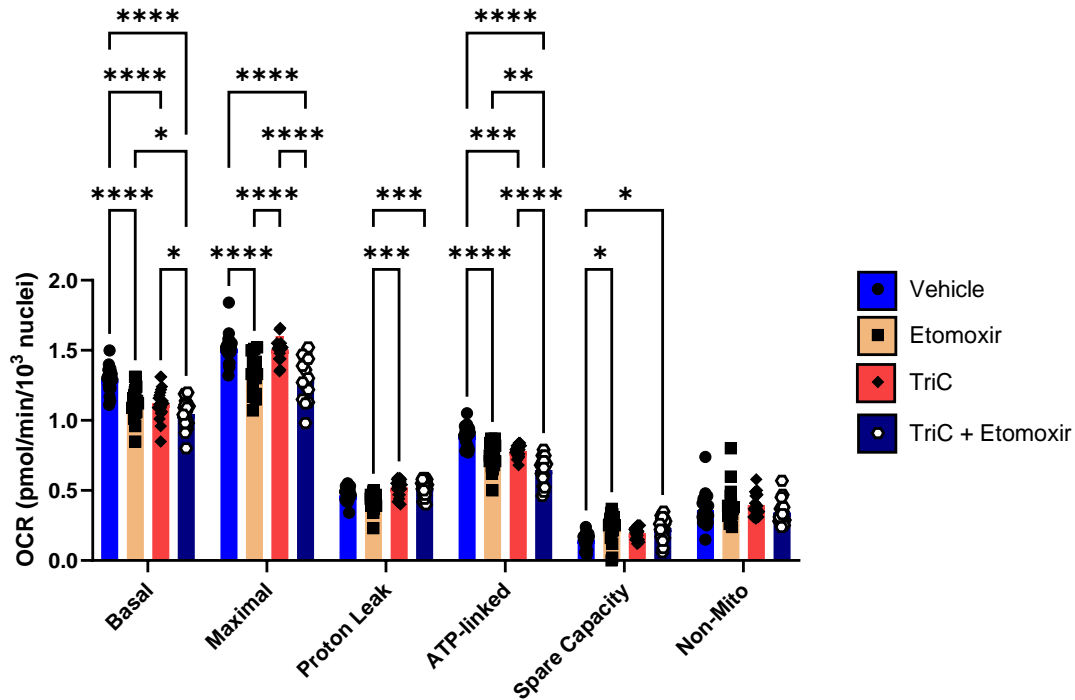


Figure 42. MM.1S Cells May Utilize Fatty Acid Oxidation for their Respiration

A) Cellular respiration (oxygen consumption rate, OCR) in ATCC MM.1S cells treated with 1 μ M triacin C (TriC) for 24 hours and subjected to a Mitochondrial Stress test with 5 μ M etomoxir, a CPT1 (rate-limiting enzyme for fatty acid oxidation) inhibitor. Values are normalized to the number of nuclei. Individual points represent technical replicates for each condition. n=1 **Statistics:** A two-way ANOVA with Tukey's multiple comparison test was used. Data are mean \pm StDev *p<0.05, **p<0.01, ***p<0.001 ****p<0.0001

qRT-PCR Primer Information

Table 11. qRT-PCR Forward Primers

Ensembl ID	Target Gene Name	Forward Primer (5'-3')	Tm (C)
ENSG00000160179	<i>ABCG1</i>	GTCTCGCTGATGAAAGGGCT	60.11
ENSG00000278540	<i>ACACA</i>	ACAACGCAGGCATCAGAAGA	57
ENSG00000151726	<i>ACSL1</i>	GTGGAACACTACAGGCAACCCC	58.2
ENSG00000123983	<i>ACSL3</i>	GGAACAATTTCCGAAGTGTGGG	56.5
ENSG00000068366	<i>ACSL4</i>	CCGCCCTCCGCACAATAA	60.6
ENSG00000197142	<i>ACSL5</i>	TGCCAAAACCAAGTCAAAGCC	56.8
ENSG00000164398	<i>ACSL6</i>	AAATCGGCCAGAGTGGATCA	56.4
ENSG00000169020	<i>ATP5ME</i>	GCCACGCGCTACAATTACCT	61.09
ENSG00000128965	<i>CHAC1</i>	GTGTGGAGGCCCGACTTC	60.05
ENSG00000178741	<i>COX5A</i>	TTGATGCTCGCTGGGTAACA	59.68
ENSG00000126267	<i>COX6B1</i>	CGGGGTGCCTTTAGGATTCA	59.75
ENSG00000175197	<i>DDIT3</i>	GAGCTGGAAGCCTGGTATGA	59.17
ENSG00000168209	<i>DDIT4</i>	GGTTTGACCGCTCCACGAG	61.03
ENSG00000086232	<i>EIF2AK1</i>	CAACTCCGGGGTCCGCAA	62.32
ENSG00000172071	<i>EIF2AK3</i>	GCCAATTCATGCCTGGGAC	59.82
ENSG00000128829	<i>EIF2AK4</i>	ATAACAAGCCCCCTCCCAAG	59.37
ENSG00000178607	<i>ERN1</i>	ACCCAGAGAAGCACGAAGAC	59.68
ENSG00000167468	<i>GPX4</i>	CAGTGAGGCAAGACCGAAGT	59.97
ENSG00000178127	<i>NDUFV2</i>	CCCGCCATGTTCTTCTCCG	60.82
ENSG00000188747	<i>NOXA1</i>	TGTGGATCGTGGGGACTGG	61.29
ENSG00000137843	<i>PAK6</i>	TCCAGCCCATGAAGACAGTG	59.67
ENSG00000158828	<i>PINK1</i>	CCTCCAGACGTGAGACAGTT	59.04
ENSG00000109819	<i>PPARGC1A</i>	CCAAAGGATGCGCTCTCGTTCA	63.42
ENSG00000155846	<i>PPARGC1B</i>	GGCGCTTTGAAGTGTTTGGT	59.9
ENSG00000087074	<i>PPP1R15A</i>	CCCTAAAGGCCAGAAAGGTGC	61.23
ENSG00000170667	<i>RASA4B</i>	ATCGTGGAGGGGAAGAACCT	60.25
ENSG00000099194	<i>SCD</i>	GCTGTCAAAGAGAAGGGGAGT	59.65
ENSG00000168003	<i>SLC3A2</i>	GATGGGTTCCAGGTTCCGGG	60.08
ENSG00000151012	<i>SLC7A11</i>	TGTGCTGACAAATGTGGCCT	60.47
ENSG00000112592	<i>TBP</i>	GTGGGGAGCTGTGATGTGAA	59.6
ENSG00000108064	<i>TFAM</i>	GCTCAGAACCCAGATGCAAAA	59.11
ENSG00000141510	<i>TP53</i>	TCAGATAGCGATGGTCTGGC	59.32
ENSG00000101255	<i>TRIB3</i>	TTCGCTGACCGTGAGAGGAAG	62.08

Table 12. qRT-PCR Reverse Primer Information

Ensembl ID	Target Gene Name	Reverse Primer (5'-3')	Tm (C)	Product Length (bp)
ENSG00000160179	<i>ABCG1</i>	TGACTCAGGACGTAAAGCTGG	59.73	110
ENSG00000278540	<i>ACACA</i>	GTTTCACCGCACACTGTTCC	56.9	92
ENSG00000151726	<i>ACSL1</i>	ATCATCTGGGCAAGGATTGAC	55	113
ENSG00000123983	<i>ACSL3</i>	CCCTGGGGTGTGGCTTATC	58.2	127
ENSG00000068366	<i>ACSL4</i>	ACAAGTGGACAGGCAGCAAAA	57.7	129
ENSG00000197142	<i>ACSL5</i>	TGTTGGTGTCAAGAGCCCAT	56.8	75
ENSG00000164398	<i>ACSL6</i>	TCATAGAGCGGGACCACCA	58	72
ENSG00000169020	<i>ATP5ME</i>	TCTCTGGCAATCCGTTTCAGT	59.65	101
ENSG00000128965	<i>CHAC1</i>	ACACGGCCAGGCATCTTG	60.36	119
ENSG00000178741	<i>COX5A</i>	ACAAGTGTGTTTATCCCTTTACGC	59.79	79
ENSG00000126267	<i>COX6B1</i>	GGGGCGGTCTTGTAGTTCTT	59.68	72
ENSG00000175197	<i>DDIT3</i>	GGTGAAGATTTTTGATTCTTCCTCT	57.54	111
ENSG00000168209	<i>DDIT4</i>	GGTAAGCCGTGTCTTCCTCC	60.11	93
ENSG00000086232	<i>EIF2AK1</i>	TTCTGCTGGAACATCAGATTCGTC	61.15	127
ENSG00000172071	<i>EIF2AK3</i>	TCCCAGCCAATTCCCTATTG	59.86	120
ENSG00000128829	<i>EIF2AK4</i>	GCAGGATTTACGTTGCTCC	59.83	120
ENSG00000178607	<i>ERN1</i>	GCTCCAGAAGAACGGGTGTT	60.25	116
ENSG00000167468	<i>GPX4</i>	TTACTCCCTGGCTCCTGCTT	60.55	124
ENSG00000178127	<i>NDUFV2</i>	ATTCCTTACATGTCTTCCCCAGT	59.15	78
ENSG00000188747	<i>NOXA1</i>	GGCTTGGTCAAATGCCCGC	62.65	142
ENSG00000137843	<i>PAK6</i>	AGGGTGTGGAGCTGATGAC	59.67	109
ENSG00000158828	<i>PINK1</i>	CTCGGGCAGATGGTCTCTTG	60.18	70
ENSG00000109819	<i>PPARGC1A</i>	CGGTGTCTGTAGTGGCTTGACT	62.23	147
ENSG00000155846	<i>PPARGC1B</i>	CCGTA CTCTCGCTCTCCT	60.75	73
ENSG00000087074	<i>PPP1R15A</i>	TGCGATCCCGAGCAAGC	60.18	120
ENSG00000170667	<i>RASA4B</i>	CACTGTGGCTGTCCTGATGA	59.68	105
ENSG00000099194	<i>SCD</i>	AGCCAGGTTTGTAGTACCTCCT	60.49	91
ENSG00000168003	<i>SLC3A2</i>	CGCAATCAAGAGCCTGTCTTC	59.6	108
ENSG00000151012	<i>SLC7A11</i>	CGCTCAGAAAAGGTCACTGC	59.49	87
ENSG00000112592	<i>TBP</i>	TGCTCTGACTTTAGCACCTGT	59.31	183
ENSG00000108064	<i>TFAM</i>	GCCACTCCGCCCTATAAGC	60.3	115
ENSG00000141510	<i>TP53</i>	CTCATAGGGCACCACCACAC	60.39	117
ENSG00000101255	<i>TRIB3</i>	TTGTCCACAGGGAATCATCTG	60.03	89

Table 13 Primers For Determining OPM-2 and HL-60 Identity

Primer Name	Primer Sequence (5'→3')	Predicted Product Size (bp)
hCDKN2A_Ex1F	CCCAGTCTGCAGTTAAGGGG	383
hCDKN2A_Ex1R	CCTGGGCTAGAGACGAATTATC	
hCDKN2A_Ex2F	ACACAAGCTTCCTTTCCGTC	342
hCDKN2A_Ex2R	ATGGTTACTGCCTCTGGTGC	
hNRAS_Ex3F	GTTAGATGCTTATTTAACCTTGGC	358
hNRAS_Ex3R	TGTGGTAACCTCATTTCCCC	
TP53Arg175_Fwd	ATAAGATGCTGAGGAGGGGC	187
TP53Arg175_Rev	TGGCCATCTACAAGCAGTCA	
hChr17proxF	CCCATAGATGCGGAAAGTGC	176 (OPM-2) N/A (HL-60)
hChr17proxR	CCTTTCAGACAAGCAAGCAGT	
hChr17distF	ACCAGCCATGCACTTCTTTG	185 (OPM-2) N/A (HL-60)
hChr17distR	GCTGAGATCATGCCACTGTG	

Table 14. Average Chronos Scores of Modified Hallmark Fatty Acid Metabolism Genes in 21 Human Myeloma Cell Lines from the Cancer Dependency Map

Ensembl Gene ID	Gene Symbol	Gene Name	Avg Chronos Score	Std Dev
ENSG00000204370	SDHD	succinate dehydrogenase complex subunit D	-1.435	0.244
ENSG00000143252	SDHC	succinate dehydrogenase complex subunit C	-1.420	0.266
ENSG00000112972	HMGCS1	3-hydroxy-3-methylglutaryl-CoA synthase 1	-1.230	0.379
ENSG00000164032	H2AZ1	H2A.Z variant histone 1	-1.201	0.334
ENSG00000164687	FABP5	fatty acid binding protein 5	-1.118	0.308
ENSG00000198856	OSTC	oligosaccharyltransferase complex non-catalytic subunit	-1.034	0.239
ENSG00000126088	UROD	uroporphyrinogen decarboxylase	-0.928	0.318
ENSG00000073578	SDHA	succinate dehydrogenase complex flavoprotein subunit A	-0.896	0.280
ENSG00000100412	ACO2	aconitase 2	-0.854	0.338
ENSG00000092010	PSME1	proteasome activator subunit 1	-0.852	0.283
ENSG00000119689	DLST	dihydrolipoamide S-succinyltransferase	-0.799	0.172
ENSG00000080819	CPOX	coproporphyrinogen oxidase	-0.704	0.250
ENSG00000025770	NCAPH2	non-SMC condensin II complex subunit H2	-0.614	0.368
ENSG00000091140	DLD	dihydrolipoamide dehydrogenase	-0.564	0.250
ENSG00000183955	KMT5A	lysine methyltransferase 5A	-0.530	0.226
ENSG00000072506	HSD17B10	hydroxysteroid 17-beta dehydrogenase 10	-0.521	0.414
ENSG00000099194	SCD	stearoyl-CoA desaturase	-0.486	0.297
ENSG00000188690	UROS	uroporphyrinogen III synthase	-0.365	0.201
ENSG00000158473	CD1D	CD1d molecule	-0.337	0.196
ENSG00000160124	MIX23	mitochondrial matrix import factor 23	-0.328	0.170
ENSG00000068366	ACSL4	acyl-CoA synthetase long chain family member 4	-0.314	0.361
ENSG00000091483	FH	fumarate hydratase	-0.298	0.144
ENSG00000278540	ACACA	acetyl-CoA carboxylase alpha	-0.295	0.234
ENSG00000146701	MDH2	malate dehydrogenase 2	-0.269	0.231
ENSG00000117592	PRDX6	peroxiredoxin 6	-0.264	0.174
ENSG00000102172	SMS	spermine synthase	-0.251	0.212
ENSG00000123983	ACSL3	acyl-CoA synthetase long chain family member 3	-0.229	0.274

Table 14 Continued				
ENSG00000124370	MCEE	methylmalonyl-CoA epimerase	-0.218	0.115
ENSG00000164024	METAP1	methionyl aminopeptidase 1	-0.198	0.212
ENSG00000110090	CPT1A	carnitine palmitoyltransferase 1A	-0.188	0.106
ENSG00000128245	YWHAH	tyrosine 3-monooxygenase/tryptophan 5-monooxygenase activation protein eta	-0.181	0.107
ENSG00000122971	ACADS	acyl-CoA dehydrogenase short chain	-0.169	0.188
ENSG00000115255	REEP6	receptor accessory protein 6	-0.160	0.130
ENSG00000157184	CPT2	carnitine palmitoyltransferase 2	-0.160	0.121
ENSG00000205560	CPT1B	carnitine palmitoyltransferase 1B	-0.160	0.111
ENSG00000116882	HAO2	hydroxyacid oxidase 2	-0.148	0.152
ENSG00000131686	CA6	carbonic anhydrase 6	-0.141	0.113
ENSG00000163541	SUCLG1	succinate-CoA ligase GDP/ADP-forming subunit alpha	-0.136	0.168
ENSG00000133835	HSD17B4	hydroxysteroid 17-beta dehydrogenase 4	-0.130	0.152
ENSG00000151726	ACSL1	acyl-CoA synthetase long chain family member 1	-0.127	0.137
ENSG00000083123	BCKDHB	branched chain keto acid dehydrogenase E1 subunit beta	-0.122	0.138
ENSG00000167315	ACAA2	acetyl-CoA acyltransferase 2	-0.119	0.112
ENSG00000198189	HSD17B11	hydroxysteroid 17-beta dehydrogenase 11	-0.118	0.136
ENSG00000169710	FASN	fatty acid synthase	-0.118	0.199
ENSG00000137106	GRHPR	glyoxylate and hydroxypyruvate reductase	-0.117	0.099
ENSG00000065833	ME1	malic enzyme 1	-0.107	0.084
ENSG00000161533	ACOX1	acyl-CoA oxidase 1	-0.103	0.121
ENSG00000109814	UGDH	UDP-glucose 6-dehydrogenase	-0.103	0.185
ENSG00000117305	HMGCL	3-hydroxy-3-methylglutaryl-CoA lyase	-0.103	0.100
ENSG00000136143	SUCLA2	succinate-CoA ligase ADP-forming subunit beta	-0.101	0.134
ENSG00000197375	SLC22A5	solute carrier family 22 member 5	-0.100	0.087
ENSG00000004961	HCCS	holocytochrome c synthase	-0.100	0.123
ENSG00000112033	PPARD	peroxisome proliferator activated receptor delta	-0.099	0.134
ENSG00000010932	FMO1	flavin containing dimethylaniline monooxygenase 1	-0.095	0.114

Table 14 Continued				
ENSG00000168291	PDHB	pyruvate dehydrogenase E1 subunit beta	-0.083	0.205
ENSG00000108515	ENO3	enolase 3	-0.082	0.159
ENSG00000095321	CRAT	carnitine O-acetyltransferase	-0.082	0.102
ENSG00000138413	IDH1	isocitrate dehydrogenase (NADP(+)) 1	-0.081	0.169
ENSG00000180902	D2HGDH	D-2-hydroxyglutarate dehydrogenase	-0.080	0.129
ENSG00000119471	HSDL2	hydroxysteroid dehydrogenase like 2	-0.078	0.104
ENSG00000138796	HADH	hydroxyacyl-CoA dehydrogenase	-0.077	0.062
ENSG00000104823	ECH1	enoyl-CoA hydratase 1	-0.077	0.107
ENSG00000080824	HSP90AA1	heat shock protein 90 alpha family class A member 1	-0.071	0.113
ENSG00000148090	AUH	AU RNA binding methylglutaconyl-CoA hydratase	-0.071	0.110
ENSG00000240972	MIF	macrophage migration inhibitory factor	-0.070	0.133
ENSG00000106605	BLVRA	biliverdin reductase A	-0.068	0.110
ENSG00000104267	CA2	carbonic anhydrase 2	-0.066	0.154
ENSG00000101473	ACOT8	acyl-CoA thioesterase 8	-0.066	0.113
ENSG00000060971	ACAA1	acetyl-CoA acyltransferase 1	-0.064	0.094
ENSG00000111674	ENO2	enolase 2	-0.060	0.131
ENSG00000116791	CRYZ	crystallin zeta	-0.056	0.090
ENSG00000198130	HIBCH	3-hydroxyisobutyryl-CoA hydrolase	-0.053	0.088
ENSG00000213316	LTC4S	leukotriene C4 synthase	-0.051	0.202
ENSG00000140465	CYP1A1	cytochrome P450 family 1 subfamily A member 1	-0.051	0.068
ENSG00000143819	EPHX1	epoxide hydrolase 1	-0.050	0.105
ENSG00000144724	PTPRG	protein tyrosine phosphatase receptor type G	-0.049	0.168
ENSG00000005187	ACSM3	acyl-CoA synthetase medium chain family member 3	-0.047	0.144
ENSG00000115361	ACADL	acyl-CoA dehydrogenase long chain	-0.046	0.090
ENSG00000139112	GABARAPL1	GABA type A receptor associated protein like 1	-0.042	0.113
ENSG00000241644	INMT	indolethylamine N-methyltransferase	-0.040	0.122
ENSG00000186951	PPARA	peroxisome proliferator activated receptor alpha	-0.039	0.084
ENSG00000104320	NBN	nibrin	-0.036	0.109
ENSG00000138029	HADHB	hydroxyacyl-CoA dehydrogenase trifunctional multienzyme complex subunit beta	-0.035	0.103

Table 14 Continued				
ENSG00000167434	CA4	carbonic anhydrase 4	-0.033	0.093
ENSG00000164398	ACSL6	acyl-CoA synthetase long chain family member 6	-0.031	0.121
ENSG00000172340	SUCLG2	succinate-CoA ligase GDP-forming subunit beta	-0.031	0.089
ENSG00000176194	CIDEA	cell death inducing DFFA like effector a	-0.030	0.140
ENSG00000074416	MGLL	monoglyceride lipase	-0.028	0.071
ENSG00000042445	RETSAT	retinol saturase	-0.027	0.080
ENSG00000134333	LDHA	lactate dehydrogenase A	-0.027	0.144
ENSG00000167969	ECI1	enoyl-CoA delta isomerase 1	-0.026	0.111
ENSG00000198721	ECI2	enoyl-CoA delta isomerase 2	-0.024	0.116
ENSG00000170835	CEL	carboxyl ester lipase	-0.020	0.099
ENSG00000164434	FABP7	fatty acid binding protein 7	-0.017	0.106
ENSG00000131828	PDHA1	pyruvate dehydrogenase E1 subunit alpha 1	-0.013	0.258
ENSG00000115159	GPD2	glycerol-3-phosphate dehydrogenase 2	-0.012	0.067
ENSG00000135821	GLUL	glutamate-ammonia ligase	-0.012	0.131
ENSG00000170323	FABP4	fatty acid binding protein 4	-0.009	0.120
ENSG00000078804	TP53INP2	tumor protein p53 inducible nuclear protein 2	-0.006	0.117
ENSG00000105679	GAPDHS	glyceraldehyde-3-phosphate dehydrogenase, spermatogenic	-0.005	0.091
ENSG00000012660	ELOVL5	ELOVL fatty acid elongase 5	-0.004	0.069
ENSG00000167588	GPD1	glycerol-3-phosphate dehydrogenase 1	-0.001	0.084
ENSG00000197142	ACSL5	acyl-CoA synthetase long chain family member 5	0.000	0.070
ENSG00000104951	IL4I1	interleukin 4 induced 1	0.001	0.096
ENSG00000109576	AADAT	aminoadipate aminotransferase	0.003	0.062
ENSG00000104325	DECR1	2,4-dienoyl-CoA reductase 1	0.005	0.093
ENSG00000137274	BPHL	biphenyl hydrolase like	0.007	0.107
ENSG00000147383	NSDHL	NAD(P) dependent steroid dehydrogenase-like	0.009	0.126
ENSG00000123689	G0S2	G0/G1 switch 2	0.009	0.151
ENSG00000115758	ODC1	ornithine decarboxylase 1	0.009	0.143
ENSG00000197416	FABP12	fatty acid binding protein 12	0.011	0.147
ENSG00000101365	IDH3B	isocitrate dehydrogenase (NAD(+)) 3 non-catalytic subunit beta	0.012	0.198
ENSG00000089248	ERP29	endoplasmic reticulum protein 29	0.015	0.112
ENSG00000113790	EHHADH	enoyl-CoA hydratase and 3-hydroxyacyl CoA dehydrogenase	0.017	0.091
ENSG00000065057	NTHL1	nth like DNA glycosylase 1	0.018	0.114

Table 14 Continued				
ENSG00000139547	RDH16	retinol dehydrogenase 16	0.018	0.090
ENSG00000135218	CD36	CD36 molecule (CD36 blood group)	0.020	0.094
ENSG00000156587	UBE2L6	ubiquitin conjugating enzyme E2 L6	0.020	0.116
ENSG00000121769	FABP3	fatty acid binding protein 3	0.020	0.049
ENSG00000112299	VNN1	vanin 1	0.020	0.068
ENSG00000127884	ECHS1	enoyl-CoA hydratase, short chain 1	0.021	0.119
ENSG00000132196	HSD17B7	hydroxysteroid 17-beta dehydrogenase 7	0.023	0.123
ENSG00000072778	ACADVL	acyl-CoA dehydrogenase very long chain	0.024	0.100
ENSG00000154930	ACSS1	acyl-CoA synthetase short chain family member 1	0.025	0.098
ENSG00000163586	FABP1	fatty acid binding protein 1	0.027	0.096
ENSG00000151790	TDO2	tryptophan 2,3-dioxygenase	0.029	0.073
ENSG00000166228	PCBD1	pterin-4 alpha-carbinolamine dehydratase 1	0.030	0.083
ENSG00000159231	CBR3	carbonyl reductase 3	0.030	0.178
ENSG00000138696	BMPR1B	bone morphogenetic protein receptor type 1B	0.036	0.157
ENSG00000159228	CBR1	carbonyl reductase 1	0.042	0.113
ENSG00000138698	RAP1GDS1	Rap1 GTPase-GDP dissociation stimulator 1	0.042	0.068
ENSG00000170231	FABP6	fatty acid binding protein 6	0.043	0.065
ENSG00000119673	ACOT2	acyl-CoA thioesterase 2	0.044	0.090
ENSG00000169169	CPT1C	carnitine palmitoyltransferase 1C	0.046	0.109
ENSG00000111897	SERINC1	serine incorporator 1	0.047	0.108
ENSG00000150787	PTS	6-pyruvoyltetrahydropterin synthase	0.053	0.091
ENSG00000196344	ADH7	alcohol dehydrogenase 7 (class IV), mu or sigma polypeptide	0.055	0.071
ENSG00000100097	LGALS1	galectin 1	0.057	0.087
ENSG00000189221	MAOA	monoamine oxidase A	0.060	0.084
ENSG00000120694	HSPH1	heat shock protein family H (Hsp110) member 1	0.060	0.158
ENSG00000132170	PPARG	peroxisome proliferator activated receptor gamma	0.070	0.104
ENSG00000103150	MLYCD	malonyl-CoA decarboxylase	0.074	0.106
ENSG00000100577	GSTZ1	glutathione S-transferase zeta 1	0.078	0.102
ENSG00000197747	S100A10	S100 calcium binding protein A10	0.080	0.092
ENSG00000067829	IDH3G	isocitrate dehydrogenase (NAD(+)) 3 non-catalytic subunit gamma	0.082	0.110
ENSG00000105607	GCDH	glutaryl-CoA dehydrogenase	0.087	0.132

Table 14 Continued				
ENSG00000145384	FABP2	fatty acid binding protein 2	0.088	0.071
ENSG00000117054	ACADM	acyl-CoA dehydrogenase medium chain	0.088	0.111
ENSG00000014641	MDH1	malate dehydrogenase 1	0.091	0.111
ENSG00000162365	CYP4A22	cytochrome P450 family 4 subfamily A member 22	0.092	0.147
ENSG00000067064	IDI1	isopentenyl-diphosphate delta isomerase 1	0.096	0.098
ENSG00000120437	ACAT2	acetyl-CoA acetyltransferase 2	0.096	0.117
ENSG00000171503	ETFDH	electron transfer flavoprotein dehydrogenase	0.104	0.118
ENSG00000072042	RDH11	retinol dehydrogenase 11	0.105	0.112
ENSG00000116133	DHCR24	24-dehydrocholesterol reductase	0.112	0.108
ENSG00000187048	CYP4A11	cytochrome P450 family 4 subfamily A member 11	0.115	0.106
ENSG00000164120	HPGD	15-hydroxyprostaglandin dehydrogenase	0.122	0.124
ENSG00000134240	HMGCS2	3-hydroxy-3-methylglutaryl-CoA synthase 2	0.124	0.089
ENSG00000136750	GAD2	glutamate decarboxylase 2	0.140	0.144

RNA-Seq-Related Data of MM.1S^{gfp/luc} Cells Treated with 1.00 μ M Triacsin C

R Code for Identification of Differentially Expressed Genes RNA-Sequencing

```
title: "DE analysis for CM"  
author: "Princess Rodriguez"  
date: "12/9/2022"  
output: html_document  
---
```

```
```${r setup, include=FALSE}  
knitr::opts_chunk$set(echo = TRUE)
library(DESeq2)
library(dplyr)
library(ggplot2)
library(pheatmap)
library(magrittr)
library(knitr)
library(kableExtra)
library(hypeR)
library(msigdb)
```
```

```
## Load data
```

```
```${r}  
countdata <- read.csv("CM.salmon.merged.gene_counts.csv", header=TRUE,
row.names=1)
colnames(countdata) <- colnames(countdata)
countdata <- as.matrix(countdata)
head(countdata)
```
```

```
## Load annotation data
```

```
```${r}  
filter low read counts
keep <- rowSums(countdata) > 10
countdata <- countdata[keep,]
dim(countdata)
```

```
assign condition
```

```
annotation <- read.table("anno.txt", header = T, row.names = 1)
replicate <- factor(annotation$replicate)
treatment <- factor(annotation$treatment)
```

```

coldata <- data.frame(row.names=colnames(countdata), treatment, replicate)
head(coldata)
```

# Setup DESeq2 design
```{r}
dds <- DESeqDataSetFromMatrix(countData = round(countdata),
 colData = coldata,
 design= ~treatment)
dds <- DESeq(dds)
```

# Principal components analysis
```{r}
#pdf("PCAplot.pdf")
vstcounts <- vst(dds, blind=TRUE)
plotPCA(vstcounts, intgroup=c("treatment"))
#dev.off()
```

```{r}
Sample correlation analysis
vst <- varianceStabilizingTransformation(dds, blind=TRUE)
vst_mat <- assay(vst)
vst_cor <- cor(vst_mat)
annotation_heatmap <- data.frame(row.names=colnames(vst_mat), treatment)

pheatmap(vst_cor,
 annotation_col = annotation_heatmap, main = "sample correlation", show_rownames
 = F, show_colnames = F)
```

# Run DESeq2
```{r}
dds <- DESeq(dds)

res_drug <- results(dds, contrast=c("treatment",'drug', 'control'))

###
res_drug <- res_drug[order(res_drug$padj),]
res_drug_data <- merge(as.data.frame(res_drug), as.data.frame(counts(dds,
normalized=TRUE)), by="row.names", sort=FALSE)
names(res_drug_data)[1] <- "Gene"

#Get DEG up/down lists
res_drug_DEGs <- as.data.frame(res_drug) %>% dplyr::filter(abs(log2FoldChange) > 1
& padj < 0.05) %>% tibble::rownames_to_column("Gene")

```

```

write.csv(res_drug_DEGs, "DEG_drugvscontrol.csv", row.names = TRUE)
```

# Pathway analysis
```{r}
using the biomaRt.outputs create the genelists.csv
gene_lists<- read.csv("gene_list.csv")
gene_lists<- as.data.frame(gene_lists)
gene_lists <- mutate_all(gene_lists, .funs=toupper)

#load geneset
KEGG <- msigdb_gsets(species = "Homo sapiens", category = "C2", subcategory =
"CP:KEGG")
#https://www.gsea-msigdb.org/gsea/msigdb/human/genesets.jsp?collection=C2

#load gene list - this gene list is ALL DE genes - not separated by UP or DOWN
x<- gene_lists[which(gene_lists$gene != ""),1]

#KEGG
#pdf("KEGG-pathway.pdf")
hyp_1 <- hyperR(x, KEGG, test = "hypergeometric", background = 50000, fdr = 0.05,
plotting = TRUE)
print(hyp_1)
hyp_dots(hyp_1, title = "KEGG - drug vs control", abrv = 30, val = "fdr")
#dev.off()

```

### **Modified R Code for Identification of Differentially Expressed Genes RNA-Sequencing for P-values for All Detect Transcripts**

This code was modified by Christian Potts and the data derived from this code in was used to make the volcano plot seen in Figure 17B

```

title: "DE analysis for CM_v2_CMP"
author: "Princess Rodriguez and Christian M. Potts"
date: "12/9/2022 and 04/23/24"
output: csv document

```

```

```{r setup, include=FALSE}
knitr::opts_chunk$set(echo = TRUE)
library(DESeq2)
library(dplyr)
library(ggplot2)
library(pheatmap)

```

```

library(magrittr)
library(knitr)
library(kableExtra)
library(hypeR)
library(msigdb)
```



```

## Load data

```{r}
#CMP heavily edited here to convert data into a named numeric matrix per
requirements for rowSums function.
countdata.orig <- read.table("salmon.merged.gene_counts.tsv", header=TRUE,
row.names=1)
What is this line accomplishing?
#colnames(countdata) <- colnames(countdata)
countdata.orig <- as.matrix(countdata.orig)
countdata <- countdata.orig[,2:7]
countdata <- matrix(as.numeric(countdata),ncol = 6)
rownames(countdata) <- countdata.orig[,1]
colnames(countdata) <- colnames(countdata.orig)[2:7]
head(countdata)
summary(countdata)
```

## Load annotation data

```{r}
filter low read counts
CMP added subset so the gene_name column was not being included in the
rowSums
keep <- rowSums(countdata) > 10
countdata <- countdata[keep,]
dim(countdata)

assign condition
annotation <- read.table("anno.txt", header = T, row.names = 1)
replicate <- factor(annotation$replicate)
treatment <- factor(annotation$treatment)
coldata <- data.frame(row.names=colnames(countdata), treatment, replicate)
head(coldata)
```

# Setup DESeq2 design
```{r}
dds <- DESeqDataSetFromMatrix(countData = round(countdata),

```


```

```

        colData = coldata,
        design= ~treatment)
dds <- DESeq(dds)
...

# Principal components analysis
```{r}
#pdf("PCAplot.pdf")
vstcounts <- vst(dds, blind=TRUE)
plotPCA(vstcounts, intgroup=c("treatment"))
#dev.off()
...

```{r}
# Sample correlation analysis
vst <- varianceStabilizingTransformation(dds, blind=TRUE)
vst_mat <- assay(vst)
vst_cor <- cor(vst_mat)
annotation_heatmap <- data.frame(row.names=colnames(vst_mat), treatment)

pheatmap(vst_cor,
          annotation_col = annotation_heatmap, main = "sample correlation",
          show_rownames = F, show_colnames = F)
...

# Run DESeq2
```{r}
dds <- DESeq(dds)

res_drug <- results(dds, contrast=c("treatment','drug', 'control'))

####
res_drug <- res_drug[order(res_drug$padj),]
res_drug_data <- merge(as.data.frame(res_drug), as.data.frame(counts(dds,
normalized=TRUE)), by="row.names", sort=FALSE)
names(res_drug_data)[1] <- "Gene"

#Get DEG up/down lists
res_drug_DEGs <- as.data.frame(res_drug) %>% dplyr::filter(abs(log2FoldChange) > 1
& padj < 0.05) %>% tibble::rownames_to_column("Gene")
#CMP adjustment based on what Connor asked for
res_drug_all <- as.data.frame(res_drug) %>% tibble::rownames_to_column("Gene")

write.csv(res_drug_all, "all_drugvscontrol.csv", row.names = TRUE)
#CMP did not proceed further beyond this point
...

```



**Table 15 Significantly Differentially Expressed Upregulated Genes in TriC-Treated MM.1S<sup>gfp/luc</sup> Cells for 24 hours**

Ensembl ID	Gene Symbol	Log2(FC)	p-value
ENSG00000146592.16	CREB5	5.89	6.15E-09
ENSG00000165029.15	ABCA1	5.62	1.67E-144
ENSG00000139269.2	INHBE	4.82	2.35E-12
ENSG00000275302.1	CCL4	4.26	4.90E-14
ENSG00000276070.4	CCL4L2	3.82	1.32E-13
ENSG00000160179.18	ABCG1	3.51	1.06E-113
ENSG00000140044.12	JDP2	3.47	1.56E-08
ENSG00000175197.12	DDIT3	3.43	1.03E-13
ENSG00000162772.16	ATF3	3.29	6.41E-14
ENSG00000060982.14	BCAT1	3.06	2.41E-08
ENSG00000128965.12	CHAC1	3.05	2.79E-25
ENSG00000151012.13	SLC7A11	3.00	9.20E-70
ENSG00000235823.2	OLMALINC	2.97	4.88E-34
ENSG00000120738.7	EGR1	2.71	1.90E-06
ENSG00000196517.11	SLC6A9	2.64	8.65E-23
ENSG00000128165.8	ADM2	2.60	1.92E-12
ENSG00000150051.13	MKX	2.49	1.08E-06
ENSG00000164647.8	STEAP1	2.48	6.67E-08
ENSG00000099194.5	SCD	2.40	8.32E-154
ENSG00000153714.5	LURAP1L	2.38	1.29E-08
ENSG00000226380.9	LINC-PINT	2.36	2.83E-15
ENSG00000172164.14	SNTB1	2.35	5.35E-07
ENSG00000271204.1	AC016831.4	2.30	8.31E-09
ENSG00000072310.16	SREBF1	2.24	2.26E-136
ENSG00000101255.10	TRIB3	2.22	7.37E-08
ENSG00000157514.16	TSC22D3	2.18	3.50E-37
ENSG00000130766.4	SESN2	2.16	4.22E-12
ENSG00000244405.7	ETV5	2.12	5.70E-33
ENSG00000168209.4	DDIT4	2.11	8.22E-38
ENSG00000100889.11	PCK2	2.08	9.04E-11
ENSG00000130707.17	ASS1	2.04	2.22E-09
ENSG00000087074.7	PPP1R15A	2.00	2.32E-08
ENSG00000173930.8	SLCO4C1	1.99	1.80E-14
ENSG00000172216.5	CEBPB	1.96	5.64E-06
ENSG00000119138.4	KLF9	1.95	2.86E-10
ENSG00000187678.9	SPRY4	1.94	2.36E-06
ENSG00000146859.6	TMEM140	1.91	3.40E-13
ENSG00000135069.13	PSAT1	1.89	4.87E-15

Table 15 Continued			
ENSG00000177606.6	JUN	1.88	6.03E-09
ENSG00000138162.18	TACC2	1.86	4.10E-06
ENSG00000134070.4	IRAK2	1.81	1.58E-09
ENSG00000007944.14	MYLIP	1.81	6.99E-17
ENSG00000145362.17	ANK2	1.80	1.86E-05
ENSG00000163683.11	SMIM14	1.80	5.76E-07
ENSG00000204103.3	MAFB	1.76	1.15E-04
ENSG00000128272.14	ATF4	1.74	3.15E-56
ENSG00000173208.3	ABCD2	1.74	8.06E-05
ENSG00000139112.10	GABARAPL1	1.71	7.70E-05
ENSG00000168003.16	SLC3A2	1.69	9.77E-17
ENSG00000186480.12	INSIG1	1.67	1.15E-17
ENSG00000105327.17	BBC3	1.65	2.56E-09
ENSG00000123329.17	ARHGAP9	1.64	7.42E-06
ENSG00000223891.5	OSER1-DT	1.64	4.26E-04
ENSG00000155961.4	RAB39B	1.63	4.71E-12
ENSG00000178878.12	APOLD1	1.63	5.98E-05
ENSG00000136010.13	ALDH1L2	1.63	6.55E-09
ENSG00000285725.1	AC004967.2	1.62	5.32E-03
ENSG00000130164.13	LDLR	1.61	2.29E-60
ENSG00000169710.8	FASN	1.61	1.85E-17
ENSG00000141682.11	PMAIP1	1.59	4.43E-17
ENSG00000166123.13	GPT2	1.57	3.36E-22
ENSG00000111266.8	DUSP16	1.55	1.25E-07
ENSG00000273338.1	AC103591.3	1.55	1.08E-03
ENSG00000184014.7	DENND5A	1.55	3.15E-03
ENSG00000137331.11	IER3	1.54	1.09E-04
ENSG00000276085.1	CCL3L1	1.52	7.95E-07
ENSG00000185338.5	SOCS1	1.52	8.68E-04
ENSG00000146733.13	PSPH	1.50	3.37E-24
ENSG00000160200.17	CBS	1.49	8.40E-06
ENSG00000285106.1	AC016831.6	1.47	9.81E-09
ENSG00000135842.16	FAM129A	1.47	1.06E-07
ENSG00000197646.7	PDCD1LG2	1.47	5.80E-03
ENSG00000248323.6	LUCAT1	1.47	2.47E-03
ENSG00000143507.17	DUSP10	1.47	3.35E-04
ENSG00000124762.13	CDKN1A	1.46	9.81E-36
ENSG00000168672.3	FAM84B	1.46	1.37E-09
ENSG00000280800.1	FP671120.3	1.45	1.07E-06
ENSG00000163297.16	ANTXR2	1.44	3.35E-15
ENSG00000198855.6	FICD	1.43	1.89E-15

Table 15 Continued			
ENSG00000155304.5	HSPA13	1.42	2.13E-29
ENSG00000170345.9	FOS	1.42	1.95E-03
ENSG00000172071.11	EIF2AK3	1.41	2.47E-30
ENSG00000130522.5	JUND	1.41	3.57E-27
ENSG00000132718.8	SYT11	1.41	1.84E-19
ENSG00000145860.11	RNF145	1.40	5.20E-29
ENSG00000185022.11	MAFF	1.40	1.15E-12
ENSG00000277632.1	CCL3	1.39	2.21E-05
ENSG00000274180.1	NATD1	1.38	3.40E-03
ENSG00000101986.11	ABCD1	1.38	2.92E-06
ENSG00000134294.13	SLC38A2	1.36	5.06E-12
ENSG00000260916.7	CCPG1	1.36	2.18E-06
ENSG00000106105.13	GARS	1.35	2.50E-13
ENSG00000123983.13	ACSL3	1.33	1.09E-46
ENSG00000279192.1	PWAR5	1.33	2.63E-09
ENSG00000116852.14	KIF21B	1.33	4.10E-31
ENSG00000135604.9	STX11	1.33	1.37E-03
ENSG00000166750.9	SLFN5	1.31	8.78E-10
ENSG00000156675.15	RAB11FIP1	1.31	3.31E-23
ENSG00000008086.11	CDKL5	1.30	1.37E-06
ENSG00000143333.6	RGS16	1.30	4.41E-11
ENSG00000205189.11	ZBTB10	1.29	2.03E-12
ENSG00000132846.5	ZBED3	1.29	8.00E-07
ENSG00000105856.13	HBP1	1.28	1.87E-13
ENSG00000100288.19	CHKB	1.28	3.00E-04
ENSG00000173334.3	TRIB1	1.28	8.81E-25
ENSG00000070669.16	ASNS	1.27	1.82E-17
ENSG00000278540.4	ACACA	1.27	1.68E-41
ENSG00000102271.13	KLHL4	1.26	1.81E-03
ENSG00000070540.12	WIPI1	1.25	2.16E-17
ENSG00000112972.14	HMGCS1	1.25	2.79E-27
ENSG00000171703.16	TCEA2	1.25	1.51E-04
ENSG00000163082.9	SGPP2	1.24	2.11E-03
ENSG00000166575.16	TMEM135	1.24	1.51E-18
ENSG00000147650.11	LRP12	1.23	2.88E-03
ENSG00000165175.15	MID1IP1	1.23	1.22E-21
ENSG00000231721.7	LINC-PINT	1.23	2.44E-16
ENSG00000124615.19	MOCS1	1.22	3.14E-03
ENSG00000073910.21	FRY	1.22	1.01E-03
ENSG00000148841.16	ITPRIP	1.22	4.27E-08
ENSG00000183696.13	UPP1	1.21	4.55E-11

Table 15 Continued			
ENSG00000100100.12	PIK3IP1	1.21	3.10E-07
ENSG00000006652.13	IFRD1	1.21	4.83E-11
ENSG00000132510.10	KDM6B	1.21	1.10E-08
ENSG00000133874.1	RNF122	1.20	3.09E-10
ENSG00000074935.13	TUBE1	1.20	3.57E-07
ENSG00000135338.13	LCA5	1.20	4.36E-04
ENSG00000130066.16	SAT1	1.20	8.48E-09
ENSG00000176399.3	DMRTA1	1.20	1.50E-03
ENSG00000115956.9	PLEK	1.20	8.26E-20
ENSG00000112715.21	VEGFA	1.18	8.15E-17
ENSG00000144802.11	NFKBIZ	1.16	1.11E-04
ENSG00000141582.14	CBX4	1.16	3.91E-08
ENSG00000167797.7	CDK2AP2	1.16	9.17E-23
ENSG00000110619.17	CARS	1.15	4.16E-15
ENSG00000162645.12	GBP2	1.15	6.65E-04
ENSG00000082641.15	NFE2L1	1.14	1.69E-24
ENSG00000164010.14	ERMAP	1.14	2.59E-03
ENSG00000178607.15	ERN1	1.13	2.61E-27
ENSG00000172893.15	DHCR7	1.13	4.83E-14
ENSG00000181218.5	HIST3H2A	1.13	1.54E-06
ENSG00000150961.14	SEC24D	1.12	2.32E-07
ENSG00000185262.8	UBALD2	1.12	1.42E-06
ENSG00000167552.13	TUBA1A	1.11	1.41E-10
ENSG00000079335.19	CDC14A	1.11	4.89E-04
ENSG00000008283.15	CYB561	1.11	5.29E-04
ENSG00000065911.11	MTHFD2	1.11	2.59E-23
ENSG00000150527.17	MIA2	1.10	1.24E-12
ENSG00000071242.11	RPS6KA2	1.10	1.38E-06
ENSG00000196376.10	SLC35F1	1.10	1.83E-03
ENSG00000148154.9	UGCG	1.08	6.50E-14
ENSG00000121989.14	ACVR2A	1.08	1.39E-03
ENSG00000120129.5	DUSP1	1.08	8.12E-05
ENSG00000111684.10	LPCAT3	1.07	4.52E-08
ENSG00000154359.12	LONRF1	1.06	1.82E-10
ENSG00000151917.17	BEND6	1.05	1.92E-03
ENSG00000235636.1	NUS1P1	1.04	7.85E-04
ENSG00000087510.6	TFAP2C	1.03	7.60E-05
ENSG00000135269.17	TES	1.03	3.29E-19
ENSG00000170379.20	TCAF2	1.03	5.29E-03
ENSG00000168016.14	TRANK1	1.03	6.61E-11
ENSG00000100292.16	HMOX1	1.02	1.51E-13

Ensembl ID	Gene Symbol	Log2(FC)	p-value
ENSG00000144481.16	TRPM8	1.01	4.77E-04
ENSG00000211459.2	MT-RNR1	1.01	5.87E-09
ENSG00000089041.16	P2RX7	1.01	1.00E-09
ENSG00000172183.14	ISG20	1.01	4.06E-10
ENSG00000185650.9	ZFP36L1	1.00	4.16E-07
ENSG00000151135.9	TMEM263	1.00	9.81E-06

**Table 16 Significantly Differentially Expressed Downregulated Genes in TriC-Treated MM.1S<sup>gfp/luc</sup> Cells for 24 hours**

Ensembl ID	Gene Symbol	Log2(FC)	p-value
ENSG00000112309.10	B3GAT2	-2.93	1.04E-04
ENSG00000165966.15	PDZRN4	-2.39	1.12E-05
ENSG00000260456.6	C16orf95	-2.17	9.76E-04
ENSG00000154646.8	TMPRSS15	-1.98	8.36E-09
ENSG00000214827.9	MTCP1	-1.89	4.10E-03
ENSG00000172159.15	FRMD3	-1.82	1.41E-03
ENSG00000132470.13	ITGB4	-1.80	6.66E-04
ENSG00000170667.14	RASA4B	-1.70	2.66E-07
ENSG00000137843.11	PAK6	-1.68	2.07E-04
ENSG00000168329.13	CX3CR1	-1.64	1.06E-12
ENSG00000120832.9	MTERF2	-1.51	8.75E-04
ENSG00000284989.1	AL451062.3	-1.51	5.76E-04
ENSG00000165238.16	WNK2	-1.50	1.30E-04
ENSG00000100167.20	SEP3	-1.42	3.41E-03
ENSG00000255562.2	UNC93B6	-1.41	8.28E-04
ENSG00000150510.16	FAM124A	-1.40	4.18E-06
ENSG00000185028.3	LRRC14B	-1.39	3.96E-04
ENSG00000183876.8	ARSI	-1.33	2.81E-04
ENSG00000184489.11	PTP4A3	-1.31	3.26E-04
ENSG00000149403.12	GRIK4	-1.31	2.58E-03
ENSG00000049323.15	LTBP1	-1.31	2.16E-03
ENSG00000172379.20	ARNT2	-1.30	8.08E-04
ENSG00000198853.11	RUSC2	-1.23	2.43E-03
ENSG00000064692.18	SNCAIP	-1.22	1.92E-03
ENSG00000197256.10	KANK2	-1.17	5.40E-09
ENSG00000213366.12	GSTM2	-1.11	1.97E-03
ENSG00000140326.13	CDAN1	-1.10	3.01E-05
ENSG00000126351.12	THRA	-1.10	1.23E-03
ENSG00000134369.15	NAV1	-1.08	3.11E-10
ENSG00000127334.10	DYRK2	-1.08	3.90E-13
ENSG00000213160.9	KLHL23	-1.07	5.62E-03

Table 16 Continued			
ENSG00000137942.16	FNBP1L	-1.06	2.44E-03
ENSG00000104936.17	DMPK	-1.06	2.53E-03
ENSG00000136929.12	HEMGN	-1.06	1.99E-11
ENSG00000078053.16	AMPH	-1.05	3.43E-05
ENSG00000259932.1	AC051619.7	-1.04	5.53E-04
ENSG00000165449.11	SLC16A9	-1.04	4.62E-05
ENSG00000164684.13	ZNF704	-1.03	1.98E-04
ENSG00000142677.3	IL22RA1	-1.02	1.91E-03
ENSG00000181449.3	SOX2	-1.01	3.77E-07
ENSG00000242574.8	HLA-DMB	-1.01	3.99E-03

**Table 17 Top 10 Significantly Upregulated Reactome Pathways in MM.1S Cells Treated with Triacsin C for 24 hours**

Reactome Term	p-value	q-value	Significantly Associated Genes
Response Of EIF2AK1 (HRI) To Heme Deficiency R-HSA-9648895	1.16E-13	5.05E-11	[PPP1R15A, CEBPB, DDIT3, ASNS, TRIB3, CHAC1, ATF3, ATF4]
Regulation Of Cholesterol Biosynthesis By SREBP (SREBF) R-HSA-1655829	1.66E-08	3.61E-06	[SREBF1, HMGCS1, SCD, INSIG1, FASN, DHCR7, SEC24D, ACACA]
Cellular Responses To Stress R-HSA-2262752	1.45E-07	1.96E-05	[PPP1R15A, KDM6B, JUN, CEBPB, CDKN1A, CBX4, EIF2AK3, ASNS, WIPI1, SLC7A11, FOS, HSPA13, VEGFA, ERN1, DDIT3, RPS6KA2, SESN2, HMOX1, TRIB3, CHAC1, ATF3, ATF4]
Cellular Responses To Stimuli R-HSA-8953897	2.02E-07	1.96E-05	[PPP1R15A, KDM6B, JUN, CEBPB, CDKN1A, CBX4, EIF2AK3, ASNS, WIPI1, SLC7A11, FOS, HSPA13, VEGFA, ERN1, DDIT3, RPS6KA2, SESN2, HMOX1, TRIB3, CHAC1, ATF3, ATF4]
PERK Regulates Gene Expression R-HSA-381042	2.26E-07	1.96E-05	[CEBPB, DDIT3, EIF2AK3, ASNS, ATF3, ATF4]
Unfolded Protein Response (UPR) R-HSA-381119	7.59E-07	5.49E-05	[ERN1, CEBPB, DDIT3, EIF2AK3, ASNS, WIPI1, ATF3, ATF4]

<b>Table 17 Continued</b>			
Activation Of Gene Expression By SREBF (SREBP) R-HSA-2426168	1.22E-06	7.58E-05	[SREBF1, HMGCS1, SCD, FASN, DHCR7, ACACA]
NR1H2 And NR1H3-mediated Signaling R-HSA-9024446	2.12E-06	0.0001	[ABCA1, MYLIP, SREBF1, SCD, FASN, ABCG1]
ATF4 Activates Genes In Response To Endoplasmic Reticulum Stress R-HSA-380994	2.58E-06	0.0001	[CEBPB, DDIT3, ASNS, ATF3, ATF4]
Metabolism Of Lipids R-HSA-556833	3.92E-05	0.0016	[ABCA1, ARHGAP9, SREBF1, CHKB, HMGCS1, INSIG1, MID1IP1, ACSL3, SGPP2, ACACA, UGCG, SCD, FASN, LPCAT3, TRIB3, DHCR7, SEC24D, ABCD1]

**Table 18. Top 10 Significantly Upregulated KEGG Pathways in MM.1S Cells Treated with Triacsin C for 24 hours**

<b>KEGG Term</b>	<b>p-value</b>	<b>q-value</b>	<b>Significantly Associated Genes</b>
Ferroptosis	0.000001	0.000172	[LPCAT3, HMOX1, SLC3A2, SLC7A11, ACSL3, SAT1]
Lipid and atherosclerosis	0.000002	0.000172	[ERN1, ABCA1, JUN, CCL3L1, DDIT3, EIF2AK3, CCL3, FOS, LDLR, ABCG1, ATF4]
Apoptosis	0.000003	0.000178	[ERN1, JUN, TUBA1A, DDIT3, EIF2AK3, PMAIP1, FOS, ATF4, BBC3]
Parathyroid hormone synthesis, secretion and action	0.000029	0.001338	[EGR1, CDKN1A, JUND, MAFB, FOS, ATF4, CREB5]
Fluid shear stress and atherosclerosis	0.000163	0.005457	[JUN, DUSP1, HMOX1, FOS, ACVR2A, ASS1, VEGFA]
MAPK signaling pathway	0.000179	0.005457	[JUN, JUND, DUSP10, DUSP1, DDIT3, RPS6KA2, FOS, DUSP16, ATF4, VEGFA]
Toll-like receptor signaling pathway	0.000232	0.006055	[JUN, CCL3L1, CCL4L2, CCL4, CCL3, FOS]
Non-alcoholic fatty liver disease	0.000318	0.00727	[ERN1, SREBF1, JUN, DDIT3, EIF2AK3, FOS, ATF4]
Fatty acid biosynthesis	0.000418	0.008501	[FASN, ACSL3, ACACA]
AMPK signaling pathway	0.000500	0.008702	[SREBF1, SCD, FASN, ACACA, PCK2, CREB5]

## Proteomics Hits in MM.1S<sup>gfp/luc</sup> Cells Treated with 1 or 2 $\mu$ M Triacsin for 48 Hours

**Table 19 Significantly Upregulated Proteins of MM.1S<sup>gfp/luc</sup> Cells Treated with 1.0  $\mu$ M Triacsin for 48 hours**

UniProt ID	Protein Symbol	Log2(FC)	p-value
Q9HCU5	PREB	1.62	0.02603
P50416	CPT1A	1.02	0.02552
Q9HA77	CARS2	0.72	0.014
P08133	ANXA6	0.64	0.0405
O95573	ACSL3	0.61	0.04346
P26440	IVD	0.58	0.03686
O75131	CPNE3	0.53	0.00624
Q9GZR7	DDX24	0.50	0.04785
P35580	MYH10	0.49	0.02639
P61201	COPS2	0.46	0.00812
P49770	EIF2B2	0.43	0.00981
P61026	RAB10	0.42	0.03875
Q969N2	PIGT	0.41	0.04862
P35606	COPB2	0.40	0.03181
P51665	PSMD7	0.38	0.02548
Q9UBU9	NXF1	0.34	0.04457
P52789	HK2	0.32	0.03924
P49748	ACADVL	0.31	0.04167
Q9NVP1	DDX18	0.308682	0.04786
Q96HV5	TMEM41A	0.272561	0.03795
Q8NEV1	CSNK2A3	0.248528	0.02013
Q5JTH9	RRP12	0.218496	0.01967
P42765	ACAA2	0.199683	0.02503



P62750	RPL23A	0.189744	0.00994
O15084	ANKRD28	0.174864	0.01279
P46459	NSF	0.162472	0.03706
Q13428	TCOF1	0.158698	0.01182
P53999	SUB1	0.13977	0.04665
P05388	RPLP0	0.130633	0.04985
Q92621	NUP205	0.130517	0.01514
P18124	RPL7	0.100304	0.04337

**Table 20 Significantly Downregulated Proteins of MM.1S<sup>gfp/luc</sup> Cells Treated with 1.0  $\mu$ M Triacsin for 48 hours**

<b>UniProt ID</b>	<b>Protein Symbol</b>	<b>Log2(FC)</b>	<b>p-value</b>
P14854	COX6B1	-2.43	0.00036
P07108	DBI	-1.99	0.0058
P48539	PCP4	-1.88	0.00798
P16949	STMN1	-1.76	0.01058
P00441	SOD1	-1.70	0.00311
P30046	DDT	-1.65	0.0025
P30086	PEBP1	-1.65	0.00274
Q96HC4	PDLIM5	-1.56	0.02285
P54819	AK2	-1.44	0.00546
Q13404	UBE2V1	-1.39	0.00441
P14174	MIF	-1.34	0.00439
P61960	UFM1	-1.32	0.02884
O15212	PFDN6	-1.24	0.00103
Q04760	GLO1	-1.20	0.00295

Table 20 Continued			
P60174	TPI1	-1.19	0.0077
P56385	ATP5ME	-1.13	0.03366
O75347	TBCA	-1.13	0.02534
P25774	CTSS	-1.11	0.02113
Q06323	PSME1	-1.11	0.01176
P62937	PPIA	-1.04	0.00243
O14737	PDCD5	-1.03	0.02147
Q8WU39	MZB1	-1.01	0.0018
P31949	S100A11	-0.94	9.61E-05
P12955	PEPD	-0.92	0.02933
Q969H8	MYDGF	-0.90	0.00622
Q9NPA8	ENY2	-0.90	0.00188
P07602	PSAP	-0.88	0.00251
Q9UBT2	UBA2	-0.88	0.02055
P01591	JCHAIN	-0.87	0.00424
P20674	COX5A	-0.85	0.01349
O60888	CUTA	-0.85	0.03677
Q96AE4	FUBP1	-0.85	0.0303
Q9HB40	SCPEP1	-0.81	0.02587
P10599	TXN	-0.81	0.02117
Q9BRA2	TXNDC17	-0.78	0.00955
Q9P1F3	ABRACL	-0.77	0.01639
P62136	PPP1CA	-0.77	0.00324
Q9BWD1	ACAT2	-0.76	0.04915
Q9UHV9	PFDN2	-0.76	0.02221

Table 20 Continued			
Q9Y3D6	FIS1	-0.76	0.00941
P19404	NDUFV2	-0.74	0.00352
P63279	UBE2I	-0.71	0.02546
P14406	COX7A2	-0.71	0.0032
P61586	RHOA	-0.71	0.00462
P68402	PAFAH1B2	-0.68	0.0227
Q14137	BOP1	-0.67	0.00276
P30044	PRDX5	-0.66	0.0071
P61758	VBP1	-0.66	0.03197
P04066	FUCA1	-0.66	0.00319
O75340	PDCD6	-0.65	0.00793
P37235	HPCAL1	-0.65	0.0088
B9A064	IGLL5	-0.63	0.00482
P62979	RPS27A	-0.62	0.03995
P60953	CDC42	-0.61	0.04743
Q92520	FAM3C	-0.61	0.00359
P04233	CD74	-0.60	0.01737
P15121	AKR1B1	-0.59	0.02052
O00483	NDUFA4	-0.59	0.02549
P31153	MAT2A	-0.58	0.03409
P32119	PRDX2	-0.58	0.02419
Q99497	PARK7	-0.57	0.03034
P52815	MRPL12	-0.56	0.01673
O14745	SLC9A3R1	-0.56	0.00474
Q96T88	UHRF1	-0.56	0.01155

Table 20 Continued			
Q96IX5	ATP5MK	-0.56	0.01901
P49773	HINT1	-0.56	0.00617
Q9B XK5	BCL2L13	-0.55	0.00836
Q06830	PRDX1	-0.55	0.01014
Q15907	RAB11B	-0.53	0.0006
P54727	RAD23B	-0.51	0.02716
O95881	TXNDC12	-0.51	0.03741
P30041	PRDX6	-0.49	0.02302
P40926	MDH2	-0.48	0.00938
O15382	BCAT2	-0.46	0.02622
Q9NR45	NANS	-0.46	0.03282
P07737	PFN1	-0.46	0.03798
Q96FW1	OTUB1	-0.46	0.03874
Q99459	CDC5L	-0.46	0.04299
P36405	ARL3	-0.44	0.01956
P67775	PPP2CA	-0.44	0.0143
P46013	MKI67	-0.44	0.047
P14314	PRKCSH	-0.44	0.01997
Q15424	SAFB	-0.43	0.01338
P26010	ITGB7	-0.43	0.01047
P22314	UBA1	-0.43	0.01877
Q8NCW5	NAXE	-0.42	0.03351
Q9H5X1	CIAO2A	-0.42	0.00736
P49189	ALDH9A1	-0.40	0.02836
Q86V81	ALYREF	-0.39	0.04203

Table 20 Continued			
Q15181	PPA1	-0.37	0.0082
Q02790	FKBP4	-0.37	0.04027
Q13242	SRSF9	-0.36	0.0182
Q13151	HNRNPA0	-0.34	0.04288
P12004	PCNA	-0.34	0.02858
P31948	STIP1	-0.33	0.04582
O15067	PFAS	-0.33	0.04029
Q12906	ILF3	-0.32	0.03873
P10747	CD28	-0.32	0.02036
Q03252	LMNB2	-0.32	0.01578
P14618	PKM	-0.32	0.00326
Q8NBJ7	SUMF2	-0.31	0.03212
O76003	GLRX3	-0.31	0.02591
O00154	ACOT7	-0.30	0.00249
P05387	RPLP2	-0.30	0.03781
P27797	CALR	-0.30	0.01821
P49458	SRP9	-0.29	0.00989
Q9NT62	ATG3	-0.29	0.00649
P30566	ADSL	-0.28	0.04414
P04406	GAPDH	-0.27	0.04388
Q8WXX5	DNAJC9	-0.27	0.00801
Q9BYG3	NIFK	-0.27	0.03119
Q15287	RNPS1	-0.26	0.00801
P19623	SRM	-0.25	0.02923
O95319	CELF2	-0.25	0.03777

Table 20 Continued			
Q9H7B2	RPF2	-0.24	0.02887
P45974	USP5	-0.24	0.01607
Q9BSC4	NOL10	-0.24	0.04576
P19338	NCL	-0.24	0.0388
P55769	SNU13	-0.24	0.00683
P17844	DDX5	-0.23	0.01053
P07814	EPRS1	-0.23	0.02249
Q9BTY7	HGH1	-0.21	0.0168
P98179	RBM3	-0.21	0.02586
P00505	GOT2	-0.21	0.03319
P43686	PSMC4	-0.19	0.04668
Q12904	AIMP1	-0.19	0.04765
P22102	GART	-0.19	0.00754
P49368	CCT3	-0.18	0.03312
Q5SRE5	NUP188	-0.17	0.03088
P38159	RBMX	-0.17	0.04715
Q9C0C9	UBE2O	-0.16	0.02252
P50991	CCT4	-0.16	0.04639
P50990	CCT8	-0.15	0.01614
P68371	TUBB4B	-0.15	0.04662
P07910	HNRNPC	-0.14	0.00094
P41252	IARS1	-0.12	0.02433

**Table 21 Significantly Upregulated Proteins of MM.1S<sup>gfp/luc</sup> Cells Treated with 2.0  $\mu$ M Triacsin for 48 hours**

UniProt ID	Protein Symbol	Log2(FC)	p-value
Q6FI13	H2AC19	2.29	0.00059
P12259	F5	2.26	0.03708
Q9HA77	CARS2	1.51	0.00215
O14662	STX16	1.43	0.01726
Q9Y5M8	SRPRB	1.29	0.01658
P35610	SOAT1	1.27	0.02952
Q8WVX9	FAR1	1.12	0.04806
P50416	CPT1A	1.05	0.00218
Q9UJS0	SLC25A13	1.02	0.00209
Q7Z4W1	DCXR	0.97	0.00915
O75460	ERN1	0.96	0.00761
P03905	MT-ND4	0.94	0.00221
P26440	IVD	0.90	0.0087
Q86YN1	DOLPP1	0.88	0.00647
P30536	TSPO	0.87	0.00809
Q7KZN9	COX15	0.86	0.01161
Q9UJZ1	STOML2	0.81	0.00312
P43307	SSR1	0.79	0.00035
Q13405	MRPL49	0.79	0.01717
Q5XKP0	MICOS13	0.79	0.03481
Q9C0D9	SELENOI	0.78	0.00509
Q9UBV2	SEL1L	0.78	0.00156
P03891	MT-ND2	0.78	0.00998
Q9NR50	EIF2B3	0.77	0.01477
Q96S52	PIGS	0.77	0.01462

<b>Table 21 Continued</b>			
P61026	RAB10	0.73	0.00074
P68871	HBB	0.72	0.04873
P62341	SELENOT	0.69	0.00572
P12235	SLC25A4	0.69	0.01044
O95573	ACSL3	0.69	0.02013
Q9Y6N5	SQOR	0.68	0.0029
Q9H9B4	SFXN1	0.68	0.0031
O95563	MPC2	0.67	0.00559
P35580	MYH10	0.67	0.04866
O00217	NDUFS8	0.67	0.00147
Q9H061	TMEM126A	0.67	0.01126
Q5JTV8	TOR1AIP1	0.67	0.03827
P48449	LSS	0.66	0.04981
Q9UIQ6	LNPEP	0.66	0.04491
Q9BUB7	TMEM70	0.65	0.02898
O95202	LETM1	0.65	0.00469
Q9BUQ8	DDX23	0.65	0.04524
Q96JJ7	TMX3	0.64	0.00028
P61619	SEC61A1	0.63	0.00065
Q53GQ0	HSD17B12	0.62	0.011
Q96KA5	CLPTM1L	0.62	0.00073
P53007	SLC25A1	0.61	0.01884
Q9NTJ5	SACM1L	0.61	0.04408
Q9NVI7	ATAD3A	0.61	0.00782
Q9BQ75	CMSS1	0.61	0.00595
Q96HY6	DDRGK1	0.60	0.00903



<b>Table 21 Continued</b>			
Q9Y697	NFS1	0.60	0.0397
Q9UM00	TMCO1	0.60	0.03391
Q9GZR7	DDX24	0.59	0.03783
Q96DZ1	ERLEC1	0.59	0.00038
Q96G23	CERS2	0.59	0.00029
Q96A33	CCDC47	0.58	0.00381
P50995	ANXA11	0.58	0.0004
Q9H3U1	UNC45A	0.58	0.0115
P49770	EIF2B2	0.57	0.00854
O60762	DPM1	0.57	0.01586
Q8N5K1	CISD2	0.57	0.00084
Q15738	NSDHL	0.56	0.02174
P56134	ATP5MF	0.56	0.00505
P61009	SPCS3	0.56	0.00148
Q8NF37	LPCAT1	0.56	0.00318
P08133	ANXA6	0.56	0.04365
Q9BSJ8	ESYT1	0.56	0.02172
O75844	ZMPSTE24	0.56	0.0283
Q92643	PIGK	0.55	0.00893
O75131	CPNE3	0.55	0.0074
Q9BXW7	HDHD5	0.55	0.00992
Q9BVL2	NUP58	0.55	0.01667
P61201	COPS2	0.55	0.01475
P82930	MRPS34	0.54	0.00397
Q96HV5	TMEM41A	0.54	0.00341
Q9UBX3	SLC25A10	0.54	0.00355

<b>Table 21 Continued</b>			
Q9BUN8	DERL1	0.54	0.00965
O75915	ARL6IP5	0.53	0.01198
P04844	RPN2	0.52	0.00466
Q9UKN8	GTF3C4	0.51	0.02881
Q9HCC0	MCCC2	0.51	0.01297
O00487	PSMD14	0.50	0.00407
Q6DD88	ATL3	0.50	0.02551
Q96GW9	MARS2	0.50	0.00615
O15260	SURF4	0.50	0.00789
P25685	DNAJB1	0.49	0.01512
P10515	DLAT	0.49	0.01268
O75746	SLC25A12	0.49	0.0015
Q6NUQ4	TMEM214	0.49	0.00764
P00846	MT-ATP6	0.49	0.03619
P24390	KDELR1	0.48	0.04852
Q9Y678	COPG1	0.47	0.02964
O15228	GNPAT	0.47	0.01693
Q9H845	ACAD9	0.47	0.04336
Q5JTH9	RRP12	0.46	0.00808
Q92665	MRPS31	0.46	0.03221
Q9BPW8	NIPSNAP1	0.46	0.00255
Q9UNL2	SSR3	0.45	0.02766
Q9UBS4	DNAJB11	0.45	0.00163
P35232	PHB1	0.45	0.0401
Q9BWS9	CHID1	0.45	0.04769
Q13155	AIMP2	0.45	0.03138

<b>Table 21 Continued</b>			
Q92552	MRPS27	0.45	0.00247
P09543	CNP	0.45	0.01904
P39656	DDOST	0.44	0.00222
Q8WWC4	MAIP1	0.44	0.00395
Q9Y399	MRPS2	0.44	0.03361
Q5JPE7	NOMO2	0.43	0.00138
Q32P28	P3H1	0.43	0.0018
Q86UE4	MTDH	0.43	0.0096
Q13724	MOGS	0.43	0.0034
O15173	PGRMC2	0.42	0.01182
P00387	CYB5R3	0.42	0.0141
Q3ZCQ8	TIMM50	0.42	0.03737
O00203	AP3B1	0.42	0.02084
P08195	SLC3A2	0.42	0.01749
P62841	RPS15	0.41	0.03194
Q02978	SLC25A11	0.41	0.00381
Q9NS69	TOMM22	0.41	0.01129
O14880	MGST3	0.41	0.04202
Q8TCT9	HM13	0.41	0.04255
Q96GM8	TOE1	0.41	0.00622
Q8TCJ2	STT3B	0.41	0.02606
Q00325	SLC25A3	0.40	0.02337
P49755	TMED10	0.40	0.00695
Q15005	SPCS2	0.40	0.01322
O43615	TIMM44	0.40	0.00919
Q13586	STIM1	0.40	0.01535

<b>Table 21 Continued</b>			
P48723	HSPA13	0.40	0.00274
Q9BUR5	APOO	0.39	0.00431
Q71UI9	H2AZ2	0.39	0.02566
Q99623	PHB2	0.39	0.02229
P82673	MRPS35	0.39	0.03019
Q15125	EBP	0.39	0.01891
Q9Y3L5	RAP2C	0.39	0.03938
P08240	SRPRA	0.38	0.00784
Q53H12	AGK	0.38	0.0445
Q9HC16	APOBEC3G	0.38	0.03621
Q9Y4L1	HYOU1	0.38	0.01113
Q8N0U8	VKORC1L1	0.37	0.00264
O76094	SRP72	0.37	0.04735
P16435	POR	0.37	0.0425
P51571	SSR4	0.37	0.00824
Q12769	NUP160	0.37	0.01996
P49748	ACADVL	0.37	0.01064
Q8N2K0	ABHD12	0.37	0.00534
Q9BY50	SEC11C	0.37	0.0141
Q07065	CKAP4	0.37	0.00296
O95831	AIFM1	0.37	0.03263
Q9Y277	VDAC3	0.37	0.02064
P56937	HSD17B7	0.36	0.00339
P00403	MT-CO2	0.36	0.03173
Q96JB5	CDK5RAP3	0.35	0.01318
Q9Y3A6	TMED5	0.35	0.00339

<b>Table 21 Continued</b>			
P18085	ARF4	0.35	0.01524
Q5JVF3	PCID2	0.35	0.01581
O14656	TOR1A	0.35	0.02459
Q9NVP1	DDX18	0.34	0.03875
Q10713	PMPCA	0.34	0.00397
Q15008	PSMD6	0.34	0.00843
P51398	DAP3	0.34	0.04196
P41240	CSK	0.33	0.00073
P51659	HSD17B4	0.33	0.01653
Q9Y512	SAMM50	0.33	0.03496
Q8WUM4	PDCD6IP	0.33	0.00864
Q5SSJ5	HP1BP3	0.33	0.04385
O75489	NDUFS3	0.33	0.02815
Q9BTE7	DCUN1D5	0.32	0.00675
P82933	MRPS9	0.32	0.02751
Q86VU5	COMTD1	0.32	0.04893
P04843	RPN1	0.32	0.0045
P49585	PCYT1A	0.31	0.01823
P40939	HADHA	0.31	0.03995
Q9P0J0	NDUFA13	0.31	0.02758
Q13057	COASY	0.31	0.02537
P54886	ALDH18A1	0.31	0.01609
Q16650	TBR1	0.31	0.02256
P61020	RAB5B	0.31	0.03118
P67812	SEC11A	0.30	0.04814
Q9H6S0	YTHDC2	0.30	0.00734

Table 21 Continued			
Q13084	MRPL28	0.30	0.01024
O75352	MPDU1	0.30	0.02921
P55160	NCKAP1L	0.30	0.03351
Q9UM54	MYO6	0.30	0.04663
Q9Y295	DRG1	0.29	0.03757
P42765	ACAA2	0.29	0.00956
P11172	UMPS	0.29	0.01125
P43246	MSH2	0.29	0.03028
Q96F07	CYFIP2	0.29	0.03978
Q07812	BAX	0.28	0.01419
P16615	ATP2A2	0.28	0.03621
Q93050	ATP6V0A1	0.28	0.00398
P46459	NSF	0.27	0.00657
P61421	ATP6V0D1	0.27	0.01577
Q9BVC6	TMEM109	0.27	0.01654
O15084	ANKRD28	0.27	0.02484
P0C7P4	UQCRFS1P1	0.27	0.04018
O96005	CLPTM1	0.27	0.04906
Q9Y3E0	GOLT1B	0.27	0.03187
Q96ST3	SIN3A	0.26	0.03364
Q00059	TFAM	0.26	0.03011
O14735	CDIPT	0.26	0.00106
Q9NX63	CHCHD3	0.26	0.03322
Q15084	PDIA6	0.26	0.00116
Q14566	MCM6	0.26	0.00571
Q8NEV1	CSNK2A3	0.25	0.00994

Table 21 Continued			
Q9H5Q4	TFB2M	0.25	0.00988
O95757	HSPA4L	0.24	0.02411
P62333	PSMC6	0.24	0.0344
Q8IYS1	PM20D2	0.24	0.0381
Q96EY7	PTCD3	0.24	0.02838
Q9BW27	NUP85	0.23	0.04811
P61106	RAB14	0.23	0.04901
P13489	RNH1	0.23	0.00845
P82650	MRPS22	0.23	0.01192
P15153	RAC2	0.22	0.04509
Q9BVK6	TMED9	0.22	0.01109
Q8N1F7	NUP93	0.22	0.04333
Q92979	EMG1	0.21	0.04737
Q9NWX4	HPF1	0.21	0.0446
Q8IXB1	DNAJC10	0.21	0.01089
Q9BVK2	ALG8	0.21	0.00062
Q13895	BYSL	0.21	0.01588
P30101	PDIA3	0.20	0.03479
P27824	CANX	0.19	0.02492
P07099	EPHX1	0.19	0.01699
Q9NRP0	OSTC	0.18	0.04007
Q04837	SSBP1	0.18	0.02473
Q9Y265	RUVBL1	0.18	0.00965
P55209	NAP1L1	0.18	0.02572
P18124	RPL7	0.13	0.03231
P68366	TUBA4A	0.11	0.01502

P22033	MMUT	0.10	0.02619
Q16186	ADRM1	0.08	0.00338
P42126	EC11	-0.06	0.03335

**Table 22 Significantly Downregulated Proteins of MM.1S<sup>gfp/luc</sup> Cells Treated with 2.0  $\mu$ M Triacsin for 48 hours**

<b>UniProt ID</b>	<b>Protein Symbol</b>	<b>Log2(FC)</b>	<b>p-value</b>
P14854	COX6B1	-3.16	0.00196
P48539	PCP4	-3.00	0.01429
P06454	PTMA	-2.63	0.00019
P16949	STMN1	-2.44	0.01961
Q96HC4	PDLIM5	-2.35	0.01091
P00441	SOD1	-2.32	0.0058
P07108	DBI	-2.28	0.01357
P56385	ATP5ME	-2.25	0.00585
P30086	PEBP1	-2.17	0.00035
P30046	DDT	-2.09	0.00148
P14174	MIF	-2.04	0.0057
Q13404	UBE2V1	-1.89	0.00383
P25774	CTSS	-1.88	8.57E-05
P61960	UFM1	-1.87	0.00141
O75347	TBCA	-1.87	9.25E-06
P54819	AK2	-1.86	1.56E-06
P60174	TPI1	-1.81	4.34E-05
Q14157	UBAP2L	-1.69	0.0108
Q01469	FABP5	-1.63	0.00041
Q06323	PSME1	-1.59	0.00083
Q96AE4	FUBP1	-1.55	4.13E-05
Q6EEV6	SUMO4	-1.54	0.00025
Q9UBT2	UBA2	-1.51	0.00611
Q04760	GLO1	-1.50	0.00087
P01591	JCHAIN	-1.49	0.00621
P46926	GNPDA1	-1.46	0.00296
O14737	PDCD5	-1.43	0.00196
Q9UQ35	SRRM2	-1.42	0.02126
Q9HB40	SCPEP1	-1.39	0.00452
Q9H299	SH3BGRL3	-1.38	0.00244
P25787	PSMA2	-1.38	0.04665



<b>Table 22 Continued</b>			
P39687	ANP32A	-1.36	0.00015
O15212	PFDN6	-1.32	0.00192
P61088	UBE2N	-1.31	0.0002
P40925	MDH1	-1.30	0.00516
Q9BRA2	TXNDC17	-1.30	0.00022
P0DP25	CALM3	-1.27	0.00187
Q13813	SPTAN1	-1.25	0.00102
O60888	CUTA	-1.25	0.00068
P04075	ALDOA	-1.25	0.00372
P07602	PSAP	-1.23	6.43E-05
P12955	PEPD	-1.20	0.00224
Q969H8	MYDGF	-1.20	0.01055
P10599	TXN	-1.19	0.00051
O60828	PQBP1	-1.19	0.00142
Q14847	LASP1	-1.19	0.00186
P99999	CYCS	-1.17	0.00124
Q9C005	DPY30	-1.16	0.04991
Q9BXK5	BCL2L13	-1.16	0.00317
Q9NPA8	ENY2	-1.15	0.00498
P60900	PSMA6	-1.15	0.00061
P37837	TALDO1	-1.13	0.00055
P23588	EIF4B	-1.12	0.0017
P06744	GPI	-1.11	0.0028
Q8WU39	MZB1	-1.10	0.00413
Q92520	FAM3C	-1.10	0.01981
P26010	ITGB7	-1.10	0.00096
P29401	TKT	-1.09	0.00257
P17174	GOT1	-1.09	0.0031
Q13435	SF3B2	-1.09	0.00299
Q99459	CDC5L	-1.09	0.00621
P25789	PSMA4	-1.09	0.00095
P62937	PPIA	-1.06	0.00489
O00151	PDLIM1	-1.06	0.00098
Q9UHV9	PFDN2	-1.05	0.00106
P52566	ARHGDI B	-1.04	0.0036
P63279	UBE2I	-1.03	0.01008
P61586	RHOA	-1.02	0.00477
P25788	PSMA3	-1.01	0.00153
Q9P1F3	ABRACL	-1.01	0.00426
P33316	DUT	-1.00	0.00247

<b>Table 22 Continued</b>			
Q86V81	ALYREF	-0.99	0.00536
P28072	PSMB6	-0.98	0.00041
Q9UHX1	PUF60	-0.98	0.00544
Q9BWD1	ACAT2	-0.98	0.00058
P43490	NAMPT	-0.96	0.02735
P61758	VBP1	-0.96	0.00016
Q15424	SAFB	-0.96	0.00058
P14317	HCLS1	-0.95	0.03364
Q01082	SPTBN1	-0.95	0.00434
O14818	PSMA7	-0.94	0.00398
P55327	TPD52	-0.94	0.00156
Q9UKV3	ACIN1	-0.94	0.0071
Q13867	BLMH	-0.92	0.00975
Q01518	CAP1	-0.92	0.00136
Q9Y320	TMX2	-0.91	0.02741
Q8IZP2	ST13P4	-0.91	0.00205
P09960	LTA4H	-0.91	0.01299
P09234	SNRPC	-0.91	0.00199
P19404	NDUFV2	-0.90	0.01528
O14745	SLC9A3R1	-0.90	0.0011
P56556	NDUFA6	-0.90	0.04703
Q99497	PARK7	-0.89	0.00112
P20674	COX5A	-0.88	0.00256
Q9Y617	PSAT1	-0.88	0.02187
Q14242	SELPLG	-0.87	0.01956
P34932	HSPA4	-0.87	1.63E-06
P22392	NME2	-0.86	0.01744
Q8WXX5	DNAJC9	-0.85	0.0031
P49720	PSMB3	-0.85	0.00566
P31949	S100A11	-0.84	0.0034
P41567	EIF1	-0.84	0.00306
P09936	UCHL1	-0.83	0.00963
P62979	RPS27A	-0.83	0.01422
P62136	PPP1CA	-0.83	0.01815
Q9UL46	PSME2	-0.82	0.02012
P37235	HPCAL1	-0.82	0.00749
O95777	LSM8	-0.82	0.00024
Q15907	RAB11B	-0.82	0.00046
P06733	ENO1	-0.82	0.00425
Q15637	SF1	-0.81	0.00108
Q96T88	UHRF1	-0.81	0.00381

Table 22 Continued			
Q9NTZ6	RBM12	-0.81	0.00744
P28066	PSMA5	-0.81	0.00097
P30520	ADSS2	-0.80	0.02359
O15144	ARPC2	-0.79	0.0254
Q13151	HNRNPA0	-0.78	0.00721
Q9NUQ9	CYRIB	-0.78	0.00478
P08621	SNRNP70	-0.78	0.00016
Q13242	SRSF9	-0.78	0.00136
P31153	MAT2A	-0.77	0.00286
Q13347	EIF3I	-0.77	0.02053
Q9Y3D6	FIS1	-0.77	0.01764
P06753	TPM3	-0.76	0.00632
O15511	ARPC5	-0.76	0.00176
P53674	CRYBB1	-0.76	0.0373
P54727	RAD23B	-0.76	0.00501
P35637	FUS	-0.76	0.0089
P46013	MKI67	-0.76	0.01929
Q96KP4	CNDP2	-0.75	0.00361
P17096	HMGA1	-0.75	0.0123
Q5TEC6	H3-7	-0.75	0.01384
P45973	CBX5	-0.75	0.03725
P37802	TAGLN2	-0.75	0.00082
P55795	HNRNPH2	-0.75	0.01342
Q13283	G3BP1	-0.74	6.36E-05
Q15388	TOMM20	-0.73	0.00271
P09104	ENO2	-0.73	0.00013
P32119	PRDX2	-0.73	0.00307
P09012	SNRPA	-0.73	0.0213
P49590	HARS2	-0.72	0.01741
Q59GN2	RPL39P5	-0.72	0.00136
Q06203	PPAT	-0.72	0.03977
P67809	YBX1	-0.72	0.00515
P26038	MSN	-0.72	0.00072
B9A064	IGLL5	-0.72	0.00272
P09211	GSTP1	-0.72	0.00097
Q99439	CNN2	-0.71	0.00019
E9PAV3	NACA	-0.71	0.00198
P51572	BCAP31	-0.71	0.00279
P50395	GDI2	-0.71	0.00802
P62316	SNRPD2	-0.70	0.00434
Q14232	EIF2B1	-0.70	0.02111

<b>Table 22 Continued</b>			
Q9NPF0	CD320	-0.70	0.02005
P82979	SARNP	-0.70	0.00166
P51858	HDGF	-0.70	0.00179
P62310	LSM3	-0.69	0.01337
P42166	TMPO	-0.69	0.00582
Q99808	SLC29A1	-0.69	0.02607
Q96DH6	MSI2	-0.69	0.04811
P08758	ANXA5	-0.69	0.04761
P00338	LDHA	-0.68	0.00582
P16070	CD44	-0.68	0.00289
P31350	RRM2	-0.68	0.01445
P13987	CD59	-0.68	0.01801
P15121	AKR1B1	-0.68	0.01443
Q16851	UGP2	-0.67	0.03156
O43592	XPOT	-0.67	0.0365
Q03252	LMNB2	-0.67	0.03561
P15311	EZR	-0.67	0.00781
Q14011	CIRBP	-0.67	0.02076
Q96FW1	OTUB1	-0.67	0.01235
P11142	HSPA8	-0.66	0.00408
P60953	CDC42	-0.66	0.03967
P04066	FUCA1	-0.65	0.01219
P31943	HNRNPH1	-0.65	0.00924
P07195	LDHB	-0.65	0.00133
Q12874	SF3A3	-0.65	0.01469
P40926	MDH2	-0.65	0.00099
P13796	LCP1	-0.64	0.01251
Q06830	PRDX1	-0.64	0.00579
Q9H444	CHMP4B	-0.64	0.01014
P42574	CASP3	-0.64	0.01407
Q9BYG3	NIFK	-0.64	0.00354
P14324	FDPS	-0.63	0.00916
P63104	YWHAZ	-0.63	0.00196
Q96PK6	RBM14	-0.63	0.03119
P00558	PGK1	-0.63	0.02851
P55072	VCP	-0.62	0.00816
P49721	PSMB2	-0.62	0.0094
Q14980	NUMA1	-0.62	0.00408
Q92945	KHSRP	-0.61	0.00819
Q12906	ILF3	-0.61	0.005
P17480	UBTF	-0.61	0.01919

<b>Table 22 Continued</b>			
Q9Y5S9	RBM8A	-0.60	0.00556
P23193	TCEA1	-0.60	0.01079
P00390	GSR	-0.59	0.01004
P10747	CD28	-0.59	0.01876
P14406	COX7A2	-0.59	0.02682
Q8N5L8	RPP25L	-0.59	0.02352
Q16555	DPYSL2	-0.59	0.01043
Q96C90	PPP1R14B	-0.59	0.02914
P11233	RALA	-0.58	0.00153
Q9H5X1	CIAO2A	-0.58	0.00269
P30044	PRDX5	-0.58	0.00767
Q06265	EXOSC9	-0.57	0.02635
P78417	GSTO1	-0.57	0.04868
P11940	PABPC1	-0.57	0.01402
P07737	PFN1	-0.57	0.0064
P62306	SNRPF	-0.57	0.00526
Q9UMY1	NOL7	-0.57	0.02609
Q16629	SRSF7	-0.56	0.0041
Q07955	SRSF1	-0.56	0.0338
P05387	RPLP2	-0.56	0.01911
Q16531	DDB1	-0.55	0.00365
P30041	PRDX6	-0.55	0.0104
P14314	PRKCSH	-0.55	0.0105
P62258	YWHAE	-0.55	0.04387
O15347	HMGB3	-0.55	0.00396
Q9H7B2	RPF2	-0.54	0.00228
P19338	NCL	-0.54	0.00852
P08559	PDHA1	-0.54	0.01352
Q13185	CBX3	-0.54	0.02675
Q9UMS4	PRPF19	-0.54	0.00343
P04233	CD74	-0.54	0.00528
P00492	HPRT1	-0.53	0.00292
Q9NQG5	RPRD1B	-0.53	0.00979
Q9NR45	NANS	-0.53	0.02081
P51991	HNRNPA3	-0.53	0.04734
Q9H814	PHAX	-0.53	0.04635
Q9H8S9	MOB1A	-0.52	0.00827
P53634	CTSC	-0.52	0.00444
Q9BTY7	HGH1	-0.52	0.00661
Q14141	SEPTIN6	-0.52	0.02378
O43707	ACTN4	-0.51	0.01034

Table 22 Continued			
Q14444	CAPRIN1	-0.51	0.00084
P21926	CD9	-0.51	0.0167
P14550	AKR1A1	-0.51	0.04106
P25398	RPS12	-0.51	0.01576
P61247	RPS3A	-0.51	0.00327
P31948	STIP1	-0.51	0.0217
Q96IX5	ATP5MK	-0.50	0.01773
O95319	CELF2	-0.50	0.00536
P62308	SNRPG	-0.49	0.0168
O43852	CALU	-0.49	0.04242
O95881	TXNDC12	-0.49	0.03429
P0DMV9	HSPA1B	-0.49	0.01612
P49189	ALDH9A1	-0.49	0.01914
P62857	RPS28	-0.49	0.0001
Q16881	TXNRD1	-0.49	0.00457
P67775	PPP2CA	-0.49	0.01451
Q9Y4Z0	LSM4	-0.48	0.00013
P09496	CLTA	-0.48	0.02463
P68402	PAFAH1B2	-0.48	0.02808
Q15370	ELOB	-0.48	0.00501
P62140	PPP1CB	-0.48	0.01734
Q92688	ANP32B	-0.48	0.00766
P38432	COIL	-0.47	0.00644
P63220	RPS21	-0.47	0.04698
Q9P289	STK26	-0.47	0.03376
Q01130	SRSF2	-0.47	0.04323
A5YKK6	CNOT1	-0.47	0.04325
P23528	CFL1	-0.47	0.016
P43243	MATR3	-0.46	0.01547
P59998	ARPC4	-0.46	0.0418
P35613	BSG	-0.46	0.0291
Q9BWF3	RBM4	-0.46	0.02733
P22626	HNRNPA2B1	-0.46	0.01575
P11388	TOP2A	-0.45	0.03784
P26599	PTBP1	-0.45	0.00343
P62829	RPL23	-0.44	0.01592
Q8NCW5	NAXE	-0.44	0.04732
P49458	SRP9	-0.44	0.00498
P84103	SRSF3	-0.44	0.01914
Q9Y3B4	SF3B6	-0.43	0.00533
P31946	YWHAB	-0.43	0.01855

<b>Table 22 Continued</b>			
Q13601	KRR1	-0.43	0.03034
Q14684	RRP1B	-0.43	0.01457
O96019	ACTL6A	-0.43	0.00951
Q15287	RNPS1	-0.42	0.00658
P62318	SNRPD3	-0.42	0.00585
Q14683	SMC1A	-0.42	0.01863
Q7Z2W4	ZC3HAV1	-0.42	0.02879
Q15181	PPA1	-0.42	0.02249
P63173	RPL38	-0.41	0.02023
Q15393	SF3B3	-0.41	0.00314
P17844	DDX5	-0.41	0.01265
Q14839	CHD4	-0.41	0.03661
O14672	ADAM10	-0.40	0.0028
Q9BUJ2	HNRNPUL1	-0.40	0.04684
P04899	GNAI2	-0.40	0.04641
P24928	POLR2A	-0.40	0.01509
Q9Y2W1	THRAP3	-0.40	0.00482
P40429	RPL13A	-0.40	0.01341
P60866	RPS20	-0.40	0.02314
P36405	ARL3	-0.40	0.026
P12004	PCNA	-0.40	0.01891
O95478	NSA2	-0.39	0.04778
Q9Y2W2	WBP11	-0.39	0.01106
Q9BSC4	NOL10	-0.39	0.01063
Q92890	UFD1	-0.39	0.00168
O43684	BUB3	-0.39	0.0378
Q9Y2Q5	LAMTOR2	-0.38	0.03645
Q9BPX5	ARPC5L	-0.38	0.03649
P51610	HCFC1	-0.38	0.00599
O43670	ZNF207	-0.38	0.00012
P04406	GAPDH	-0.38	0.00747
Q12905	ILF2	-0.38	0.01063
O75340	PDCD6	-0.37	0.01137
Q9Y2K7	KDM2A	-0.37	0.01357
P62263	RPS14	-0.37	0.0072
P52272	HNRNPM	-0.37	0.03332
Q00839	HNRNPU	-0.37	0.02801
P30049	ATP5F1D	-0.37	0.01623
O14929	HAT1	-0.36	0.0394
Q92608	DOCK2	-0.36	0.01782
Q16706	MAN2A1	-0.36	0.0148

Table 22 Continued			
P00505	GOT2	-0.36	0.0133
Q15717	ELAVL1	-0.35	0.01652
Q13310	PABPC4	-0.35	0.00367
P08865	RPSA	-0.35	0.00062
P62280	RPS11	-0.35	0.01968
Q96SU4	OSBPL9	-0.35	0.02321
O43390	HNRNPR	-0.34	0.00434
Q9BZZ5	API5	-0.34	0.0022
O43809	NUDT21	-0.34	0.02487
O75533	SF3B1	-0.33	0.02697
O95782	AP2A1	-0.33	0.03288
P25205	MCM3	-0.33	0.04007
P55786	NPEPPS	-0.33	0.02223
Q15365	PCBP1	-0.33	0.00234
P51149	RAB7A	-0.33	0.04288
P31483	TIA1	-0.32	0.03235
Q5T9A4	ATAD3B	-0.32	0.02501
P24534	EEF1B2	-0.32	0.02479
O95347	SMC2	-0.31	0.01066
P27797	CALR	-0.31	0.01418
O14979	HNRNPDL	-0.31	0.01541
Q13247	SRSF6	-0.30	0.02535
P46777	RPL5	-0.30	0.03698
P61160	ACTR2	-0.30	0.0262
P46060	RANGAP1	-0.30	0.00272
O60216	RAD21	-0.29	0.04896
Q8NBJ7	SUMF2	-0.29	0.01996
P61289	PSME3	-0.28	0.00216
O00541	PES1	-0.28	0.02787
Q00765	REEP5	-0.27	0.00351
Q9ULV4	CORO1C	-0.27	0.01044
P55769	SNU13	-0.27	0.01928
Q13162	PRDX4	-0.25	0.0106
P09661	SNRPA1	-0.25	0.01952
Q9P2E9	RRBP1	-0.25	0.02631
Q9BXP5	SRRT	-0.24	0.026
P13073	COX4I1	-0.24	0.00201
P18858	LIG1	-0.24	0.02071
Q92769	HDAC2	-0.23	0.00695
Q14103	HNRNPD	-0.23	0.0448
Q92797	SYMPK	-0.23	0.00254



<b>Table 22 Continued</b>			
P62826	RAN	-0.22	0.04098
P07814	EPRS1	-0.22	0.03945
O75251	NDUFS7	-0.21	0.04814
P63244	RACK1	-0.20	0.00213
Q92974	ARHGEF2	-0.20	0.03824
Q6P2E9	EDC4	-0.19	0.02478
Q8NC51	SERBP1	-0.19	0.00807
P62424	RPL7A	-0.19	0.02895
P62851	RPS25	-0.18	0.0091
P07437	TUBB	-0.18	0.00074
P68371	TUBB4B	-0.17	0.02135
Q9UQ80	PA2G4	-0.17	0.00945
P42677	RPS27	-0.17	0.03005
Q8N163	CCAR2	-0.17	0.04497
Q9HD33	MRPL47	-0.17	0.02789
Q96FV9	THOC1	-0.15	0.02558
Q68CZ2	TNS3	-0.14	0.04763
O00148	DDX39A	-0.14	0.03456
Q01844	EWSR1	-0.10	0.0436
P26368	U2AF2	-0.07	0.0028
P42126	ECI1	-0.06	0.03335

**Table 23 Proteomics Hits in MM.1S<sup>gfp/luc</sup> Cells Treated with 1  $\mu$ M Triacsin for 48 Hours Compared to Vehicle Treated Cells**

<b>Ingenuity Canonical Pathways</b>	<b>-log (p-value)</b>	<b>% Total Terms in Pathway</b>	<b>Significantly Associated Proteins</b>
Phagosome Maturation	4.78	5.06	CALR, CTSS, NSF, PRDX1, PRDX2, PRDX5, PRDX6, TUBB4B
Protein Ubiquitination Pathway	4.61	3.66	DNAJC9, PSMC4, PSMD7, PSME1, RPS27A, UBA1, UBE2I, UBE2O, UBE2V1, USP5
Purine Nucleotides De Novo Biosynthesis II	4.27	27.3	ADSL, GART, PFAS
Oxidative Phosphorylation	3.87	5.41	ATP5ME, COX5A, COX6B1, COX7A2, NDUFA4, NDUFV2
NADH Repair	3.83	66.7	GAPDH, NAXE
5-aminoimidazole Ribonucleotide Biosynthesis I	3.83	66.7	GART, PFAS
Mitochondrial Dysfunction	3.76	2.9	ATP5ME, COX5A, COX6B1, COX7A2, FIS1, NDUFA4, NDUFV2, PARK7, PRDX6, SOD1
Isoleucine Degradation I	3.59	16.7	ACAA2, ACAT2, BCAT2
Eumelanin Biosynthesis	3.53	50	DDT, MIF
Glutaryl-CoA Degradation	3.52	15.8	ACAA2, ACAT2, PARK7
FAT10 Signaling Pathway	3.19	7.14	PSMC4, PSMD7, PSME1, UBA1
Tryptophan Degradation III (Eukaryotic)	3.1	11.5	ACAA2, ACAT2, PARK7
Sumoylation Pathway	3.09	4.85	CDC42, PCNA, RHOA, UBA2, UBE2I
Glycolysis I	3.05	11.1	GAPDH, PKM, TPI1
Aspartate Degradation II	3	28.6	GOT2, MDH2
EIF2 Signaling	2.94	3.08	EIF2B2, PPP1CA, RPL23A, RPL7, RPLP0, RPLP2, RPS27A
HER-2 Signaling in Breast Cancer	2.94	3.08	CDC42, COX5A, COX6B1, COX7A2, ITGB7, NUP188, NUP205
Tight Junction Signaling	2.77	3.35	CDC42, MYH10, NSF, PPP2CA, RHOA, SAFB
Leucine Degradation I	2.77	22.2	BCAT2, IVD
Fatty Acid $\beta$ -oxidation I	2.72	8.57	ACAA2, ACSL3, IVD
Ketolysis	2.67	20	ACAA2, ACAT2
Ketogenesis	2.59	18.2	ACAA2, ACAT2
tRNA Charging	2.59	7.69	CARS2, EPRS1, IARS1
Mevalonate Pathway I	2.37	14.3	ACAA2, ACAT2
NER (Nucleotide Excision Repair, Enhanced Pathway)	2.2	3.85	COPS2, PCNA, RAD23B, UBE2I
Superpathway of Geranylgeranyldiphosphate Biosynthesis I (via Mevalonate)	2.16	11.1	ACAA2, ACAT2
Mitochondrial L-carnitine Shuttle Pathway	2.11	10.5	ACSL3, CPT1A

<b>Table 23 Continued</b>			
Polyamine Regulation in Colon Cancer	2.08	5.08	CSNK2A3, RHOA, SRM
Regulation of Actin-based Motility by Rho	2.05	3.48	CDC42, ITGB7, PFN1, RHOA
ILK Signaling	1.85	2.49	CDC42, ITGB7, MYH10, PPP2CA, RHOA
Spermidine Biosynthesis I	1.85	50	SRM
Gluconeogenesis I	1.81	7.41	GAPDH, MDH2
Granzyme A Signaling	1.8	4	LMNB2, NDUFA4, NDUFV2
Clathrin-mediated Endocytosis Signaling	1.8	2.4	CDC42, CSNK2A3, ITGB7, RAB11B, RPS27A
Hypoxia Signaling in the Cardiovascular System	1.78	3.95	UBE2I, UBE2O, UBE2V1
Macropinocytosis Signaling	1.78	3.95	CDC42, ITGB7, RHOA
Superpathway of Cholesterol Biosynthesis	1.75	6.9	ACAA2, ACAT2
Sirtuin Signaling Pathway	1.75	2.05	ATG3, CPT1A, GOT2, NDUFA4, NDUFV2, SOD1
L-carnitine Biosynthesis	1.68	33.3	ALDH9A1
Methylglyoxal Degradation I	1.68	33.3	GLO1
Inosine-5'-phosphate Biosynthesis II	1.68	33.3	ADSL
Glutamate Degradation II	1.68	33.3	GOT2
S-adenosyl-L-methionine Biosynthesis	1.68	33.3	MAT2A
Aspartate Biosynthesis	1.68	33.3	GOT2
BAG2 Signaling Pathway	1.67	3.57	PSMC4, PSMD7, PSME1
Epithelial Adherens Junction Signaling	1.6	2.55	CDC42, MYH10, PPP2CA, RHOA
NRF2-mediated Oxidative Stress Response	1.58	2.11	DNAJC9, PRDX1, SOD1, STIP1, TXN
MIF-mediated Glucocorticoid Regulation	1.58	5.56	CD74, MIF
Inhibition of ARE-Mediated mRNA Degradation Pathway	1.56	2.47	PPP2CA, PSMC4, PSMD7, PSME1
L-cysteine Degradation I	1.56	25	GOT2
Actin Nucleation by ARP-WASP Complex	1.55	3.23	CDC42, ITGB7, RHOA
Actin Cytoskeleton Signaling	1.53	2.05	CDC42, ITGB7, MYH10, PFN1, RHOA
Antigen Presentation Pathway	1.51	5.13	CALR, CD74
Superpathway of Methionine Degradation	1.47	4.88	GOT2, MAT2A
Tetrahydrofolate Salvage from 5,10-methenyltetrahydrofolate	1.46	20	GART
CMP-N-acetylneuramate Biosynthesis I (Eukaryotes)	1.46	20	NANS
Glutathione Redox Reactions II	1.46	20	TXNDC12
MIF Regulation of Innate Immunity	1.42	4.55	CD74, MIF
Regulation of eIF4 and p70S6K Signaling	1.41	2.21	EIF2B2, ITGB7, PPP2CA, RPS27A

<b>Table 23 Continued</b>			
Coronavirus Replication Pathway	1.4	4.44	COPB2, TUBB4B
Ephrin A Signaling	1.36	4.26	CDC42, RHOA
MicroRNA Biogenesis Signaling Pathway	1.36	2.14	DDX5, ILF3, NUP188, NUP205
Production of Nitric Oxide and Reactive Oxygen Species in Macrophages	1.34	2.09	CDC42, PPP1CA, PPP2CA, RHOA
Trehalose Degradation II (Trehalase)	1.32	14.3	HK2
Thioredoxin Pathway	1.32	14.3	TXN
Huntington's Disease Signaling	1.3	1.77	NSF, PSMC4, PSMD7, PSME1, RPS27A

**Table 24. Proteomics Hits in MM.1S<sup>gfp/luc</sup> Cells Treated with 2  $\mu$ M Triacsin for 48 Hours Compared to Vehicle Treated Cells**

<b>Ingenuity Canonical Pathways</b>	<b>-log (p-value)</b>	<b>% Total Terms in Pathway</b>	<b>Significantly Associated Proteins</b>
Mitochondrial Dysfunction	14	11.3	AIFM1, ATP5F1D, ATP5ME, ATP5MF, BAX, CALM1 (includes others), CASP3, COX15, COX4I1, COX5A, COX6B1, COX7A2, CYB5R3, CYCS, DLAT, FIS1, FUS, GSR, GSTP1, MGST3, MT-ATP6, MT-CO2, MT-ND2, MT-ND4, NDUFA13, NDUFA6, NDUFS3, NDUFS7, NDUFS8, NDUFV2, PARK7, PDHA1, PRDX6, SAMM50, SOD1, TFAM, TOMM20, TOMM22, VDAC3
BAG2 Signaling Pathway	12.5	22.6	CASP3, HSPA1A/HSPA1B, HSPA4, HSPA8, PSMA2, PSMA3, PSMA4, PSMA5, PSMA6, PSMA7, PSMB2, PSMB3, PSMB6, PSMC6, PSMD14, PSMD6, PSME1, PSME2, PSME3
EIF2 Signaling	11.9	12.8	EIF1, EIF2B1, EIF2B2, EIF2B3, EIF3I, PABPC1, PPP1CA, PPP1CB, PTBP1, RALA, RPL13A, RPL23, RPL38, RPL5, RPL7, RPL7A, RPLP2, RPS11, RPS12, RPS14, RPS15, RPS20, RPS21, RPS25, RPS27, RPS27A, RPS28, RPS3A, RPSA
FAT10 Signaling Pathway	11.1	26.8	PSMA2, PSMA3, PSMA4, PSMA5, PSMA6, PSMA7, PSMB2, PSMB3, PSMB6, PSMC6, PSMD14, PSMD6, PSME1, PSME2, PSME3
Inhibition of ARE-Mediated mRNA Degradation Pathway	10.5	14.2	CNOT1, EDC4, EXOSC9, PPP2CA, PSMA2, PSMA3, PSMA4, PSMA5, PSMA6, PSMA7, PSMB2, PSMB3, PSMB6, PSMC6, PSMD14, PSMD6, PSME1, PSME2, PSME3, TIA1, YWHAB, YWHAE, YWHAZ
Oxidative Phosphorylation	10.2	17.1	ATP5F1D, ATP5ME, ATP5MF, COX15, COX4I1, COX5A, COX6B1, COX7A2, CYCS, MT-ATP6, MT-CO2, MT-ND2, MT-ND4, NDUFA13, NDUFA6, NDUFS3, NDUFS7, NDUFS8, NDUFV2
Huntington's Disease Signaling	10.2	10.6	ATP5F1D, BAX, CASP3, CLTA, CYCS, DNAJB1, HDAC2, HSPA1A/HSPA1B, HSPA4, HSPA8, NSF, POLR2A, PSMA2, PSMA3, PSMA4, PSMA5, PSMA6, PSMA7, PSMB2, PSMB3, PSMB6, PSMC6, PSMD14, PSMD6, PSME1, PSME2, PSME3, RPS27A, SIN3A, STX16
Protein Ubiquitination Pathway	9.87	10.6	DNAJB1, DNAJB11, DNAJC10, DNAJC9, ELOB, HSPA13, HSPA1A/HSPA1B, HSPA4, HSPA4L, HSPA8, PSMA2, PSMA3, PSMA4, PSMA5, PSMA6, PSMA7, PSMB2, PSMB3, PSMB6, PSMC6, PSMD14,

Table 24 Continued			
			PSMD6, PSME1, PSME2, RPS27A, UBE2I, UBE2N, UBE2V1, UCHL1
Spliceosomal Cycle	8.52	24.5	CDC5L, DDX23, HSPA8, PRPF19, RBM8A, SF1, SF3A3, SF3B1, SF3B2, SF3B3, SF3B6, U2AF2
Sirtuin Signaling Pathway	8.51	9.56	ADAM10, ATP5F1D, BAX, CPT1A, GOT2, LDHA, LDHB, MT-ATP6, MT-ND2, MT-ND4, NAMPT, NDUFA13, NDUFA6, NDUFS3, NDUFS7, NDUFS8, NDUFV2, PDHA1, PGK1, SLC25A4, SOD1, TIMM44, TIMM50, TOMM20, TOMM22, TSPO, TUBA4A, VDAC3
Regulation of eIF4 and p70S6K Signaling	8	11.6	EIF1, EIF2B1, EIF2B2, EIF2B3, EIF3I, ITGB7, PABPC1, PPP2CA, RALA, RPS11, RPS12, RPS14, RPS15, RPS20, RPS21, RPS25, RPS27, RPS27A, RPS28, RPS3A, RPSA
MicroRNA Biogenesis Signaling Pathway	7.05	10.7	DDX5, DNAJB1, EWSR1, EXOSC9, FUS, HNRNPA2B1, HNRNPD, HSPA8, ILF2, ILF3, KHSRP, NUP160, NUP58, NUP85, NUP93, POLR2A, RALA, RAN, SRSF1, SRSF3
Phagosome Maturation	6.82	11.4	ATP6V0A1, ATP6V0D1, CALR, CANX, CTSC, CTSS, NSF, PRDX1, PRDX2, PRDX5, PRDX6, RAB5B, RAB7A, RAC2, STX16, TUBA4A, TUBB, TUBB4B
Remodeling of Epithelial Adherens Junctions	6.82	17.6	ACTN4, ACTR2, ARPC2, ARPC4, ARPC5, ARPC5L, RAB5B, RAB7A, RALA, TUBA4A, TUBB, TUBB4B
Gluconeogenesis I	6.57	29.6	ALDOA, ENO1, ENO2, GAPDH, GPI, MDH1, MDH2, PGK1
Superpathway of Cholesterol Biosynthesis	6.3	27.6	ACAA2, ACAT2, EBP, FDPS, HADHA, HSD17B7, LSS, NSDHL
Unfolded protein response	6.28	14.4	CALR, CANX, DNAJB1, DNAJB11, DNAJC10, DNAJC9, ERN1, HSPA1A/HSPA1B, HSPA4, HSPA8, PDIA6, SEL1L, VCP
Coronavirus Pathogenesis Pathway	5.8	9.31	BAX, CASP3, HDAC2, PA2G4, RAB7A, RPS11, RPS12, RPS14, RPS15, RPS20, RPS21, RPS25, RPS27, RPS27A, RPS28, RPS3A, RPSA, SIN3A, ZC3HAV1
Glutathione Redox Reactions II	5.67	80	AIFM1, GSR, PDIA3, TXNDC12
mTOR Signaling	5.49	8.88	CDC42, EIF3I, EIF4B, PPP2CA, RAC2, RALA, RHOA, RPS11, RPS12, RPS14, RPS15, RPS20, RPS21, RPS25, RPS27, RPS27A, RPS28, RPS3A, RPSA
Glycolysis I	5.38	25.9	ALDOA, ENO1, ENO2, GAPDH, GPI, PGK1, TPI1
Actin Cytoskeleton Signaling	5.22	8.2	ACTN4, ACTR2, ARPC2, ARPC4, ARPC5, ARPC5L, CDC42, CFL1, CSK, CYFIP2, EZR, ITGB7, MSN, MYH10, NCKAP1L, PFN1, PPP1CB, RAC2, RALA, RHOA

<b>Table 24 Continued</b>			
Sumoylation Pathway	4.85	11.7	ARHGDIB, CDC42, HDAC2, PCNA, RAC2, RAN, RANGAP1, RHOA, SERBP1, SUMO4, UBA2, UBE2I
Aspartate Degradation II	4.84	57.1	GOT1, GOT2, MDH1, MDH2
Granzyme A Signaling	4.65	13.3	ANP32A, LMNB2, MT-ND2, MT-ND4, NDUFA13, NDUFA6, NDUFS3, NDUFS7, NDUFS8, NDUFV2
Insulin Secretion Signaling Pathway	4.53	7.35	DLAT, EIF1, EIF2B1, EIF2B2, EIF2B3, NSF, PABPC1, PDHA1, PDIA3, SEC11A, SEC11C, SEC61A1, SPCS2, SPCS3, SRP72, SRP9, SSR1, SSR3, SSR4, STX16
Clathrin-mediated Endocytosis Signaling	4.51	8.17	ACTR2, AP2A1, AP3B1, ARPC2, ARPC4, ARPC5, ARPC5L, CDC42, CLTA, CSNK2A3, HSPA8, ITGB7, MYO6, RAB11B, RAB5B, RAB7A, RPS27A
Regulation of Actin-based Motility by Rho	4.37	10.4	ACTR2, ARPC2, ARPC4, ARPC5, ARPC5L, CDC42, CFL1, ITGB7, PFN1, PPP1CB, RAC2, RHOA
RAC Signaling	4.25	9.49	ACTR2, ARPC2, ARPC4, ARPC5, ARPC5L, CD44, CDC42, CFL1, CYFIP2, ITGB7, RAC2, RALA, RHOA
Epithelial Adherens Junction Signaling	4.23	8.92	ACTR2, ARPC2, ARPC4, ARPC5, ARPC5L, CDC42, CFL1, MYH10, PPP2CA, RALA, RHOA, YWHAB, YWHAE, YWHAZ
RHOA Signaling	4.21	7.73	ACTR2, ARHGDIB, ARHGEF2, ARPC2, ARPC4, ARPC5, ARPC5L, CD44, CDC42, CFL1, EZR, GNAI2, ITGB7, MSN, MYH10, RAC2, RHOA
RHOA Signaling	4.05	9.68	ACTR2, ARPC2, ARPC4, ARPC5, ARPC5L, CFL1, EZR, MSN, PFN1, PPP1CB, RHOA, SEPTIN6
Glutaryl-CoA Degradation	4.01	26.3	ACAA2, ACAT2, HADHA, HSD17B4, PARK7
Actin Nucleation by ARP-WASP Complex	3.84	10.8	ACTR2, ARPC2, ARPC4, ARPC5, ARPC5L, CDC42, ITGB7, RAC2, RALA, RHOA
NRF2-mediated Oxidative Stress Response	3.81	7.17	AKR1A1, DNAJB1, DNAJB11, DNAJC10, DNAJC9, EPHX1, GSR, GSTO1, GSTP1, MGST3, PRDX1, RALA, SOD1, STIP1, TXN, TXNRD1, VCP
Estrogen Receptor Signaling	3.75	5.87	ATP5F1D, CFL1, DDX5, EIF2B1, EIF2B2, EIF2B3, GNAI2, HNRNPD, MT-ATP6, MT-ND2, MT-ND4, NDUFA13, NDUFA6, NDUFS3, NDUFS7, NDUFS8, NDUFV2, PCNA, PDIA3, PPP1CB, RALA, RHOA, TFAM, THRAP3
Neutrophil Extracellular Trap Signaling Pathway	3.68	5.81	ATP5F1D, CASP3, JCHAIN, MT-ATP6, MT-ND2, MT-ND4, NDUFA13, NDUFA6, NDUFS3, NDUFS7, NDUFS8, NDUFV2, PDIA3, PRDX6, RAC2, SELPLG, SLC25A4, STIM1, TIMM44, TIMM50, TOMM20, TOMM22, TSPO, VDAC3
Fatty Acid $\beta$ -oxidation I	3.61	17.1	ACAA2, ACSL3, ECI1, HADHA, HSD17B4, IVD

<b>Table 24 Continued</b>			
Cholesterol Biosynthesis I	3.58	30.8	EBP, HSD17B7, LSS, NSDHL
Cholesterol Biosynthesis II (via 24,25-dihydrolanosterol)	3.58	30.8	EBP, HSD17B7, LSS, NSDHL
Cholesterol Biosynthesis III (via Desmosterol)	3.58	30.8	EBP, HSD17B7, LSS, NSDHL
NER (Nucleotide Excision Repair, Enhanced Pathway)	3.44	9.62	COPS2, DDB1, LIG1, PCNA, POLR2A, RAD23B, TCEA1, TOP2A, UBE2I, UBE2N
HIPPO signaling	3.42	10.5	CD44, MOB1A, PPP1CA, PPP1CB, PPP1R14B, PPP2CA, YWHAB, YWHAE, YWHAZ
Tryptophan Degradation III (Eukaryotic)	3.33	19.2	ACAA2, ACAT2, HADHA, HSD17B4, PARK7
Thioredoxin Pathway	3.26	42.9	SELENOT, TXN, TXNRD1
Granzyme B Signaling	3.2	25	CASP3, CYCS, LMNB2, NUMA1
Parkinson's Signaling	3.2	25	CASP3, CYCS, PARK7, UCHL1
Fcy Receptor-mediated Phagocytosis in Macrophages and Monocytes	3.14	9.57	ACTR2, ARPC2, ARPC4, ARPC5, ARPC5L, CDC42, EZR, RAB11B, RAC2
HER-2 Signaling in Breast Cancer	3.06	6.61	ARF4, CASP3, CDC42, COX15, COX4I1, COX5A, COX6B1, COX7A2, ITGB7, MT-CO2, NUP160, NUP58, NUP85, NUP93, RALA
Isoleucine Degradation I	3	22.2	ACAA2, ACAT2, HADHA, HSD17B4
Superpathway of Geranylgeranyldiphosphate Biosynthesis I (via Mevalonate)	3	22.2	ACAA2, ACAT2, FDPS, HADHA
Integrin Signaling	2.89	6.6	ACTN4, ACTR2, ARF4, ARPC2, ARPC4, ARPC5, ARPC5L, CDC42, ITGB7, PFN1, PPP1CB, RAC2, RALA, RHOA
Induction of Apoptosis by HIV1	2.85	10.8	BAX, CASP3, CYCS, SLC25A10, SLC25A13, SLC25A3, SLC25A4
Signaling by Rho Family GTPases	2.78	5.99	ACTR2, ARHGEF2, ARPC2, ARPC4, ARPC5, ARPC5L, CDC42, CFL1, EZR, GNAI2, ITGB7, MSN, RAC2, RHOA, SEPTIN6, STMN1
14-3-3-mediated Signaling	2.77	7.87	BAX, PDCD6IP, PDIA3, RALA, TUBA4A, TUBB, TUBB4B, YWHAB, YWHAE, YWHAZ
Ketolysis	2.75	30	ACAA2, ACAT2, HADHA
NADH Repair	2.71	66.7	GAPDH, NAXE
D-glucuronate Degradation I	2.71	66.7	AKR1A1, DCXR
Glutamate Degradation II	2.71	66.7	GOT1, GOT2
Aspartate Biosynthesis	2.71	66.7	GOT1, GOT2
fMLP Signaling in Neutrophils	2.67	7.63	ACTR2, ARPC2, ARPC4, ARPC5, ARPC5L, CALM1 (includes others), CDC42, GNAI2, RAC2, RALA
Immunogenic Cell Death Signaling Pathway	2.64	8.89	BAX, BCAP31, CALR, CASP3, HSPA1A/HSPA1B, HSPA4, HSPA8, PDIA3



<b>Table 24 Continued</b>			
Ephrin Receptor Signaling	2.63	6.44	ACTR2, ADAM10, ARPC2, ARPC4, ARPC5, ARPC5L, CDC42, CFL1, GNAI2, ITGB7, RAC2, RALA, RHOA
Ketogenesis	2.62	27.3	ACAA2, ACAT2, HADHA
Pyrimidine Deoxyribonucleotides De Novo Biosynthesis I	2.58	17.4	APOBEC3G, DUT, NME2, RRM2
Vitamin-C Transport	2.58	17.4	GSTO1, SELENOT, TXN, TXNRD1
Tumoricidal Function of Hepatic Natural Killer Cells	2.51	16.7	AIFM1, BAX, CASP3, CYCS
CSDE1 Signaling Pathway	2.5	10.7	EDC4, FUS, HNRNPD, PABPC1, PABPC4, PTBP1
Reelin Signaling in Neurons	2.5	7.25	ACTR2, ARHGEF2, ARPC2, ARPC4, ARPC5, ARPC5L, CDC42, CFL1, PAFAH1B2, RHOA
Antigen Presentation Pathway	2.5	12.8	CALR, CANX, CD74, PDIA3, PSMB6
Eumelanin Biosynthesis	2.41	50	DDT, MIF
L-cysteine Degradation I	2.41	50	GOT1, GOT2
VEGF Signaling	2.39	8.08	ACTN4, EIF1, EIF2B1, EIF2B2, EIF2B3, ELAVL1, RALA, YWHAE
Mevalonate Pathway I	2.3	21.4	ACAA2, ACAT2, HADHA
Glutathione Redox Reactions I	2.2	13.8	GSR, GSTP1, MGST3, PRDX6
Tight Junction Signaling	2.16	6.15	ARHGEF2, CDC42, MYH10, NSF, NUDT21, PPP2CA, RHOA, SAFB, SPTAN1, STX16, SYMPK
Ferroptosis Signaling Pathway	2.13	6.82	ARF4, G3BP1, H2AC18/H2AC19, H2AZ2, NFS1, PEBP1, RALA, SLC3A2, TXNRD1
Necroptosis Signaling Pathway	2.13	6.41	SLC25A10, SLC25A13, SLC25A3, SLC25A4, TIMM44, TIMM50, TOMM20, TOMM22, TSPO, VDAC3
Kinetochores Metaphase Signaling Pathway	2.09	7.21	BUB3, H2AC18/H2AC19, H2AZ2, PPP1CA, PPP1CB, PPP1R14B, RAD21, SMC1A
Synaptogenesis Signaling Pathway	2.09	5.08	ACTR2, AP2A1, ARPC2, ARPC4, ARPC5, ARPC5L, CALM1 (includes others), CDC42, CFL1, HSPA8, NAP1L1, NSF, RAB5B, RALA, RHOA, STX16
Pyruvate Fermentation to Lactate	2.03	33.3	LDHA, LDHB
Pentose Phosphate Pathway (Non-oxidative Branch)	2.03	33.3	TALDO1, TKT
Zymosterol Biosynthesis	2.03	33.3	HSD17B7, NSDHL
Mismatch Repair in Eukaryotes	1.98	16.7	LIG1, MSH2, PCNA
Ephrin B Signaling	1.97	8.33	CAP1, CDC42, CFL1, GNAI2, RAC2, RHOA
Acetyl-CoA Biosynthesis I (Pyruvate Dehydrogenase Complex)	1.89	28.6	DLAT, PDHA1
Axonal Guidance Signaling	1.87	4.32	ACTR2, ADAM10, ARPC2, ARPC4, ARPC5, ARPC5L, CDC42, CFL1, DPYSL2, GNAI2, ITGB7, LNPEP, PDIA3, PFN1, PMPCA, PSMD14,

<b>Table 24 Continued</b>			
			RAC2, RALA, RHOA, TUBA4A, TUBB, TUBB4B
Aldosterone Signaling in Epithelial Cells	1.85	5.81	DNAJB1, DNAJB11, DNAJC10, DNAJC9, HSPA13, HSPA1A/HSPA1B, HSPA4, HSPA4L, HSPA8, PDIA3
Cell Cycle Control of Chromosomal Replication	1.84	8.93	LIG1, MCM3, MCM6, PCNA, TOP2A
ILK Signaling	1.81	5.47	ACTN4, CASP3, CDC42, CFL1, ITGB7, MYH10, NACA, PPP1R14B, PPP2CA, RAC2, RHOA
Endoplasmic Reticulum Stress Pathway	1.79	14.3	CALR, CASP3, ERN1
tRNA Charging	1.75	10.3	CARS2, EPRS1, HARS2, MARS2
Apoptosis Signaling	1.74	6.73	ACIN1, AIFM1, BAX, CASP3, CYCS, RALA, SPTAN1
Chemokine Signaling	1.74	7.41	CALM1 (includes others), CFL1, GNAI2, PPP1CB, RALA, RHOA
HIF1 $\alpha$ Signaling	1.71	5.29	ELOB, GPI, HSPA1A/HSPA1B, HSPA4, HSPA8, LDHA, LDHB, RAC2, RACK1, RALA, RAN
Semaphorin Signaling in Neurons	1.69	8.2	CDC42, CFL1, DPYSL2, RAC2, RHOA
Superpathway of Methionine Degradation	1.68	9.76	GOT1, GOT2, MAT2A, MMUT
Leucine Degradation I	1.67	22.2	IVD, MCCC2
Lanosterol Biosynthesis	1.59	100	LSS
Alanine Biosynthesis III	1.59	100	NFS1
Calcium Transport I	1.58	20	ANXA5, ATP2A2
Estrogen Biosynthesis	1.55	8.89	HSD17B12, HSD17B4, HSD17B7, POR
Coronavirus Replication Pathway	1.55	8.89	COPG1, TUBA4A, TUBB, TUBB4B
Sucrose Degradation V (Mammalian)	1.5	18.2	ALDOA, TPI1
Pentose Phosphate Pathway	1.5	18.2	TALDO1, TKT
Purine Nucleotides De Novo Biosynthesis II	1.5	18.2	ADSS2, PPAT
Dolichyl-diphosphooligosaccharide Biosynthesis	1.5	18.2	ALG8, DPM1
Apelin Adipocyte Signaling Pathway	1.5	6.52	GNAI2, GSTP1, MGST3, PRDX6, RAC2, SOD1
Germ Cell-Sertoli Cell Junction Signaling	1.49	5.29	ACTN4, CDC42, CFL1, RAC2, RALA, RHOA, TUBA4A, TUBB, TUBB4B
Ephrin A Signaling	1.49	8.51	ADAM10, CDC42, CFL1, RHOA
Virus Entry via Endocytic Pathways	1.48	5.93	AP2A1, AP3B1, CDC42, CLTA, ITGB7, RAC2, RALA
Cell Cycle: G2/M DNA Damage Checkpoint Regulation	1.4	8	TOP2A, YWHAB, YWHAE, YWHAZ
Glioma Invasiveness Signaling	1.39	6.85	CD44, CDC42, RAC2, RALA, RHOA
Sertoli Cell-Sertoli Cell Junction Signaling	1.38	4.85	ACTN4, CDC42, ITGB7, RALA, SPTAN1, SPTBN1, SYMPK, TUBA4A, TUBB, TUBB4B

<b>Table 24 Continued</b>			
UDP-N-acetyl-D-galactosamine Biosynthesis II	1.37	15.4	GNPDA1, GPI
ATM Signaling	1.35	6	CBX3, CBX5, HP1BP3, PPP2CA, SMC1A, SMC2
Macropinocytosis Signaling	1.33	6.58	ACTN4, CDC42, ITGB7, RALA, RHOA
Phenylalanine Degradation IV (Mammalian, via Side Chain)	1.31	14.3	GOT1, GOT2
Colanic Acid Building Blocks Biosynthesis	1.31	14.3	GPI, UGP2

**Table 25. Top 10 Significantly Downregulated Reactome Pathways in MM.1S Cells Treated with Triacsin C for 24 hours**

<b>Reactome Term</b>	<b>p-value</b>	<b>q-value</b>	<b>Significantly Associated Genes</b>
Aryl Hydrocarbon Receptor Signaling R-HSA-8937144	0.0142	0.3086	[ARNT2]
POU5F1 (OCT4), SOX2, NANOG Repress Genes Related To Differentiation R-HSA-2892245	0.0183	0.3086	[SOX2]
Activation Of Ca-permeable Kainate Receptor R-HSA-451308	0.0183	0.3086	[GRIK4]
Type I Hemidesmosome Assembly R-HSA-446107	0.0183	0.3086	[ITGB4]
POU5F1 (OCT4), SOX2, NANOG Activate Genes Related To Proliferation R-HSA-2892247	0.0243	0.3086	[SOX2]
Activation Of Arylsulfatases R-HSA-1663150	0.0263	0.3086	[ARSI]
Clathrin-mediated Endocytosis R-HSA-8856828	0.0342	0.3086	[AMPH, FNBP1L]
Gastrulation R-HSA-9758941	0.0342	0.3086	[SOX2]
Syndecan Interactions R-HSA-3000170	0.0402	0.3086	[ITGB4]
Laminin Interactions R-HSA-3000157	0.0441	0.3086	[ITGB4]

**Table 26. Top 10 Significantly Downregulated KEGG Pathways in MM.1S Cells Treated with Triacsin C for 24 hours**

<b>KEGG Term</b>	<b>p-value</b>	<b>q-value</b>	<b>Significantly Associated Genes</b>
Renal cell carcinoma	0.0088	0.35041	[ARNT2, PAK6]
Viral protein interaction with cytokine and cytokine receptor	0.0178	0.35041	[IL22RA1, CX3CR1]
Mannose type O-glycan biosynthesis	0.0461	0.35041	[B3GAT2]

## **8. BIOGRAPHY OF AUTHOR**

Connor S. Murphy was born in Hull, Massachusetts and received his B.S. in Biology in 2014. Connor is a candidate for the Doctor of Philosophy Degree from the University of Maine in May 2024.